NEW TECHNIQUES FOR IMAGING PHOTON-COUNTING AND PARTICLE DETECTORS

Jonathan Stephen Lapington

A thesis submitted to the University of London

for the degree of Doctor of Philosophy

Mullard Space Science Laboratory

Department of Space and Climate Physics

University College London

May 2003

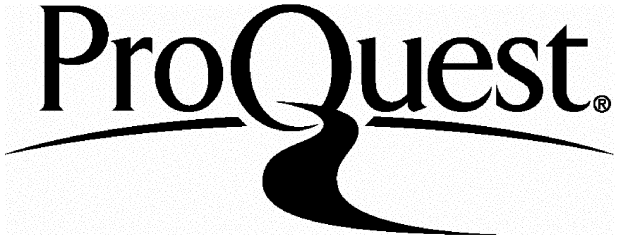

To my Parents...

To my Father, who tragically never lived to see,
And to my Mother, who never expected to see,

The joyful day I would submit this thesis.

Abstract

Since the advent of space-based astronomy in the early 1960's, there has been a need for space-qualified detectors with sufficient sensitivity and resolution to detect and image single photons, ions or electrons. This thesis describes a research programme to develop detectors that fulfil these requirements.

I begin by describing the role of detectors in space astronomy and follow with a review of detector technologies, with particular emphasis on imaging techniques. Conductive charge division image readouts offer high performance, simplicity, and flexibility and their potential is investigated in both theory and practice. I introduce the basic design concept and discuss the fundamental factors limiting performance in relation to physical design and to underlying physical processes. Readout manufacturing techniques are reviewed and a novel method presented. I describe specific space and ground-based readout applications which proved valuable in teaching lessons and raising questions. These questions initiated an experimental programme, whose goals were to understand limiting physical processes and find techniques to overcome them. Results are presented, and the innovation of the progressive geometry readout technique, which this programme also spawned, is described.

Progressive geometry readout devices, such as the Vernier anode, offer dramatically improved performance and have been successfully flight-proven. I describe the development of a Vernier readout for the J-PEX sounding rocket experiment, and discuss the instrument calibration and the flight programme.

First investigations into a next generation of charge division readout design are presented. These devices will use charge comparison instead of amplitude measurement to further enhance resolution and count rate capability.

In conclusion, I summarize the advances made during the course of this research, and discuss ongoing technological developments and further work which will enable MCP detectors to continue to excel where characteristics such as true photon-counting ability, high spatial resolution, format flexibility, and high temporal resolution are required.

Acknowledgements

Many people have contributed to the discussions, and sometimes arguments, which have often been seminal in the formulation of the ideas and concepts put forward, and hopefully justified in this thesis. A large proportion of these people work or have worked at the Mullard Space Science Laboratory, and I have a great debt to both them and MSSL as an institution, for the grounding I was given in the scientific method necessary to accomplish a successful research programme.

To name names, my original mentor was Hugo Schwarz, whose competitive style set the tone; a hard act to follow. But follow they did, and I gratefully acknowledge the significant inputs of Alan Smith, Dave Walton, Mick Edgar, Bob Kessel, Ady James, Hajime Kawakami, and Dhiren Kataria and the many others who know who they are, and who provided so much help, advice, and cranial stimulation along the way.

Many thanks must go to Matt Whyndham, Liam Worth, and Ben Sanderson, without whom life would have been immensely poorer, and ideas and amounts of data immeasurably thinner, and Jason Tandy and Nigel Bannister, the two rocketeers and New Mexican compadres without whose expertise, enthusiasm, and humour, White Sands would pale even more.

I would especially like to give my thanks Len Culhane for his continuing support since beginning my studies and his assistance in finally submitting this thesis.

Lastly, I would like to thank Linda and Pandora for sacrificing several months of my companionship and giving me the opportunity to finally pen what follows...

Contents

List of Figures

List of Tables

Chapter 1

Introduction – a Thesis Roadmap

From time immemorial humankind has observed the heavens for a variety of reasons; to seek the realm of the Gods, to look for answers to explain our worldly woes, and today as scientists to search for the elusive answers to the fundamental questions about the nature of the universe. Whatever the motivation behind the activity, it can never be in anything other than awe and wonderment that we nightly observe the almost inexplicable, incomprehensible environment of space from the comfort of mother earth.

Our earliest observations of the heavens were by necessity carried out in the natural realm of human physical experience, using the most "remote-sensing" of all our senses, namely that of sight. Even when the first instrument was developed to enhance this experience, and improve the 'data', it remained limited to the bandpass defined by the detector system; the observer's, namely Galileo's, eyes [1].

The momentous discoveries made in the physical sciences during the period from the renaissance to the early twentieth century, which encompassed mechanics, gravity, electrostatics, electrodynamics, and quantum mechanics to name but a few, made us aware of the much broader spectra of phenomena that might be observable from space. However it was not until the birth of radio astronomy in the 1940's, which evolved from the development of radio technologies, accelerated by the Second World War, that the universe outside the sphere of influence of the earth was observed in anything other than optical light.

The war also accelerated the development of rocket technology, giving rise to the infamous and iniquitous V2, which fortunately came into existence too late to maximize its negative impact. This technology exerted a positive influence, in astronomy at least, with the sounding-rocket experiments that began post-war in the USA. Sub-orbital rocket-launched instruments allowed us for the first time to escape the earth's protective umbrella, the motherly atmosphere which fortunately shields us from all manner of exciting electromagnetic wavelengths and particles. Space-based astronomy had begun.

Once above the atmosphere, for the first time, the possibility to detect the full spectrum of electromagnetic radiation was available. Whilst in the optical waveband photon fluxes are

relatively high, natural phenomena generally obey a law whereby as photon energy increases, flux decreases. Since increase in understanding generally progresses with the ability to see ever fainter objects at ever further distances, this predicated the development of more sensitive and sophisticated instruments for higher energies in the UV and beyond.

The first celestial X-rays were observed in 1948 by Burnight [2]. This experiment used photographic film as the detecting medium, its poor sensitivity limiting it to the detection of solar X-rays. The observation of more distant X-ray extra-solar sources, which were expected to have many orders of magnitude lower fluxes, would have to await the application of more sensitive quantum detectors such as the Geiger counter [3]. Giacconi *et al.*[4] utilized such a device to observe the first extra-solar source, Sco-X1 in 1962. In parallel, the development of imaging techniques such as the modulation collimator [5] and grazing incidence optics by Wolter [6], introduced the possibility of accurately imaging the sky at X-ray wavelengths. A role for imaging photon-counting detectors in space-based instrumentation had been defined.

In parallel with these investigations in electromagnetic phenomena, the same launch vehicles were being used for missions exploring the ionosphere [7]. Today, a major instrument in this field of study is the plasma analyser which detects ions or electrons and measures their energy and angular distribution. A common thread between these two fields of study is the detector design. This is especially true in the case of microchannel plate (MCP) based detectors which are of very similar design and use the same technologies.

Today, imaging photon-counting and particle detectors play an important role on many of the major observatory class missions such as SOHO, CLUSTER, XMM, HST, CHANDRA together with a host of smaller satellite and sounding rocket missions. The detector technologies used for these applications come from a range of disciplines. The traditional role of gas proportional counters has been diminishing as alternative strategies have proven more competitive, however the development of a variety of micro-patterned gaseous detectors [8] have rejuvenated this area. Vacuum tube devices, such as the MCP image intensifier [9] have always played a role, though their area of predominance has been eaten into by developments in solid state semiconductor technology. The improvement in quantum efficiency of the charge coupled device (CCD) [10] at UV wavelengths has strongly challenged the traditional predominance of the MCP based device, even though the CCD is not truly photon counting. Cryogenic detectors are relative newcomers to the field but offer the potential for non-dispersive simultaneous energy and position resolution with high effective areas. The latest cutting edge developments in this area are the production of arrays of either Transition Edge Sensors (TES) [11] or superconducting tunnelling junctions (STJ) [12], currently offering limited spatial resolution but with the prospect of improvement. However the situation is constantly in flux as continuing technological improvements in all these device types push performance boundaries ever upwards, fuelled by competition to win mission selection. This thesis describes a research programme undertaken by the author to take part in these technological improvements and develop designs with improved performance in the fields

of both gaseous and vacuum based detectors, namely proportional counters and MCP image intensifiers. Particular emphasis was placed on the development of imaging technologies for these devices, primarily to provide high spatial resolution and linearity at higher count rates.

1.1 Research Programme

The programme was initiated with the development of the imaging capability for a large format multi-step gas proportional counter, the Penning Gas Imager (PGI) [13], proposed as a focal plane instrument for the AXAF (renamed CHANDRA) satellite observatory [14], and eventually flown on a sounding rocket experiment. The PGI utilized a large format wedge and strip anode (WSA) image readout [15], a charge division device traditionally associated with MCP detectors, which required modification to suit the proportional counter characteristics. A novel mechanical implementation was used in order to reduce WSA capacitance which would have otherwise impacted performance. Following this, similar techniques were applied to redesign an imaging MCP image intensifier. This initial work provided an invaluable introduction to the merits and pitfalls of charge division image readouts used in differing applications and, in a wider context, to the variety of other competitive detector and image readout technologies vying for supremacy in this branch of space–based instrumentation. After reviewing the competing techniques and in the light of the requirements of a number of particular missions, I chose to focus my research on the development of detector systems utilizing the generic readout types categorized by the term "conductive charge division readout", perceiving this technique to be a relatively simple, flexible and having unrealised potential if some of its drawbacks could be overcome.

The programme proceeded with the development of a prototype one-dimensional imaging proportional counter for Yohkoh-BCS [16] and the definition of the MCP detector design for the SRG-Tauvex [17] and MARS96-Fonema [18] satellite based instruments. A parallel series of experiments was undertaken to understand and overcome physical processes underlying detector operation and limiting performance. These experiments were used to investigate loss of resolution in both the charge amplification and readout charge collection processes, and looked into issues such as charge footprint distribution, secondary electron production, charge redistribution, and substrate charge-up. This experimental programme also spawned readout pattern development, which led to the invention of a new readout technique, coined the "progressive geometry readout", a generic term for a family of readout designs, the first of which provided high resolution imaging capability for the SOHO-GIS [19] spectrometer detectors. The Vernier anode, the latest in the line of these progressive geometry readouts, provides state-of-the-art spatial resolution, overall detector resolution being limited by the quantisation due to the MCP pore geometry, and has already been demonstrated successfully on the J-PEX [20] UV spectrometer sounding rocket experiment [21]. However the "state-of-the-art" never rests and the next stage in readout evolution has also been started within this research programme. A new scheme has been designed which still retains the high spatial resolution exemplified by the Vernier anode, but uses

charge comparison instead of charge measurement to achieve much higher count rate potential. The eventual goal of this development is to integrate the readout with electronics on a single substrate. Alongside other recent technological advancements such as smaller pore size MCPs and miniaturized electronics using multi-channel charge sensitive ASICs, this will enable the manufacture of a rugged, compact, low-mass and low-power detector with state-of-the-art imaging performance and dynamic range.

1.2 Thesis Outline and Contribution

Chapter 2 is a review of the variety of detector types available with particular emphasis on techniques used for image readout. Current state-of-the-art designs are discussed and a brief account is given of the merits and limitations of each type. I conclude that conductive charge division readouts realize high performance, simplicity and flexibility and their potential makes them worthy of further development.

Chapter 3 focuses on the operation of charge division imaging devices, both in theory and practice. The basic design concept is introduced and the many variants are described. The fundamental factors limiting performance are discussed in relation to the image readout design and to the physical processes controlling their operation. Manufacturing techniques are reviewed and a new method described.

The practicalities of operation of conductive charge division readouts in a variety of instruments are dealt with in chapter 4. I discuss specific examples of the application of these readouts to sounding rocket and satellite missions with particular reference to the lessons learnt and questions raised.

Chapter 5 describes a series of experimental programmes undertaken to answer these questions with the goals of understanding limiting physical processes, enhancing performance and evaluating new techniques. Experimental results are described and solutions to some of the common limitations previously encountered with charge division devices are presented.

Chapter 6 maps the evolution of the progressive geometry readout designs, including the Vernier and SPAN anodes developed during this research. I discuss both the theoretical concepts of their operation and their practical design, manufacture and performance. First experimental results are presented

The further development of the Vernier readout is described in Chapter 7. The very high spatial resolution of the Vernier is demonstrated and an analysis of image data is used investigate image nonlinearities, ascertain the physical causes and remedy them. I discuss the application of the Vernier technology to the J-PEX high resolution FUV spectrometer mission and calibration and present results from the flight.

Chapter 8 introduces the next generation of charge division readouts under development in this research programme. Whilst having similar physical characteristics to other charge division designs, these designs will use charge comparison instead of charge amplitude measurement, giving them the capability to maintain high spatial resolution at higher count rates.

Chapter 9 summarizes the advances in technology in imaging, photon counting and particle detectors achieved during the research described in this thesis. I discuss the on-going technological developments in the field and conclude with a proposal for a next generation detector design.

This thesis makes original contributions to the field of research in several areas; the further understanding of physical principles underlying the operation of proportional counter and MCP detectors, the development of practical techniques to mitigate performance limiting factors and allow improvement of spatial resolution, linearity and event rate, enhancement in detector performance through the invention of novel readout designs which advance the state-of-the-art, and the development and application of new readout manufacturing techniques.

Chapter 2

A Review of Imaging, Photon-counting Detector Technologies

Imaging photon-counting and particle detectors are vital research tools in a diverse range of scientific disciplines; from astronomy to biology, high energy physics to medical diagnostics. The inter-disciplinary nature of this field of instrumentation means that cross fertilisation of ideas between fields is valuable, thus while the subject of this particular research programme is the development of detectors for space-based astronomy, techniques used in other fields are discussed where relevant.

This chapter is divided into three sections. The first is an overview of the five major categories of detector types used in this field, namely gas counters, vacuum tubes, semiconductors, hybrid, and cryogenic devices. Developments in semiconductor and cryogenic detectors are briefly mentioned but excluded from further discussion, being outside the scope of this thesis. The second section details a wide variety of imaging photon-counting and particle detector types from the gas counter, vacuum tube, and hybrid detector categories, focusing particularly on those with higher spatial resolution. Though not comprehensive, it includes many types of imaging detectors used to detect and image photons in the optical to X-ray spectrum, and low energy charged particles and describes the event detection, signal amplification and method of imaging. The third section focuses on the higher resolution electronic position readouts employed in these devices, including those which compete directly with the charge division progressive geometry readouts, developed during the course this research.

2.1 An Overview of the Detector Categories

The operation of a quantum detector can generally be characterized by a sequence of actions initiated by the arrival of an event; the detection process, the amplification process, and the measurement process, where the amplified signal is used to determine event parameters such as energy, position and time of arrival. In our case the event will be a photon or charged particle. For the former, the dominant mechanism for interaction with matter at energies below 100 keV is by

the photoelectric effect, producing a photoelectron, at which stage both photon and particle detectors become operationally equivalent. The photoelectron or particle initiates charge amplification, using a variety of means to generate a charge signal large enough to be measured. A smaller number use other techniques such as light amplification, or in the case of the microcalorimeter, direct measurement of temperature rise, which corresponds to input energy. Ultimately the result of all these techniques is to produce a signal that, combined with sufficient signal-to-noise-ratio, can be measured electronically to determine event parameters. In today's instruments these signals are almost exclusively digitized to facilitate data processing and telemetry. The principles of operation and device features particular to each of the generic detector types described in this chapter are described in the following section.

2.1.1 Gaseous detectors

Gas filled counters can be used to detect X-ray photons with energies typically higher than 250 eV. For energies below 100 keV they are commonly operated in the proportional regime, whereby the amplitude of the output signal represents the photon energy. These detectors are known as proportional counters and function by absorbing the X ray photons in their fill gas and amplifying the small number of primary electrons produced to a size large enough to be measured electronically. The amplification process is achieved by means of an electric field, either via electron avalanche, whereby the electron signal is directly amplified, or by a scintillation process, in which the gas fill atoms are excited by the primary electrons and scintillate producing a larger number of UV photons whose number and centroid can be measured.

Gas counters evolved from the basic wire proportional counter, being extended to a multi-wire configuration area detector [22][23] which, when combined with an electronic image readout device, was capable of two-dimensional imaging. Other gaseous detector systems were also developed, such as the parallel plate [24], multi-step [25], and gas scintillation proportional counters [26]. The role of gas counters has diminished over the years, though the development of micro-patterned devices [28], such as the micro-strip proportional counter, has extended their useful life.

2.1.2 Vacuum Tubes

As their name indicates these vacuum based devices rely on in-vacuo event detection and amplification processes. This may be provided by an evacuated enclosure, requiring an input window and placing a lower wavelength limit of ~110 nm on detectable radiation, or they may be open-faced detectors exposed to the relative vacuum of space or, for ground-based applications, an external vacuum enclosure.

In photon counting applications a solid state photocathode is commonly used which emits photo-electrons on absorption of an incident photon. The photocathode is usually deposited on the inner

surface of an input window (semi-transparent), or directly on the face of the amplification element. Either a light or charge amplification process takes place, the former typified by the Imaging Photon Counting System (IPCS) [30] which uses Gen-I type [32] intensifiers used in cascade, the latter by the nowadays more commonly used photomultiplier and MCP designs. The charge amplification process uses the photoelectron, or particle in the case of particle detectors, to produce a cascade of secondary electrons from a series of dynodes (discrete as in the photomultiplier tube [33], or continuous as in the MCP [9]). The resultant amplified electron signal can be measured directly by an electronic image readout, or converted by means of a phosphor into light which can then be collected and converted to electrical signals, for instance, using a semiconductor device such as a charge coupled device (CCD) [34]. The imaging techniques, especially those used for systems utilizing charge amplification with electronic readouts, have much in common with those developed and used for gaseous detectors.

2.1.3 Semiconductor Devices

The basic principle underlying the operation of semiconductor detectors is the conversion of the energy deposited by an incident photon (or possibly particle) within the charge carrier depleted region of a reverse biased junction of a diode or in intrinsic semiconductor. This energy is used to promote charge carriers from the valence band to the conduction band of the solid state device, the number of which is proportional to the input energy. Semiconductor materials typically have a conversion gain of several eV of incident energy per electron-hole pair (3.6 eV in silicon). This generates a large number of electron-hole pairs at X-ray energies, producing a signal large enough for electronic measurement providing both image and energy information. At lower input energies, at UV and longer wavelengths, semiconductor detectors are not true photon counting devices although their higher quantum efficiency and low readout noise compared to vacuum devices, provide signal-to-noise ratios which make them highly competitive with photon counting detectors except at low fluxes or if high time resolution is required.

The avalanche photodiode (APD) [35] is a special case having a region of high electric field, akin to the proportional counter, where signal amplification via electron avalanching can occur within the semiconductor solid. The higher signal to noise ratio allows it to photon count at longer wavelengths than traditional semiconductors, but imaging using APD arrays is limited by physical size constraints.

The charge coupled device (CCD) has totally revolutionized electronic imaging in most fields, providing image formats up to 9216 × 9216 pixels [36] and pixel sizes down to 2.4 μm. Its impact as a true photon counting detector is limited to X-ray wavelengths, however the recent development of low light level CCDs, which utilizes a solid state amplification scheme similar to the APD, offers the possibility of providing near photon-counting performance at optical wavelengths.

Other semiconductor imaging arrays are also available such as charge injection devices (CID) [37] and CMOS image sensors [38]. These devices offer advantages over the CCD such as single pixel addressing and higher effective frame rates, lack of image blooming and charge transfer effects, and higher dynamic range.

The Medipix chip[39] is a recently developed semiconductor device for high speed X-ray imaging, photon counting applications. The device is a totally parallel, electronic readout chip ASIC using CMOS technology, the latest version of which (Medipix2) has a 256 × 256 format. This chip, made possible by progress in sub-micron CMOS technology and dense interconnection technology, provides direct electronic readout from a variety of sensor materials (Si, GaAs, CdZnTe,...). It was initially developed for particle detection in high energy physics experiments, but its high sensitivity and large dynamic range (up to 0.4 GHz/mm^2), coupled with its true photon counting capability which provides low contrast detectability, make it a valuable tool for a variety of applications including low dose medical X-ray imaging.

2.1.4 Hybrid Technologies

There are several types of hybrid devices which use a combination of vacuum and solid state technologies. These include electron bombarded CCDs (EBCCD) [40], intensified CCDs (ICCD) [34], the Precision Analog Photon Address (PAPA) [41] detector, and hybrid vacuum photodiodes [42].

EBCCDs photon count by directly detecting individual photoelectrons with a CCD. They have been demonstrated in several configurations, using semi-transparent photocathodes with electrostatic and proximity focusing, and opaque photocathodes magnetically focused to CCDs. The single photoelectron is accelerated by several kilovolts giving it sufficient energy to penetrate to the depleted region of the CCD and deposit energy to generate an event signature.

The intensified CCD uses a sealed tube image intensifier comprising an input window coated with a semi-transparent photocathode, an MCP stack and an output phosphor. The intensifier is coupled via fibre-optic taper to a CCD. For high resolution applications the light spot is spread over several CCD pixels, allowing centroiding.

The PAPA detector uses an ingenious scheme comprising a conventional image intensifier whose light output is spatially encoded by a series of masks. The intensity of each encoded signal is measured by an array of photomultiplier tubes and used to decode the event position coordinates.

Hybrid photodiodes have been manufactured using a compact vacuum diode design, the photocathode coated input window being proximity focused on to a PIN diode array with typically 32 elements within the vacuum tube.

2.1.5 Cryogenic Techniques

This relatively new branch of photon counting detectors is characterized by their requirement to operate at very low temperatures, of typically 0.1 – 4K.

Microcalorimeters [43] are in essence very sensitive thermometers, designed so that their thermal noise is low enough to detect the temperature rise caused by absorption of an X ray. This is generally carried out by measuring the variation of resistance with temperature of a thermistor. Resolution is highly dependent on temperature and operation in the milli-Kelvin regime is required.

The Transition Edge Sensor (TES) [11] is an ingenious development of the microcalorimeter, which utilizes the transition between the superconducting and non-superconducting states of the thermistor to enhance the sensitivity of the temperature measurement, and is dynamically stabilized at the transition temperature using a feedback technique.

The Superconducting Tunnelling Junction (STJ) [12] has more in common with semiconductor detectors, relying on the splitting of Cooper pairs, bound pairs of electrons in very low energy states found only within superconductors. The detector is designed so that absorption of a photon causes the Cooper pairs to split adjacent to a thin insulating barrier across which the free electrons can tunnel, creating a signal proportional to the photon energy and measured using very sensitive SQUID based charge measurement electronics. Though the STJ's theoretical potential as a high energy resolution X-ray detector remains unrealized, STJ arrays are under development which offer non-dispersive, broadband spectral coverage at longer wavelengths in the UV and optical bands.

Rudimentary microcalorimeter and STJ imaging arrays are now being developed, which along with space compatible cryogenic coolers, are likely to place these devices at the forefront of X-ray astronomy in the next decade.

2.2 A Review of Detector Types

2.2.1 Gaseous Detectors

This section begins with an explanation of the fundamental principles of operation of gas counters followed by a description of the first ever photon counting device, the wire counter. Its imaging capabilities are essentially limited by its geometry to one dimension, however in 1968 Charpak [22] developed the imaging capability of the multi-wire proportional counter (MWPC), extending the technique into two dimensions. Other techniques have been developed since such as the gas scintillation proportional counter (GSPC), parallel plate detector, and the multi-step detector.

Gas filled detectors can have large imaging areas combined with good sensitivity and moderate energy resolution (typically 15% FWHM at 5.9keV), a combination of factors which led to their

role as a workhorse imager in particle physics experiments. They were also used in astronomical applications on a number of space-based X ray observatories, for example, the imaging proportional counters on the Einstein IPC [47] and the ROSAT PSPC [48].

Beginning with the Micro-Strip Proportional Counter (MSPC) [28], the essence of the MWPC technique was embodied in a monolithic structure consisting of an electrode pattern supported on a solid substrate, with practical and performance advantages. The MSPC and its various progeny, such as the Micro-Gap Counter (MGC) [44] and newer variants , together with other micro-patterned devices such as the Gas Electron Multiplier (GEM) [45] and the Micro-Dot and Well pixelated detectors, have brought a new lease of life to large area, high resolution proportional counters, and they are now being proposed again for space applications [46].

2.2.1.1 Principle of Operation

Proportional counters detect photons by their interaction with the detector fill gas. This interaction, which is dominantly photoelectric absorption, produces a photoelectron and other de-excitation products (Auger electrons, fluorescence photons, etc.) which interact further with the gas to produce ionization until thermalized. The net result is the liberation of a quantity of charge whose magnitude is proportional to the incident photon energy. The energy to charge conversion factor is gas dependent and has a typical value of 20-25 eV per electron thus around 40-50 electrons are liberated per kiloelectron volt of incident energy assuming that none escapes by means of fluorescent photons or collision with the counter wall.

The amount of charge liberated by an X-ray is insufficient to measure electronically without some form of amplification. The most common approach is to accelerate the electrons in a potential field such that electron energy is raised above the gas ionization threshold. In this case further ionization can occur resulting in signal amplification. Typically, gas gains up to 10,000 can be stably achieved, however this is highly dependent on the detector geometry. At higher gains, high voltage breakdown caused by cosmic rays, field emission etc. can become a problem. Alternatively, if the electric field strength is just below that necessary for charge multiplication, the primary electrons can be made to produce metastable states of the gas filling which decay with the emission of scintillation light. This amplified signal in the form of light is collected and measured using photomultiplier tubes.

Imaging can be accomplished for either type of detector by determining the centroid of the charge or photon cloud produced. This is measured electronically with either a position sensitive cathode or anode, or a position sensitive PMT or array of PMTs.

2.2.1.2 The Wire Counter

The development of the proportional counter began with Rutherford and Geiger in 1908 [49] and its use had become widespread by the early 1950's. Geiger's original design, the wire counter,

consists of a thin wire stretched axially along a cylindrical gas containment vessel. X-rays enter the vessel through a X-ray transparent entrance window, usually of Beryllium or thin plastic and interact with the fill gas liberating a small cloud of primary electrons. The wire is held at a high positive potential, V, relative to the conductive inner surface of the containment vessel establishing a radial electric field whose strength, E(r) is given by the formula:-

$$(2\text{-}1)\quad E(r) = V/r \ln(b/a)$$

where a and b are the anode (wire) radius and cathode inner (containment vessel) radius respectively. The field causes the primary electrons to drift towards the anode wire towards which they are accelerated by the increasing field. At the point where the field reaches a suitably high value, the electrons gain sufficient kinetic energy between collisions with fill gas to cause ionization on further collision, producing secondary electrons which themselves produce more ionization. In a typical detector, the critical field value of $\sim 10^5$ Vcm^{-1} occurs at only a few wire radii from the anode wire and so the vast majority of events, which are absorbed outside this volume, undergo the same gas gain. Each primary electron can produce a large number of secondaries (typically $\sim 10^4$) in the avalanche. However, if the multiplication factor, commonly referred to as the gas gain, is too large, the space charge effect at the leading edge of the avalanche reduces the local electric field strength, further gain is suppressed, and pulse saturation occurs. In this operating regime, true proportionality has been lost, i.e. the signal amplitude is no longer a linear function of the absorbed energy and the detector is operating in what is known as the region of limited proportionality. The variation of gas gain with voltage is shown in Figure 2-1. Even when operating in the proportional regime, there are significant statistical fluctuations in the gas gain from event to event owing to the variation in the relative amounts of energy divided between ionization and the formation of excited states of the fill gas in the first few multiplication steps of the avalanche. The proportionality between energy and pulse height is only accurately reflected when the mean pulse height for a large number of events is measured. After multiplication, the charge collected on the wire is now large enough to be measured electronically with sufficient signal to noise ratio.

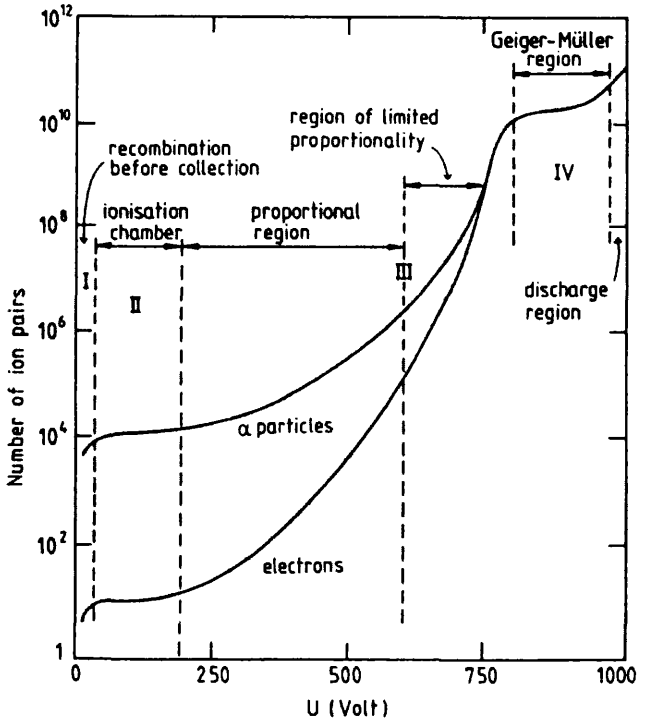

Figure 2-1. The variation in gas gain with voltage for a typical wire counter [22].

The small dimension of the avalanche region (a few wire radii) endows the wire counter with a fast pulse risetime. The electron transit through the avalanche is extremely fast, but most of the signal is actually developed as the positive ion cloud drifts away from the anode wire. Due to the geometry of the electric field, the ions traverse through the greater part of the electric field potential, and thus induce the bulk of the signal, in a few wire radii corresponding to a risetime of order 1μs. A much slower signal of lower amplitude is produced as the ions drift relatively slowly in the much weaker field towards the cathode, their eventual destination.

The gas gain achieved in a proportional detector is a function of the geometry of the detector, the voltage applied between the cathode and anode wire and the atomic and molecular species making up the gas fill. A typical wire chamber has a thin anode wire of 25μm diameter, a cathode radius of a few centimetres, a gas filling pressure of one atmosphere and operates at useable gains with an applied voltage of 500-1000V using a typical gas fill.

The gas fill itself is usually based on a noble gas since these are the only atomic gases, and as such, do not have the rotational and vibrational energy states common to molecular species which soak up energy otherwise used to produce valuable ionization. However this is not the end of the story since pure noble gases produce UV light due to excitation during the avalanche process when used even at moderate gas gains. This results in unstable operation since the UV can liberate further photoelectrons from the detector body causing after pulses. This effect can be mitigated by the addition of a small proportion of quench gas (a few percent), which is generally molecular in nature, and serves to safely absorb the UV before it can cause harm and to de-excite the metastable noble atoms before they produce UV. Argon or Xenon is the commonly used noble gas component along with a methane or carbon dioxide quench. The choice of gas fill is heavily

dependent on the energy range of the detector. At energies greater than 10-20keV the stopping power of Argon diminishes rapidly and Xenon, with a higher atomic mass is used because the photoelectric cross-section varies as Z^n, where n is 4 to 5. For energies greater than 100keV, even Xenon in a high pressure detector with a thick (10cm) absorption region is almost transparent.

The quench gases serve to enhance the detector performance in other ways. Electron drift speeds in pure atomic gases are low because collisions are elastic and the electron follows a highly random path from collision to collision. With the addition of a polyatomic quench, inelastic collisions with the quench cause the electrons to lose momentum and their motions are more dominated by the prevailing electric field. Drift speeds can be increased by an order of magnitude reducing the drift time by a corresponding factor. This is useful in reducing loss of charge through recombination which occurs even in the presence of minute concentrations of electronegative contaminants which outgas from the detector components. One drawback of quench gases is their ability to form deposits due to polymerization, though this is only a problem for long lifetime applications.

A family of quench gases exist which produce an enhanced detector response by exploiting the Penning effect [50]. The quench in 'Penning' gas mixture has an ionization potential sufficiently low to itself be ionized during de-excitation of metastables or absorption of UV photons. This extra ionization equates to a higher efficiency both for X ray absorption and multiplication and the statistics governing these two processes are improved resulting in lower operating voltages and improved energy resolution. Penning quench gases can be molecular or noble gases. Two common mixtures are Xenon-Argon and Argon-Isopropane; Argon and Isopropane being the respective quench gases. The PGI detector discussed in chapter 4 demonstrates the enhanced performance which can be achieved using the Penning effect.

2.2.1.3 The Multi Wire Proportional Counter

The MWPC was first developed in the 1940's and its imaging capability fully exploited by Charpak in 1968 [22]. The design consists of an array of anode wires arranged either as a number of discrete cells each containing an anode wire and separated by cathode wire planes, or as a planar array. The former arrangement can utilize the entire gas volume for X ray absorption whereas the latter has an absorption and drift region and a separate, shallow avalanche region close to the planar wire array. The latter design is generally chosen for imaging detectors as it allows two dimensional imaging within one counter.

A typical geometry found in an MWPC detector, as shown in Figure 2-2, has a plane of anode wires of 50μm diameter spaced 1mm apart. Cathode wire planes a few millimetres above and below the anode wire array, having a similar geometry to the anode wires, are used to separate and define the electrostatic fields of the absorption/drift region and the amplification region. The cathode wire planes are commonly strung orthogonally so that the charge induced on the planes

can be used to determine charge centroid in two axes and hence provide two dimensional imaging.

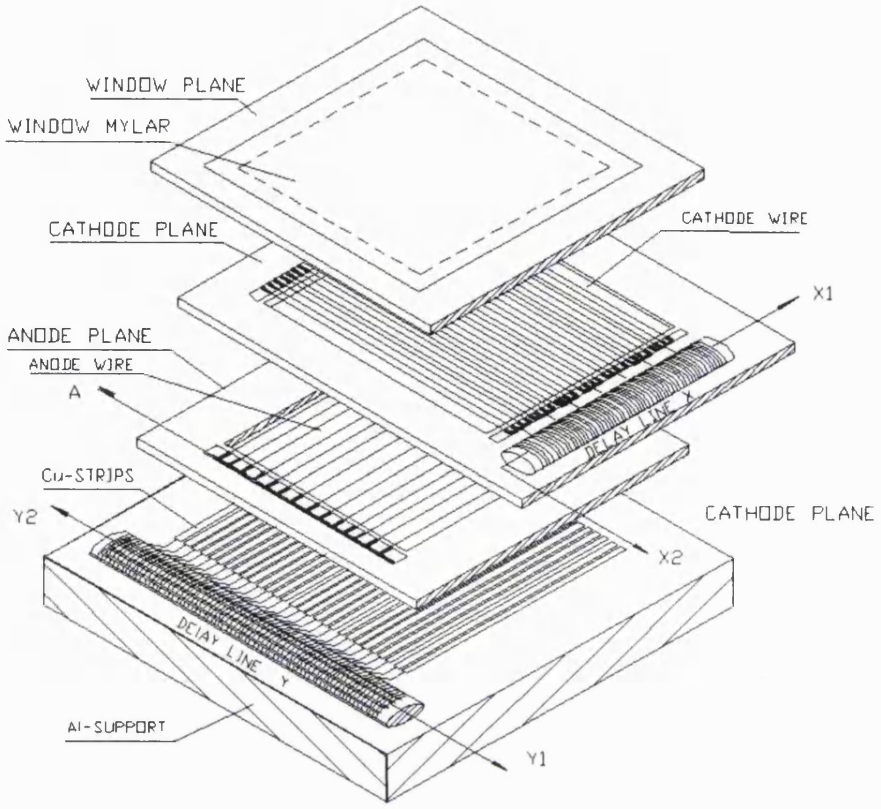

Figure 2-2. A typical MWPC layout with a delay line position readout.

Various techniques can be used to determine the charge centroid position. Firstly, the electron signal from the anode can be used directly. The event position along the wire can be determined by using a resistive anode wire, and the position calculated using either charge division or by means of timing methods via preamplifiers at each end of the wire. Position in the alternate axis can be determined by measuring the charge deposited on each wire. The use of a drift region and closely spaced anode wires ensures that the charge from one photon interaction is spread over several anode wires. Centroiding techniques can be used to determine the charge cloud centroid in the alternate axis to an accuracy smaller than the wire spacing. The number of electronics channels can be reduced by resistively coupling the ends of each wire and again using either charge division or timing methods to determine position in this axis.

The second, alternative method is to measure the charge induced on the cathode wires. The two cathode planes are electrostatically isolated from one another by the intermediate anode wire plane and constitute two independent one-dimensional readouts. As for the anode wires, various methods exist to sense position using resistive elements, either the wires themselves or discrete components, and using again charge division or timing methods. The non-dispersive LC delay line is an alternative approach using signal timing. Centroiding techniques may also be used, the induced charge being sensed either on each wire or on small groups of wires, and the centroid calculated using a centre of gravity or distribution fitting method. This technique has the

disadvantage of requiring a large number of independent processing channels but possesses a high degree of parallelism so that simultaneous events can be detected so long as they are spatially separated in both axes. The ability to detect simultaneous events can have advantages other than count rate. A valuable technique of improving background rejection useful at higher energies is known as fluorescence gating and will be discussed later.

A different approach is to use a planar charge division cathode pattern as typified by the backgammon [84] and wedge and strip patterns [15]. These provide, respectively one and two dimensional imaging, replacing the lower cathode wire plane.

Whereas these cathode plane readouts function using an induced charge pulse, the readouts used with the 'Parallel Plate' type of detector such as the EXOSAT PSD [51] and the Penning Gas Imager (which also falls into the category of multi-step), collect the avalanche electrons directly.

2.2.1.4 The Parallel Plate Proportional Counter

The Parallel Plate Proportional Counter as typified by the PSD detector on EXOSAT uses a uniform electric field, defined by two parallel electrodes, for amplification. The upper electrode is a transparent grid which allows primary electrons created in the absorption region above, to drift into the high field region between the two electrodes where the high field causes gas amplification to occur. The upper grid electrode is mechanically simpler than a wire array and the lower electrode can be easily used for position sensing. The readout constitutes an anode since the electron signal resulting from the avalanche is collected by it, as opposed to a positive charge being induced on it, the case with MWPC cathode readouts. Charge division readouts are well suited to this geometry and both wedge and strip anodes (WSA) and resistive anodes have been used for two dimensional imaging in this context. The EXOSAT detector used a resistive disk readout and the PGI detector [13], described in chapter 4 used a conductive, charge division WSA.

Detectors employing a single parallel field amplification stage utilize similar gas mixtures to wire counters and can be operated at gains of up to 10^4. At higher gains they run into breakdown problems, the effects of which are accentuated by the capacitance between the grid and anode. Breakdown, initiated by a charged particle track or field emission from the grid, produces an ionization path between the two electrodes which is self sustaining along its entire length, unlike the wire counter where the electric field is only strong enough for amplification near the wire. The ionization produces a low impedance path along which the charge stored in the electrode capacitance can discharge in a spark. The large current surge can cause 'cracking' of common quench gases such as methane, can disable the detector pulse counting electronics for a long period, or can destroy them unless protection circuitry is used. This breakdown, known as "pinging" is named after the sound which is characteristic of this breakdown mechanism.

Despite this gain limiting effect, the parallel field geometry is attractive for reasons of relative mechanical simplicity, lack of position modulation due to wire spacing and compatibility with planar position readouts. The gain limit of a single stage parallel plate detector can be overcome by using several stages in series, each stage defined by a transparent conductive electrode. This is known as a multi-step detector.

The parallel plate scheme was revived in the MicroMEGAS scheme [52], which uses a smaller cathode to anode gap than used previously, of 100 μm. This scheme has the interesting property that small fluctuations in the gap do not affect the gain. This feature occurs because, at an optimum gap, the gain versus gap function is monotonic. Operating the MicroMEGAS detector at the maximum gain makes it very insensitive to fluctuations due to mechanical defects, atmospheric pressure or temperature variations. Spatial resolution as low as 12 μm (for minimum ionizing particle tracks) using small pitch anode strips and energy resolution of 13 % FWHM at 5.9 keV have been reported.

2.2.1.5 Multi-Step Detectors

The multi-step detector was first developed by Charpak in 1978 [25] for high rate applications in particle physics. This geometry can be used to resolve the performance trade-off found in most proportional counters between energy and position resolution. Since the variance of the gas amplification generally increases with gas gain, a single amplification stage cannot simultaneously achieve good energy resolution (requiring relatively low gain) and position resolution (requiring improved signal to noise ratio and thus higher gain). Multi-step counters, such as the PGI attempt to overcome this problem.

These detectors use multiple amplification stages in order to achieve the good energy resolution in an initial low gain stage, and the overall high gain necessary for accurate position determination with large format detectors. The first avalanche (or preamplification) stage which usually has a parallel plate geometry, is operated at moderate gain such that the trade-off between electronic signal to noise ratio and the gas multiplication variance produces the best energy resolution.

Transferral of a suitable fraction of electrons formed in the first avalanche takes place through the drift region between the two amplification regions. This region serves as a barrier to prevent after pulsing due to photon feedback from the lower amplification stage and also enables the electron cloud spread to be controlled to suit the requirements of the position readout.

The second stage can have either parallel plate or MWPC geometry. The two amplification regions operating in series allow the detector to operate stably at very high gains ($>10^5$). The large signal, several picocoulombs at 5.9 keV, can be used to provide good spatial resolution even in large format two dimensional imaging detectors. Two dimensional imaging can be accomplished using the same techniques employed with single stage parallel plate detectors or MWPCs but

operating with the added benefit of a much improved signal to noise ratio as a result of the higher gain. The operation of the multi-step detector including discussion of the electron transfer mechanism and the role of Penning gases in this process is elaborated in section 4.1.

2.2.1.6 Micro Strip Proportional Counters

The Micro Strip Proportional Counter (MSPC) [28] is a device in which the anode and cathode wire planes of the MWPC are replaced by electrodes deposited on a planar substrate. The anode electrodes have been constructed as narrow as 3 microns wide and pitches of 300 microns have been achieved using photolithographic reproduction techniques.

The MSPC geometry, shown in Figure 2-3 overcomes the traditional energy resolution limiting aspects of MWPCs such as wire placement inaccuracies resulting in local gain variations, wire non-uniformity and diameter. The region of the avalanche can be small in size offering improved energy resolution and faster signal risetimes at lower operating voltages. The higher, more localized electric field of the avalanche region in the MSPC results in increased ionization efficiency, at the expense of UV and metastable production. Thus detectors of this type have been operated without any quench admixture and have demonstrated proportional counter energy resolution (<11% FWHM at 5.9keV) which is bettered only by the GSPC. Fast signal risetimes give the MSPC a high count rate capability up to three orders of magnitude higher than the MWPC.

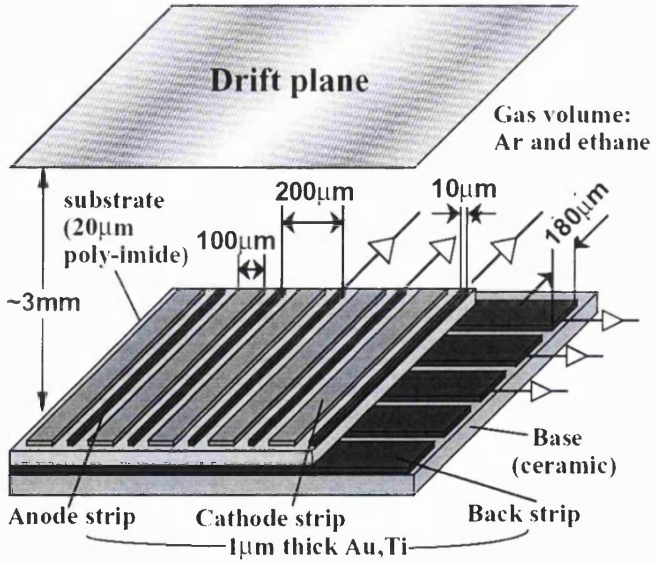

Figure 2-3. A schematic showing the layout of a typical MSPC [27].

The charge induced on the cathode strips can be used for one dimensional imaging in the axis normal to the strips. The strips may be read out independently and the position centroid calculated using a centre of gravity algorithm. The large number of processing channels may be reduced by employing one of a variety of multiplexing schemes, which rely on the fact that a genuine event signature will only excite a predictable number of adjacent channels. Alternatively, the cathodes

can be connected at regular spaced intervals to a resistive or delay line (L-C) circuit, as described under MWPCs, which can provide imaging using as few as two electronic channels. The orthogonal axis may be encoded using a similar arrangement of cathodes arranged orthogonally to the cathode strips and implemented either as a wire plane above the MSPC or as a cathode strip pattern on the underside of the MSPC substrate. The former method is mechanically more complex and both methods have the disadvantage of a poor electrostatic coupling from the charge avalanche region. These cathodes collect significantly less than 50% of the total induced charge and have poorer signal to noise ratio than those encoding the axis normal to the strip pattern. This problem can be alleviated by using a thin substrate with cathode strips deposited on its underside. The thin substrate needs to be bonded to a further mechanically stiff substrate for robustness.

Initial problems in gain stability resulting from substrate charge-up, polarization and component diffusion, owing to the large electric fields near the anode strips, were overcome by using Pestov or S8900 glass as a substrate. These materials have sufficient conductivity to prevent surface charge-up and subsequent field distortion.

2.2.1.7 Developments in Micro-patterned Detectors

The application of micro-electronic manufacturing processes and the simpler, less costly advanced printed circuit board techniques has led to an explosion of new designs of micro-patterned readouts, some of the more influential of which are described below.

Micro-gap Counter

The micro-gap counter (MGC) [44] is a development of the MSPC, designed to reduce the anode cathode distance further, increasing the electric field and speed of signal development. Whereas the MSPC is a planar pattern, the MGC uses fine anode strips separated from the sheet cathode by an insulating layer, as shown in Figure 2-4. The patterns are generally fabricated using photolithography and typical dimensions are 200 μm anode to anode pitch, using a 10 μm wide anode supported on an insulator 9 μm wide by 5 μm thick. The small cathode to anode gap produces a fast signal which develops within 20 ns at a working voltage of ~500 V. These detectors have an intrinsic high rate capability of greater than 10^6 counts mm^{-2} s^{-1} making them well suited to applications with high fluxes in particle physics experiments, X-ray diffraction and neutron scattering and tomography.

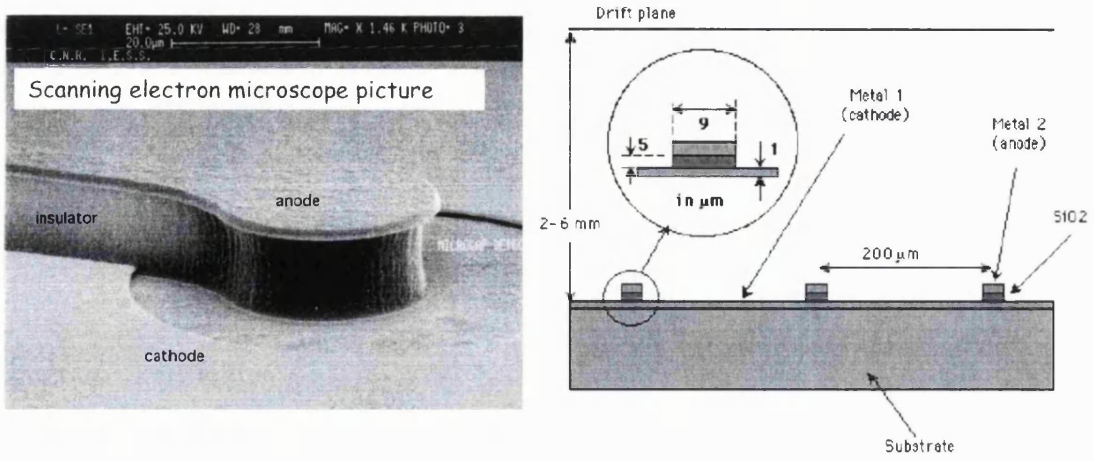

Figure 2-4. A photograph and schematic of a micro-gap counter [44].

GEM detector

Whereas the MSPC and MGC require the delicate and expensive production methods used for micro-electronics, the Gas Electron Multiplier (GEM) [45] was developed by exploiting advanced printed circuit board techniques to achieve an easily manufactured, cheaper, robust, free standing gas gain structure resistant to radiation damage. A single GEM consists of a kapton substrate which is metalized on both sides and perforated with an array of fine holes. The typical geometry is 5 µm copper deposited on a 50 µm kapton substrate, with a hole diameter of 70 µm at a hexagonally packed pitch of 140 µm. A GEM can be used as a preamplification stage above an MSPC, MGC or other such device. It has also been demonstrated with a 2-D multi-pixel pattern for two dimensional imaging. Configurations of up to three serial GEMs have been shown to achieve gains ~ 10^5. The distribution of gain among an assembly of multiple GEMS allows high gains to be achieved at lower overall voltage minimizing the possibility of HV discharge, in the same manner as the multi-step chamber. The small scale of the high gain region provides very fast signal development (~20 ns) and gains of a few thousand are achieved with voltages of 350-500 volts per GEM. Spatial resolution down to 50 µm has been reported.

Micro-Groove Counter and variants

The micro-groove counter [53] uses the advanced printed circuit board techniques to implement an electrode design similar to the MGC. The device is manufactured using a 50 µm kapton substrate, metalized on both sides, and mounted on an insulating substrate. The amplification region is a groove etched in the kapton which is deep enough to expose the lower metallization layer. Two dimensional readout is provided in one axis by division of the upper electrode into strips, by the trenches themselves. The lower electrode is also divided orthogonally into strips to provide position determination in the second axis. This is a low cost, robust, two dimensional device which can be large in size. One disadvantage over the MGC however is its larger amplification region, where the lower field reduces the signal speed and hence maximum count

rate. Gains up to 10^4 have been reported with good uniformity over the whole detector area. The energy resolution is moderate being 20 % FWHM at 5.4 keV.

The Well detector is similarly constructed to MGC except that the linear grooves are replaced by holes, arranged in a square array with a diameter of 68 μm and a pitch of 120 μm. The Well detector has similar properties and performance, though signal development is somewhat slower

Microdot Detector

The Microdot (MDOT) gas avalanche detector was developed by Biagi *et al.*[54]. It is a variant of the MSGC, where instead of using linear anodes and cathodes it uses an array of pixel elements, each consisting of a point-like anode of 12-20 μm diameter surrounded by a circular cathode 20-40 μm wide. It is manufactured using micro-electronic techniques on a silicon substrate. The pixels are arranged in a hexagonal lattice with a pitch of 100 – 200 μm. Both anodes and cathodes are connected to their respective busses which are divided into strips and arranged orthogonally so as to provide a two dimensional imaging capability. Gains up to 4×10^4 have been reported and energy resolution of 14 % FWHM at 8 keV. The symmetry of the microdot pixel means that the quadratic form of the surface potential divider between the electrodes theoretically matches the anode field, and thus surface charge up should not occur as in the MSPC, where these components are mismatched. Gain stability at rates of ~ 1MHz mm^{-2} has been reported and image resolution is predicted to be better than 50 μm.

2.2.1.8 The Gas Scintillation Proportional Counter

This device is included by virtue of its energy resolution, the best achieved by a proportional counter, though its position resolution is unremarkable. The GSPC [26] is a proportional counter in which, instead of using a high electric field to produce amplification via collisional multiplication, uses a slightly lower parallel electric field to accelerate the primary electrons which transfer enough energy to the gas atoms to excite but not ionize them. The excited atoms decay to their ground state by the emission of scintillation light in the ultraviolet band. The relatively large number of photons constitutes the amplified event signal, the number of photons representing the energy of the incident X ray. The wavelength of the emitted UV light is dependent on the particular gas used and is 150-200 nm for pure Xenon.

The purity requirement for the gas in a GSPC is the highest found in a proportional counter. Molecular components which act as a quench must be specifically avoided since contamination with these will reduce the scintillation light available for measurement. This is a particular problem at low X-ray energies, when the thin entrance window must prevent diffusion of contaminants into the detector volume.

Scintillation light produced in the gas is collected using one or more photomultiplier tubes via a UV transparent window (usually of fused silica) forming the base of the GSPC. The GSPC achieves the best energy resolution found in a proportional counter since it replaces the statistical

fluctuations of the avalanche with the statistics relating to the number of photons that can be collected (always<<2π sr). Gas gain statistics are dominated by fluctuations of the first few multiplication stages due to the serial nature of the avalanche, whereas the GSPC equivalent is improved due to the production of scintillation photons being completely independent events. If the light yield is high and collection efficiency is reasonable (typically 10%), Fano factor limited resolution can be approached. There are two designs of GSPC, with and without drift region. The former benefit from having a constant distance over which the scintillation light is produced, but lose primary electrons to the field defining grid which degrades the energy resolution. The latter have no grid and so the amount of light produced depends on the X-ray interaction height. This can be correct at the expense of significantly higher data post-processing.

Imaging GSPCs

An array of photomultiplier tubes (PMT) or an imaging PMT are arranged to collect light from as large a solid angle around the detector as possible. Even so, only a small fraction of the light is collected owing to several factors:-

1. absorption in the gas from contaminants.
2. absorption in the scintillation light transmitting window. Only a few materials are suitable and these bring other problems e.g. brittle, hygroscopic.
3. the geometrical factor. Only a relatively small solid angle can be covered by PMTs in a practical design.
4. The detective quantum efficiency (DQE) of the PMT is typically 20%.

The total amplitude of the light collected by the all of the PMTs is proportional to the X-ray energy and thus provides spectrographic information. The magnitudes detected by each PMT can be used to determine the light spot centroid and hence the X ray photon interaction site. Practical detector design constraints restrict the proximity of the light source to the PMTs, hence the large physical size of the light distribution reaching the PMTs limits the best position resolution attainable to 0.5-1.0mm.

An alternative approach is to use an imaging detector sensitized for UV detection. This may take the form of a MCP based device using a photocathode on its front surface, an imaging PMT with discrete anode readout, or a photoionization chamber. The imaging performances of the first two devices will be discussed in their own right later. The photoionization chamber is itself a form of proportional counter, based on the MWPC but with the addition of a UV ionizable gas admixture. The most commonly used such admixtures are triethylamine (TEA) or tetrakis-diethylamino-ethylene (TMAE).

For large detectors, the mechanical problems posed by a large UV transmitting window are difficult to overcome. One solution which provides both energy and position measurement uses

crossed arrays of waveshifting fibres inside the pressure vessel. The fibres modify the scintillation light wavelength towards the visible spectrum and transmit this light to an array of phototubes outside the detector body.

2.2.1.9 Photon Position Determination

Certain features of the proportional counter limit the position resolution irrespective of the position readout used. The photo-ionization produced by the X ray is mediated by several means. The charge representative of the event is not deposited at one location. The initial photoelectric interaction of an X ray with a gas atom is characterized by :-

1. the emission of a photoelectron
2. the emission of an Auger electron or fluorescence X ray photon
3. locally produced ionization

The range of the photoelectron is energy dependent, depending on the difference between the X ray energy and the relevant electron binding energy in the gas fill atom. The range of an Auger electron is determined by the energy of the metastable state giving rise to it. The production of fluorescence photons in general are a nuisance at low energies, sometimes escaping from the detector resulting in an escape peak, characteristic of the gas, in the energy spectrum. At higher energies, detector pressures tend to be higher for quantum efficiency reasons and so fluorescent photons are more likely to be contained and can be even used to advantage. Escape gating can be used to significantly improve background rejection when the X ray signature consists of two simultaneous events, corresponding to the primary interaction and the fluorescent photon interaction. It is the characteristic energy of the fluorescent photon which positively identifies the valid event. This large advantage is however mitigated by the uncertainties in its accurate identification owing to the limitations imposed by the detector energy resolution.

All the above effects cause spread and non-uniformity of the primary electron cloud which results in the cloud centroid not reflecting exactly the interaction site. A further charge spreading is caused by diffusion of the electrons due to their thermal motion as they are drifted towards the multiplication region.

At low energies, the photoelectron and Auger electron ranges are small compared to the effects of diffusion. The effect of the latter is amplified by the relatively small number of primary electrons created at low X ray energies.

At higher energies, the photoelectron range dominates. This range is several millimetres at 30 keV in 2 atmospheres of Argon and greater than 1 cm at 60 keV. It can be improved by using gas fills of higher atomic number (in practice this means Xenon) at higher pressures, also improving the quantum efficiency and reducing energetic electron and fluorescent photon ranges.

2.2.2 Vacuum Tubes

2.2.2.1 Introduction

The term "Vacuum Tube" in the context of this review covers the three major categories of image intensifier, all of which require in-vacuo operation, namely basic image intensifiers, position sensitive photomultipliers, and MCPs. The categories are grouped by the mechanisms they use for intensification.

The first and simplest category, which comprises basic image intensifiers [32], uses no charge amplification, relying on the increase in energy of a single photoelectron imparted by an electric field. This energy is converted, on collision with a phosphor, to release a large number of photons.

The second category, imaging photomultipliers [56], are vacuum devices which use a discrete dynode structure to amplify charge by means of secondary electron emission. Imaging PMTs use a specialized dynode structure, which maintains spatial registration of the charge centroid, in combination with an electronic image readout to determine the event charge centroid position

The detectors in the third category utilize MCP [9] intensifiers. The MCP is an electron multiplication device where the inner surfaces of microscopic glass pores act as continuous dynodes. An MCP consists of a thin glass wafer perforated by hexagonally packed arrays of these microscopic pores. An electron entering a pore and undergoing amplification produces an output charge cloud whose position is representative of the input electron. The position of the amplified charge cloud can be used with a phosphor to produce an amplified optical image or its centroid directly detected with an electronic readout. The miniature scale of MCP pores, together with the MCPs sensitivity to X-rays, ultraviolet light, charged particles and neutrons, have led to its wide use as a component in all manner of high resolution quantum detectors.

2.2.2.2 Basic image intensifiers

The generic design of basic image intensifier comprises a transparent window, through which photons pass and interact with a semi-transparent photocathode, deposited on the inside of the window. Photoelectrons are released and accelerated in an electric field. Image registration may be maintained by proximity, electrostatic or electromagnetic focusing techniques. The choice of focusing method has a large impact on the spatial resolution, size and mass of the intensifier. The accelerated photoelectrons gain an energy of typically 5-15 keV and impact on a phosphor, producing hundreds of fluorescence photons of which a sizeable fraction escape through the exit window, commonly a fibre optic.

There have been several generations of intensifier design [33]. The very first image intensifier design, the so-called 'generation zero', was an infra-red device. The generation ½ device worked at shorter, optical wavelengths and used electromagnetic focusing to provide improved image resolution of 45 lp mm^{-1}. The generation I intensifier was produced for the military to answer the

need for a small, light weight, brightness scaleable passive night vision device. It typically used a multi-alkali photocathode with a response in the optical/infra-red range of 400-900 nm and utilized electrostatic focusing to achieve a position resolution of 25-36 lp mm^{-1} at a gain of 20 – 100 provided by an accelerating voltage of 5-15 kV. Some variants used electromagnetic focusing. The generation II design was the first to use proximity focusing with an MCP electron multiplier, producing a much more compact device. The generation III device used a similar design, but the bi-alkali and multi-alkali photocathodes of the Gen-II were replaced by gallium arsenide, having a higher sensitivity due to its negative electron affinity (NEA). The increased sensitivity of this material to contamination required the use of a filmed MCP to prevent ion feedback reaching the photocathode.

Before the advent of MCP based intensifier, sophisticated designs using these detectors have been used to achieve photon counting and imaging. One such device, the Imaging Photon Counting System (IPCS) is described below.

The IPCS

Probably the most well known is the Imaging Photon Counting System (IPCS), developed by Boksenberg [30], which was used for ground based astronomy and for the detector on the Hubble Space Telescope Faint Object Camera. This device comprises four 40 mm diameter image intensifiers coupled end to end. Each intensifier has a semi-transparent photocathode magnetically focused by means of an external magnet to an output phosphor. The magnetic focusing operates by confining the radial components of velocities to circles centred on the magnetic field lines. The focusing condition requires that the photoelectron makes one (or more) complete loops around the field line before it impacts the phosphor. This technique can provide spatial resolution of better than 100 line pairs per millimetre. Its major drawback is that it requires heavy external permanent magnets or coils. The light output of the fourth intensifier is optically coupled using a transfer lens to Plumbicon television camera. The IPCS used four stages of light amplification in order to provide enough light output for the television camera to detect the light spot from a single photon, to fulfil its photon counting specification. The television camera is used to view the final phosphor and record the position of photon events occurring during each frame of the camera scan. Figure 2-5 shows a schematic of the ground-based IPCS. The system uses event centre detection (ECD) logic to identify the centroid of the light spot representing each photon event, minimizing the degradations imposed by the electron optics and increasing spatial resolution.

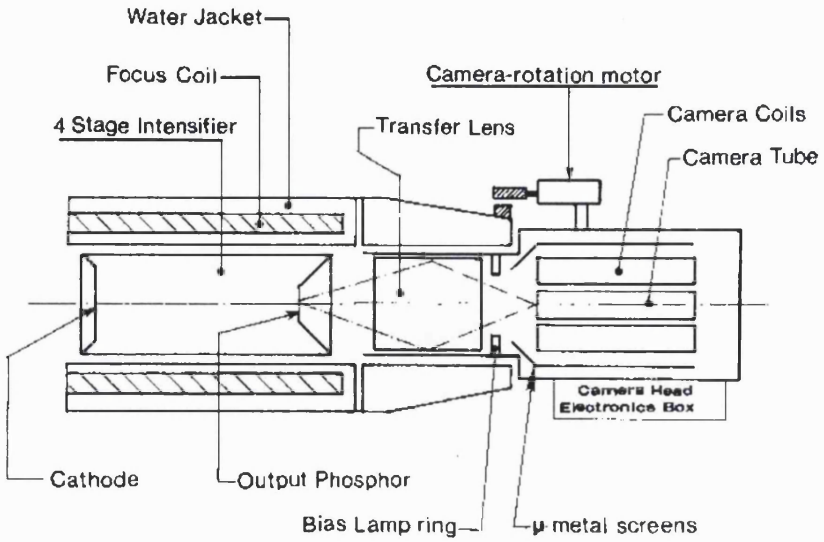

Figure 2-5. A schematic of a 4-stage IPCS used for ground-based astronomy [31].

2.2.2.3 Imaging Photomultiplier Tubes

There are several commercially available imaging photomultiplier tubes [56]. These use the same basic principle as standard PMTs, using a dynode structure to provide charge amplification. Imaging PMTs use dynode geometries designed to reduce the lateral spread of the electron cloud as it increases in size moving downward through the dynode structure. Even so, the extent of this lateral spread limits their usefulness to applications requiring only moderate spatial resolution.

Their discrete dynode structure does however endow imaging PMTs some advantages. Recharging of the PMT dynodes after an electron cascade has resulted in partial depletion is very fast due to their laterally conductive design. In addition they are more suitable than MCPs for applications where a simultaneous pulse of photons requires energy and position measurement. In this instance the response of an MCP would vary depending on the spatial distribution of the input pulse.

They are commonly used for applications where spatial resolution is not paramount and these positive features can give them particular advantage, such as providing an imaging capability for GSPCs and in conjunction with scintillators for gamma ray imaging.

2.2.2.4 Microchannel Plate based detectors

Introduction

The microchannel plate (MCP) is an evolution of the channel electron multiplier (CEM), first suggested in 1930 by Farnsworth [57] but not constructed until 1960 in the USSR (Oshchepkov et al.,1960 [58]). The CEM is basically a glass tube with electrodes at both ends, with a very thin, semi-conducting surface layer along its inside which has a high secondary electron emission coefficient. A high voltage is applied between the electrodes and the inner surface of the tube acts as both a resistive divider and a continuous dynode. The electric field set up along the length of

the tube accelerates an initial electron and collision with the dynode surface produces a number of secondary electrons which are similarly amplified. Charge can thus be magnified by a factor $>10^7$ along the length of the tube. Typical CEMs have tube diameters of 0.1-1mm and lengths of several centimetres.

The first operational MCPs were manufactured by assembling arrays of CEMS (Wiley and Hendee,1962 [59]). The military requirement for "night sight" image intensifiers accelerated the development of the "two draw, etchable core" manufacturing method that made possible production of MCPs with microscopically small pores.

The major market for MCPs still resides in simple "night sight" intensifiers, where in the Gen-II tube, they supply significantly more gain and thus light output than their "Gen-I" precursor. A smaller market, but one in which development is being actively pursued, is in photon and particle imaging. Detectors using MCP stacks are used in many scientific disciplines, including both ground –based and space-based applications in astronomy, where they provide a very high, saturated gain suitable for photon or particle detection and high resolution imaging.

Description

The MCP is an electron multiplication device comprising of a large number of microscopically small pores running in parallel from front to back of a wafer of glass. Each pore functions as a miniature CEM, as shown in Figure 2-6. The cylindrical pores typically have diameters ranging from 4 μm upwards and are hexagonally packed with a pitch of ~20-25% larger than their diameter. A typical MCP will consist of millions of pores. The length to diameter ratio (L/d) of the pore is commonly 40:1 (known as single-thickness), 80:1 (double thickness) or 120:1 (triple thickness). The common MCP geometries of 8, 10, and 12.5 μm pores produce MCP thicknesses from 320 μm to 1.5 mm depending on the L/d ratio. MCPs may be manufactured with a solid glass edge making them more robust and easy to handle, but with the possibility of stress induced warpage, or they may be soft-edged, the pore structure running right up to the MCP perimeter. MCPs are manufactured in a variety of formats and custom shapes up to sizes as large as 150 × 150 mm^2.

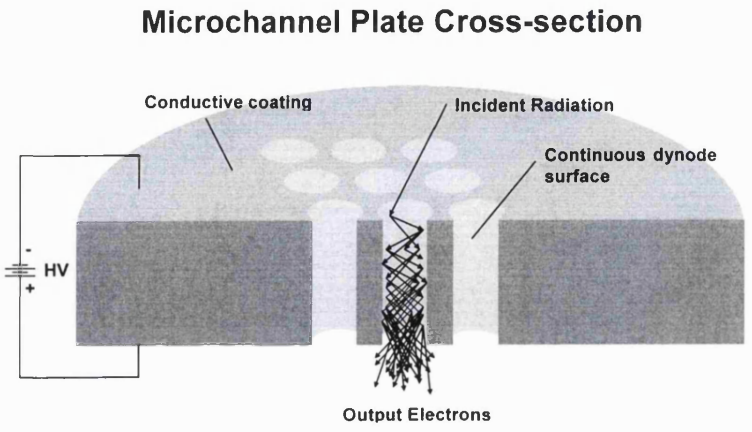

Figure 2-6. A schematic showing the gain process in an MCP.

One commonly used MCP manufacturing process [60], shown in Figure 2-7, begins with the accurate mating of a hollow billet of lead glass with a rod of etchable glass. This combination is drawn vertically through an oven, where it is reduced in diameter to a fibre of ~1 mm diameter. Lengths of this 'first draw' fibre are stacked together by hand into a hexagonal array, which is again drawn vertically through an oven to produce a hexagonal multi-fibre. The boule from which the final MCP is manufactured is assembled by stacking lengths of multi-fibre together and fusing them in a vacuum oven. The boule is sliced to the required MCP thickness and the etchable core glass removed chemically. The MCP is then baked in a hydrogen oven, which chemically reduces the lead glass creating an inner pore surface consisting of a very thin SiO_2 layer (~100 Å thick) over a semiconducting layer. This semiconducting layer endows the MCP with a non-ohmic resistance of anywhere from a few tens of MΩ to GΩ between its upper and lower surfaces.

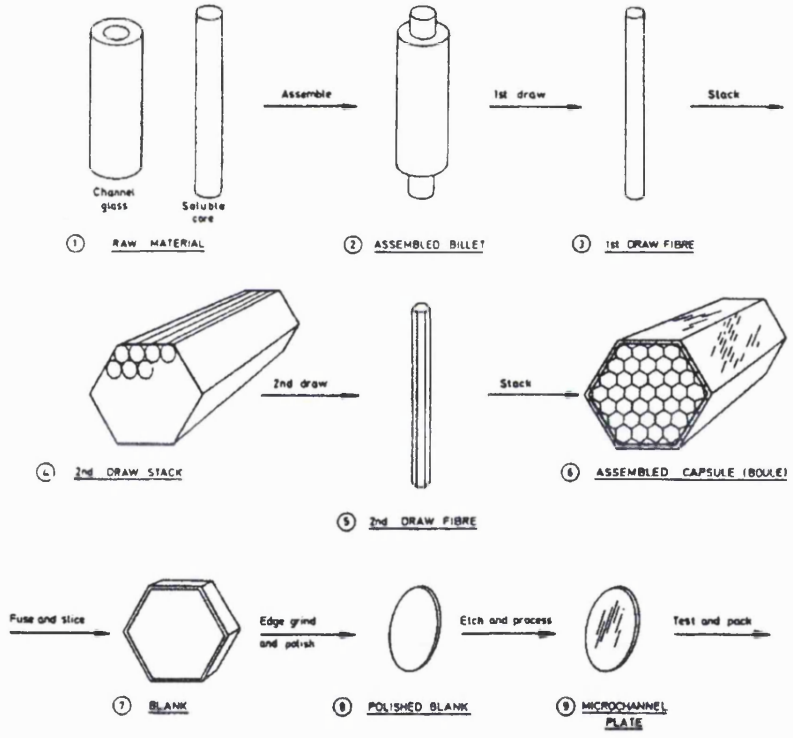

Figure 2-7. A timeline of the stages in the manufacture of an MCP [60].

In order to operate as an electron multiplier, the upper and lower surfaces of the MCP are coated with a conductor, typically nichrome, and a high voltage is applied in vacuo (ideally better than 10^{-5} mbar to avoid high voltage breakdown). The resistive layer down the length of the pore establishes a linear voltage gradient along its length, providing an accelerating field for electrons and allowing its inner surface to act as a continuous dynode. The thin SiO_2 layer has a high secondary electron emission coefficient to maximize the amplification every time an electron collides with the pore wall. After an electron avalanche down the pore, it is effectively paralyzed for a short time while the positively charged SiO_2 layer discharges by means of electron flow from the input cathodic input surface through the resistive layer, followed by electron tunnelling from the resistive layer to the positively charged surface of the pore wall.

MCP gain

A typical single thickness MCP will produce a mean gain of 10^3-10^4 e^- at a voltage of 800 V. In this regime the pulse height distribution is exponential. MCPs can be stacked in series to produce gains as high as 10^8 e^- [76]. As the voltage across the MCPs is increased, the energy given to avalanche electrons between collisions increases, together with their secondary electron yield (at typical mean electron energies of 100-200 eV, the secondary electron emission coefficient is still rising with increasing energy), thus the MCP gain increases. When MCPs are stacked together, increasing voltage does not indefinitely increase the MCP gain. As the gain increases there comes a point where MCP stacks exhibit pulse height saturation [61]. In this situation the pulse height distribution becomes quasi-gaussian and can have with a width of less than 30 % FWHM. The gain of an MCP stack can also be increased by introducing charge spread between MCPs by means of a gap (particularly in the first interface).

Saturation occurs in lower MCP because charge-up of pore wall causes a dynamic change in the potential gradient down the pore. The exponential nature of the avalanche process leads to the vast majority of the gain taking place in the last few dynode stages near the pore exit of the final MCP. At high gain, the leading part of the avalanche causes positive charge to build up on the pore wall. The semiconducting pore walls only allow this to be discharged very slowly with respect to the pulse development time, which is at the timescale hundreds of picoseconds. The effectively static positive charge reduces both the secondary electron yield and the potential field experienced by the following electrons, reducing their energy on impact and reducing the number of secondary electrons produced. This dynamic reduction in gain limits the maximum achievable gain and saturates the pulse height.

If an MCP stack is already in pulse height saturation and the voltage is increased further, gain will not continue to increase appreciably due to saturation, but the pulse height distribution may exhibit a high energy tail. This is due to ion feedback inside the MCP pores. One effect of the electron avalanche is to degas the walls of the MCP pore, releasing and ionizing adsorbed materials such as water vapour and other volatile contaminants. The higher the voltage, the more vigorously the MCP is degassed. As voltage is increased, MCP saturation will also dynamically increase and displace the field inside the upper region of the MCP pore, possibly accentuating this effect by increasing electron energy and displacing the effective last dynode location. The positively charged ions drift back along the electric field lines which are axial to the pore owing to the geometry of the dynode resistance. Unchecked they could drift right back through the MCP stack to the very top, where if they collided with the wall, they could initiate a further, virtually simultaneous, event. This positive feedback causes the high energy tail. In fact, steps are taken to prevent ions travelling back up through the stack. The pores are biased. Their axes are not normal to the MCP faces, but angled slightly away, at angles typically between 6 and 13°. Stacked MCPs are oriented so that their pore bias axes are opposed. There is no line of sight for ions to travel

back along. Any that do so, are the exception. Even so this effect can be seen but only at voltages above those where saturation has already limited gain increase.

The curved channel MCP (C-plate) [62] is a special design of MCP manufactured using a specialized technique involving 'slumping' the glass while still molten. This produces an MCP with curved pores which is intrinsically resistant to ion feedback. C-plates are manufactured with longer than average L/d ratios, typically 125:1, enabling them to be operated singly, at high gain, in saturation. Though C-plates are a very attractive option owing to the mechanical simplicity they endow the detector, they proved difficult to reliably manufacture uniformly and have never achieved their promise.

MCPs exhibit gain depression [63][64] resulting either from an excessive local or global count rate, or from long term exposure when under operation. The dynamic gain reduction caused by count rate is fully recoverable. It results from the pore paralysis discussed earlier, and is determined by the pore recharge time constant. Count rate induced gain depression has been shown to be related not just to the local count rate per pore but to the size of the illuminated area, indicating that individual pores cannot be treated as independent entities and suggesting that a lateral mechanism is operating between neighbouring pores, possibly by means of capacitive coupling and/or distortion of equipotential surfaces. Count rate induced gain depression can be reduced by operating at lower gain, using lower resistance MCPs, or by replacing the nichrome MCP electrode with gold [64].

Long term exposure under operation can cause irrecoverable gain depression. This is brought about by removal of adsorbed materials from the pore wall as well as compositional changes in the pore wall, and causes the secondary electron emission coefficient to be lowered resulting in depressed gain.

Long range gain depression [65] is a phenomenon characterized by gain drop in an unilluminated region of the MCP surrounding a brightly illuminated point. It can also lead to irrecoverable long term gain depression, suggesting that it is a compositional change, maybe brought about by electric field driven compositional changes, and/or the introduction of static field distortions.

Intrinsic background

Intrinsic MCP background [66] noise comes from two main sources. Internal radioactive decay of the radioactive isotopes of the glass constituents potassium and rubidium cause a background level of ~0.5 count s^{-1} cm^{-2} . This can be reduced by an order of magnitude by using a different MCP glass composition called 'low noise glass'. The second, potentially avoidable internal noise source is due to MCP defects and damage. Either of these can produce field emission of electrons. If this occurs near the front surface of the MCP, the resulting event can have a similar pulse height distribution and be completely indistinguishable from a real event, its only identifying feature being its constant presence. These artefacts, called hotspots, can be due to particulate

contamination, damage as a result of high voltage breakdown, or as a result of mechanical damage. Over time, they cause long term gain depression in their local area, becoming less visible or may even disappear. However, even if not visible, they leave that area of the MCP permanently affected.

Quantum efficiency

MCP devices require only a single electron in order to register an event. This can be a photoelectron produced by a photon interaction with the MCP front surface (moderately efficient only at X-ray wavelengths) or with a photocathode, deposited either on the front surface of the MCP stack or on a transparent substrate which is typically proximity focused to the MCP stack. Its sensitivity to single electrons makes the MCP based detector [60] useful for imaging with low energy ions, which interact directly with the MCP typically producing several electrons. MCPs can also be used to detect neutrons [67].

The quantum efficiency of MCPs is highest for soft X-rays and in the UV. Some of the most commonly used photocathode materials at these wavelengths are CsI, KBr, CsTe, and MgF_2. Detectors at these wavelengths are open faced due to the lack of transparent window materials, the photocathode being deposited directly on to the front surface of the MCP stack. In this mode a repeller grid [68] is commonly used to enhance the quantum efficiency by up to a factor of 2. This effect is due to the grid defining a field which allows photoelectrons ejected from the interchannel web, which would normally be lost, to be detected by the MCP. The downside of this scheme is that they are collected some distance away from their correct position in the image. This can result in a halo around a bright point source, reducing the spatial resolution.

The quantum efficiency of MCPs shows an angular dependence [69], which is approximately symmetric around the pore bias angle, being close to zero when aligned with the bias angle. Experimental results have been shown to support theoretical modelling based on the variation of absorption length of photons and escape length of photoelectrons with angle of incidence and photon energy.

In recent years the quantum efficiency of both bare and photocathode coated MCPs has inexplicably diminished by a factor of ~2 [70]. This has had a major impact especially for space based astronomy missions where signal is precious and achieving the optimal signal to noise ratio often makes the difference between success and failure. Overall MCP gain does not seem to be affected and the experimental evidence suggests that the problem could stem from low gain in the initial multiplication stages, increasing the statistical likelihood that an event will effectively peter out at an early stage. Process changes in manufacture, especially the reduction step which strongly influences the secondary electron emission coefficient of the MCP, are suspected culprits. It is known that the manufacturing processes have evolved over the years and experimental work is underway to establish a cause and regain the lost performance. Even more inexplicably, the effect

seems to be present in MCPs from different manufacturers, possibly suggesting that the raw glass composition may be to blame.

Imaging

The use of MCPs for imaging in the Gen-II intensifier has already been mentioned. In this device, a single MCP operating in a non-saturated linear mode provides basic image amplification. However the operation of MCP stacks at high gain, and in saturation, allow true photon counting to be undertaken, and the microscopic pore sizes of MCPs are ideal for high resolution imaging. Typically, stacks of between 2 and 5 MCPs are used, producing charge gains of between 10^5 and 10^8 electrons. The coordinates of the initial photon interaction are reflected by the centroid position of the charge cloud produced by the MCP. Thus, a readout which detects a charge centroid position can be used for imaging. There are two major techniques used for this purpose. Firstly there are devices which accelerate the amplified charge on to a phosphor, producing an amplified light spot whose centroid can be determined using various means. Examples of these are the Intensified CCD (ICCD) [34] and the Precision Analog Photon Address (PAPA) detector [41], both of which are described later in this section. Secondly, the amplified charge can be detected and measured directly using electronic means. There are many different types of electronic readouts, each with their own strengths and weaknesses. Some of the electronic image readout techniques used with MCPs are also commonly used in gas proportional counters, though their formats and the practicalities of operation can be quite different. Section 3 provides a review of some of the devices available for both MCP detectors and gas proportional counters.

2.2.3 Hybrid Technologies

2.2.3.1 The Intensified Charge Coupled Device (ICCD)

The intensified CCD (ICCD) [34] has been successfully used for ground-based and space-based optical photon counting applications requiring high resolution imaging. For example, the high spatial resolution MIC detector [71] uses a modified Gen-II intensifier, with the standard single thickness single MCP replaced by an MCP stack consisting of 3 MCPs. The tube has an optical S-20 photocathode with quantum efficiency (QE) better than 20%. proximity focused to the MCP stack, operating at a gain of $\sim 2 \times 10^5$ e.

Much research has been carried out to develop a tube capable of long term operation, without photocathode degradation, whilst using a non-filmed top MCP. The top MCP of high gain MCP stack is commonly filmed, using a very thin layer of aluminium oxide to prevent ion feedback reaching the photocathode surface and damaging it. The film has the downside of reducing the quantum efficiency by up to a factor 2. A suitably rigorous MCP scrubbing procedure has been developed which reduces adsorbed materials, and thus ion feedback levels sufficiently, so that the

film can be safely removed. This conditioning also enables the MCP to be operated at low gain whilst maintaining a narrow pulse height distribution, reducing ion feedback further.

The amplified charge output of the MCP stack is proximity focused to an output phosphor which fluoresces when excited by the electron cloud. Despite the relatively low MCP gain, the phosphor gain provides an overall high gain of over 10^7 photons per photoelectron. The light spot, representing an individual photon, is imaged using a CCD detector. Because of a size mismatch between the standard intensifier tube size (25mm) and the CCD (typically 8mm square), it is necessary to reduce the image size on the CCD by about a factor three. This can be achieved either with lenses or a fibre optic taper. The fibre optic taper results in a lower light loss, but can cause distortions, owing to the difficulties of manufacturing a geometrically perfect tapered fibre-optic.

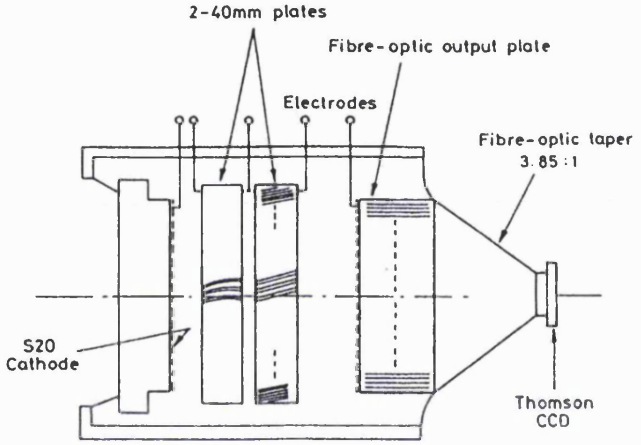

Figure 2-8. A schematic showing the layout of a photon-counting ICCD [34].

For high resolution applications ICCDs use a pixel centroiding technique. The light spot when imaged on the CCD is about 1.5 CCD pixels across. Measurement of the magnitude of light collected by the central pixel of the event together with the two adjacent pixels in each axis allows centroiding to sub-pixel accuracy and MCP pore limited spatial resolution has been reported [71][34]. Alternatively the CCD can be operated in a non photon-counting analogue mode, without the time penalty of the centroid calculations, to extend the system dynamic range.

When using the pixel centroiding technique a relatively small CCD format is commonly used of typically 256 X 256 pixels square. Each CCD frame can read many photon events as long as they are not spatially overlapping. Thus the maximum count per frame is extremely dependent on the image form: point sources having the lowest count per frame, flat field illumination the highest. Frame rates can be as high as 1kHz if the CCD is windowed. Care must be taken in choosing the intensifier phosphor to avoid a long timescale fluorescence which could cause a single event to be detected in more than one CCD frame and multiply counted.

2.2.3.2 The electron bombarded CCD (EBCCD)

An EBCCD is essentially a Gen-I type image intensifier with a CCD replacing the phosphor and output fibre-optic. EBCCD devices have been manufactured in a variety of configurations. Some utilize conventional tube designs with semi-transparent photocathodes coated on to the input window [72]. Configurations using window-less, opaque photocathodes with magnetic focusing have also been described [73]. The CCD is commonly a back-thinned device and constitutes the anode of the EBCCD detector. Photoelectrons emitted from the photocathode are accelerated by the applied voltage, gaining energy and entering the CCD through the thinned back surface. Signal amplification occurs within the solid state device due to the conversion of the photoelectron energy by generation of electron-hole pairs within the semiconductor.

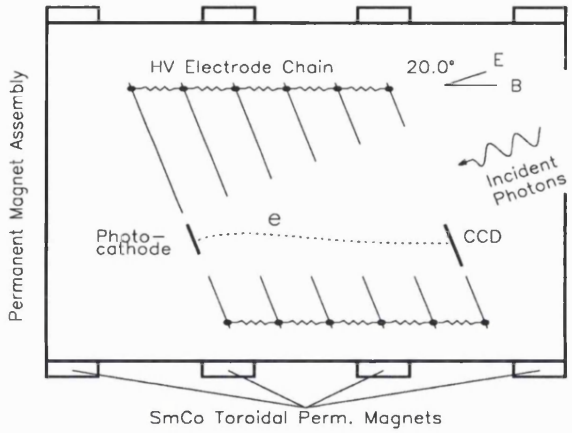

Figure 2-9. A magnetically focused EBCCD using an opaque photocathode [73].

This process is virtually noiseless compared with amplification in an MCP and can provide gains in excess of 3000, well above the typical readout noise.

As well as having a high signal to noise, other performance advantages of EBCCDs include high dynamic range, limited only by the CCD pixel full well depth, and good spatial resolution, usually limited by the photoelectron focusing technique. However EBCCDs have some distinct drawbacks. Their manufacture into intensifier tubes is made awkward by the cleanliness and low contamination requirement imposed by the photocathode chemical sensitivity. In addition, operation of a CCD inside the vacuum enclosure requires a provision of sufficient electrical feedthroughs which need to be leak-proof to UHV specifications. The high energy of the photoelectrons can also cause long term damage to the CCD, degrading performance. These problems have so far prevented EBCCDs exploiting their potential and becoming a standard device.

2.2.3.3 The PAPA Detector

The precision analog photon address (PAPA) detector, described by Papaliolios *et al.*[41], is a hybrid detector system using an MCP-based image intensifier with a light output coupled via a

series of masks to a number photomultiplier tubes. The light spot generated by a photon, emanating from the phosphor of the MCP intensifier is imaged by a large collimating lens followed by an array of smaller lenses on to 19 masks in parallel. A further lens behind each mask optically couples the masked image on to one of 19 small PMTs which measure the transmitted light intensity. 9 + 9 PMTs are used for two dimensional image encoding, providing a 512 × 512 pixel format. Each of the 2 sets of 9 masks providing imaging information consists of alternate transparent and opaque strips organized as a binary gray code. If the light spot image falls on a transparent region of the mask, the coupled PMT registers a '1', or a '0' if the region is opaque. The 9 bit address provided by the 9 PMTs in each axis provides spatial resolution of 2^9 i.e. 512 pixels and the gray code prevents ambiguities which could otherwise result from spatially coincident mask transitions. The 19th clear mask provides a spatially unfiltered image to its PMT which acts as an event trigger, strobing the PMT outputs when an event is detected and generating event timing information. A simplified schematic of the PAPA detector is shown in Figure 2-10.

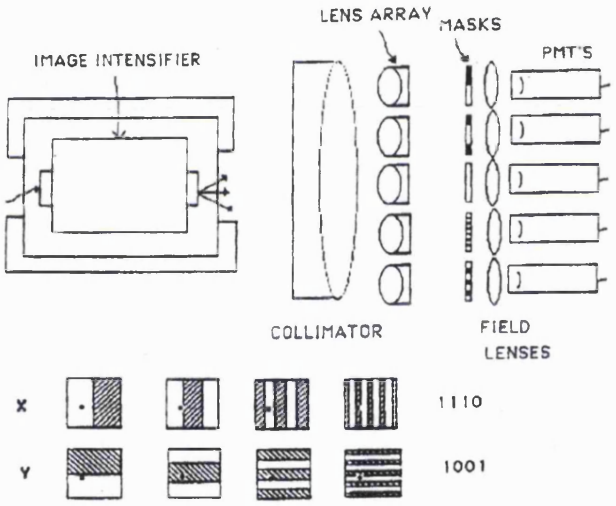

Figure 2-10. A simplified schematic PAPA detector [41].

This system has been used for ground based applications including speckle interferometry and long baseline interferometry [74]. A modified design with a resolution of 2000 × 2000 pixels using a Cadmium telluride photocathode has been developed for UV applications and is capable of count rates as high as 2M counts per second [75].

2.3 Electronic Position Readouts

This section describes a broad range of electronic image readout devices commonly used in both gas proportional counters and microchannel based detectors. These devices operate by locating the centroid coordinates of the charge cloud produced in the detector. There are various ways these devices could be categorized and I have chosen to segregate them into the three groups defined by the primary electronic method they utilize, namely charge measurement, charge detection, and signal timing. The first category is defined as those devices where the electrode

geometry provides a continuous variation in output. These devices require the amplitude of charge collected on any electrode to be measured for position determination. The second category is comprised of those devices where charge is collected on discrete electrodes and whose presence identified digitally, typically using a discriminator. Devices in the third category use signal timing information to determine position information, usually by means of relative signal delay. The following hierarchical tree shows how these fundamental categories can be further subdivided, and how the various readout devices are assigned. Since the best readout schemes, by their nature, often ingeniously use features belonging to several categories, these groupings can only be seen as approximations :-

1. Charge Measurement
    a. Resistive charge division
        i. Resistive wire
        ii. Resistive disk – MEPSICRON, RANICON
        iii. Crossed wire grid – HRI
    b. Conductive charge division – geometric area
        i. Quadrant
        ii. Backgammon, wedge-wedge
        iii. Wedge and strip
        iv. Progressive geometry – SPAN, Vernier
        v. Graded density electrode
    c. Conductive charge division – uniform element
        i. RAPID detector
        ii. Cross-strip
    d. Capacitive charge division
        i. Wire grid
        ii. Planar electrodes
2. Charge Detection
    a. Discrete electrodes
    b. Coincidence
        i. MAMA
    c. Comparison
        i. CODACON
3. Signal Timing
    a. Delay line
        i. Wire wound
        ii. DDL
        iii. XDL

2.3.1 Charge Measurement

2.3.1.1 Resistive Charge Division

The Resistive Wire

Simple one dimensional imaging of the position of the interaction along the wire of a proportional counter can be achieved using a resistive anode wire. Electrons reaching the wire are collected by amplifiers connected to each end of the wire. The resistive wire shares the charge between the amplifiers such that the ratio of collected charge is directly proportional to the position along the wire :-

$$(2\text{-}2)\quad x = \frac{q1}{q1 + q2}$$

Resistively Coupled Wire Planes/Resistive Wires

MWPCs and other proportional counters of similar geometry commonly use multiple planes of wires or electrodes, acting as cathodes, to define the detector electric fields. These can double up as position sensing elements, and if arranged orthogonally, allow two dimensional imaging to be carried out. The anode wires can also be used for this purpose. The number of processing channels this requires per axis can be reduced to two by resistively coupling the wires of each cathode plane and connecting a preamplifier to each end of the resistive dividers formed. The resistive dividers themselves perform the centroiding by one of two ways.

1. the charge can be measured at the two ends of the divider chain, and the position coordinate calculated as for the resistive wire.
2. the distributed resistance and the capacitance of each cathode wire cause the signal risetime at ends of the resistive divider to be modulated as a function of position. Measurement of the relative timing of the two signals can be used to yield the event position.

Higher performance can be achieved by increasing the number of charge measurement electronic channels and connecting at regular intervals (nodes) along the resistive divider. The linear algorithm above cannot deal adequately with events at the nodal positions and a centre of gravity algorithm is used. This is the principle behind the HRI..

The High Resolution Imager (HRI)

There have been High Resolution Imager (HRI) detectors flown very successfully on several missions, The HEAO-B Einstein observatory, ROSAT, and the still operational CHANDRA mission, and all use the same basic detector design.

Photon detection is carried out by an MCP intensifier, which in the case of the CHANDRA HRC-I [79] comprises a chevron stack of MCPs operated at a gain of ~10^7 electrons . The position readout comprises two orthogonally strung wire planes; one for each axis. Each wire plane consists of a series of parallel wires 100μm in diameter at a 200 μm pitch, shown in Figure 2-11.

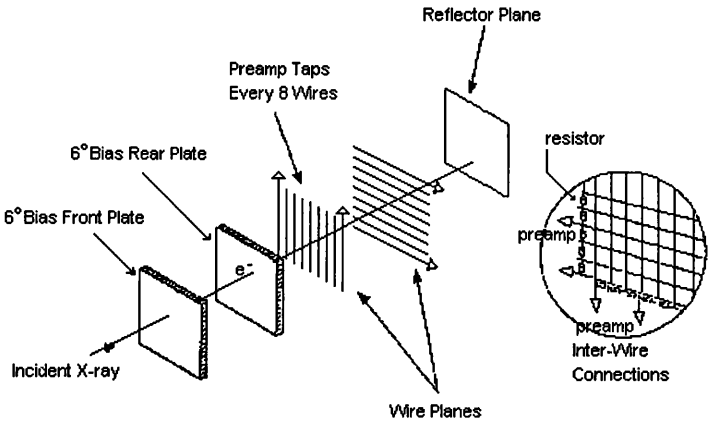

Figure 2-11. A schematic showing of the HRC-I detector [79].

The wire planes are held at ~+300 V with respect to the rear MCP and the voltages of individual planes are balanced to share the charge evenly between them. The wires in each plane are resistively coupled externally. A preamplifier and associated charge measurement electronics is attached to every eighth wire, which constitute nodal points. The resistive coupling of intermediate wires acts as a charge divider similar to the one dimensional resistive readout but with the charge collected by individual electrodes being injected at discrete points dispersed along its length. Knowledge of the node on which the maximum charge has been collected provides the coarse position, and fine position is calculated uses an algorithm calculating the centre of gravity for the three taps over which the charge is collected. The three tap position resolution algorithm is given by :-

$$(2\text{-}3)\quad x = x_{coarse} + x_{fine} = x_i + \frac{Q_{i-1} - Q_{i+1}}{Q_{i-1} + Q_i + Q_{i+1}},$$

where Q_i is the charge collected on the x_i tap.

The CHANDRA HRC-I uses 65 pre-amplifiers per axis which divide the 93 × 93 mm^2 active area into 64 × 64 coarse position elements. Position resolution of better than 25 μm FWHM has been demonstrated.

The Resistive Disk

The Resistive Disk Anode (RDA) is one of the best known and commercially popular image readouts and has been used for both image intensifier [76][77] and proportional counter [51] applications. It consists of a resistive sheet of typically 0.1-1 MΩ per square, on which the event charge cloud is collected and can have a variety of format and sizes. The charge is resistively

divided amongst four contacts on the perimeter which collect the charge allowing it to be electronically measured and the event coordinate calculated using the following algorithm :-

$$(2\text{-}4)\quad x = \frac{Q_A + Q_B}{Q_A + Q_B + Q_C + Q_D}, \qquad y = \frac{Q_B + Q_C}{Q_A + Q_B + Q_C + Q_D},$$

where Q_A, Q_B, Q_C, and Q_D are the charges collected at each of the anode's four contacts.

RDAs have been employed in a variety of ground based and space based applications. For example the RANICON detector [77], used for ground-based telescopes (see Figure 2-12), is an MCP sealed intensifier tube which uses an RDA to achieve resolution as low as 42 μm, albeit at a rather high gain of 4×10^7 electrons. Space-based applications include the ROSAT WFC [48] and the EXOSAT Position Sensitive Detector (PSD) [51], a parallel plate proportional counter, using an RDA position readout as the detector anode in the parallel plate type geometry.

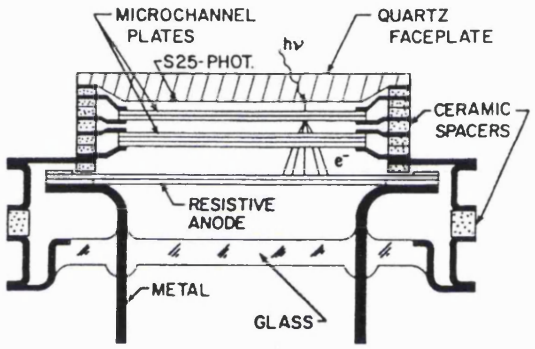

Figure 2-12. A cross-section of the RANICON used for ground-based astronomy [77].

Square or circular RDAs can suffer from image distortion problems especially near the perimeter. These can be overcome to a large degree by the modification of the perimeter geometry, of which there are several alternatives [78].

The resolution of the RDA is limited by two noise components, the resistive thermal noise or 'Johnson' noise, due to the nature of the RDA itself, coupled with the pre-amplifier equivalent noise charge. The intrinsic rms position error for a one dimensional device due to the thermal resistive noise alone is given by :-

$$(2\text{-}5)\quad \Delta x \propto \frac{\sqrt{4kT\tau / r}}{Q}$$

where k is Boltzmann's constant, T is the temperature, τ is the electronic shaping time constant, r is the resistance per square of the RDA, and Q is the total collected charge. In order to overcome this noise, the MCPs must be operated at fairly high gain. MCP gains above 10^7 electrons are required to provide reasonable resolution.

As with other resistive devices, relative signal timing can also be used to determine event position.

2.3.1.2 Conductive Charge Division – geometric area

This family of devices rely for their imaging capability on the division of the charge cloud, produced by an event, among all electrodes of the readout, which may vary in number from as little as two to as many as twelve, depending on the readout design and dimensionality. The implicit assumption underlying their operation is that the ratio of charge collected on a set of electrodes accurately represents the ratio of their mean local geometrical areas at the charge centroid position. Thus the unique determination of a position coordinate relies on the uniqueness of the electrode area ratios at all points on the active pattern. The pattern is finely divided for reasons of practical implementation. This requires that a sufficiently large charge cloud is used to spread over all the electrodes, integrating out the fine structure of the electrode pattern so that the measured charges reflect only the mean local electrode areas.

These devices are usually planar in construction having a metallic conductive electrode material, commonly copper, gold or aluminium, deposited on an insulating substrate, such as plastic or ceramic. Linear breaks in the conductor form the insulating gaps between individual electrodes, defining the shape of the electrode pattern. The electrode areas are defined locally by modulating the widths of the individual electrodes, which are usually organised into pseudo-repetitive pitches with all electrodes being represented in every pitch. The simplest patterns with two or three electrodes can be manufactured without the need for interconnections out of the plane of the pattern.

These readouts have been widely used for ground-based and space-based applications [81]. They owe their success to their relative simplicity, requiring a minimal electronics for substantial resolution, their flexibility, being easily adapted to almost any size, format, and coordinate type (Cartesian, polar, logarithmic, etc.), and their ease of manufacture using simple printed circuit board techniques.

The two major factors limiting spatial resolution for this type of readout are electronic noise, generated in the pre-amplifier and sensitive to the loading of the readout impedance, and partition noise, a charge level fluctuation resulting from the binomial statistics which determine the division of a finite number of charge quanta (electrons) among a small number of electrodes. Apart from pre-amplifier design, the major factor influencing electronic noise is the pattern capacitance which amplifies the voltage noise source in the pre-amplifier FET. Electronic noise varies as $1/Q$, where Q is the total charge. Partition noise varies as $1/\sqrt{Q}$ and so would eventually become the dominant factor as Q increases, though in practice this never occurs.

Quadrant anode

The Quadrant anode was first described by Wijnaendts *et al.*[82] and Lampton *et al.*[83] in 1976. It is used commercially but its highly nonlinear performance limits its usefulness. It is the simplest two dimensional charge division readout, comprising a circular conductor, subdivided

into four quadrants, as shown in Figure 2-13. The charge footprint size is chosen so that charge is collected by all four electrodes in the active imaging area of the detector, and the algorithm used to determine x and y coordinates, is given by :-

$$(2\text{-}6)\quad X = \frac{Q_2 + Q_3 - (Q_1 + Q_4)}{Q_1 + Q_2 + Q_3 + Q_4}, \text{ and } Y = \frac{Q_1 + Q_2 - (Q_4 + Q_3)}{Q_1 + Q_2 + Q_3 + Q_4}$$

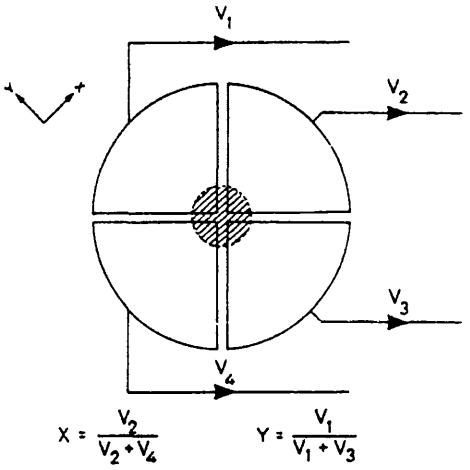

Figure 2-13. The Quadrant anode electrode pattern and decoding algorithm[83].

The Quadrant Anode can achieve fairly high resolution over a small range, and is reasonably linear when the charge event coordinate is close to or at the centre of the pattern. In this region the two orthogonal pattern divisions lie close to the centre of symmetry of the charge footprint distribution integrated across one dimension, thus the rate of change of the charge collected on either pair of electrodes (1 & 2, or 2 & 3) is almost stationary with position, this being the requirement for linearity using the above algorithms. Further away from the centre, the rate of change of charge with position diminishes, the resolution degrades and the image exhibits ever increasing nonlinearity, until charge is no longer collected on all electrodes and positional information all but disappears.

In the purest sense, the Quadrant Anode does not qualify as a geometric charge division readout because it uses the charge footprint distribution as the charge modulator as opposed to the electrode area.

The Backgammon Readout

This one dimensional readout is the simplest of this family of devices [84]. It has a structure consisting of two interlocking electrodes each constructed of many wedges in a comb-like arrangement. The charge cloud produced by the detector, whether it is directly collected as electrons on to an anode, or induced in the case where a proportional counter anode wire is suspended above, is required to spread over several wedge repeats of the pattern. Each electrode collects a fraction of the charge proportional to its width at the coordinate of the centroid of the

charge cloud. The operation of a Backgammon readout in a proportional counter is described in section 4.2. The two dimensional analogue of the Backgammon anode is the WSA.

The Wedge and Strip Anode

The Wedge and Strip Anode (WSA) is the most widely used charge division readout. It was first described by Anger [15] in 1966, and in its simplest form consists of three electrically isolated conductors, the Wedge, Strip and Z electrodes, as shown in Figure 2-14. Further discussion on design and operation is left until chapter 3.

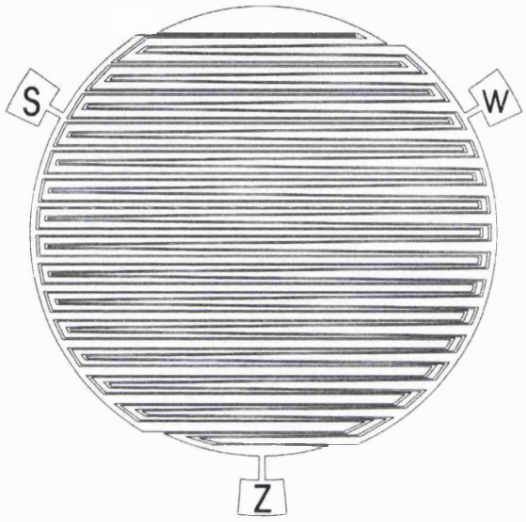

Figure 2-14. The 3 electrode wedge and strip anode.

Many different formats have been used, square, rectangular and circular patterns, with sizes up to 185 mm diameter [80]. WSAs have been manufactured on fused silica and ceramics for use in sealed intensifier tubes, thin 12.5 μm kapton substrates to reduce capacitance of large patterns for proportional counters, and have been assembled in a mosaic array [102] to produce larger areas whilst maintaining resolution . Resolutions as low as 18.5 μm FWHM have been reported [85] for small diameter MCP-based device, though resolutions of 40 -50 μm FWHM are more typical.

Progressive Geometry Readouts

The characteristics of progressive geometry readout devices [86] will be briefly mentioned for completeness, even though they were invented during the course of this study and were not part of the initial review. Both the Vernier and Spiral anode belong to this family of devices. The fundamental difference between progressive geometry readouts and the more traditional schemes described previously is their use of cyclic or pseudo-cyclically varying electrode geometries. During each electrode cycle the electrode dynamic range is visited twice, enabling a fine position coordinate, represented by a rotational phase coordinate, to be more accurately determined. In addition, by using a variety of techniques to establish the cycle number, such as the Vernier or Spiral schemes, a coarse position coordinate can also be determined. This enables the pattern as a whole to utilize the electrode dynamic range many times over its active length, as opposed to linear devices which utilize this only once. This makes it possible to achieve a spatial resolution many times better than the charge resolution, or equivalently, to encode a number of position resolution elements much greater than the signal-to-noise ratio.

Further description of the design, manufacture and operation of both the Vernier and Spiral position readouts will be left until chapter 6.

Graded density electrode

The graded density electrode readout, described by Mathieson *et al.*[87], is a scheme which implements linear geometric charge division by means of a wire plane. The wires are connected to one of two sets, A and B, so that the density of wires in each group varies linearly with position, in the opposite sense for groups A and B respectively. A second dimension can be provided by stacking a second plane of wires arranged orthogonally to the first plane. A simple linear algorithm is used to calculate the position coordinate from the charge levels measured on the two wire groups per axis. A spatial resolution of 40 μm was reported using an MCP-based detector.

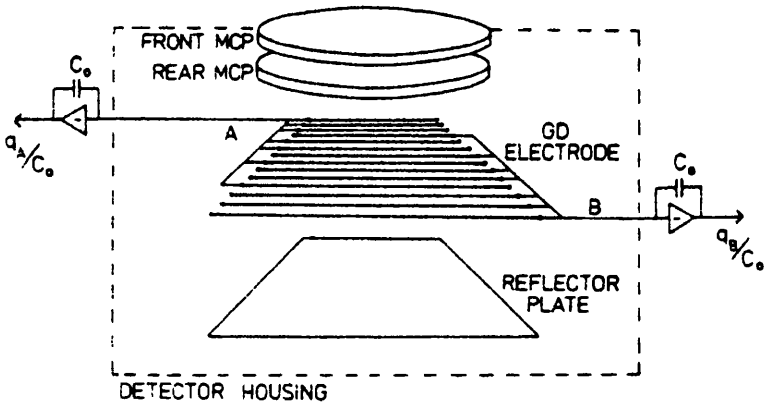

Figure 2-15. A schematic of a 1-dimensional graded density anode [87].

2.3.1.3 Conductive charge division – uniform element

RAPID Detector

Developed as a very high count rate imager primarily for biological applications on a synchrotron beam-line, the RAPID detector [88] uses the wire micro-gap technique. The RAPID detector is a 30cm square adaptation of the MWPC design, having a cathode plane separated by only 500 μm from the anode wire plane. This allows ions formed in the avalanche around the anode wire to be quickly neutralized on the cathode and space charge suppression of the avalanche to be reduced, allowing the detector to operate at higher count rates.

The anode wire plane and the solid cathode plane, which is subdivided into strips orthogonal to the anode wires, provide the two dimensional position readout. Independent electronic channels are attached to every wire and strip, using discriminators to provide timing and coarse position information, and ADCs to provide the digitized pulse height for the four readout elements closest to the event position. The ADCs use double correlated sampling to minimize pile-up at very high count rates. The digitized signals are used to determine x and y coordinates using an algorithm implemented in a look-up table for high speed operation. Timing information together with the calculated coordinates are correlated to form a complete data set of the event which is used to address a histogramming memory. The system can generate x,y event coordinates at a maximum rate of 20 million events per second. A linear (1-D) and an area (2-D) detector have been built.

In general, detectors employing this readout scheme require complex electronics exhibiting a high degree of uniformity between channels and also require high reliability since the component count is large. The latter factor also implies high cost, especially since each channel uses charge measurement electronics requiring analogue to digital conversion at high speed. However, they can achieve very high position resolution coupled with high speed operation because of the parallel nature of their operation.

Cross-strip anode

The cross-strip anode is a two dimensional image readout using a multilayer ceramic construction, primarily designed for MCP-based detectors [89]. It consists of two orthogonal arrays of metallic strips supported on an alumina substrate which directly collect the charge (see Figure 2-16). The strips have a 0.5 mm pitch and the charge footprint spreads over several pitches, allowing position determination accuracy to a small fraction of the pitch. The charge on each strip is sensed by chip level pre-amplifiers mounted on the anode, followed by analogue to digital conversion and software centroid determination.

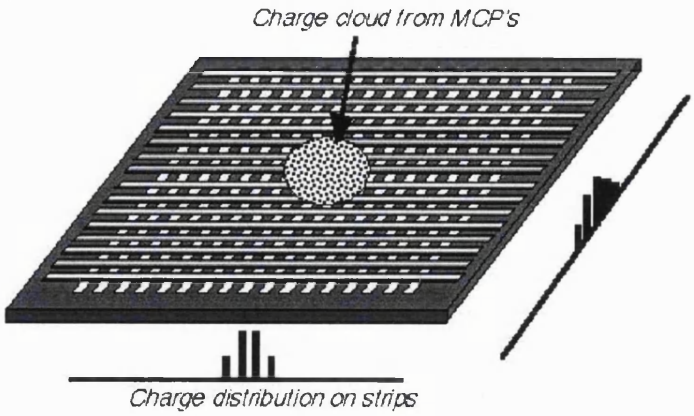

Figure 2-16. The cross-strip anode, showing the charge distribution on the strips [89].

This design has distinct similarities with both the HRI and the RAPID detector, in that independent orthogonal elements are used to provide two dimensional position, and the charge is spread among several sensing elements and centroided to provide a fractional pitch fine position coordinate. It differs from the HRI in that every readout element is instrumented individually, as opposed to being resistively coupled, and it is a monolithic device integrated with its preamplifiers, whereas both RAPID and the HRI use wire planes or cathode strips and separate electronics. The sophisticated electronics of the RAPID detector endow it with a very high rate capability by virtue of parallel event processing, a feature which can be achieved in principle by the cross-strip, but has not yet been reported.

Spatial resolutions of less than 7 μm have been reported, sufficient to image both 12.5 μm and 7 μm diameter MCP pores. This can be achieved at relatively low MCP gains of 1.5-5.5 × 10^6 electrons, allowing higher MCP local counting rates (several hundred events $pore^{-1}$ s^{-1}) Thus far, the cross-strip has only been implemented over an 8 × 8 mm^2 area, requiring 16 pre-amplifiers, a number which will scale linearly with readout dimension..

2.3.1.4 Capacitive Charge Division

The capacitive division image readout technique has never been as popular as either resistive or conductive charge division, though in principle in offers potential for excellent performance. The major reasons for this are practical. Whereas both conductive and resistive devices can use either simple planar geometric patterns such as the WSA, or resistive surfaces such as the RDA, the there is no such trivial arrangement to satisfy the needs of a device using capacitively coupled elements. This is due to :-

1. The need for each element to also be resistively coupled to ground so that collected charge can bleed away.
2. The difficulty in producing a purely geometric pattern to provide the necessary accurately defined, and relatively small capacitance values required for such a device.

3. The distortion effects produced by unavoidable parasitic capacitances to other adjacent conductors.

This leads to capacitively coupled devices requiring discrete components for both the resistive and capacitive coupling needed for every pattern element, which adds to the degree of difficulty of their design and manufacture. Even using discrete components there is also the problem of matching nominally equal value items with sufficient accuracy to avoid nonlinearities.

Wire grid

A capacitive charge division technique was demonstrated early on in the development of MCP detector image readouts. Gott *et al.* reported in 1969 [90] on an "image dissection" scheme using a capacitively coupled wire plane. The first device was only one dimensional and used a plane of 100 μm diameter wires at a 200 μm pitch , spaced at 300 μm from a single MCP, and extending over a 10 × 10 mm^2 area. The MCP for this experiment was supplied by Mullard Research Laboratories as an "experimental" device, indicating that this was truly at the forefront of the emerging MCP technology. This initial detector, having a single MCP operating at low mean gain of 1.25×10^5 electrons with an exponential pulse height distribution, still managed to achieve a spatial resolution of better than 200 μm FWHM.

Planar electrodes

Despite the practical difficulties outlined above, planar patterns have been manufactured and successfully demonstrated. One such two dimensional device, designed as a particle detector for a toroidal electrostatic analyzer, is reported by Tromp *et al.*[91]. This device is shaped to suit the analyzer, as a segment of an annulus, and consists of 97 triangular elements with their long axes radially, and arranged in two interlocking and electrically isolated sets, with half the triangles pointing towards, and half away from the centre. The elements of each set were capacitively coupled with preamplifiers attached to the elements at either end of each set, numbering four in total. The pattern was manufactured on a quartz substrate which provided a rigid attachment for the surface mount resistors and capacitors which were glued on using conductive epoxy to provide the resistive and capacitive coupling for each element.

Simple linear algorithms were used to determine the radial and angular event coordinates. The use of similar algorithms for both axes disguises the fact that this detector used geometric charge division for the radial axis, the interlocking triangular electrodes being equivalent to a Backgammon readout.

The resolution reported for this device in the capacitively coupled axis was 0.4°, equivalent to a spatial resolution of ~1 mm at gains of between $10^6 - 10^7$ electrons. This was achieved using illumination with ions. The production of multiple electrons from ion collisions with the MCP, whose spread above the MCP could well degrade position, and would suggest that this figure is not representative of the intrinsic readout resolution.

2.3.2 Charge Detection

This group of devices uses charge collection on discrete electrodes to identify event position. The accuracy of position determination is limited by the size of the electrode elements. Very high count rates can be achieved using the simplest configuration with an amplifier and discriminator on every element operating in a fully parallel mode. The number of electronic channels required prohibits high resolution in this configuration, and so several designs use a coincidence scheme to reduce electronic complexity at the expense of count rate performance.

2.3.2.1 Discrete pixels

Discrete pixels, either arranged as a one or two dimensional array of charge collection pads provide one of the simplest image readout schemes. Each pad represents an individual image pixel and a valid event is usually indicated by the signal level exceeding a discriminator threshold. These devices require a number of electronic event detection channels equal to the number of pads. One of the drawbacks of this technique is the sheer number of electronic channels required for even moderate resolution, and thus practicalities of scale limit the resolution attainable. However advances in microelectronics, as exemplified by the 256 x 256 Medipix2 electronic readout chip [39], have expanded the potential for this technique, though as yet theses devices have only been applied to solid state detectors. Perhaps the major benefit of the discrete electrode solution is that it can provide extremely high count rate capability due to the complete parallelism of the readout, each electrode element being completely independent and in principle being able to detect events simultaneously with all other electrodes. One such scheme in an MCP detector with 400 individual readout pads has been described [92].

Limitations of these devices include non-linear position dependent counting statistics due to mis-counting of events occurring near pad boundaries. The charge from these events is shared between pads and low amplitude events may trigger neither discriminator, resulting in a lost event. Conversely large amplitude events in similar locations can trigger both discriminators resulting in double counting. Similar effects can result from signal crosstalk due to stray capacitance between pads, a factor accentuated by the fast electronics used to handle the high count rate capability. These effects are very much dependent on the intensifier pulse height distribution and are further accentuated when used in conjunction by a charge amplification device which undergoes gain reduction at high count rates, such as an MCP intensifier.

2.3.2.2 Coincidence

Coincidence readouts operate by collecting event charge on a small number of electrodes out of the total number comprising the readout pattern. The pattern is designed so that the particular electrode combination represents a single unique position on the pattern. The coincidence method of position encoding allows high resolution imaging without charge measurement electronics and without using an excessive number of electronic channels. Coincidence devices generally process

events serially. Although a single event activates only a few channels, it temporally disables the entire readout since all events use the same coincidence detection circuitry. The high count rates achieved by the discrete electrode readout are not achievable with this method. However, since accurate charge measurement is not required, the electronics can be operated at higher speed than typically used for charge division readouts and thus higher maximum count rates are possible.

An example of such a device is the Multi-Anode Microchannel Array (MAMA) detector, developed by Timothy [93].

The MAMA Detector

The MAMA multi-layer coincidence anode is a monolithic structure comprising two sets of anode strips, insulated from one another but exposed to the MCP output charge. The two sets of anode strips are arranged orthogonally and supported on a quartz substrate, as shown in Figure 2-17. MAMA readouts have been constructed with up to 1024 strips in each axis with a strip pitch of 25 μm, the active readout area being 25 × 25 mm^2. The MCP output charge is divided between the two sets of anodes and, in its simplest incarnation, is collected by one anode of each set. The identity of the particular anode pair assigns the event position to a 25 × 25 μm^2 pixel. Thus a readout comprising m × n anode strips requires only m + n electronic channels compared to the m × n channels required by a discrete readout. The low signal to noise requirement of the coincidence electronics allows the MCP gain to be as low as 10^6 electrons. Initial devices used single curved channel MCPs (C-plates), but manufacturing and other difficulties cause these to be replaced by chevron MCP stacks.

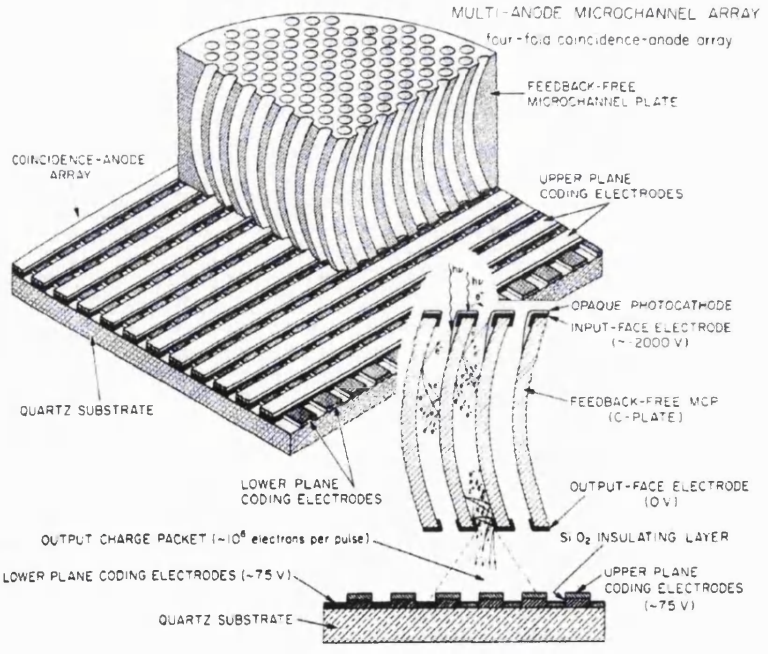

Figure 2-17. A cut-away view of the MAMA detector [93].

In later designs more elaborate coincidence criteria were used that required charge to be detected on either 2 or 3 strips in each axis. The net result of this being to reduce the number of electronic channels to $\sqrt{8(m+n)}$ for $m \times n$ pixels, at the expense of increased processing complexity. Spatial resolution of 25 μm has been reported [94].

Both electrode structure and interconnections are minute and complex requiring fabrication methods similar to those used for micro-electronic circuits. In an attempt to improve performance devices have been constructed with flying bridge electrodes of sub-10 micron scale to reduce inter-electrode capacitance, the intermediate support being etched away afterwards.

2.3.2.3 Comparison

The CODACON

The CODACON [95] is a one dimensional readout consisting of an array of charge collecting elements (charge spreaders) capacitively coupled to a number of code tracks, *n*, which are configured to provide an immediate *n*-bit digital position coordinate. Each charge spreader represents a unique image pixel and each code track consists of a pair of electrodes whose relative widths are modulated in a binary mode, as shown in Figure 2-18. The two charge levels from each code track are measured by a differential preamplifier generating either a 1 or 0 per for each pixel. Thus *n* code tracks can uniquely encode 2^n pixels. The pixel addresses are Gray-coded to prevent ambiguities that could result from having transitions in more than one bit between pixels. An additional, unmodulated electrode, the (n+1)th, is used as a discriminator to detect events and trigger the electronics. Since every event uses the same electronics, the readout operates in a serial mode and thus maximum count rate is limited by the deadtime of the processing electronics.

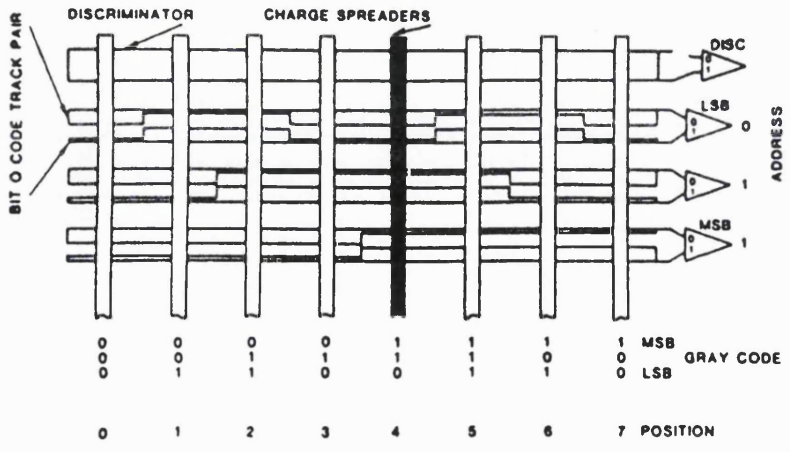

Figure 2-18. A schematic of the one-dimensional CODACON readout [95].

McClintock et al [95] described a one dimensional device with 1024 pixels and 25 μm resolution, requiring 10+1 electronic channels. More recently Pearson et al [96] have designed and manufactured a two dimensional CODACON providing a polar readout for the TEARES electron

analyzer. This ingenious design uses two coupled 1D encoder tracks to provide two dimensional imaging. Five code tracks provide 32 radial pixels and a further seven code tracks are used to define 128 angular positions in a range of 360°.

2.3.3 Signal Timing

2.3.3.1 Delay Lines

Delay line readouts operate by means of measuring the time delay between signals propagated from a point along a delay line to each of its ends. This point corresponds to the position of the charge collection, i.e. the event coordinate. The charge collecting electrode can either constitute part of the delay line, or may be connected to an intermediate tap on a remote delay line. The ideal delay line is a distributed inductive-capacitive network with no resistive component; a transmission line with a relatively low propagation velocity. For a given timing resolution, the lower the signal propagation velocity, the larger the signal delay, and hence the better the spatial resolution. Resistive components in the delay line cause signal dispersion, which results in longer signal risetimes and greater uncertainty in the timing measurement, at the cost of resolution.

The time delay between signals is commonly measured using the rising edge of the signals. Various schemes have been used to reduce the sensitivity of the timing to signal amplitude, such as the Constant Fraction Discriminator (CFD) and the Extrapolated Zero Strobe. In order to overcome the problem of measuring positive and negative time intervals, one solution is to use a fixed time delay in series with the output from the one end of the line whose period is slightly longer than the period of the readout delay line itself. The two timing signals can be used to generate a pulse whose width is proportional to the time delay, which is then digitised using a Time to Digital Converter (TDC) producing a digital output corresponding to the position of the event along the physical delay line.

Delay lines can achieve very high position resolution but temperature instability of the timing circuitry can degrade performance. Reflections from the ends back along the delay line due to non ideal termination can also limit the count rate. Though events which produce simultaneous pulses on the electronics cannot be processed correctly, there are schemes which can accommodate events with overlapping delays. This capability coupled with the intrinsically fast nature of timing pulses used, in principle allow delay lines to typically operate at higher count rates than readout techniques requiring charge amplitude measurement.

Wire wound

A common mechanical design is a wound wire frame comprised of two wires arranged as a helically wound delay line, constituting a transmission line, with the charge being collected on one wire only by means of a bias voltage. A two dimensional readout can be constructed by using a second orthogonal wire frame inside the first, using a bias voltage is to share charge equally

between the two delay lines. Williams et al [97] report a resolution of 18 μm at a gain of 2.4×10^7 e for a two dimensional large area delay line with a size of 140×140 mm^2

Double Delay Line (DDL)

The DDL is a planar two dimensional imaging device whose active area consists of two sets of interlocking wedges. The device has a resemblance to the Backgammon anode one dimensional charge division readout and charge division is used to generate the position coordinate for the axis along the length of the wedges. The wedge components in each set are connected via an external meandering delay line to encode the orthogonal axis. Four pre-amplifiers are connected to the elements at the ends of both sets of wedges and the signals summed so that the full event charge is used for both the delay line and the charge division measurements in both axes. These devices have been used for space missions and Siegmund et al [70] have reported resolutions, for flight instruments, of <20 μm along the delay line encoded axis, over a range of 94 mm, and resolution of ~50 μm along the 20 mm range of the wedge-wedge charge division axis.

Crossed Delay Line (XDL)

The XDL is a multilayer, two dimensional image readout utilising delay lines for position determination in both axes. It consists of two sets of orthogonal conductive 'fingers' making up the x and y axis on to which the event charge is shared equally. The two sets of fingers are separated by another set of conductive fingers connected to the ground plane, all the conductors being isolated using thin insulators shaped as the upper fingers and serving to minimize crosstalk between the axes. The fingers of each axis are connected to external 'serpentine' shaped delay lines manufactured on the same substrate. The pattern is manufactured on a copper coated, high dielectric alumina substrate using a photolithographic process. Figure 2-19 shows zoomed detail of a 65 mm XDL. The substrate dielectric constant and geometry of the serpentine determine the overall delay.

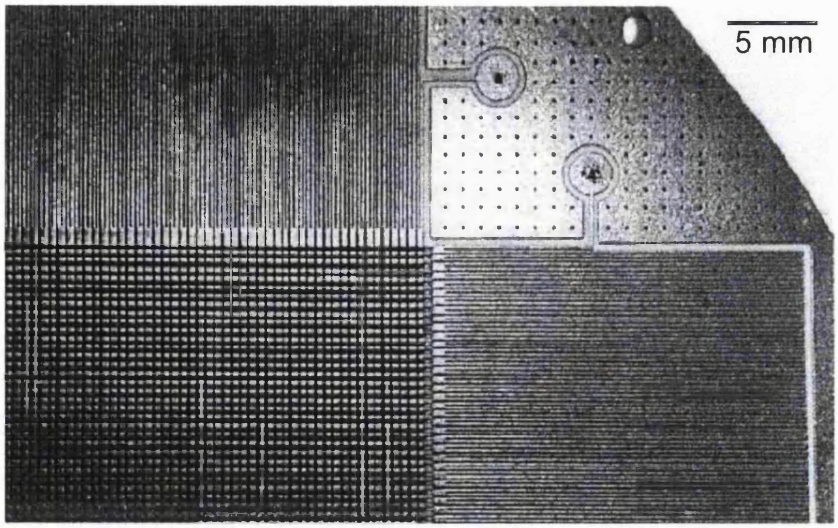

Figure 2-19. A zoomed photograph of a copper on alumina 65 mm XDL readout [98].

XDL devices up to 65 × 65 mm^2 have been described by Siegmund et al [98]. A resolution of 22 μm in both axes was reported at an MCP gain of 3×10^7 e, and a count rate of 200 kHz (at 20% deadtime) using a modified electronic design was projected.

Chapter 3

Conductive Charge Division Readouts – The Basics

3.1 Introduction

The electronic position readouts in photon-counting detectors which utilize charge division techniques can be divided into four basic groups by virtue of the means used to divide the charge cloud whose centroid is to be determined :-

1. Resistive division, as used in devices such as the RDA. Whilst the linearity can be improved by application of specific termination geometry, the spatial resolution of resistive anodes is limited by thermal noise in the resistive component.
2. Geometric charge division using conductive electrodes. This technique avoids the thermal noise of the resistive device, and the practical difficulties encountered with the capacitive device. These devices use an extended charge footprint which is collected over all the electrodes, the geometric areas of the electrode elements themselves performing the charge division.
3. Division amongst multiple uniform conductive elements. These schemes utilize the charge footprint to perform the division and the centroiding accuracy and linearity depends on the form and stability of its distribution. They require higher numbers of electronic channels but are capable of parallel event processing of spatially separated events.
4. Capacitive division, as used in some early cross-grid readouts and occasionally for planar designs. Though theoretical performance is good, practical designs commonly require the capacitive coupling and resistive electrode discharging elements to be implemented using discrete components. This requirement makes the pattern design and manufacture more involved and combined with limitations due to component accuracy and stray capacitances limits the usefulness of this technique.

At the beginning of this research work, an analysis of the benefits and drawbacks of the three categories 1, 2 and 4 was undertaken (category 3 was discounted at the time because of electronic complexity) and it was determined that the second category, that of geometric charge division, offered the best potential for development and performance gains. The following discussion details the theory and manufacture of such devices.

3.2 Conductive geometric charge division

The major advantages of the geometric charge division technique are its simplicity, flexibility, and high performance. In its simplest form it comprises only a few electrodes, requiring an equally small number of electronic charge measurement channels. In its planar electrode form, this device need be little more than a specialized printed circuit board, which can be constructed relatively inexpensively in any size or shape; circular, rectangular or square. It can be designed to provide either one or two dimensional imaging with Cartesian, polar or custom coordinates. The axes can be linear, logarithmic or customised to suit varying applications. A typical device consists of a square or circular pattern returning a two-dimensional, Cartesian x,y coordinate with an imaging performance of typically 512 × 512 pixels. More elaborate devices (such as the Vernier anode, described in Chapters 6 and 7) have been designed which are capable of resolutions in excess of 4000 × 4000 pixels.

3.2.1 Theory of operation

This family of imaging devices consists of two or more isolated electrodes which detect the charge cloud produced by detector, either directly or using induced charge. The geometry of the electrodes is chosen so that the ratio of average areas at any position is unique. In general these devices rely on an electrode geometry which varies linearly with position in either one or two dimensions. The charge cloud is allowed to spread over all the electrodes which are arranged to lie side by side on a plane in a quasi-repetitive structure. This can be in the form of a wire plane [99] or a pattern of planar electrodes [15] deposited on an insulating substrate, similar to a printed circuit board.

The pitch of this quasi-repetitive electrode structure, representing the dimension in which all electrodes are present at least once, is selected so that it over-samples the charge cloud footprint. This has the effect of smoothing out the repetitive structure on the electrode amplitudes whilst retaining the lower frequency electrode geometry information. It also means that charge from an event is collected on all electrodes whatever the spatial location of the event. This limits these devices to serial operation; events are processed on an event by event basis. All geometric charge division readouts perform in this manner, only the number of electrodes and the function describing the idealized geometry being different.

An event position coordinate is determined by measuring the charge collected on each electrode, and calculating the charge cloud centroid using a decoding algorithm based on the idealized electrode geometry. The charge collected on each electrode is typically measured using a number of identical electronics channels each comprising a charge-sensitive preamplifier, shaping amplifier and analogue to digital converter (ADC). Depending on its complexity, the coordinate decoding algorithm can be carried out in either the analogue or digital regime, i.e. before or after the ADCs respectively.

3.2.2 Performance

Position resolution is primarily controlled by two factors, partition noise and electronic noise. Both affect the accuracy with which the measured charge levels reflect the electrode geometry. Partition noise is a statistical noise resulting from the division of a finite number of charge quanta between a small number of discrete electrodes and is only present when charge is directly collected, as opposed to being induced. Electronic noise is dominated by the front-end preamplifier noise, which is strongly dependent on the input capacitance to the preamplifiers. This noise increases approximately linearly with increasing input capacitance load from its no-load level. Most of the input capacitance is due to the readout inter-electrode capacitance which can be reduced by minimizing capacitance by using thinned or low dielectric anode substrates [100].

The maximum event rate of a conductive geometric charge division readout is limited by the event processing time because events are processed serially. This is governed by the dead-time of the electronics, usually set by the recovery time of the analogue pulse shaping circuitry to allow a given charge measurement accuracy for successive pulses.

The centroiding nature of the geometric charge division technique is extremely tolerant of differential nonlinearities such as flaws in the pattern. The charge cloud footprint acts as a spatial filter attenuating high frequency noise (including the pattern fine structure) to insignificant levels while the lower frequency integral nonlinearities are mapped directly from the pattern to the image plane. The overall linearity of the image is in principle defined by the pattern electrode geometry. Since the pattern can be manufactured with great accuracy, the potential for excellent linearity exists. However this is difficult to achieve in practice. A discussion of the linearity deficiencies and their causes associated with this type of readout together with practical solutions to overcome them is presented in the following chapters.

3.2.3 Design Types

Several different designs have been suggested [101]. Some are alternative approaches to the solution solved by the WSA but employing a larger number of electrodes with some gain in resolution usually at the cost of elegance and ease of manufacture i.e. requiring interconnections. Others are modifications of the standard pattern so that the r, θ coordinates of the event are

encoded instead of the usual *x,y* Cartesian coordinates. Extensions to linear patterns have been suggested either by means of concatenating several patterns in a mosaic arrangement [102] or by reflecting and repeating linear structures [103][104].

Optimised designs of existing linear devices, such as the enhanced circular WSA, and new designs such as the 120° WSA and the Tetra-Wedge Anode (TWA) are introduced in section 3.3.2.2.

A device called the Split-Strip Anode, described in chapter 5, is an adaptation of the principle of operation of the one dimensional Backgammon readout [84] and was designed specifically to measure the form of the charge cloud distribution produced by an MCP

3.3 The Wedge and Strip Anode

The WSA was first developed by Anger [15] and subsequently several different forms of similar pattern were published [101], the simplest having only three electrodes and requiring no sub-plane connections. Some of these designs are shown in Figure 3-1.

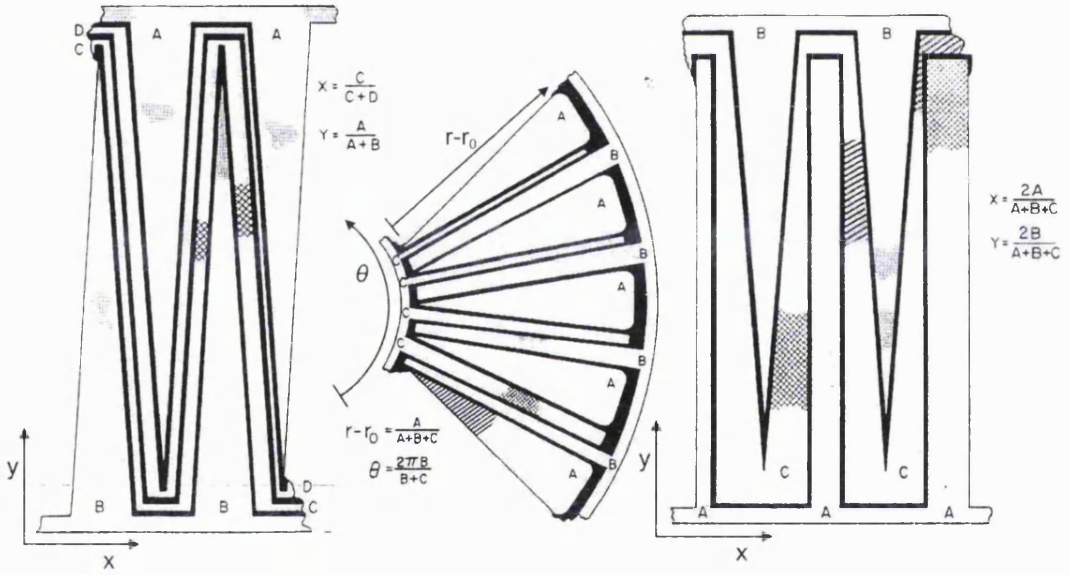

Figure 3-1. The WSA and alternative electrode designs with their decoding algorithms [101].

The standard WSA consists of a planar pattern of three isolated conductors, the wedge, strip and Z electrodes. The wedge and strip electrodes resemble interlocking comb-like structures, while the Z (or zig-zag) electrode makes up the remaining space, meandering through the pattern as continuous conductor. The width of each wedge varies uniformly along its length, the position axis it encodes, and the strip widths are incremented linearly in an orthogonal axis. The width per pitch of the Z electrode also varies linearly along the diagonal direction (defined by the *–ve x,-ve y* direction) and is required for normalization in the algorithm denominator. Figure 3-2 shows a schematic of the three electrode WSA. The pitch of the pattern, defined as the repeat pitch of the wedges or strips, is typically ~1 mm. A charge cloud of diameter of several times larger than the pitch is used to smooth out the comb-like structure of the pattern, which results in the collected

charge on each of the electrodes being proportional to their mean local area. The mean local area is itself proportional to the fractional electrode width and thus the fractional charge collected on the wedge and strip electrodes varies linearly along their respective orthogonal axes. This property can be used to calculate the *x,y* position co-ordinate for the centroid of a photon event using the following position decoding algorithms shown in Figure 3-2. These algorithms indicate the convention for *x,y* coordinate determination used for WSAs in the rest of this work.

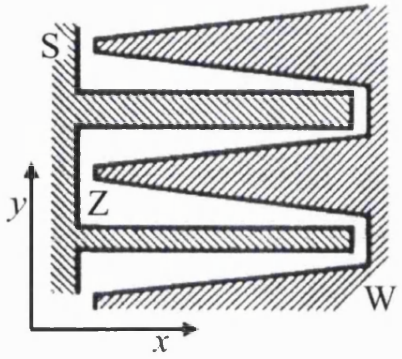

$$x = \frac{2Q_W}{Q_W + Q_S + Q_Z}$$

$$y = \frac{2Q_S}{Q_W + Q_S + Q_Z}$$

Figure 3-2. The electrode layout of the 3-electrode WSA with its position algorithm.

3.3.1 Performance

3.3.1.1 Position Resolution

Electronic Noise

Electronic noise is usually the dominant factor limiting the position resolution of the WSAs. Its effect can be visualized qualitatively by considering its representation in the charge domain. Figure 3-3 is a diagram showing the mapping of the two dimensional position space of the WSA on to the three dimensional volume defined by the charges collected on the W, S, and Z electrodes. The triangular boundary represents the extent of the physical region where all electrode values are positive. For clarity, the mapping of the WSA on to the plane of constant charge is shown for only one pulse height. The planes corresponding to other pulse heights stack in parallel above and below this plane; the mapping of the WSA expands or contracts to fit the triangular boundary as pulse height varies.

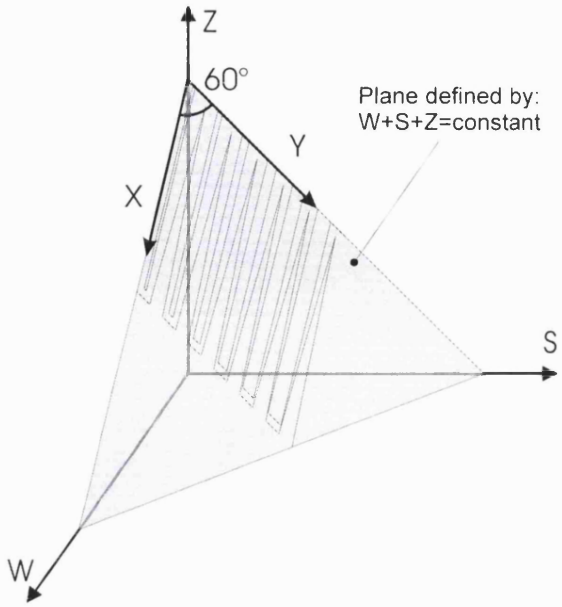

Figure 3-3. The mapping of the WSA area on to the charge domain volume.

The electronic noise on each channel is independent and is a gaussian distribution. The three noises add quadratically to produce a 3 dimensional noise distribution whose probability at position, W,S,Z in the charge domain is given by :-

$$(3\text{-}1)\quad P_{W,S,Z} \propto e^{-\left(\frac{W-W_0}{2N_W}\right)^2-\left(\frac{S-S_0}{2N_S}\right)^2-\left(\frac{Z-Z_0}{2N_Z}\right)^2}$$

where N_W, N_S, and N_Z, are the electronic noises on the W, S, and Z channels, and W_0,S_0,Z_0 is the nominal charge coordinate.

The scale of this distribution is independent of its location in the charge domain, and if all noise contributions are equal, it equates to a spherically symmetric charge uncertainty in the charge domain. The position error caused by this distribution at a particular W_0,S_0,Z_0 coordinate can be visualized by projecting it on to the plane of normalized charge, defined by $W + S + Z = 1$. The representation of any point in the charge domain on the normalized charge plane is given by the intersection of the line joining the point to the origin, with this plane. The projected noise distribution can then be converted from its normalized charge plane co-ordinates, x', y' to image space x,y using a conformal transformation shown graphically in Figure 3-4.

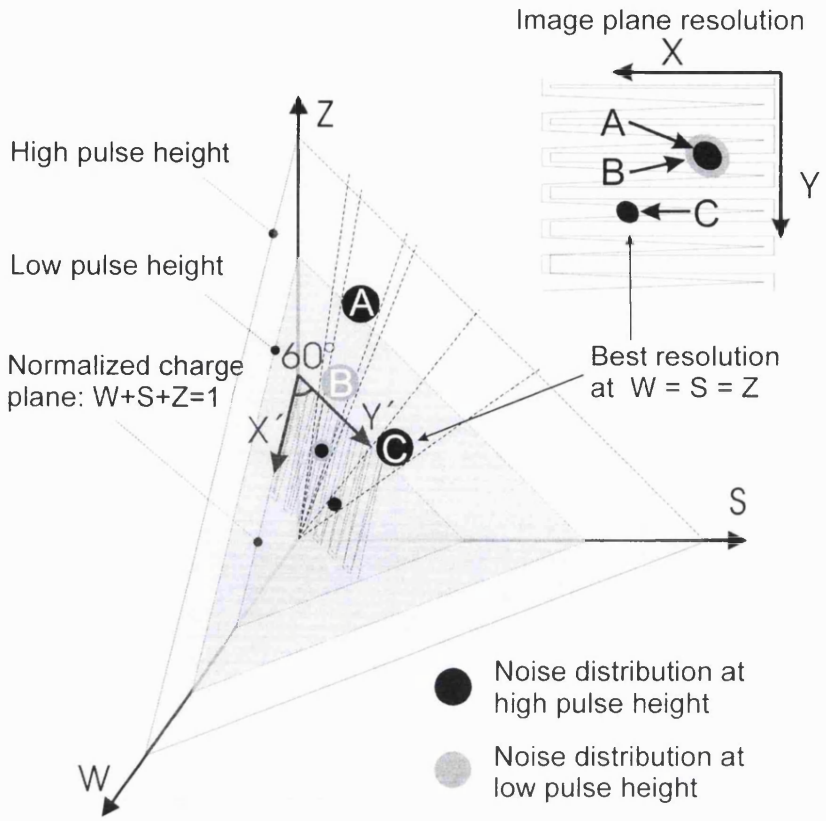

Figure 3-4. The effect of event position and pulse height on electronic noise.

Qualitative assessment of this visualization indicates that :-

1. At higher pulse heights i.e. at a point further from the origin, the size of the projected noise distribution on the plane of normalized charge diminishes. In fact its size is inversely proportional to pulse height.

2. Owing to the asymmetry of the WSA mapping (the 60° angle between the x and y axes), the projected noise distribution on to the WSA x,y plane is not circularly symmetric. It is elliptical with its minor axis along the Z direction. This is understandable since along this direction, the Z electrode also varies and provides imaging information, thus reducing the overall noise along this axis.

3. The minimum noise occurs where the projected noise distribution is smallest, where the projection is normal to the plane i.e. along the centre diagonal of the charge domain defined by $W = S = Z$.

The electronic noise contribution, EN, to position resolution as a function of position can be calculated analytically by differentiating the position decoding algorithm :-

$$(3\text{-}2) \quad X = \frac{L}{F}\left(\frac{W}{W+S+Z}\right)$$

where: X is the position coordinate

L is the size of the pattern

F is the dynamic range of the wedge electrode

W,S,Z are the charges measured on the WSA electrodes

$$(3\text{-}3)\quad \therefore \delta X = \frac{L}{F}\left(\frac{S+Z}{(W+S+Z)^2}\delta W - \frac{W}{(W+S+Z)^2}\delta S - \frac{W}{(W+S+Z)^2}\delta Z\right)$$

Since $f = \dfrac{W}{W+S+Z}$, and $Q = W+S+Z$, it follows that :-

$$(3\text{-}4)\quad \therefore \delta X = \frac{L}{F}\left(\frac{(1-f)}{Q}\delta W - \frac{f}{Q}\delta S - \frac{f}{Q}\delta Z\right)$$

where: f is the fractional area of the wedge electrode at position, X

Q is the total charge landing on all electrodes

Since the W, S, and Z electronic noises are independent, they add quadratically. Thus the FWHM electronic noise limited position resolution, EN_x, is given by :-

$$(3\text{-}5)\quad EN_x = \frac{2.36L}{FQ}\sqrt{(1-f)^2 N_W^2 + f^2 N_S^2 + f^2 N_Z^2}$$

where: N_W, N_S, and N_Z are the rms equivalent noise charges on the pre-amplifiers.

An equivalent equation is used for position resolution in the strip axis by swapping *Nw* and *Ns* and measuring f, the fractional area of the strip electrode at the relevant position.

$$(3\text{-}6)\quad \text{If } N_W = N_S = N_Z, \text{ then } EN_x = \frac{2.36L}{FQ}\sqrt{\left(3\left(f-\frac{1}{3}\right)^2 + \frac{2}{3}\right)N_W^2}$$

From which it follows that the minimum value for the resolution is :-

$EN_x = \dfrac{2.36L}{FQ}\sqrt{\dfrac{2}{3}}N_W$ which occurs at $f = \dfrac{1}{3}$ as predicted from Figure 3-4.

The number of position resolution elements, N_{res}, is given by :-

$$(3\text{-}7)\quad N_{res} = \frac{L}{EN_X} = \frac{FQ}{\delta Q}\sqrt{\frac{3}{2}}$$

where $\delta Q = 2.36N_W$, the FWHM noise charge.

This is of fundamental importance in assessing the ultimate potential of the WSA, showing that theoretically, the number of position resolution elements can never exceed ~0.6 times the number of charge resolution elements, $\dfrac{Q}{\delta Q}$, since for a square WSA, the fractional dynamic range cannot be greater than 0.5. In practice, practical constraints for any pattern shape typically limit F to less than 0.35, reducing the position resolution further.

The charge amplitudes on each electrode are commonly digitized before being applied to the decoding algorithm. This results in the subdivision of the charge domain into cubic volumes, each corresponding to $Q_{i,j,k}$ where i,j,k are integer values over the range of the ADCs. The planes of constant total charge (pulse height) on to which the wedge and strip image space is mapped, dissect these cubes into triangular and hexagonal pixels, whose size in image space scale with pulse height.

The terms N_w, N_s, and N_z are dominated by electronic noise produced in the front end of the preamplifier. It is not within the scope of this thesis to discuss the preamplifier design, however one major factor due to the readout pattern which affects these values is discussed in section 3.3.2.1, namely inter-electrode capacitance. This has a direct bearing on the magnitude of the effective charge noise, Q_n, as discussed in section 3.3.1.2.

Partition Noise

All readouts using the analogue division of collected charge amongst a number of electrodes to encode position suffer from partition noise. Partition noise results from the statistical fluctuations in the amount of charge collected on each electrode as a result of the collection of a finite number of charge quanta (i.e. electrons) being divided amongst a small number of electrodes. In a practical sense, the cause of partition noise in conductive charge division devices is the random spatial distribution of the discrete charge quanta within the envelope of the charge footprint.

The magnitude of the partition noise limited position resolution can be obtained using equation (3-4). In the case of partition noise, the W, S and Z components are not independent, in fact $\delta W + \delta S + \delta Z = 0$, since partition noise is effectively a redistribution of a fixed number of charge quanta. Therefore using the condition $\delta S + \delta Z = -\delta Q$ equation (3-4) can be reorganised as follows :-

$$(3\text{-}8) \quad \delta X = \frac{L}{F}\left(\frac{(1-f)}{Q}\delta W - \frac{f}{Q}(\delta S + \delta Z)\right) = \frac{L}{F}\frac{\delta W}{Q}$$

The standard deviation of a binomial distribution is given by :-

$$(3\text{-}9) \quad \sigma_M = \sqrt{f(1-f)N}$$

where fN is the mean value and N is the number of discrete elements. Thus the FWHM partition noise limited position resolution, PN_{res}, can be expressed as :-

$$(3\text{-}10) \quad PN_{res} = \frac{2.36L\sqrt{f(1-f)Q}}{FQ} = \frac{2.36L\sqrt{f(1-f)}}{F\sqrt{Q}}$$

reaching a maximum at a value of $f = 0.5$. The dependence on $\frac{1}{\sqrt{Q}}$ means that increasing gain produces a much slower improvement in resolution compared to the case with electronic noise.

However, in most cases, the level of partition noise in practical detectors is usually lower than the corresponding electronic noise.

It must be noted that this source of position error only occurs when charge is actively collected by the readout. If a signal is induced by a remote charge cloud, as is the case typically in a multi-wire proportional counter using a patterned cathode readout [105], then the random and quantised nature of the charge cloud is disguised if the charge dipole is sensed while close to the wire. If enough time elapses for the positive ions to be collected by the cathode pattern, the charge being collected, partition noise would become apparent.

3.3.1.2 Count rate

There is no fundamental limit to the count rate performance of the WSA itself, apart from the ability to achieve the required electronic signal to noise ratio for the desired resolution. The noise in a typical pulse processing system of the type used for WSA readouts, having a charge sensitive pre-amplifier and shaping amplifier, is dominated by FET at the front-end of the pre-amplifier. There are four fundamental noise sources associated with the operation of this FET; thermal noise in the gate resistor, shot noise from the gate current, thermal noise in the FET channel, and flicker noise in the FET channel. The sum total of these noises, in terms of the equivalent noise charge (ENC), is given by :-

$$(3\text{-}11)\quad ENC = \varepsilon\sqrt{\frac{kT}{2R_g}\tau + \frac{eI_g}{4}\tau + \frac{kTR_{eq}}{2}\frac{C_{in}^2}{\tau} + \frac{A_f}{2}C_{in}^2} \quad [106]$$

where ε is shaping circuit attenuation,

k is Boltzmann's constant,

T is the absolute temperature,

R_g is the gate resistance,

e is the electronic charge,

I_g is the FET gate current,

R_{eq} is the equivalent noise resistance of the channel,

C_{in} is the input load capacitance,

A_f is the $1/f$ noise constant

In a typical application using a WSA with C_{in} of order 100 pF, and shaping times of the order of a μs, the third term dominates the rest. If C_{in} is split into its component parts, the fixed internal capacitance of the FET and associated wiring, C_0, and the WSA capacitive load, C_{ext}, the noise can be represented as :-

$$(3\text{-}12)\quad ENC \approx \left(\frac{M}{\tau}\right)^{\frac{1}{2}}(C_0 + C_{ext}) = k_1 + k_2 C_{ext} \quad [106],$$

a fixed offset and a component which varies linearly with WSA capacitance.

Since the WSA is essentially a serial device, processing on an event by event basis, the maximum count rate is set by the form of the shaped pulse itself. If a second event arrives before the shaped pulse of the first event has returned to the baseline with sufficient accuracy (set by the charge measurement accuracy requirement), the second pulse piles up on top of the first, offsetting it so that an amplitude measurement at the pulse peak will contain a component of the amplitude from the first pulse. Since the pulse shape scales with the shaping time, τ, halving the shaping time will double the maximum event processing rate, for a given measurement accuracy. The dependence of the noise on $1/\sqrt{\tau}$ causes noise to increase as shaping time is reduced, and so a compromise has to be reached between count rate capability and charge measurement accuracy (or effectively position resolution). An additional factor to account for is the random arrival of pulses. Using the typical rule-of-thumb to approximate the effect of pile-up, which states that 10% of the pulses arrive within a timescale equivalent to a continuous rate of 10 times the actual random rate [107], ~10% of events will be separated by less than 10 μs at a random event rate of 10 kHz. Thus to achieve a 9 k count/sec rate from an input rate of 10 k count/sec (i.e. loss of 10% of the events, being outside the charge measurement accuracy requirement), the pulse shaping time must be sufficiently fast so that the shaped pulse returns to the baseline (to within the accuracy demanded by the required spatial resolution) in 10 μs or less. This would typically require a shaping time of 0.5-1.0 μs, depending on the shaping network used and the accuracy demanded. Identification of piled-up pulses can allow the detector to handle somewhat higher count rates, but only at the expense of greater percentage loss of the input events. If the event rate rises further, eventually all event pulses will pile-up on one another and 100% dead-time will be reached, at which point the electronics will not be able to process any events to the required charge measurement accuracy.

3.3.1.3 Linearity

Theoretically the linearity achieved by a WSA should to first order, perfectly match the linearity of the WSA pattern geometry. In practice however many effects come into play.

Modulation

The WSA has a fine, repetitive structure whose pitch is typically 1mm or less. The charge cloud footprint from the MCP must be large enough to adequately cover several pitches so that the fine structure is averaged out and the three collected charge values reflected the average local area of each electrode, if it is not, image modulation occurs [108]. In simple terms, if the charge cloud size is of the same order as the electrode widths, then it will be preferentially collected on the electrode corresponding to its centroid position. Modulation in WSAs exhibits itself as cyclic distortions of both the x and y position coordinates which, to first order, is dependent only on the y coordinate.

The onset of modulation is apparent initially in the image histogram along the y axis, where under uniform illumination, a cyclic variation with y is apparent with a wavelength equal to the pitch, as

opposed to the expected constant value. Modulation does not necessarily decrease monotonically as the charge footprint expands. However the general trend is that modulation decreases as footprint size increases. Allowing the charge footprint to expand will in general always reduce the modulation to levels below the pattern spatial resolution, unless the charge footprint retains a highly undesirable distribution, such as a sharp central peak with significant power. This gives it high frequency spatial components which can sense the fine structure of the pattern pitch, causing modulation.

Electrostatic induced distortion

Linearity at the edge of the imaging area is strongly influenced by the MCP to anode electric field. The extent of the parallel electric field is limited by several practical constraints. Firstly, the lower face of the MCP has to be supported and electrical contact made. This always necessitates an excursion of the lower MCP equi-potential surface towards the WSA near the outside diameter of the MCP producing field distortion which has azimuthal symmetry in a detector with a circular imaging aperture. Field distortion is especially unwanted in this region close to the MCP where the electrons have lowest energy and are most easily deflected. The radial extent of this field depends on the size of the MCP to WSA gap and field rings, if present.

Edge effects

The WSA active area i.e. the area within which the electrode areas represent the correct geometry, should ideally be larger than the active imaging area by the external diameter of the charge cloud footprint to prevent non-linear response as the event centroid nears the active imaging perimeter. In practice, the charge footprint often has a soft wing component which would require an excessively large readout, compromising the inter-electrode capacitance and the detector size itself. This requirement is commonly not fulfilled so design of the outer contact electrodes becomes important in reducing non-linearities which occur near the edge of the WSA as the charge footprint begins to fall off the pattern. Any redesign of electrode geometry outside the active pattern area, in order to minimise these distortions, is dependent on the charge footprint distribution of the particular detector, and thus amenable to optimisation only by somewhat empirical methods. Readout simulation software which includes realistic geometries for the outer contact electrodes has been developed and is reported on in section 5.3. This has enabled the simulated distortion of a WSA near its perimeter to be reduced by a factor of 3-5.

Crosstalk

Charge sensitive pre-amplifiers are commonly used in the charge measurement electronics for WSA readouts and the feedback technique they employ causes them to have high dynamic capacitance [106]. From the WSA's point of view they resemble a capacitance of ~5-40 nF. The typical inter-electrode capacitance of a 35 mm WSA on a fused silica substrate is ~100 pF and so with pre-amplifiers having 10 nF dynamic capacitance, 1% of the signal will be developed across

the inter-electrode capacitance. This charge is effectively measured on the coupled electrode, introducing a fixed pattern distortion which produces a diagonal stretching of the image.

Crosstalk can be reduced by either lowering the inter-electrode capacitance (there are already noise related reasons why this is as low as is practical) or increasing the pre-amplifier dynamic capacitance (though usually this is at the expense of pre-amplifier risetime). Its effect can be mitigated by removing it in software. Given the reasonable approximation that there is insignificant crosstalk between W and S electrodes, owing to the WSA layout (the Z electrode lies between W and S), crosstalk can be analysed as follows :-

$$(3\text{-}13)\quad X' = \frac{W - \delta W + \delta Z}{W + S + Z},$$

The x coordinate can be simply corrected by subtracting a factor δZ from the numerator, the term $W\text{-}\delta W$ being inconsequential because it represents a simple scale factor.

Secondary electrons

The production of secondary electrons from the surface of a WSA is a problem specific to their operation in vacuo, for example in detectors using MCPs [109]. This physical process can give rise to significant image non-linearity and image instability in such detectors. The production of secondary electrons can give rise to effects such as charge redistribution among the readout anodes, mediated by means of inter-electrode voltages, together with substrate charge-up resulting in image distortion and time dependence. These effects were identified and investigated during the course of this research work and are discussed in depth in chapters 5 and 7.

3.3.1.4 Other factors affecting Image Quality

Fixed Pattern Noise

There are two major causes of fixed pattern noise in charge division readouts. Firstly, it may be the result of non-linearity in the digitization of analogue charge levels, primarily caused by errors in the analogue to digital conversion process. This cause is, in principle, virtually totally avoidable. The second and more fundamental cause relates to the inaccuracy inherent in the digitization process itself. This digitization can produce effects which may be seen in the image under certain circumstances, as fixed pattern noise.

The ADC may itself produce fixed pattern noise in certain modes of operation. For example, Breeveld et al [110] suggested and demonstrated an electronic design where the charge normalization (represented by the division procedure in the decoding algorithm) is carried out during digitization by feeding the electrode sum signal (which varies event by event) into the ADC reference level. This is performed in order to speed up and simplify digital processing. This potentially elegant solution has several practical drawbacks. The ADC reference signal must be driven dynamically (at signal speeds of typically 2μs to peak, equivalent to a slew rate of several

V μs^{-1}. In a flash ADC, the reference signal drives a resistive divider chain, where each node supplies an incrementally increasing voltage to successive comparators. This low impedance load (< 1kΩ) has distributed capacitance which slows the signal propagation along the resistor chain, and may also be influenced by the geometrical arrangement of the chain itself. This can result in exaggerated differential non-linearities and the image may exhibit preferred pixel values. This is directly apparent because the ADC digital steps map directly into the image co-ordinate.

The second, fundamental source of fixed pattern noise is due to errors introduced when the charge amplitudes are digitized, creating discrete pixels in the charge domain. The charge co-ordinates, Q_W, Q_S, Q_Z, define a cubic volume which defined as the charge domain pixel. The relative size of the charge domain pixel scales inversely with pulse height with respect to the image meter. For almost all charge co-ordinates, the alignment of charge domain pixel positions over the range of expected pulse height variation will be random. However, along certain directions, principally the axes of symmetry of the orthogonal charge domain pixel lattice, alignments of charge domain pixels between the planes representing constant pulse height occur. These alignments are purely a result of the errors introduced by digitization (owing to truncation) of the signal amplitudes. When projected on to the image plane, these alignments cause a fixed pattern noise in the image. However fixed patterning would be avoided if the algorithm was undertaken in an analogue mode, though this would be more problematic in practice.

The scale of the fixed pattern depends on the digitization level, which depends on the ADC resolution and the event pulse height. Irrespective of ADC resolution, a small pulse height will always under-use the available resolution and the scale of the fixed patterning will be larger. The image co-ordinate associated (via the decoding algorithm) with charge domain pixel co-ordinate, is almost invariably integerized so that images can be collected as histograms, a much more efficient use of memory and telemetry than event coordinate lists in most cases . The relative scale of the fixed pattern features, compared with the image pixels is crucial in determining the magnitude of the non-uniformity in the flat field response. As long as the charge domain pixel positions (over the range of pulse height used) sufficiently over-sample the image pixels, fixed pattern noise will not be present in the image at noticeable levels.

3.3.2 Techniques to improve performance

The dominant factor driving the position resolution is the electronic noise due to the pre-amplifier which causes charge measurement errors. There are several ways that this can be reduced.

3.3.2.1 Electronic noise reduction

Gain

One way to overcome signal to noise limitations is to increase the detector gain. However, this can have other drawbacks such as increased chance of breakdown in a gas proportional counter,

ion feedback and lower count rate capability with an MCP, and thus is usually not a realistic option: the gain is usually set as high as practical for these and other reasons (for instance to produce as tight a pulse height distribution as possible with an MCP).

Inter-electrode Capacitance

Significant improvement in the position resolution of WSAs can be produced by reducing the interelectrode capacitance; the decreased capacitive loading of the preamplifier input stage reducing the electronic noise. Capacitance reduction methods fall in to two categories: substrate properties and pattern geometry. The capacitive coupling through the substrate can be minimized by either reducing the substrate thickness, or reducing the substrate dielectric constant.

Reducing the substrate thickness

The effectiveness of substrate thickness reduction was investigated as follows. Several WSAs of 70 mm diameter were manufactured on kapton substrates of varying thickness with inter-electrode gaps of ~150 μm. The interelectrode capacitance of each was measured while the WSA was immersed in Freon 113, an inert solvent having a dielectric constant of 2.44. Together with a capacitance measurement in vacuum, it was possible to calculate the fractional coupling through the substrate by solving the following equations :-

$$(3\text{-}14)\quad f\varepsilon_{kapton} + (1-f)\varepsilon_0 = kC_{vacuum}$$

$$(3\text{-}15)\quad f\varepsilon_{kapton} + (1-f)\varepsilon_{freon} = kC_{freon}$$

$$(3\text{-}16)\quad \therefore f = \frac{\varepsilon_{freon}C_{vacuum} - \varepsilon_0 C_{freon}}{(\varepsilon_{kapton} - \varepsilon_0)(C_{freon} - C_{vacuum})}$$

where f is the fractional coupling through the kapton substrate, ε_{kapton}, ε_{freon}, and ε_0 are the relative permittivities of kapton, Freon 113 and vacuum respectively, C_{freon} and C_{vacuum} are the measured pattern capacitances in Freon and vacuum respectively, and k is a pattern dependent constant. The results displayed in Figure 3-5 show that 50% of the coupling takes place through the substrate when the substrate thickness is ~1/3 of the gap electrode width.

Thin substrate WSAs have been manufactured and used for space applications. The PGI, described in chapter 4, a proportional counter that provided the imaging capability for the XOGS sounding rocket payload, used a 120 mm diameter WSA manufactured on a 12.5 μm kapton substrate.

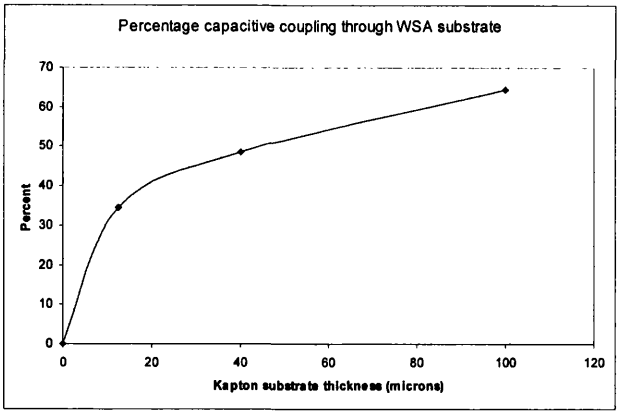

Figure 3-5. The percentage of WSA capacitive coupling through the substrate.

Substrate dielectric constant

Materials commonly used for WSA substrates include fused silica, kapton and G10 printed circuit board, with dielectric constants 3.8, 3.4, and 4.8 respectively [111][112]. These are some of the lowest dielectric constants found in materials suitable as readout substrates. There is little scope to reduce inter-electrode capacitance by choosing alternative materials.

3.3.2.2 Pattern Geometry Optimisation

Though the concept of operation of the WSA is fairly straightforward, various subtle tradeoffs have to be made between pattern parameters in order to achieve the best possible resolution for a given detector format.

Electrode Dynamic Range, F

The position resolution determined by both electronic and partition noise terms is inversely proportional to the dynamic range of the electrode, $F = f_{max} - f_{min}$. However increasing F independently of the other pattern parameters has the effect of reducing the interelectrode gap width. This increases the inter-electrode capacitance and hence the terms N_w,N_s, and N_z in the electronic noise equation. The inter-dependence of F, p (the pattern repeat pitch), E_{min} (the minimum electrode width) and g, (the inter-electrode gap width) is described as follows :-

$$(3\text{-}17)\quad F = f_{max} - f_{min} = \frac{p - 4(E_{min} + g)}{2p}$$

The above equation is constrained by the condition that the smallest Z electrode width is equal to E_{min} at the corner of the pattern where both wedge and strip electrodes are maximum. For a circular pattern, this corner and the corresponding constraint are removed (the wedge and strip electrodes do not now reach their maxima simultaneously anywhere in the pattern). The new constraint such that F is maximised is :-

$$(3\text{-}18)\quad F = f_{max} - f_{min} = \frac{p - 4(E_{min} + g)}{\left(1 + \frac{1}{\sqrt{2}}\right)p}$$

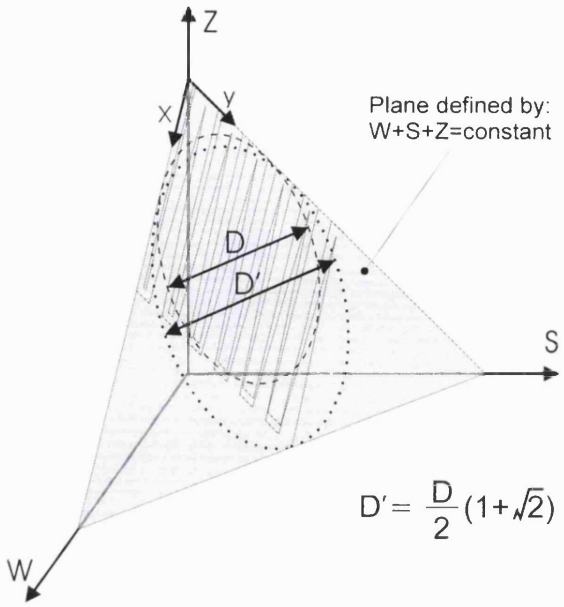

Figure 3-6. Improvement of the dynamic range in a circular WSA.

This new constraint increases the theoretical *F* for a three electrode orthogonal axis WSA from a 0.5 to 0.586 as shown in Figure 3-6. *F* can be increased further by maximising the symmetry of the pattern. This occurs when the axes of electrode variation are equi-spaced at 120 degrees. This pattern has the advantage that the noise limited resolution has circular symmetry as opposed to the elliptical symmetry of the standard WSA, improving the resolution in *x* and *y*. Its representation in the charge domain and decoding algorithm is shown in Figure 3-7. Figure 3-8 is a schematic of the 120° WSA pattern which looks very similar to the normal WSA except that the wedges vary from pitch to pitch. Added complexity in the decoding algorithm is the price paid for this increase in position resolution.

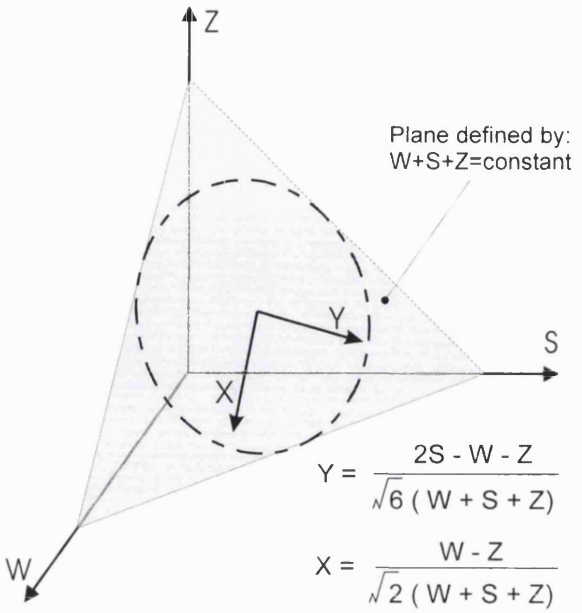

Figure 3-7. A charge domain representation of the maximally symmetric 120° WSA.

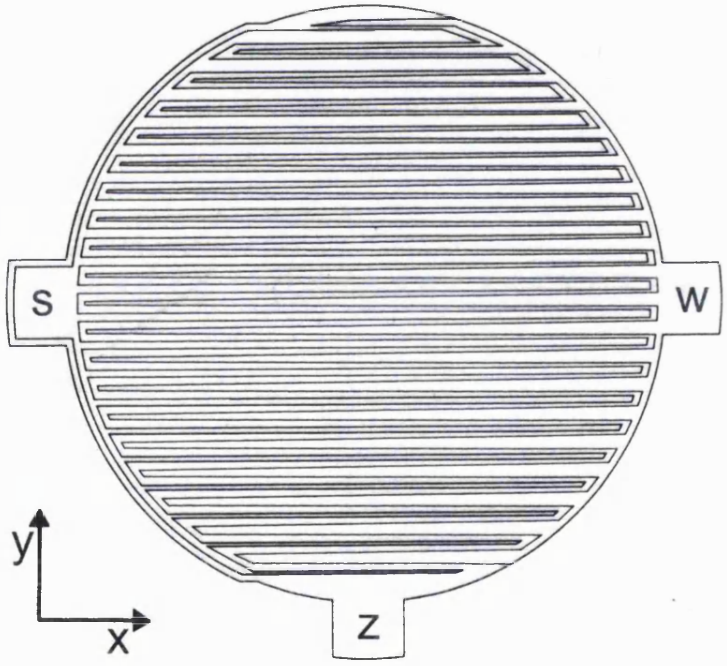

Figure 3-8. A schematic of the maximally symmetric 120° WSA pattern. It can be distinguished from the normal WSA by the variation in the shape of its wedge electrodes.

If the number of electrodes is increased to four, a theoretical *F* value of 1 can be achieved using the Tetra Wedge Anode (TWA) designed during this research. This design has applications where the ultimate resolution is required at the expense of the greater electrical complexity associated with four charge measurement channels. Figure 3-9 shows a schematic of this pattern design together with its decoding algorithm. The enhanced *F* parameter is obtained by summing electrodes (C+D), and (A+C) to generate two virtual 2 electrode patterns which vary linearly along orthogonal axes.

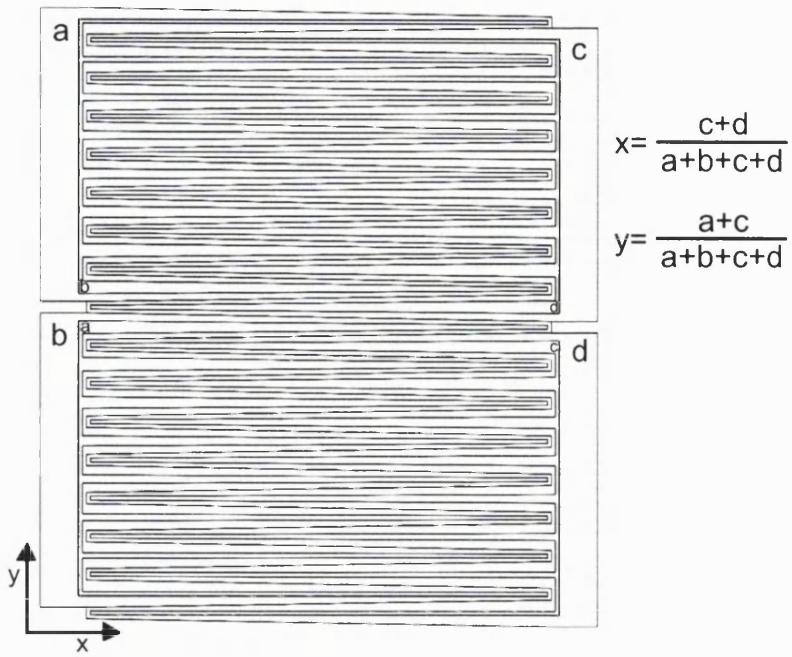

Figure 3-9. A schematic of the 4 electrode TWA. The pattern is divided horizontally in the middle to avoid thin meandering electrodes with consequent higher resistance.

Electrode Gap Width

The electrode gap width influences the position resolution in several ways. Firstly it affects the interelectrode capacitance, which directly determines the electronic noise and hence the resolution. The interelectrode capacitance can be approximated as the sum of two components:-

a) A line capacitor corresponding to the coupling between the conductor edges across the insulating gap and dependent on the total junction length, conductor thickness and insulator gap width, which may be expressed as:-

$$(3\text{-}19)\quad c_{line} = \frac{4K_1 A}{\ln(g/a)}$$

b) A strip capacitor corresponding to the bulk coupling over the area of the conductors and dependent only on this area, which may be expressed as:-

$$(3\text{-}20)\quad c_{strip} = K_2 A\left(1 - \frac{4g}{p}\right)$$

where g is the gap width, a the conductor thickness, A the area of the WSA, p the pitch and $K1$ and $K2$ are constants.

The dominant change produced by varying the electrode gap is due to the first component. This component rises slowly with decreasing gap until the gap is below ~10 times the conductor thickness, when the capacitance begins to increase rapidly.

Secondly and conversely, increasing the gap reduces either the dynamic range, F, or the minimum electrode width, E_{min}, or both. Decreasing F immediately impacts the resolution, while reducing E_{min} can cause high electrode resistance, especially for the meandering Z electrode, whose width

decreases to E_{min} a large number of times over its length. High Z resistance (>100 Ω) can cause image distortion (discussed below).

The optimum gap depends on the thickness of the substrate. For some proportional counter applications WSAs on thin, stretched 8 μm kapton sheet have been fabricated (described in section 4.1). The previous results indicate that the bulk of the capacitive coupling does not occur through the substrate until gap width is reduced to less than ~3 times the substrate thickness. The thin Kapton allowed the use of electrode gaps as low as 25 μm with little detriment to the electronic noise.

Minimum Electrode Width

The minimum electrode width, E_{min}, influences the electrode dynamic range, F. The magnitude of E_{min} is governed by two factors :-

1) The feasibility of reliably fabricating a very narrow conductor whose thickness is a significant fraction (>0.25) of this width.

2) The increasing electrical resistance encountered with narrower electrodes.

The latter becomes more of a problem for high speed applications where the distributed R-C of the long Z electrode effectively constitutes a delay line. This position dependent delay causes the Z pre-amplifier output to rise later than those of the Wedge or Strip. The charge on the Z electrode, which is capacitively coupled to the wedge and strip electrodes, is developed on the wedge and strip preamplifiers until the Z signal propagates to its pre-amplifier. Once this occurs, dependent on the delay and event position, the Z charge is collected on the Z preamplifier, being pulled off the wedge and strip pre-amplifiers. In practice the interaction between the three pre-amplifiers coupled via the delay causes the charge to oscillate between the preamplifiers for an appreciable time (but usually less than 50 nanoseconds) until an equilibrium is reached where the outputs truly reflect the measured charge. This defines the effective rise-time of the Z pre-amplifier and the shortest shaping time that can be used without ballistic deficit [107] affecting the Z signal. Ballistic deficit is due to the ratio between pulse shaping time and pre-amplifier rise-time being too small and will cause a decreased Z pulse height (the W and S signals with be oppositely affected.), which in this case will have position dependence resulting in image distortion.

For high speed operation, at shaping times less than 100 nanoseconds, the position dependent Z delay must be reduced by decreasing the distributed Z resistance as much as possible. This has been achieved by fine wire bonding between individual pitches. For instance, the end to end Z electrode resistance of an 80mm diameter, 1mm pitch WSA was reduced to less than ten ohms from an un-bonded value of 500 ohms using this method.

The Pattern Repeat Pitch, p

The inter-electrode capacitance can be reduced and the electrode dynamic range, *F*, increased by increasing the pattern repeat pitch. However position modulation [108] occurs if the charge footprint to pitch ratio becomes too small. The increased pitch requires a larger charge cloud diameter, which can be increased by :-

1) reducing the accelerating voltage between them.
2) increasing the MCP to WSA spacing.
3) decreasing the MCP end-spoiling.

In an optimized detector design, the MCP to anode geometry and voltage have already been optimized by :-

1) setting the field between MCP and WSA optimally low to maximize the charge cloud size without making the image more prone to distortions due to the bottom MCP support ring, and other stray fields.
2) keeping the MCP and WSA spacing small so as to minimize the detector dimensions.
3) Choosing low end-spoiling to maximize the charge footprint for a given combination of 1) and 2).

Since 1) and 3) cannot be improved upon, the only parameter free to provide an enlarged charge footprint is the MCP to WSA spacing. This can only be increased at the expense of the detector dimensions. The detector diameter also needs to be increased to accept a larger WSA, which is required to accommodate the larger charge footprint and prevent it from falling off the active pattern degrading the linearity. The larger WSA has the penalty of reduced resolution.

In practice, the best compromise between all competing parameter values has to be arrived at empirically. In the case of a 33mm diameter MCP-WSA combination (with an active imaging area of 25 mm ø) the optimum pattern repeat pitch of 800-1000 μm requires an MCP to WSA spacing of 5-10mm depending on the particular MCP characteristics and the accelerating voltage (typically 300-500 V).

3.4 Manufacturing techniques

WSAs have much in common with printed circuit boards (PCB) in that they are made up of a conductive layer supported on an insulating substrate and consist of isolated electrodes generated by the removal of long, narrow strips of conductor. For less demanding pattern designs with larger dimensions, they can be manufactured using the same methods and materials used for printed circuit boards. The most crucial element in the manufacture of a WSA pattern is a precision pattern generating tool.

3.4.1 Photolithographic Manufacture

3.4.1.1 The manufacturing process

The large WSA patterns used for the PGI and prototype gas proportional counters, and early WSAs used in the MCP detectors were manufactured by photo-lithographic processes using standard practices. This section describes the rather specific drawing machine requirements demanded by readout pattern such as the WSA.

Drawing Machine Precision

Wedge and Strip type patterns require a particular level of geometric precision from the drawing machine, whatever type is used either for direct manufacture or the preparation of a mask. Stepper motors are the most commonly used motor to drive the translation stages used for this application. The resolution of these, i.e. the step length is the most important factor to be considered when defining the pattern parameters. The major inflexibility occurs as a result of the requirement that the strip width be a linearly varying dimension. This constrains the strip width to vary by an integer number of table steps every pitch. A further constraint, due to a pattern symmetry requirement, demands that the increment is an even number of steps. Typically, WSAs have a pitch dimension of order 1mm for many applications. Simple examination of the free parameters available (i.e. active size, pitch and electrode dynamic range) easily show that even with a step size of 1 micron, solutions to this equation are very small in number. If the problem is ignored, the final pattern will exhibit a periodic nonlinearity resulting from beating between the stepper motor step size and the strip incremental width.

Typically a WSA pattern is drawn as a continuous line. Assuming the wedges are drawn first, the drawing machine then has to retrace its steps and cover the same ground in order to draw the strips which interlock with the wedges. Since the pattern can have a long line length (10 metres is easily possible), drawing can take a significant time (up to 6 hours). The drawing machine can be susceptible to long time-scale integral positioning errors i.e. offsets produced by thermal expansion etc. This problem does not occur in PCB manufacture. It is the specific nature of the WSA which high lights this potential failing. At low levels, the effect causes the Z electrode width to vary between its two elements in every pitch (see Figure 3-2 - it should be symmetric) and this causes a higher than necessary Z electrode resistance which can affect high speed operation. If the effect is large, it causes fatal overlap of the wedge and strip electrodes and breaks in the Z electrode.

The use of stepper motor driven translation stages inevitably means that the wedge electrodes, in fact, have the form of stepped wedges i.e. they do not have a continuous gradient but consist of alternate horizontal and vertical steps; the number of the former far exceeding that of the latter. If the previously described criterion is applied to the strips; namely that the incremental width is an even integer of steps, then it will be seen that a vertical step occurs at least every pitch width

(given that both axes have the same length and dynamic range). Thus, since the charge cloud is large enough to average out the pattern fine structure repeated every pitch, it will also average out the wedge discontinuities and effectively see a wedge of continuous gradient.

The facility actually used to draw the mask for photolithographic pattern manufacture of the PGI WSA is shown in Figure 3-10.

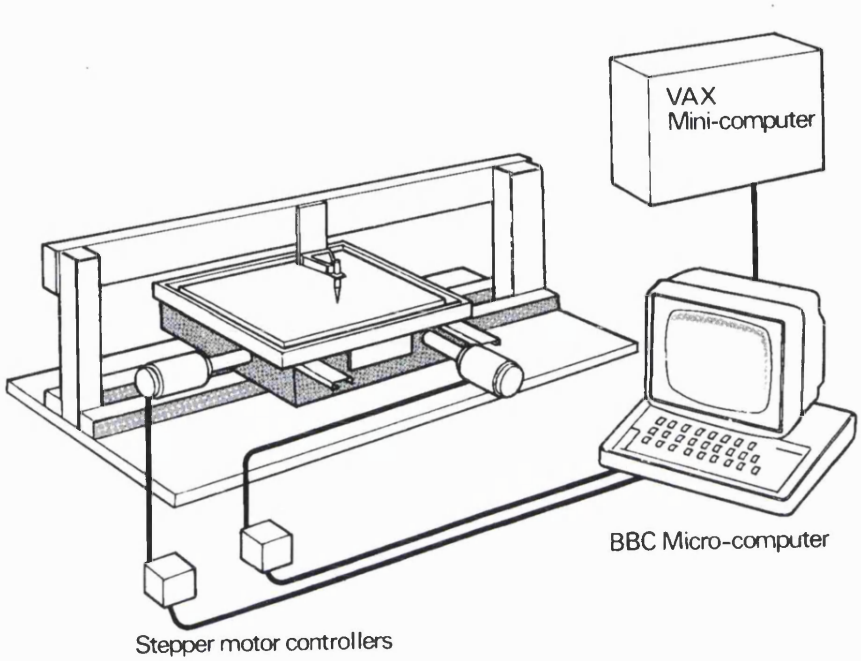

Figure 3-10. The coordinate table layout used for mask generation [113].

3.4.1.2 Photolithography and mask production in an R&D context

The photolithographic technique as described had certain setbacks when applied to pattern making in the context of a research laboratory where production is on a small scale and iteration of pattern design is required. Each new design required the manufacture of a new mask which was either manufactured oversize and reduced photographically or manufactured full size. In both cases a film scribing technique was used.

The photographic reduction method overcame the lack of precision inherent in the scribing technique but had all the cleanliness requirements of the photo-resist replication method itself. Since this had to be entrusted to an outside contractor, rigorous controls could not be applied. This method proved very unreliable for all but the most coarse patterns. Other major drawbacks were the costs and timescales involved in changing design.

Though manufacture of masks by direct scribing had proved satisfactory results for simple patterns such as the WSA, where the pitch was relatively coarse, its lack of precision fundamentally limited its usefulness for finer patterns. The polymer base which carries the scribing surface is not mechanically rigid and the act of scribing material from the surface results in a ragged line whose effect is magnified on finer patterns.

The development of the progressive geometry anodes, having finer pitch and greater precision requirement also highlighted the inadequacies of the photolithographic method. Apart from the mask production difficulties described, in-house manufacture by photolithography suffers from low overall yield because of less than adequate yield on each of the critical stages, the major problems being :-

1. Cleanliness during photo-resist coating. Inclusions in the resist tend to result in missing areas of conductor. This is due to under exposure of the thicker resist around the inclusion, owing to surface tension. The thicker resist is then developed away and a missing patch of conductor results after etching.
2. Mask faults. These are usually the result of particles being trapped between the mask and resist-coated substrate during exposure. The nature of photo-resist chemistry requires that exposure take place ideally in vacuum. Oxygen radical formation will inhibit the chemical change initiated in the photo-resist by exposure to UV illumination and correct exposure will not occur. In order to satisfactorily expose the resist, a print-down frame is used to exclude oxygen and to bring the mask and resist-coated substrate into intimate contact. Any particulate contamination not only can damage the resist coating being exposed but also degrade the mask for future use.
3. Non-uniformity during development and etch. This is caused by sensitivity of the etch rates to geometry e.g. line widths and, more generally by the difficulty in ensuring an even etch over the entire surface of a substrate. Material is preferentially etched near to the substrate perimeter even when strong etch agitation is used.

It was recognised the development of the new progressive readouts required a manufacturing flexibility not easily offered by in-house photolithography in order that pattern design iterations could be readily undertaken. Since the major advantage of photo-resist technology would not be relevant i.e. the ability to produce large numbers of the same pattern, a more relevant manufacturing technology was sought.

The progressive geometry anodes comprise at least 6 electrodes and require wire-bond interconnects to join electrode areas. Initially it was planned to uses aluminium conductor for the patterns in order to facilitate wire-bonding. The resist and etch chemistry is more difficult in this case since aluminium is vulnerable to attack by the alkaline photo-resist developer and is not easy to etch in a well controlled manner. This was yet another reason to move to an alternative pattern fabrication process.

3.4.2 Laser Micromachining

While photolithography could easily provide the required precision for generation of the new finer scale, progressive geometry readout patterns, it could not efficiently provide simple one-off production without significant capital expenditure. Laser micromachining was seen to offer an

alternative manufacturing technique. It is a one-shot process and was thus more suitable for the one-off production required in a research and development task. It was also found to overcome reliability and repeatability problems encountered with in-house photolithography.

Description

A suite of equipment was purchased with the primary aim of manufacturing progressive geometry readout devices. This suite comprised a dual magnetron sputter coating facility to deposit thin-film conductive coatings on the pattern substrates, a Q-switched Nd-YAG laser machining facility using a focused laser beam with an *x,y* coordinate table to scribe the pattern insulating gaps in the conductive coating, and a manual ultrasonic wedge-wedge wire-bonder to make the pattern inter-connects. All the manufacturing facilities were housed in the clean-room at MSSL in conditions equal to better than class 10,000.

Coating Technique

The coating facility, an Edwards ESM100 sputter coater, used a liquid nitrogen (LN_2) trapped oil diffusion pump to evacuate a stainless steel vacuum chamber equipped with two upward facing 4 inch magnetrons, a rotating substrate holder, substrate heater, shutter, and film thickness monitor. The magnetrons were powered by a choice of two power supplies, rated at 1000W DC and 600W AC respectively. The AC supply could be applied to the electrically isolated substrate platen for glow discharge substrate cleaning prior to coating. The ability to pre-clean the substrate and apply two consecutive coatings, one from each magnetron, without breaking vacuum was crucial in obtaining satisfactory coating adhesion to the fused silica pattern substrate.

The fused silica substrates were optically polished and their corners rounded to minimize the chance of fracture when mechanically clamped during handling and in the detector. The substrate coating procedure began with a manual detergent scrub followed by ultrasonic solvent cleaning and rinsing in a solvent vapour bath to avoid drying stains. The Freon 113 solvent used initially had to be replaced by Methoklone owing to Montreal Protocol restrictions on fluorocarbons. Freon 113 was excellent for all plastics being completely inert, but was a less aggressive solvent than its Methoklone replacement, a stabilized methylene chloride based solvent. The substrate was then placed in a holder and mounted in the coater and immediately evacuated.

The coater was kept pumped down whenever possible to reduce internal surface contamination and minimize pump-down times. The LN_2 trapped diffusion pump could achieve a chamber pressure of better than 10^{-6} mbar in ~1 hour and coating was always undertaken promptly to minimize substrate contamination and poor substrate adhesion, such is the difficulty of coating fused silica with good adhesion. The focus on good coating adhesion was necessary in order to achieve successful wire-bonding. Early tests showed that, even if the pattern was lased perfectly and seemed flawless, wire-bonding was the critical test of conductor adhesion, the wire pulling off small pads of conductor if adhesion was unsatisfactory.

Firstly, a ~50 Å coating of chromium was deposited on to the fused silica to act as a glue layer between the thicker conductive layer and the fused silica substrate. Initially aluminium was used for the conductive layer, but this was replaced with copper to improve pattern robustness, maintain good conductivity, and avoid the thick oxide film which coats aluminium (seen as a potential problem in enhancing secondary electron emission). A thickness of ~2 μm of copper was deposited on top of the chromium. Though ideally a thicker copper coating was desirable to reduce electrode resistance as far as possible, this was limited by the ability to lase copper (discussed later).

Lasing the pattern

The laser micro-machining facility was built around a Control Systems 620QT Continuous wave/Q-switched Nd-YAG laser operating at 1068 nm and capable of delivering 15W in continuous mode and 30kW (pulsed) at a frequency of 1 kHz in Q-switched mode. The laser was configured using the smallest laser cavity apertures (0.040") to force it into single mode operation and minimize the beam divergence. This was required because the beam divergence defines the final spot size focused on the work piece to be machined. The laser cavity was ~1 m long with a central unit containing the Nd-YAG single crystal rod and high pressure Xenon arc lamp placed at the two foci of a cooled , water-filled elliptical housing which served to optically couple them. A photodiode behind the full-silvered, laser cavity mirror monitored the laser power from the small light leakage through the mirror. This was used to tune the mirror alignment and maximize laser power, an exercise that was carried out every few months, or when the Nd-YAG rod or lamp housing was disturbed.

Though the photodiode current was only measurable in continuous mode, I discovered that the power in Q-switched mode could be measured by applying the detector pulse shaping electronics to the photodiode output and measuring the pulse heights. This provided valuable insight into the operation of the laser in Q-switched mode at low power. It could be seen that at low power (or high Q-switch repetition rate) the pulses were not all of the same amplitude. The amplitude would cycle so that a large pulse would be followed by one, two , more small pulses, the number of intermediate, smaller pulses reducing as the lamp power was increased. This was due to the lamp not providing sufficient energy to completely pump up the laser rod in between successive pulses. The effect completely disappeared if the power was increased or the Q-switch repetition rate was lowered sufficiently. This was used as a diagnostic while lasing to check that the laser was functioning at the set Q-switch repetition rate, and not at some sub-multiple of it (as was effectively happening when large pulses of nominal amplitude were interspersed with smaller ones.

The beam from the semi-transparent mirror at the front of the cavity was fed out horizontally to a 10× up-collimator which expanded the beam up to 0.400" (or 10 mm) in diameter. The main purpose of the up-collimator was to reduce the beam divergence, which it does by the same factor

as the beam diameter expansion, i.e. a factor 10. The expanded beam was then reflected downwards by a dichroic mirror, which also served to transmit visible light back up from the work piece to a CCTV camera which monitored the laser cutting process. The downward pointing parallel laser beam passed trough an objective lense, which focused the beam on to the work-piece below. The pattern was produced by the removal of a narrow strip of the thin-film conductor due to direct heating from the focused laser beam which causes it to evaporate. Figure 3-11 is a photograph of the laser facility overlaid with a schematic of the laser optics.

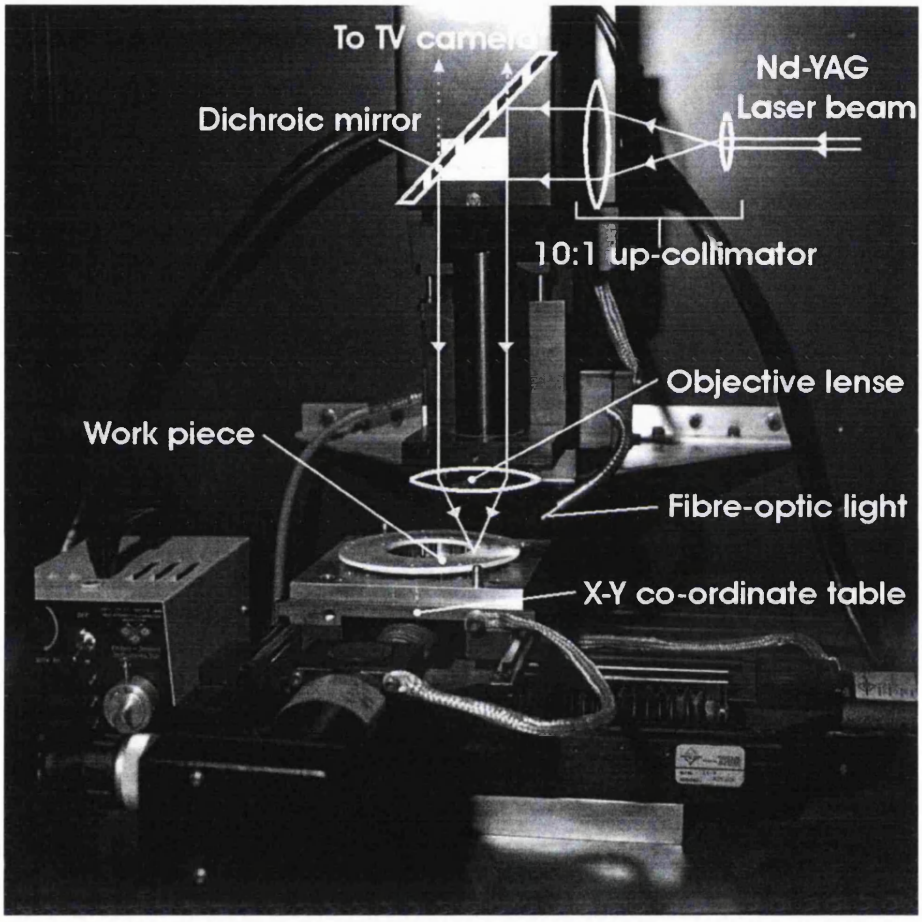

Figure 3-11. A photograph of the laser micro-machining facility. A schematic is overlaid showing the operational components.

The work-piece was mounted on a computer controlled *xy* coordinate table with a variable step size ranging from 1μm down to 80 nm. The table used a fractional stepping technique with a motor pole spacing of 80 μm. Fractional stepping is achieved by pulse width modulating two motor pole currents using weights defined in a PROM based look-up table. It was found that cyclic non-linearity in the fractional steps, though only of the scale of microns, could cause noticeable aliasing effects if significant pattern dimensions, such as the pitch, equalled multiples of 80 μm, the motor pole pitch and the cycle length of the table non-linearity.

The class 4 laser required an interlocked cabinet for the safety of users. The interlock could only be defeated in circumstances where the user wore protective goggles. This was undertaken when it was necessary to carry out laser alignment or make repairs that necessitated working on the

operating laser. The optically tight cabinet was also a thermal shroud, the heat from the fibre-optic light for the CCTV camera and from the *xy* table causing the cabinet to rise in temperature by 10-15° C. This introduced thermal drift problems owing to the long timescale over which pattern machining took place. Section 7.1 discusses the solutions that were used to overcome this problem.

The computer controlled *xy* coordinate table required custom software to draw the progressive geometry readout patterns. The specialized electrode forms cannot be drawn using accumulated error-based algorithms of the type originally invented by Bresenham for high speed line drawing using integer-only calculations [114], and the solution found was to define these particular forms as step sequences in the pattern drawing software, the lines, circles, and arcs being drawn using standard Bresenham routines.

A number of parameters were used to optimize the laser machining process. Firstly, the lamp current was adjusted to control the energy input to the laser rod. In practice it was found that in Q-switched mode, the power available was always higher than required to scribe the inter-electrode gap. Secondly the power reaching the work-piece was reduced by placing an aperture between the up-collimator and the dichroic mirror to attenuate the beam. This had the disadvantage that it caused increased beam divergence owing to diffraction, but this was not a problem since spot size was not a limitation. The third and fourth parameters used to tune the lasing process were adjustment of the Q-switch repetition rate and the *xy* coordinate table speed. Fine tuning of the process was carried out by varying the input power by means of adjusting the lamp current. All these parameters were used, in the light of previous experience, to empirically set the inter-electrode gap width and the cleanness of the line profile.

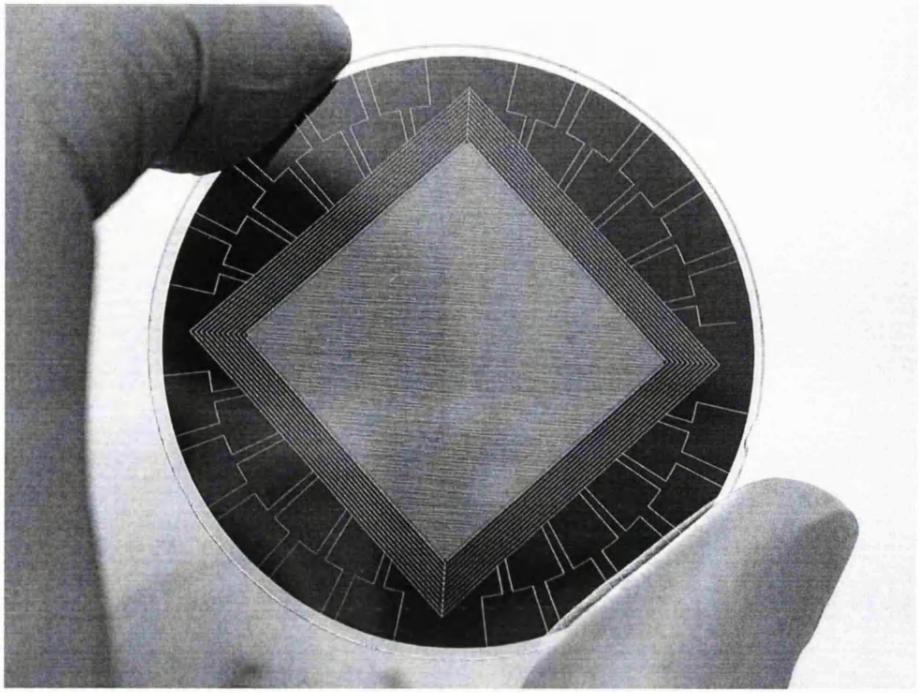

Figure 3-12. A photograph of a lased FIRE position readout pattern. The FIRE readout technique is described in chapter 8.

The laser facility was used for many materials including copper, bronze, gold, stainless steel and aluminium coated on substrates such as fused silica, glass, and even G10 PCB and kapton. In Q-switch mode it could deliver a precise amount of energy per pulse, sufficient to remove copper from copper-coated kapton with minimal damage to the polymer substrate. The laser cut width could be adjusted between 15 and 80 μm, and coupled with selective chemical etching, the laser process could be used to machine metal shim up to several hundred microns thick. It was also useful in making very fine pinhole masks, either machined in self-supporting metal shim, or in thin-layer chromium deposited on glass or fused silica. Figure 3-12 shows a photograph of a pattern lased in gold on a 50 mm diameter fused silica substrate.

Cleaning

After laser machining the pattern required a cleaning process to remove debris from the lasing process. A light mechanical scrub using cotton wool soaked in alcohol was performed for several minutes. Readouts manufactured without being cleaned post-lasing could suffer from severe image distortion which was attributed to charge-up of insulated debris on the pattern surface. Debris could also cause resistive coupling between electrodes causing high electronic noise and readout malfunction.

Pattern interconnects

The progressive geometry readouts require inter-connections between isolated electrodes. A West-bond model 7400A wedge-wedge ultrasonic wire-bonder was used with 25 μm aluminium wire to provide these connections. This device works by creating a cold weld between the wire

and a metallic coating, in this case the energy for the weld being supplied by ultrasonically shaking the two materials together at a set down-force, ultrasonic power and duration. The wire to be bonded passes through a hollow needle which is controlled manually using an *xyz* micromanipulator with a 12:1 magnification. The needle is supported on an ultrasonic horn used to supply the energy and a set of clamps controls the wire position and breaks it when necessary. The pattern to be bonded is held on a vacuum chuck and the needle and pattern environment is viewed using a binocular microscope. Figure 3-13 shows the wire-bonder being used to inter-connect a Vernier anode pattern.

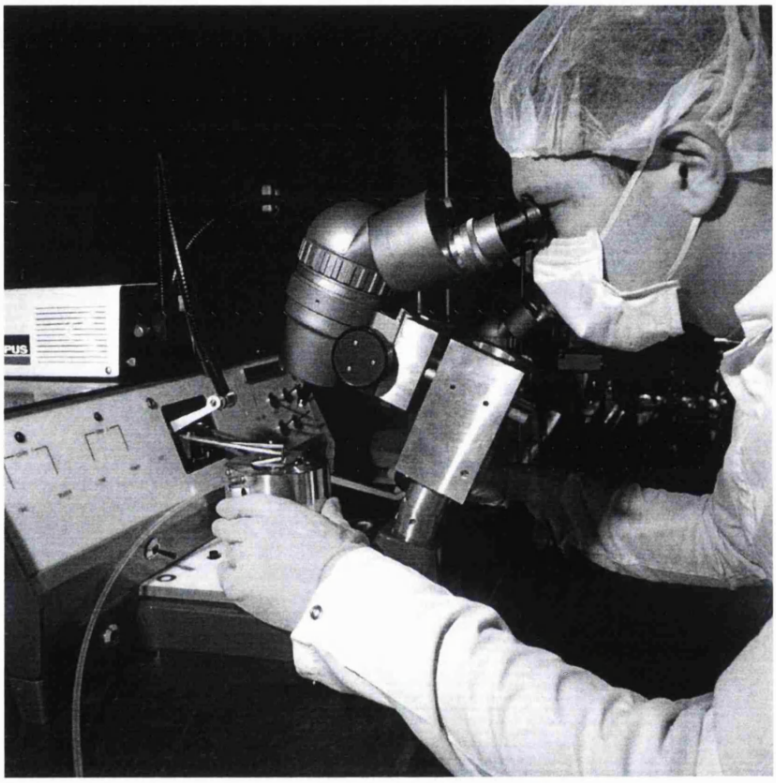

Figure 3-13. A photograph showing the wire-bonder in action.

Wire-bonding provided the ultimate test of coating adhesion. If the coating was sound, the wire bonding task, which might involve as many as 900 individual bonds (multiple bonds were used on flight anodes for redundancy), could be carried out flawlessly, but the slightest lack of coating adhesion magnified the difficulty of this task many times. Figure 3-14 shows a small region of a 12 electrode Vernier anode. The wire bonds, made using 25 μm aluminium wire, connect the electrodes in the triangular active pattern region to the surrounding bus-bars. The insulator gap widths here are 28 μm.

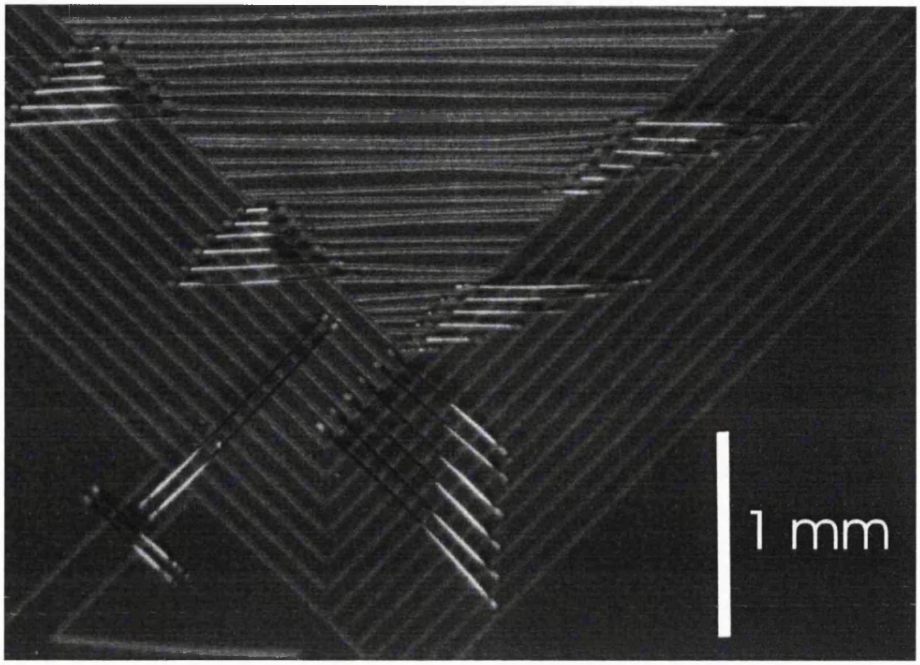

Figure 3-14. A laser micro-machined Vernier pattern showing the wire-bonds.

Chapter 4

Practical Applications of Charge Division Anodes

4.1 The Penning Gas Imager for XOGS

4.1.1 Introduction

The Penning Gas Imager (PGI) was originally conceived by Schwarz et al [13] as a focal plane X-ray imaging detector, combining good energy and position resolution in the range 0.1 - 10 keV. It was proposed for the first incarnation of Advanced X-ray Astrophysics Facility (AXAF), but failed to win selection.

The PGI design was aimed to fill the niche between the energy and position resolution performance envelopes of the Gas Scintillation Proportional Counter (GSPC) [115][116], and the Multi Wire Proportional Counter (MWPC) [117][118]. The GSPC, though capable of position resolution (typically ~1 mm FWHM) is primarily optimized for energy resolution which can be better than 10% FWHM at 5.9 keV. In contrast, the Multi Wire Proportional Counter (MWPC) can achieve a spatial accuracy of a few hundred microns (for X-ray events) but with the energy resolution of a conventional proportional counter: typically 18% FWHM at 5.9keV. The Parallel Plate Imaging Proportional Counter (PPIPC) [24][51] could improve on the spatial linearity of the MWPC by using a truly parallel field geometry but with no improvement in energy resolution.

The goal of the PGI was to combine the energy resolution of the GSPC with the imaging capabilities of the PPIPC. It had been shown that, by using Penning gas mixtures [50], the energy resolution of a conventional proportional counter could be improved to 11% FWHM at 5.9 keV [119] but at low gas gains. The parallel field geometry of the PGI was designed to allow similar energy resolution to be achieved but at significantly higher gains. A second gas amplification stage was used to produce the large overall gain required for high resolution imaging.

4.1.2 The XOGS-PGI detector design

The PGI derivative described here was developed for a sounding rocket experiment, the X-ray Objective Grating Spectrometer (XOGS). The XOGS PGI was a gas proportional counter with a 120 mm active diameter employing two stages of charge amplification and using a WSA [15] to provide two dimensional position information for X-ray energies in the range 0.5-1.5 keV. The two stage gas amplification allowed the use of a relatively low upper stage gain, optimized for energy resolution and enhanced by the use of a Penning gas mixture. The second stage of amplification allowed the overall gain to be high; a requirement for good spatial resolution with the large area WSA. Thus optimal energy and position resolution could be obtained simultaneously.

The original PGI was designed to image and measure the energy of X-rays in the range 0.1 - 10 keV, however the XOGS requirements allowed the detector to be tuned to provide best performance in the region 0.5-1.5 keV. An exploded view of the detector is shown in Figure 4-1.

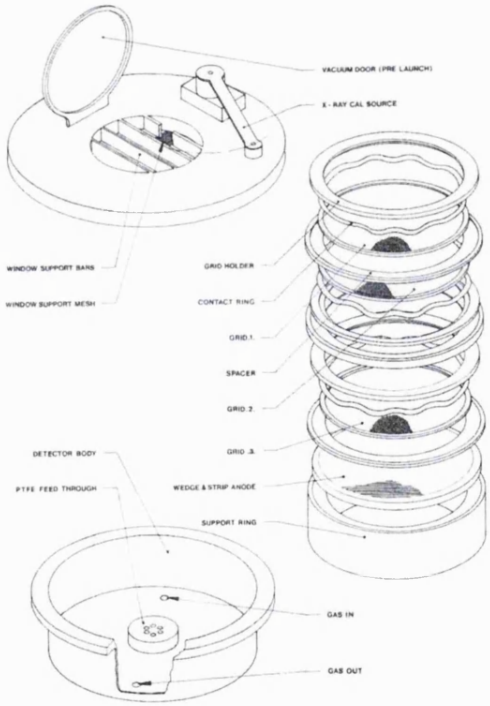

Figure 4-1. An exploded view of the PGI proportional counter.

Incident photons enter the gas volume via a thin polypropylene window where they ionize the gas, a mixture of argon plus 2% acetylene, in the absorption region. The primary electron cloud drifts through grid 1 into the first avalanche region where it undergoes a gain of ~5000. The amplitude of the signal measured on grid 1 at this intermediate gain provides the X-ray energy. A fraction (~15%) of the charge is transferred into the drift region below grid 2 and moves towards the second avalanche region, defined by grid 3 and the WSA position read-out. The electron cloud passes through grid 3 and undergoes a further gain of ~100. The final electron cloud is collected on the wedge, strip and Z electrodes of the WSA, allowing determination of the charge cloud

centroid, which reflects the original X-ray photon interaction site. The two stage amplification enables the detector to be operated stably with an overall gas gain in excess of 10^5, providing a sufficiently high signal to noise ratio for the position processing electronics. The signals on the grids and WSA electrodes measuring energy and position, and providing background rejection, are measured with charge sensitive pre-amplifiers followed by shaping amplifiers and ADC's. The telemetry bandwidth available for the XOGS sounding rocket experiment permitted the raw digital data from the detector to be directly telemetered to the ground, allowing the data reduction to be undertaken using the ground station. This removed the requirement for on-board digital processing to derive the event coordinates and allowed post-facto data analysis to make use of the most up to date instrument calibration data.

The improved energy resolution demonstrated by the detector, compared to that obtained using typical MWPCs, is achieved by using a Penning gas mixture consisting of argon plus an acetylene admixture. The special feature of this gas mixture is its potential for extra ionization. Its low ionization potential allows it to be ionized either by photons emitted from excited argon atoms, or meta-stable argon atoms. This process called the Penning effect [50] has several implications for detector operation :-

1. The first Townsend coefficient is increased resulting in a decrease in operating voltage for a given gain making the detector less prone to electrical breakdown.
2. The increased ionization is reflected in the reduction of the average energy per ion pair, W, produced by incident photons from 26.2 eV in pure argon to 20.3 eV in argon - 2% acetylene. More primary electrons are produced and the statistical fluctuation in numbers represented by the Fano factor is reduced from 0.17 to 0.08 [120].
3. The more efficient ionization process also reduces statistical fluctuations within the avalanche process. The parallel plate geometry allows the field strength, E to be chosen to minimize the avalanche factor, f, [121]. This is not possible with the wire counter, where the field strength varies throughout the avalanche.
4. Another advantage of using a Penning gas mixture is the enhanced transfer of electrons through a grid from a high field to a low field region. *UV* photons or metastable Argon atoms pass through the grid unimpeded by the field ratio, and ionize the admixture effectively transferring a significant fraction of the electrons even when the field ratio is large.

The theoretical energy resolution achievable with this particular gas composition is $14/\sqrt{E(\mathrm{keV})}\%$ FWHM. In practice the best achieved was $26/\sqrt{E(\mathrm{keV})}\%$ FWHM. The extra broadening could be explained by two factors. A small percentage of the primary electrons were captured by the grid separating the absorption region from the avalanche region. In addition the non-uniform field near the grid results in a small, position dependent gain modulation.

Secondly, the acetylene admixtures of high purity were not easily obtainable often being contaminated with acetone. The measured energy resolution varied significantly between gas samples and it was not until a supply of gas, using research grade constituents, was found that predictable and stable detector operation and performance could be achieved.

The position of the an X-ray event is determined by collecting the final charge avalanche in the second multiplication region on a WSA charge division anode pattern. The charge is divided among the three WSA electrodes and the two dimensional positional coordinates calculated from the measured charge levels. The four main factors that affect the ultimate positional accuracy of the PGI are :-

1. The range of the photo-electron produced by the initial X-ray interaction [131]. This effect only becomes the resolution limiting factor for the PGI at energies greater than 6 keV.
2. The lateral diffusion of the relatively small number of primary electrons [132]. The uncertainty in the centroid position of the charge cloud is ~110 μm at 1.5 keV in the PGI.
3. Electronic noise was minimized by reducing the WSA inter-electrode capacitance [15][100]. The pattern was manufactured in 4 μm thick copper supported on a substrate of Polyimide only 12.5 μm thick, forcing the bulk of the capacitive coupling to be via the gas reducing the effective dielectric constant. In the PGI electronic noise was the resolution limiting factor, being ~225 μm FWHM at 1.5 keV.
4. Partition noise (discussed in section 3.3.1.1). In the PGI it is typically ~50 μm at 1.5 keV.

The PGI used a large area WSA which, for the 185 mm diameter prototype, was manufactured using G10 printed circuit board, a glass reinforced epoxy composite material. This device provided an adequate imaging capability but suffered from problems associated with cleanliness, the Penning gas mixture being sensitive to contaminants, and high inter-electrode capacitance, which caused increased electronic noise and degraded position resolution. The XOGS flight detector utilized a thin substrate WSA manufactured on a 12.5 μm kapton substrate. The substrate being several times thinner than the WSA inter-electrode gap, reduces the capacitive coupling between electrodes (see section 3.3.2.1), the dominant coupling being through the detector gas. The capacitance of the 185 mm WSA pattern used for the prototype, was reduced from 1518 pF on a G10 substrate, to 708 pF on a 12.5 μm kapton substrate, the capacitance being measured between the tied wedge and strip electrodes and the Z electrode. The XOGs WSA also benefited from being reduced in size to 90 × 75 mm^2 with a further drop in inter-electrode capacitance, the full 185 mm diameter not being required to accommodate the four XOGS X-ray spectra.

The calculated quantum efficiency (QE) of the detector as a function of X-ray energy is shown in Figure 4-2. The window transmission function is included in the calculation. The detector was designed to operate at a pressure of up to 1.5 atmospheres.

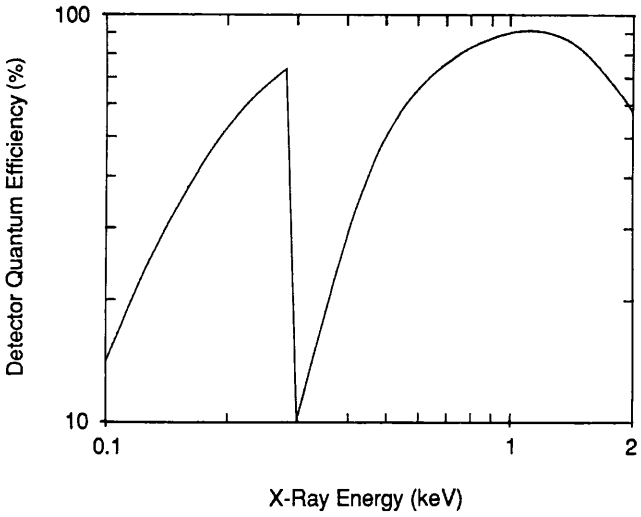

Figure 4-2. The quantum efficiency of the PGI.

The PGI used a number of background rejection techniques. The WSA was surrounded by an annular electrode, the guard anode, which was used to sense the avalanched charge from any particle tracks which passed through the detector volume above it. The extended track produced by a particle which passed from front to back of the detector and did not impinge on the gas volume above the guard anode, produced a characteristic pulse shape having an initial slow rise followed by a large step, on grid 3, the upper grid of the second amplification stage. The presence of this characteristic pulse shape was detected by using the delayed and shaped first part of the pulse, in coincidence with the second part. This coincidence pulse together with guard anode pulse was used in anti-coincidence with the energy and position signals to achieve a background rejection factor of better than 100 [123] for minimum ionizing particles.

4.1.3 Detector Manufacture

The detector body, the front plate, which provided the window support, and the vacuum door, were manufactured in aluminium coated with an alochrome surface treatment. The grids defining the avalanche and drift regions were constructed using electroformed nickel mesh, stretched and glued using a low outgassing epoxy adhesive, to aluminium rings. The rings were located, using large spring washers, in insulating spacers machined from polycarbonate. The thin kapton WSA was stretched on to its own polycarbonate spacer and the entire stack comprising three grids and the WSA, together with their associated spacers and a lower support ring, was held together by 6 polycarbonate bolts. The bolts passed through holes drilled through the bottom of the detector body, using o-rings to provide a pressure tight seal, and were fastened externally using steel nuts. The thin stretched polypropylene window was clamped between the upper flange of the detector body and the front plate. Window replacement could be carried out without disturbing the rest of the detector internals.

The thin polypropylene window was manufactured from thicker polypropylene co-polymer sheet, selected specially for its ability to be stretched uniformly. The material was attached to an annular clamp ring and stretched over the smoothed mouth of a metal cylinder (a skylark rocket segment) through which hot air was blown from a household electric fan heater. Cloth was used between the film and cylinder to allow the film to slip as the clamp ring was pushed down over the cylinder. Practice was required to achieve the desired film thickness which was fairly accurately estimated using the interference colours seen in the film. The stretched material was glued to a support ring, and coated with DAG, a colloidal graphite solution used to provide the necessary conductive surface to the window (to define the parallel counter drift field) while being transparent to the low X-ray energies.

The requirements placed on the DAG coating were uniformity, maximum X-ray transmission in the energy range observed, and electrical continuity. These were necessary to avoid modulation of the source intensity with position, attenuate the X-ray flux as little as possible, and avoid isolated islands of DAG which would charge up and distort the drift field in the absorption region. A procedure was developed for the DAG coating based on the photo-resist spin coating technique used for WSA manufacture, both using a custom-built built spin table with a 15 inch diameter capacity. The DAG thickness, surface resistance and continuity could be adjusted by varying the its viscosity by diluting with methanol, and by altering the spin table parameters, the spin-up time, maximum speed and duration of spin.

The thin window, though typically only 0.6 μm thick, was fairly robust in operation. Its lifetime was limited mainly by the number of pressure cycles it underwent when the volume between vacuum door and window was evacuated. In pre-flight operations at NASA Wallops Island and WSMR, it needed replacement every 2-3 weeks, corresponding to ~10 window pressure cycles.

WSA manufacture was made more difficult than normal owing to the thin kapton substrate used to minimize inter-electrode capacitance. It was stretched on to an aluminium ring for the entire WSA manufacturing process, to make it more manageable, and resembled a drum skin. Similar adjustment of spin parameters was used to tune the photo-resist coating uniformity and thickness for WSA manufacture. The completed WSA was again stretched and glued using low outgassing epoxy on to a polycarbonate support ring, and contact wires were attached by judicious use of soldering so as not to compromise the epoxy adhesive.

4.1.4 X-ray Objective Grating Spectrometer

The X-ray Objective Grating Spectrometer (XOGS) [124] was a sounding rocket payload built in collaboration with Lockheed Palo Alto Research Laboratories and the University of Colorado. The XOGS instrument consisted of a dispersive X-ray spectrometer designed to combine high throughput with high wavelength resolution. It comprised four sets of reflection gratings in conical diffraction, each comprising co-aligned grating triplets, which were used to diffract the

incoming X-rays so that wavelength was dispersed in angle at the entrance to the X-ray optics. . Three, nested Wolter I telescope mirrors focused the diffracted X-rays, transforming the angular dispersion to a dispersion in position at the focal plane. The mirrors themselves were the proof of concept for a novel technique of achieving the required surface accuracy using a lacquer coating method to avoid the costly and time consuming conventional lapping and polishing technique. The PGI performed as the X-ray focal plane detector, imaging the four identical spectra which covered the energy range 0.1 - 2 keV. The gratings were operated in multiple orders and the energy resolution of the PGI was required in order to separate the different orders of the spectra which overlapped spatially.

4.1.5 Detector Performance

Tests of a 70 mm prototype multi-step detector had been carried out using commercially available low-noise spectroscopy pre-amplifiers, NIM-format shaping amplifiers, linear gate and stretchers and ADC's with promising results. The left-hand plot in Figure 4-3 shows a cross-section through the image of a pinhole illuminated with *Al-K* X-rays at 1.5 keV and corresponding to a deconvolved detector resolution of 100 μm FWHM measured at an overall gain of 1.3×10^5. The energy resolution, measured in the same configuration, using a 5.9 keV Fe-55 source, was 12.5% FWHM and is shown on the right-hand side of Figure 4-3.

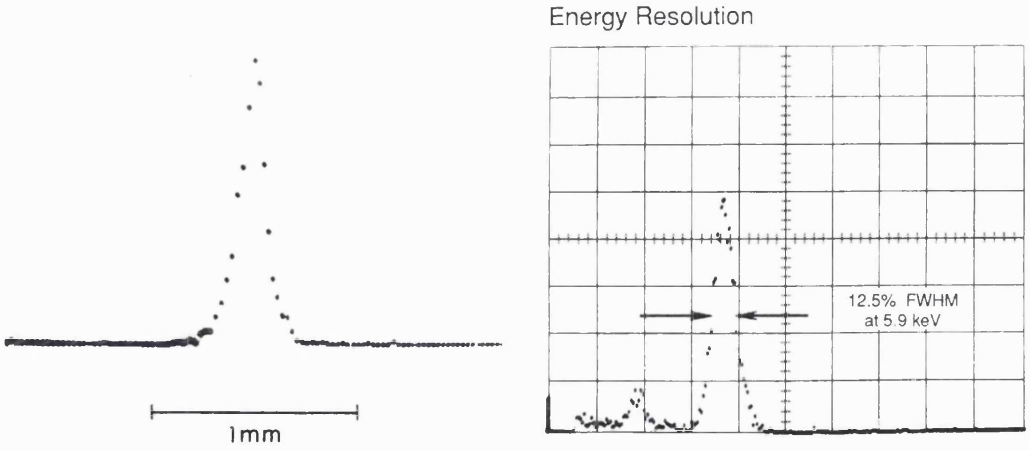

Figure 4-3. The position and energy resolution of the prototype PGI detector.

The detector was then integrated with the flight electronics and ground support equipment, which were designed and built by Jason Tandy, at MSSL. Figure 4-4 shows two images; on the left is an image of an array of large pinholes covering the entire field of view demonstrating the linearity of the WSA read-out, on the right, the instrument response to illumination of a fine pinhole array with 1.5 keV X-rays. The pinhole spacing in the right hand data was 1.7×1.0 mm^2 and the missing points result from the Moiré fringing between the hexagonal window support mesh and the rectangular pinhole array. The resulting deconvolved resolution of 350 μm FWHM was substantially degraded by an acoustic noise component generated by the mechanical pump of a vacuum system to which the detector was attached.

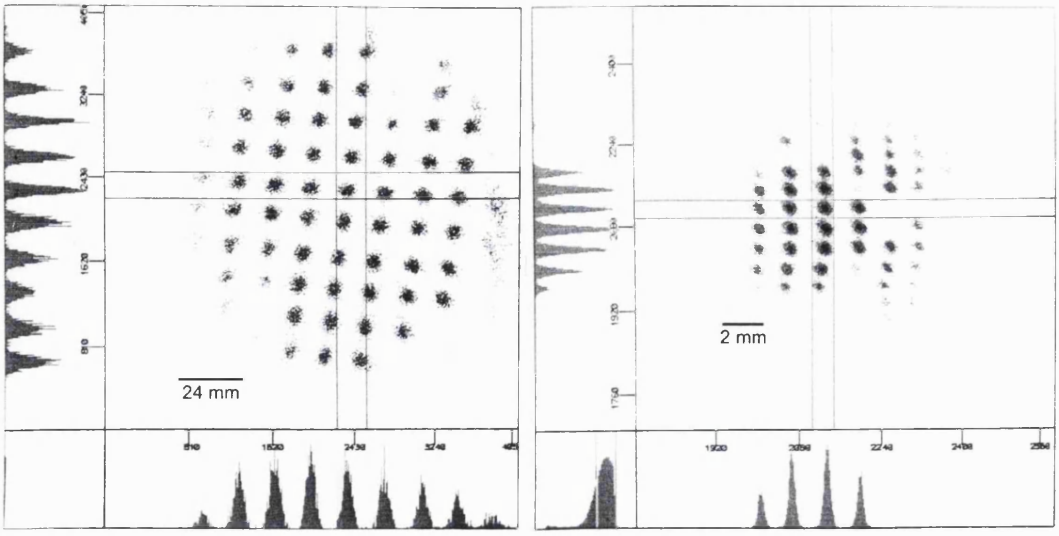

Figure 4-4. Data showing the linearity and position resolution of the XOGS PGI detector.

The detector underwent modifications to overcome a variety of operational problems including :-

1. An HV breakdown problem which caused lowered resistance across the WSA. This resulted in a much increased noise and degraded position resolution and was produced by large amplitude events (probably due to cosmic rays) outside the active WSA area which deposited a large amount of charge on the guard electrode. This produced a transient voltage to the other WSA electrodes which could, if large enough, result in further gas breakdown across the inter-electrode gap, highlighting an unwanted feature of the argon - acetylene gas mixture. Local breakdown close to the WSA caused the insulating substrate to be coated with a resistive deposit, probably due to polymerization of the acetylene and similar to the effect seen in other proportional counters [125]. The deposit could be removed by solvent washing and it was hypothesized that conductive polyacetylene was being created. The problem was avoided by enlarging the inter-electrode gap between the guard anode and other electrodes.

2. Breakdown effects were also mediated and energy resolution improved after a supplier of higher purity gas was found. The higher purity gas increased the average ionization energy, W, allowing the detector operating gain to be achieved at a lower voltage, and causing the energy resolution to improve. An image distortion effect attributed to modulation, which caused pinhole images to be diagonally extended, was also improved. This probably resulted from the decreased contaminant level, which probably acts as a quench, allowing the charge avalanche to produce a larger charge footprint on the WSA.

3. The position resolution was limited by an acoustic component of electronic noise, which resulted from the mechanical resonance of the stretched grids and WSA, held at high voltages and acting as microphones. In flight the acoustic noise from the vacuum chamber pump would be absent, however the gas solenoid valve which periodically actuated to regulate the detector pressure, also caused acoustic noise. This mechanical impulse

propagated through the electronics mounting plate to the detector via the rest of the payload. The problem was solved by improving the mechanical damping of the solenoid mount and slowing the electronic actuating pulse to lessen the high frequency 'click' of the solenoid.

Detector performance improved after the above modifications. Figure 4-5 shows an image of the 1.7×1.0 mm^2 pinhole array illuminated using *Al-K* X-rays, the measured energy and spatial resolution being 28% FWHM at 1.5 keV and ~285 μm FWHM (also at 1.5 keV) respectively. Missing pinholes result from moiré fringing with the window support grid.

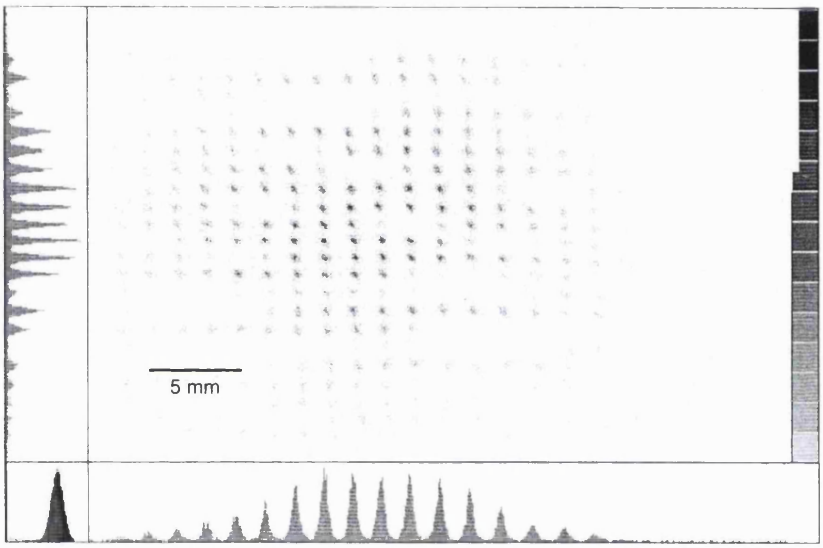

Figure 4-5. An image of a pinhole array taken using the XOGS PGI. The data indicates a simultaneous position resolution of 285 μm FWHM and energy resolution of 28 % FWHM.

The PGI flight detector and electronics were integrated with the gratings and mirrors, and the whole payload subjected to environmental testing at the Wallops Flight Facility, Virginia, and an end to end system test was performed at the High Energy Laser System Test Facility (HELSTF), at White Sands Missile range (WSMR), New Mexico.

The overall detector performance in its final flight configuration and after integration with the rest of the payload, was 34 $E^{-0.5}$ % for the energy resolution, and 350 E^{-1} for the position resolution. This did not equal the detector design goals of $30E^{-½}$% FWHM and $250E^{-1}$ μm FWHM but was limited by a residual acoustic noise from the gas solenoid, coupled with an electronic noise, attributed mainly to the DC-DC converters in the power supply for the electronics plate. The electronic noise component of the position resolution was measured, using the in-built electronic stim generator used for calibration, at ~220 μm FWHM with the payload installed integrated with the launch vehicle and sitting on the pad at WSMR. At this stage the position resolution could not be confirmed but was conservatively estimated at ~360 μm at 1.5 keV, at launch. An energy resolution of 28 % FWHM at 1.5 keV was measured before launch, sat on the pad, using the in-built fluoresced radioactive *Al-K* calibration source.

4.1.5.1 XOGS flight

The XOGS instrument was flown on an Aries rocket twice from WSMR. The first launch was marred by failure of the vacuum door squibs followed by a high voltage breakdown which caused two of the electronic charge measurement channels to fail. The dually redundant squibs should have unlatched the vacuum door once the payload reached operational altitude. The door was essential to protect the thin window from atmospheric exposure which would cause contamination of the counter gas due to diffusion through the window. With the door shut and the electronics damaged the payload performed no useful science but the flight went as planned and the payload was recovered undamaged. The re-flight, which took place several years later, was a catastrophic failure when two of the Aries four sustainer exhaust nozzles burnt away at an altitude of ~10 miles, the rocket exploding and the payload being spread across a ½ mile long swathe of New Mexican desert.

4.2 The Yohkoh BCS Detector prototype

4.2.1 Introduction

This section describes the development of the prototype position sensitive proportional counter for the Bragg Crystal Spectrometer experiment which was eventually flown on the Japanese YOHKOH mission. This mission was dedicated to the studies of high energy solar flare phenomena through coordinated X-ray and gamma-ray observation. The mission used a three-axis stabilized, sun-pointing spacecraft and was launched to coincide with the solar maximum cycle.

The Bragg Crystal Spectrometer (BCS) was built by a consortium of groups from the UK and the US, led by the Mullard Space Science Laboratory of University College London (MSSL), and including the Rutherford Appleton Laboratory (RAL), and the US Naval Research Laboratory (NRL). MSSL was responsible for building the detectors and all the electronics.

The purpose of this instrument was to study the dynamics and heating of the plasmas that make up a solar flare, especially during its impulsive phase. In order to fulfil the scientific objectives, an instrument with a higher sensitivity than in previous missions was required. Four spectral line groups were chosen for study, Fe XXVI, Fe XXV, Ca XIX and S XV. The resonance lines of these groups have energies of 6.97 keV, 6.7 keV, 3.9 keV and 2.4 keV respectively.

4.2.2 Instrument Overview

On a relatively small spacecraft such as YOHKOH, volume, power and weight constraints are important considerations in instrument design. It was therefore decided to use curved or bent crystals as the dispersive elements together with a position sensitive detector [128] rather than a scanning flat crystal with a conventional detector; a bent crystal spectrometer need have no moving parts. The bent crystal design also had the advantage of simultaneously recording all of

the wavelength channels, making it possible to run the spectrometer at a much higher time resolution.

The BCS consisted of two assemblies, known as BCS-A and BCS-B. BCS-A was designed to observe the Fe XXVI and Fe XXV lines, while BCS-B observed the Ca XIX and S XV lines. Each assembly had two crystals bent to different curvatures to suit the selected wavelength ranges. Radiation dispersed by the crystals according to the Bragg relationship was detected by a proportional counter with 1-D position sensing capability. One proportional counter was used for each pair of crystals. Each detector had two independent sets of anode wires, one devoted to each crystal. The assembly had an incorporated High Voltage Unit (HVU). The counters were milled from stainless steel and used sealed design needing no gas supply system. X-ray transmission entered the counter volume via a Beryllium foil window. Position sensing was achieved by means of a charge-dividing conductive cathode, placed at the base of the detector. This cathode was of the Wedge and Wedge (or Backgammon [84]) type.

Charge-sensitive preamplifiers were located at the back of the detector, together with the first of two stages of pulse shaping circuitry. The shaped voltage pulses were then led to a central electronics box which served both of the spectrometer assemblies. This box carried out the analogue to digital conversion and subsequent data processing. It also handled the instrument control and interfaces with the rest of the spacecraft. The electronics system was microprocessor controlled.

The BCS detector is shown in Figure 4-6. It was constructed in two halves, a top assembly including the beryllium window, and a bottom assembly on which the anodes and cathodes were mounted. The front-end analogue electronics cards were mounted onto the bottom assembly and shielded with a metal enclosure.

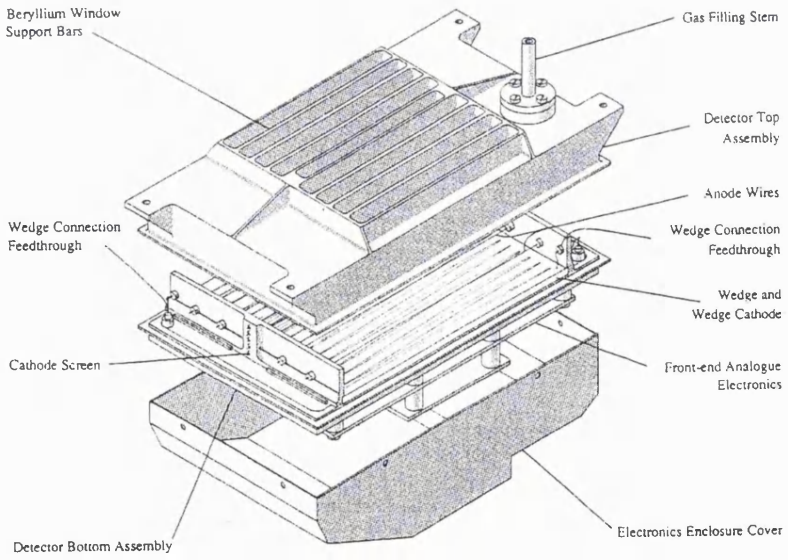

Figure 4-6. An exploded view of the YOHKOH prototype model detector.

4.2.3 Detector Performance Requirements

The BCS scientific goals required the position sensitive proportional counter to achieve the following performance specification :-

1. The detector energy resolution. Although the instrument is a crystal spectrometer relying on position measurement for the very accurate spectrographic analysis, a knowledge of the X-ray energy of the event using the proportionality of the anode signal is essential for background rejection. To satisfy the Bragg relationship for the chosen wavelength ranges, and accommodate the mechanical constraints of the instrument, various cuts of Germanium crystal were selected as the dispersive element. However, when illuminated with hard X-rays present during the impulsive phase of a solar flare, Germanium fluoresces to produce photons that have an energy corresponding to the Germanium-K edge, 9.89 keV. The energy resolution of the detector had to be sufficient for this fluorescence to be effectively discriminated out. This was more difficult for the Fe XXVI detector, the spectral line being at 6.9 keV. The success of the background rejection was modelled for various detector resolutions. An overall resolution of 18-20% FWHM at 6.9 keV was required in order to achieve the required rejection.
2. Position resolution. The projected spectral resolution of 5000 $\lambda/\Delta\lambda$ for both Fe lines equates to a position resolution on the detector of ~350 μm. The resolution requirement for the BCS-B detector was a factor two larger.
3. Maximum count rate. Several factors affect this parameter. The choice of gas mixture and the detector geometry influence signal risetimes which determine the pulse processing time. It was necessary to make a compromise between good energy and position resolution versus the count rate capability. The goal aimed at was to produce a detector capable of operating, albeit with reduced position resolution, at 30,000 counts per second.

4.2.4 Detector Development

4.2.4.1 Design envelope

Mechanical and electrical design constraints were laid down at an early stage in the project. In broad terms, these defined the overall size and mass of the detector and that of its electronics package. The dominant design specifications which have drove the choice of internal detector geometry were:-

1. The detector mass and size limits. To keep within these limits, the two detectors associated with the adjacent crystals had to be accommodated within a single gas volume. A single Wedge and Wedge cathode pattern was used to readout one-dimensional position from both detector halves.

2. The dimensions of the window (90mm × 40mm) for each detector half, and the internal transverse cross-section of the detector enclosure. The lowest aspect ratio which was allowable was 48:20 (both units in mm) for each detector half.
3. The requirement for electronics with low mass and power. This implied a maximum number of four processing channels per two detector halves; two for the independent anodes and two for the Wedge and Wedge cathode position readout.

A variety of detector operating parameters were explored in the detector development programme. The aim was to achieve the performance goals outlined in the last section, within the mechanical and electrical constraints described above. The following sections discuss, one by one, these detector parameters and describe, with reference to measured results, their influence on detector operation.

4.2.4.2 Detector body

Several factors influenced the choice of materials used for manufacture. In order to reduce the bulk and mass associated with seals, stainless steel was chosen for the detector body. This material has a high tensile strength, and is ideally suitable for welding and brazing. The 125 μm thick Beryllium window was brazed in place, and the two halves of the body were electron-beam welded together, eliminating the need for two sets of flanges. The use of stainless steel allowed the detector to have very thin walls. Because of these properties, the choice of stainless steel rather than aluminium did not significantly alter the mass of the detector body.

The electron beam welding was carried out in vacuum and did not require fluxes which could have been a cause of detector contamination. Ceramics were used for the electrical feedthroughs and the cathode pattern substrate. The use of any type of organic materials was avoided, as far as possible. The detector was constructed from materials suitable for baking to 150° C, and the procedure carried out before each gas fill. Certain parts were baked to higher temperatures.

4.2.4.3 Gas mixture

The desired quantum efficiency could not be achieved with a solely Argon based mixture in a detector of this depth at 1.2 atmospheres, the design pressure. Higher pressures could not be used because of the loss of sensitivity that would result from an increased window thickness or support bar width it would have required. Originally, a Xenon based mixture was proposed, but its sensitivity to contamination led this to be modified to Xenon-Argon which could equally well meet the quantum efficiency goal.

The lifetime requirement of the detector together with the expected average count rate precluded the use of gas mixtures which could have resulted in the formation of significant deposits on the anode wire. Thus, hydrocarbon admixtures were avoided [125]. Experiments were undertaken using various percentage carbon dioxide admixtures in a Xenon-Argon fill. Mixtures including

Argon were found to produce faster anode signal risetimes than those with Xenon alone. They could also operate stably at high gains [129].

Much development work was carried out using Argon based mixtures in a flow mode in order to measure the performance variations between different detector internal geometries without the expense involved in sealing it off with an unrecoverable, costly Xenon gas fill. Though these mixtures had different properties, they were sufficiently similar for us to extrapolate the data obtained with Argon to a Xenon-Argon fill.

The other major performance goals for which the gas is instrumental, are energy resolution, position resolution and count rate. The intrinsic energy resolution of the gas did not prove to be a problem, being 16-20% FWHM at 5.9 keV for all the mixtures tested. The energy resolution of the whole detector, i.e. the intrinsic resolution convolved with the gain variation over the active area of the detector, was larger than this. The dominant gain variation was across the detector width.

There are several effects relating to the gas which cause this variation in gain :-

1. Gain compression of events whose initial charge cloud has been reduced in size by electrostatic funnelling. This causes a local space charge effect which decreases the apparent electric field in the avalanche region resulting in lower overall gain. Obviously, it is the norm in a wire counter for the field lines to converge. The problem arises when field lines from different positions in the detector converge at different rates, some of them converging fast enough that space charge limited gain can occur even at quite low overall gains. This occurs because of the high aspect ratio of the detector cross section. The problem is accentuated by the requirement for high position resolution, which can be improved if the quench gas percentage is increased. This results in a smaller primary ionization charge cloud, which is more vulnerable to space charge effects and subsequent gain reduction. Since this effect only occurs in certain positions within the detector, the net result is to increase the width of the energy distribution.

2. The field produced by the anode voltage in the region where the majority of the absorption takes place (i.e. a volume beneath the window about 10 mm deep) varies with transverse position. This produces variable drift times for the primary electrons to reach the avalanche region around the anode wire, having three effects. First, if the drift time is long, the charge cloud becomes significantly larger by diffusion. At high gains, these large clouds are less affected by space charge limited gain than those whose drift times are shorter. Secondly, recombination can be a problem with very long drift times, resulting in a lower apparent gain. Thirdly, the electron pulse collected on the anode wire, after gas multiplication, reflects the arrival times of the primary electrons. If these are spread out, the pulse will have a longer risetime. This has implications on the minimum pulse shaping time constant of the processing electronics. To avoid ballistic deficit, there

is a minimum ratio between the signal risetime and the pulse shaping time. The maximum signal risetime defines the pulse processing deadtime and, hence, the maximum processed event rate.

The above effects can be varied by altering the quench gas (carbon dioxide) concentration. Simply, increasing the percentage reduces the electron diffusion, improving the potential position resolution. It also raises the gain at the onset of non-proportionality and decreases the likelihood of secondary avalanching. However, in reducing the charge cloud size, it can result in space charge limited gain. This manifests itself as a position dependent gain variation. Reducing the carbon dioxide concentration increases the spatial size of the primary charge cloud (degrading the position resolution). It also increases the likelihood of secondary avalanching at lower gains.

As has been previously discussed, the carbon dioxide percentage is instrumental in controlling the electron diffusion coefficients. This influences the position resolution since the inaccuracy in the centroid position (along the position measurement axis) of the primary electron cloud increases as diffusion increases the cloud size. This is due to the statistical uncertainty resulting from the relatively low number (several hundred) of primary electrons in the cloud.

The choice of gas mixture also has an effect on the maximum count rate per unit length along the anode wire. At high count rates, the positive ion mobility, being much lower than that for the electrons, results in a build up of positive charge around the anode wire. This electrostatically shields the wire and reduces the gain for subsequent events. The ion mobility is highly dependent on the gas composition.

4.2.4.4 Anode Configuration

The dimensions of the transverse cross section of the detector were defined early in the development programme due to the short time scale available for design. This imposed restrictions on the options for the anode geometry. The detector development programme was limited to optimizing this geometry to meet the performance goals within the short timescale of the project and the design constraints.

Several anode wire geometries were investigated. The solutions were limited to either one or two wire arrangements (for each detector half) since there was no capability, given the simplicity of the electronics, to detect on which anode wire an event was measured. This implied, given the energy resolution performance requirement, that the gain on each wire had to be very similar (i.e. the electric field environment around each wire must be close to identical). Three or more wires would not have suited this criterion. The solutions investigated were arrangements of one or two wires (symmetrically disposed in each case) at various positions within the detector volume, and of various diameters.

Initially, for simplicity, a single wire layout was investigated. Field modelling suggested that, for all layouts, the preferable wire position would be low in the detector volume. This arrangement

would create the most uniform field in the effective absorption region, as well as inducing a larger signal in the position readout cathode pattern. The major problem with the single wire layout was the large variation in anode signal risetimes.

A two wire arrangement produced improved results. In this case, as before, a low anode position is preferable. In addition, the inevitable zero field point lying midway between the two anode wires is lower in the detector volume, out of the effective absorption region. With higher anodes, this point can lie in the absorption region, giving rise to very long drift times and large gain variations across the detector.

As an illustration of the performance variations which these layouts produced, Figure 4-7 shows the transverse gain variations for one and two wire geometries with 15 μm diameter wire. Figure 4-8 shows the effect on signal risetime of wire position.

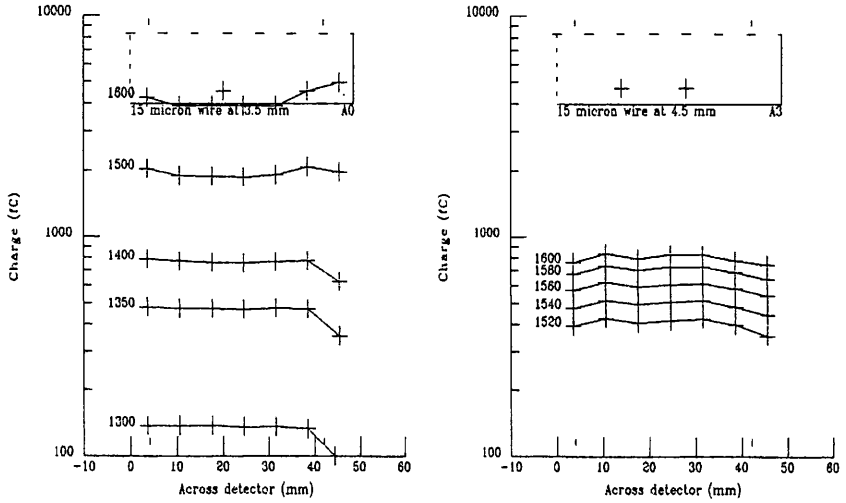

Figure 4-7. Transverse gain variations for different detector configurations. Taken using 5% CO_2 and equal Xenon:Argon concentration using 15 μm diameter wire. The numbers to the left of each plotted curve represent the anode wire voltage. The layout of the detector cross section indicating the wire position(s) is shown above.

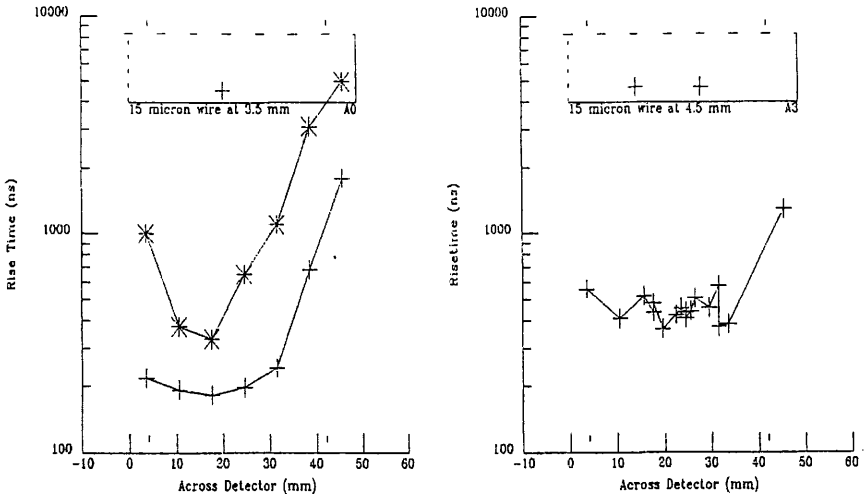

Figure 4-8. The anode signal risetime versus transverse position. The graph on the left shows data for Argon (lower +) and Xenon-Argon (upper *) mixtures, and on the right, Xenon-Argon data only.

The effect of anode wire diameter was investigated using wires of 15 μm and 25 μm diameter. The required position resolution was not achievable with the 25 μm diameter wire and the position dependent gain variation was noticeably worse (see Figure 4-9). This was probably due to azimuthal gain dependence. The primary charge cloud was small enough with respect to the wire to sense the azimuthal variation in the field around the wire. Thus, the avalanche gain exhibits an azimuthal dependence.

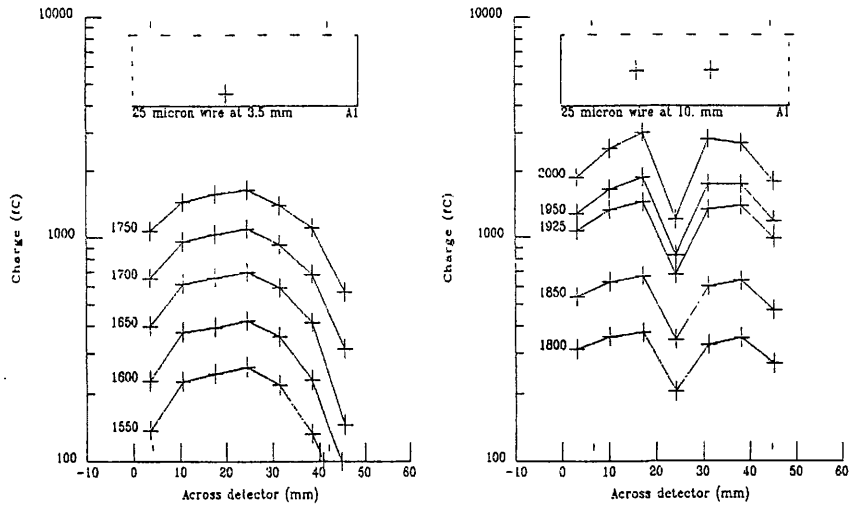

Figure 4-9. The transverse gain variations using 25 μm wire in different positions.

The 15 μm diameter wire did not show this effect because the avalanche was not azimuthally localized (i.e. spreading evenly around the wire) and so this diameter was chosen for the prototype detector anodes.

Given the initial design constraints on the detector dimensions, the layout with two anode wires symmetrically spaced horizontally and low in each detector volume (i.e. four anode wires per gas vessel) proved to be the best compromise.

4.2.4.5 Wedge and Wedge position readout

Following on the successful use of the WSA for the PGI detector, a two electrode charge division pattern was chosen to provide the one dimensional imaging capability required by the BCS detector. A schematic of the layout of the device is shown in Figure 4-10. The Wedge and Wedge pattern (otherwise known as Backgammon) consists of two interlocking wedges separated by an insulating gap. Each wedge varies linearly in width along the detector dispersion axis. Measurement of the charge induced in each electrode can be used to calculate the position of the charge centroid, corresponding to the position of the X-ray interaction.

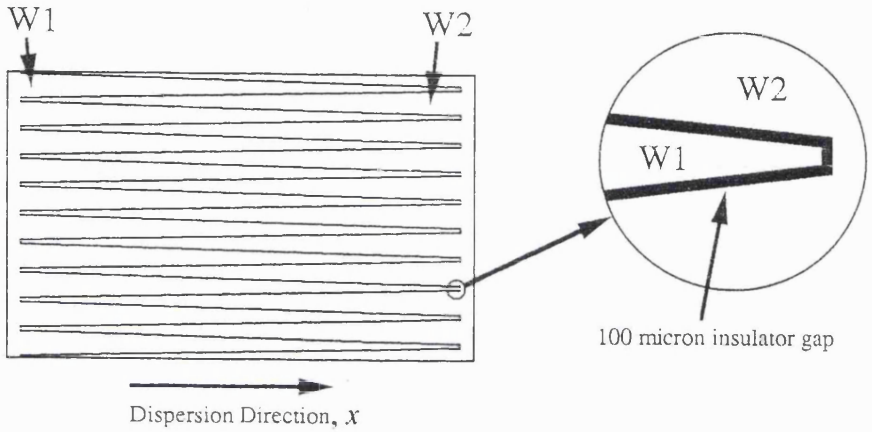

Figure 4-10. A schematic of the Wedge and Wedge Cathode readout. The number of pitches shown is reduced for clarity. The anode wires run parallel to the dispersion direction.

The x coordinate is given by

$$x = \frac{Q_{W2}}{Q_{W1} + Q_{W2}} \qquad (4\text{-}1)$$

where Q_{W1} and Q_{W2} are the induced charges on the electrodes.

The device detects charge induced in the electrodes by the rapid generation of a cloud of positive gas ions around the anode wire. These induce a signal whose risetime represents the electron transit time from the point of ionization to the anode wire (i.e. governed by the mean electron drift speed in the field near the wire). This produces a relatively fast signal with a minimum risetime (given a localized primary charge cloud) of 350ns in a Xenon-Argon, 5% CO_2 gas mixture.

The pulse shaping time constant of the processing electronics is too fast to sense the much slower positive ion drift through the low field region, towards the cathode (i.e. the surrounding detector body). Since the electronics do not measure the charge during its collection time, they do not suffer from partition noise [130].

The Position resolution of the BCS detector was limited by four factors :-

1. The position error caused by the track length of the initial photoelectron, as described for the PGI [131]. The higher X-ray energies of the BCS made this one of the dominant resolution limiting factors.
2. The lateral diffusion of the primary electron cloud [132].
3. Chaotic avalanche spread along the wire, more of a problem at high gains.
4. Electronic noise associated with the measurement of the charges on the wedge-wedge anode

Electronic noise is dominated by the front end noise of the charge sensitive preamplifier. This noise can be reduced by reducing the capacitive loading on the preamplifier input. In the case of the BCS, this was accomplished by reducing the interelectrode capacitance of the Wedge and Wedge cathode pattern as far as possible. This was achieved by using substrate with a low dielectric constant which fulfilled the outgassing criteria, fused silica, and by making the interelectrode gap and the pattern repeat pitch as large as possible within the criteria laid down by Schwarz et al [100].

Since the electronics could not detect on which anode wire an event was recorded, it was important to ensure that the position given by both anode wires of one detector half was identical. Modulation, caused by the induced charge distribution being too small, could have produced such an effect. This potential problem was avoided by ensuring that each wire was aligned identically with the pattern pitches. The pattern pitch was chosen to be a sub-multiple of the anode wire spacing. This arrangement allowed the use of as large a pitch as possible and a correspondingly lower interelectrode capacitance.

The best position resolution measured with the prototype was 250 μm FWHM. This was measured using several wire layouts, indicating that it was fairly insensitive to this parameter, but was only achieved with the 15 μm diameter wire.

4.2.5 Prototype Model Performance

The prototype model was filled with a gas mixture consisting of 47.5% Xenon, 47.5% Argon and 5% CO_2 at a pressure of 1.2 atmospheres and was virtually identical to the Flight Model Detector. They were distinguishable only by the number and spacing of their window support bars and, internally, by the fact that the Prototype was built with slightly different wire layouts in the two halves.

Figure 4-11 shows a plot of the transverse gain variation across the detector. The unwanted discontinuity in the curve was discovered after the detector was sealed. Insufficient manufacturing accuracies in the concentricity of the anode wire feedthroughs resulted in one wire not being

parallel to the surface of the Wedge and Wedge cathode. This produced a difference in gain between the two wires which varied along the length of the detector. However, the gain curve for each wire was reasonably flat, to within the required specification.

When the anode wires are near to the Wedge and Wedge cathode, the gain of each wire is more sensitive to vertical displacements, causing the problem discussed above. After this experience the manufacturing tolerances on the anode wire feedthroughs were improved.

Figure 4-12 shows a plot of 13000 detected X-ray events. The position of each event, measured by the Wedge and Wedge cathode, is plotted along the *x* axis. The charge collected at the anode is plotted along the *y* axis. The detector was illuminated by 5.9 keV X-rays from an Fe-55 source, through a metal mask containing an array of 200 μm pinholes. The pinholes were arranged in groups of six. Within each group the pinholes were spaced 1mm apart along the *x* axis and 7.2mm apart in the *y* axis. This arrangement enabled the simultaneous measurement of position resolution and gain variation across the entire detector window.

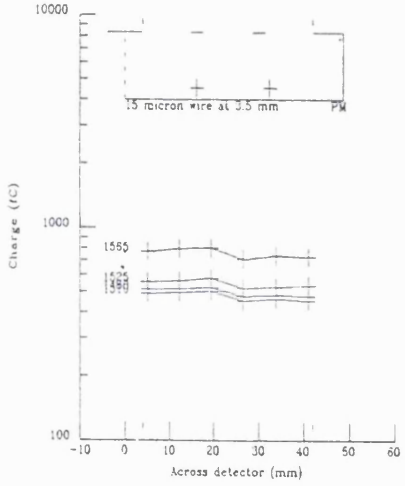

Figure 4-11. The transverse gain variation across the prototype model detector.

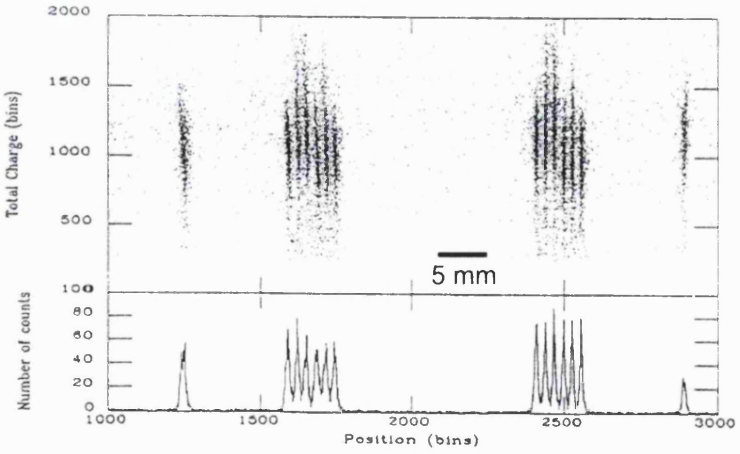

Figure 4-12. The event position (*x* axis) versus the event energy (*y* axis).

The data in Figure 4-12 represents an average position resolution of 330 μm FWHM across the central 68mm of the detector, with a best figure for a single pinhole of 270 μm FWHM. Off-axis from the source, parallax coupled with the finite absorption depth degraded the position resolution. These figures have not been deconvolved from the 200 μm diameter pinhole size used in the mask. The gain variation across this region of the detector is 2.5% for each wire. The intrinsic energy resolution is ~17%.

At this stage, the prototype described here had been demonstrated to meet the position resolution and energy resolution requirements. My practical involvement in the YOHKOH project ceased and Matthew Trow led the experimental programme. The further development of the detector, which included characterization of a spatial resolution degradation and distortion produced by space charge effects around a bright line in the spectrum, and calibration of the flight detectors was undertaken and is reported by Trow [133].

4.3 Investigations of an MCP-based WSA

This section begins by describing the SPAN intensifier, an MCP-based imaging tube using a Spiral Anode conductive charge division readout, that had been developed in conjunction with DEP, Holland. The SPAN detector was originally designed to provide an optical photon counting detector with high spatial resolution for XMM Optical Monitor instrument. The development of the Spiral Anode, and other new readout concepts, together with performance of the first SPAN sealed tube intensifier, is reported on in chapter 6.

The SPAN tube design formed the basis of a breadboard detector used for an experimental programme to research into the potential of a WSA-based intensifier. Section 4.3 describes a series of experiments to characterize and improve the imaging performance of the breadboard detector, a demountable version of the SPAN tube without an input window and using a WSA in place of the original spiral anode. The results from the breadboard detector were incorporated into a modified SPAN tube design using a WSA for imaging, which was manufactured for the Tel Aviv University UV Explorer [17] (TAUVEX) experiment on the Russian Spectrum X-γ mission.

4.3.1 The SPAN image tube design

The original SPAN tube design comprised a fused silica window with a semi-transparent, blue enhanced S20 photocathode providing spectral response from 150 nm to 650 nm on a 25 mm diameter image format. This detector was required to have a high spatial resolution of 1000 × 1000. Other performance goals were peak quantum efficiency greater than 20 % and a maximum count rate of 200 kHz.

A stack of three MCPs, operated in saturated mode, was used to produce an output electron cloud of ~$2x10^7$ electrons necessary for the required signal to noise ratio on the electronic position readout. All MCPs were hard-edged with a pore diameter of 10 μm at a centre spacing of 12 μm.

The input MCP had a 40:1 length to diameter (L/d) ratio and was separated from the second MCP by a gap of 50 μm. The second and third MCPs had an L/d ratio of 80:1. Although the MCP stack was operated at a relatively high gain, the Z bias angle configuration and a rigorously defined MCP scrubbing procedure defined by Norton [126], were used to minimize the positive ion current exiting the top MCP. The goal was to achieve an acceptable photocathode lifetime without the use of an ion barrier film on the upper face of the top MCP, which can improve the detective quantum efficiency (DQE) by almost a factor 2.

In the original tube, position determination of the photon event was carried out using the spiral anode (SPAN), a conductive, charge division anode. The electron cloud from the MCP was allowed to expand in a drift region between the MCP and anode of 6 mm to achieve a size necessary to avoid modulation. This produced a cloud size at the anode of typically 2.0 mm diameter.

4.3.1.1 SPAN tube manufacture

The detector body was designed and manufactured by DEP, Holland using similar techniques to their commercial products. It was built up from a sandwich of Covar and ceramic rings brazed together. The Covar rings were used to provide the electrical contacts to the MCP stack.

Both the SPAN and WSA patterns were manufactured by laser-micromachining using the facilities and processes described in chapter 3. These fabrication techniques provided devices which proved to be compatible with the cleanliness and bakeability requirements of the detector UHV enclosure. The WSA and SPAN devices were manufactured on 50mm diameter by 2mm thick fused silica substrates which were mounted on top of six ceramic feedthroughs, brazed into the bottom flange of the detector housing. A seventh, central feedthrough on the same flange was used to supply current to the getter, which sat under a shield below the readout substrate.

4.3.1.2 SPAN performance

The performance of the first SPAN sealed tube intensifier is reported in chapter 6. The first tube suffered from a low MCP gain due to incorrect scrubbing during manufacture. The maximum gain of ~3×10^6 limited the spatial resolution to ~60 μm but the tube exhibited good position linearity. The detective quantum efficiency of the first SPAN tube which used an S20 photocathode is shown in Figure 4-13. A maximum DQE of 21 % was measured at 190 nm [127].

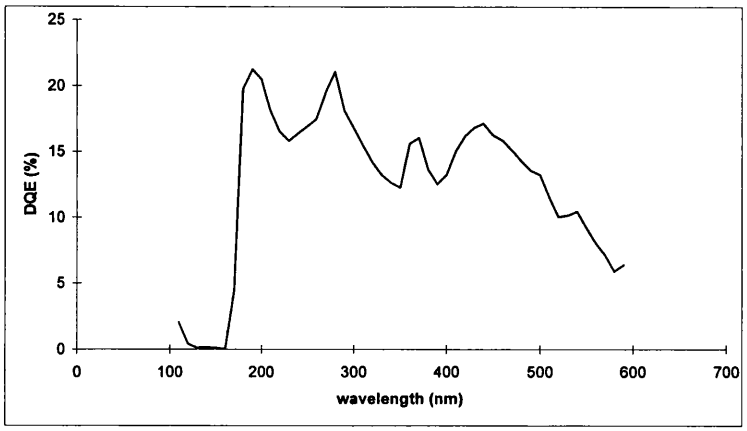

Figure 4-13. The detective quantum efficiency of the SPAN detector [127]. The small scale structure is unreal and results from systematic errors introduced when the source intensity was altered.

4.3.2 Developments with a breadboard detector

4.3.2.1 Test Configuration

Detector Geometry

The breadboard detector used a SPAN tube body with the input window removed and the tube body opened at the bottom flange by means of grinding off the original weld. The SPAN position readout was replaced by the WSA with mechanically identical electrical contacts. The MCP to WSA spacing was adjusted by assembling the detector body with variable spacers in between the upper and lower tube body at the bottom flange. In the cases where a chromium-on-glass pinhole array mask was used, the glass had the similar diameter to the original window and sat in the well used to contain the original window indium seal. The fit was loose enough such that the volume above the MCP stack could be satisfactorily pumped. The chromium face of the mask was towards the MCP input surface.

Illumination Configurations

Two different methods of illumination were used to stimulate the MCP :-

1. The vacuum system was fitted with a quartz window so that an external low pressure Mercury 'Pen-ray' UV lamp could illuminate the detector. In this case, the spectral response was limited by the quartz window, which is opaque below 150nm, and the bare MCP quantum efficiency.

2. An X-ray generator consisting of a heated filament as an electron source, an accelerating voltage and a Carbon coated target. In this case, the detector input spectrum is dominated by a strong Carbon-K X ray emission line at 44 Angstroms with a continuum at lower

intensity down to 12 Angstroms. The accelerating voltage was 1kV. Wavelengths longer than Carbon-K were attenuated with a hydrocarbon polymer filter.

In both cases the source to detector distance was of order 1400 mm. The pinhole mask was 3 mm from the front surface of the MCP and the pinholes were 42 μm in diameter. The effective pinhole size at the MCP input face due to diffraction (using the UV source) was estimated to be 64 μm.

The breadboard detector, unlike the original SPAN sealed tube device, did not suffer image degradation due to the proximity focussing between photocathode and MCP input surface: the photo-sensitive surface being the MCP itself.

WSA encoding electronics

Three channels of the standard commercial NIM electronics used for imaging with the SPAN tube, were used for the breadboard detector. Each channel comprised an ORTEC 142B charge sensitive preamplifier, an ORTEC 572 shaping amplifier, and a Canberra 8077 Fast ADC. Digital signals from the three ADCs were collated by an IBM compatible 486DX PC with a standard 8255 based digital I/O card. The input data was stored, manipulated and displayed using an in-house software package. The overall count rate of this system was limited by the event deadtime (4 μs minimum) and by the data acquisition system.

4.3.2.2 Test results

These experiments were undertaken in a limited time span to rapidly characterize the detector performance using empirical methods to optimize the detector and WSA configuration. Though detailed analysis was not undertaken at the time, the dataset as a whole provides supporting evidence for features of MCP and WSA behaviour investigated in more depth in chapter 5.

Variation of MCP gain and pulse height distribution with detector voltages

Measurements of the overall gain of the MCP stack were taken over a range of MCP voltages. The detector configuration, with contacts to the input surface of the first MCP, the interface between the first and second MCPs, and the output of the third MCP allowed the voltages on the first MCP (signified by MCP1) and on the second and third MCPs in tandem (signified by MCP23), to be altered independently. Figure 4-14 shows the variation in overall gain and pulse height distribution for a range of voltages in the central 9.5 x 6.5 mm^2 region of the detector, at an MCP to WSA voltage of 400V and an input count rate of 4kHz.

The MCPs used in the breadboard detector were of high resistance (500-1000 MΩ), unlike those used in the sealed tubes (MCP1=125 MΩ, MCP23=270 MΩ), and had not undergone a full scrubbing procedure. This may account for the lack of full saturation. The pulse height distribution was still decreasing at the highest voltages applied. One unwanted MCP characteristic was the gain difference between the centre and edge of the field of view (FOV). The gain at the

edge was higher by up to 28 % at the highest voltage, and the pulse height distribution was also wider. The data from the edge of the FOV is indicated by the isolated data points in both plots of Figure 4-14.

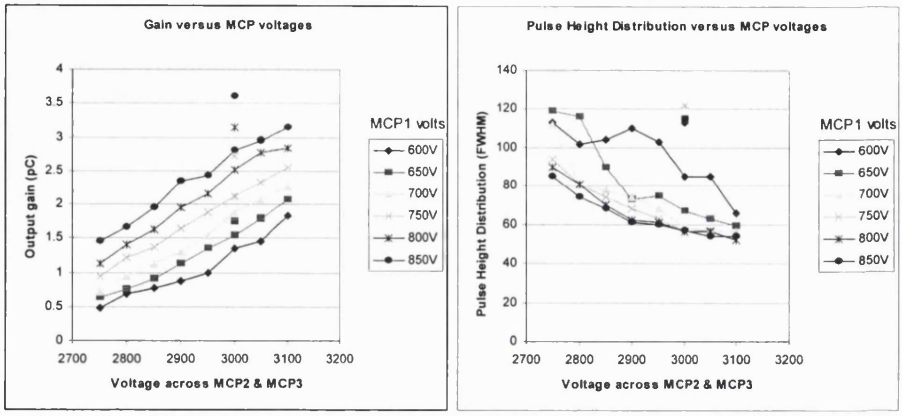

Figure 4-14. The MCP gain and pulse height distribution versus voltage. The data in lines represents the centre of the FOV and the isolated points, the edge of the FOV.

At this stage in the experiment the MCP operating voltages were set, the voltage across the top MCP being 800 V an across the bottom two double thickness MCPs being 3000 V.

WSA Image Modulation

Image modulation occurs because the charge cloud collected on the WSA is too small to smooth out the wedge and strip pattern fine structure [108]. One of the major purposes of this experiment was define the optimum detector configuration avoiding modulation while maintaining image resolution and linearity within the defined physical envelope of the detector. The major parameters controlling the size of the charge cloud are the MCP to WSA gap size, the MCP to WSA gap voltage, and the MCP endspoiling. These parameters were varied, in conjunction with changing the repeat pitch of the WSA, and the level of modulation for each configuration was assessed. The MCP to anode voltage was varied between 160 and 600 V, the MCP to WSA gap and 800 μm were tested. One of the most sensitive qualitative measures of modulation is the appearance of stripes in a flat field image, which correspond to the cyclic position error and have a wavelength equal to the pattern pitch. This feature is also visible as a cyclic amplitude variation in the *y* axis histogram.

MCP - WSA voltage

MCP-WSA voltages of between 160 and 300 V were used with an MCP to WSA spacing of 4.85 mm and a WSA pitch of 800μm at an input count rate of 14kHz.

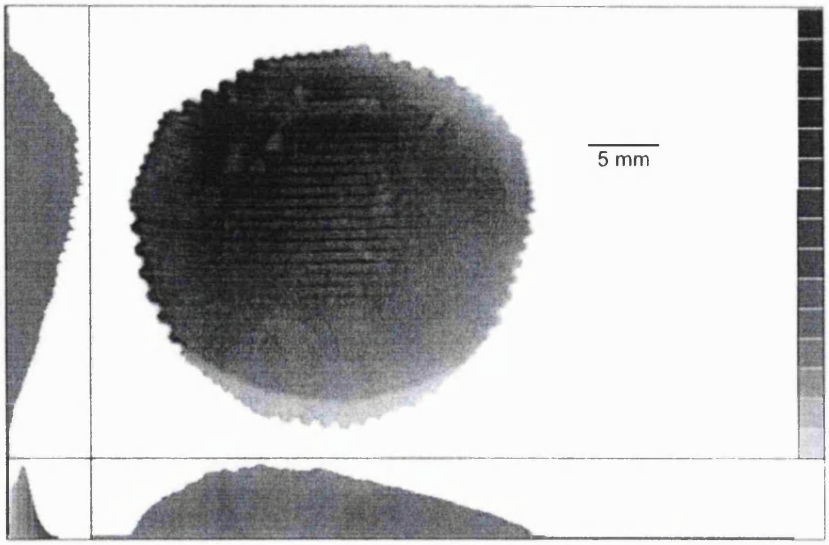

Figure 4-15. Uniform illumination showing the effect of WSA modulation.

Figure 4-15 is an image of 16M events using relatively uniform illumination which displays the structure caused by modulation, consisting of horizontal banding, also apparent in the vertical histogram. The image also shows significant non-linearity. The modulation bands can be seen to curve up at the left and down at the right, a deformation commonly known as S distortion. The increased *y* value on the left hand side is primarily a result of the strip contact bar connecting the strips together, which inflates the strip event charge level, the decreased *y* value on the right-hand side is due to the charge cloud falling off the edge of the active pattern, where the strips end. This indicates that the charge cloud is larger than active WSA region, despite the fact that it is also too small, as evidenced by the modulation stripes. The arc towards the bottom of the image shows the extent of the bright illumination. The saw-tooth perimeter of the image is the edge of the active MCP, where the hexagonal boule boundaries interface with the solid, non-imaging glass surround. The pulse height distribution from the sum of the WSA electrodes is shown in the lower left-hand histogram. Efforts to improve the pulse height distribution were carried out later and deemed less important since :-

1. the MCPs in this prototype were of a different type to the flight model (which were to be of low resistance).
2. the WSA modulation effect is sensitive to absolute gain and thus a broad pulse height distribution can be energy windowed to investigate modulation versus gain.

The modulation versus voltage was found to go through a minimum at an MCP to WSA voltage = 170V, for this particular configuration.

WSA pitch size

Since increasing the charge footprint to reduce modulation would have further increased the edge distortion, the WSA pitch was reduced to 632μm. The active diameter of the WSA was reduced to 26.6mm, resulting in severe distortion at the image perimeter which was now much closer to the

edge of the active imaging area than previously. This was purposely undertaken to better characterize the distortions near the pattern edge and hence define an optimal pattern diameter. A square Nickel mesh was used as a shadow mask to give an indication of pattern linearity.

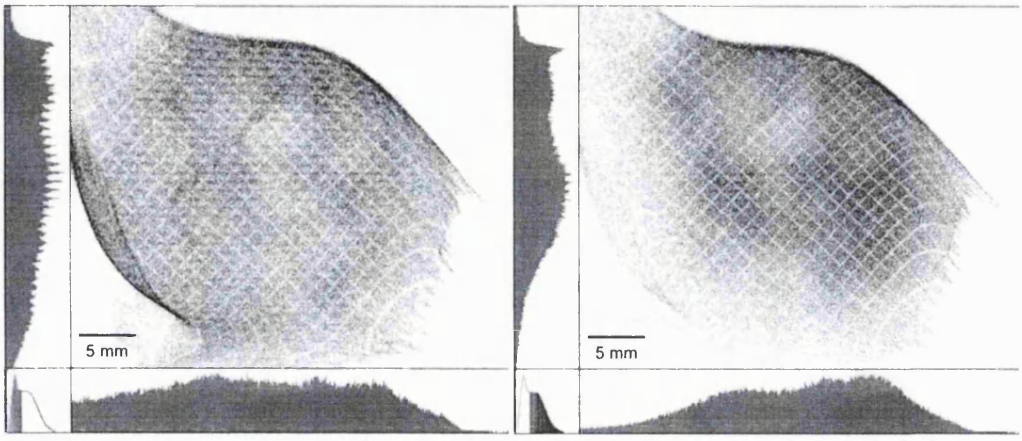

Figure 4-16. The decrease in modulation between low gain (left) and high gain (right). The pulse height window shows the selected ranges of pulse height for each image.

Figure 4-16 shows two images, the left using a low gain window (<6.25x10^6 electrons) and the right using a high gain window (6.25 to 25x10^6 electrons) with an MCP to WSA voltage of 160V an MCP to WSA spacing of 4.85 mm, and highlights the increased modulation seen in the lower gain window.

The WSA pitch was further reduced to 600 μm which helped to reduce modulation though a residual component was still present at MCP to WSA voltages of 160-280V.

MCP output endspoiling

The degree of modulation present, even at low MCP to anode voltages, with such a small WSA pitch was unexpected in the light of previous experiments Other factors that could be producing this modulation were considered. Consultations with DEP, the detector tube manufacturer, provided a potential explanation. The MCP specifications for this breadboard detector had been inherited from the original MIC intensifier tube [71], produced as a prototype for the XMM-OM. The MIC detector uses an output phosphor and the output MCP has a high value of end-spoiling (2 pore diameters) to collimate the output electrons and limit their spread in the proximity focused gap. End-spoiling is the depth that the MCP contact electrode intrudes into the pore. After consultation with DEP it was decided to invert the last MCP so that its output face would have 1/2 diameter endspoiling, as specified for the SPAN sealed tubes. In an intensifier tube endspoiling of 1/2 a diameter is commonly used on the input side of the MCP to increase the likelihood that input electrons will impact the high emission dynode surface rather than the electrode material, to maximize its sensitivity to electrons. Lower end-spoiling also increases the effective L/d ratio and gain, since L is defined by the dynode length.

With the top MCP reversed the image quality improved significantly, indicating the collimation that the MCP endspoiling had been providing. Figure 4-17 shows that with the end-spoiling reduced to 0.5, modulation is virtually non-existent at 280V.

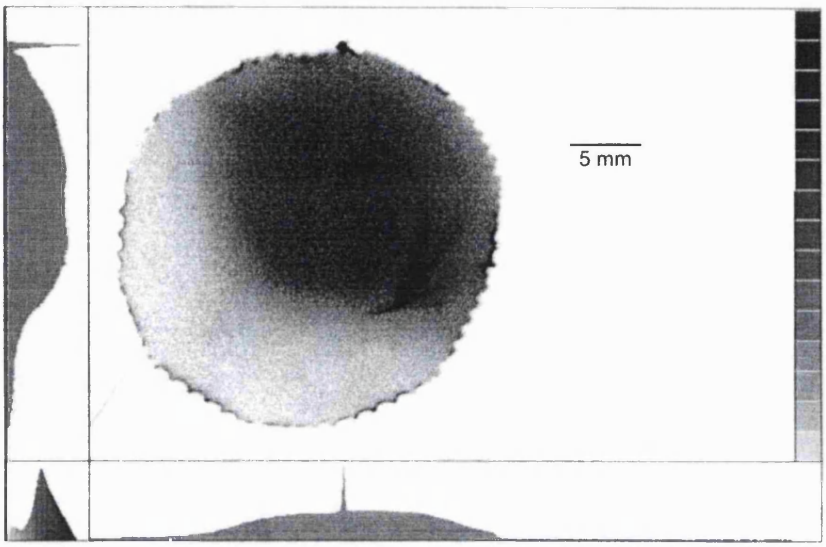

Figure 4-17. Modulation disappears at low end-spoiling (0.5 diameters). The level of modulation was virtually non-existent at an MCP to WSA voltage of 280 V.

MCP - WSA gap dimension

In order to conservatively achieve image modulation-free operation, the detector geometry was modified so that this modulation-free performance was available over a range of MCP to WSA voltages. The MCP to WSA gap was increased from 4.85mm to 7.94mm and Figure 4-18 shows a flat field image taken with an MCP to WSA gap voltage to 600V.

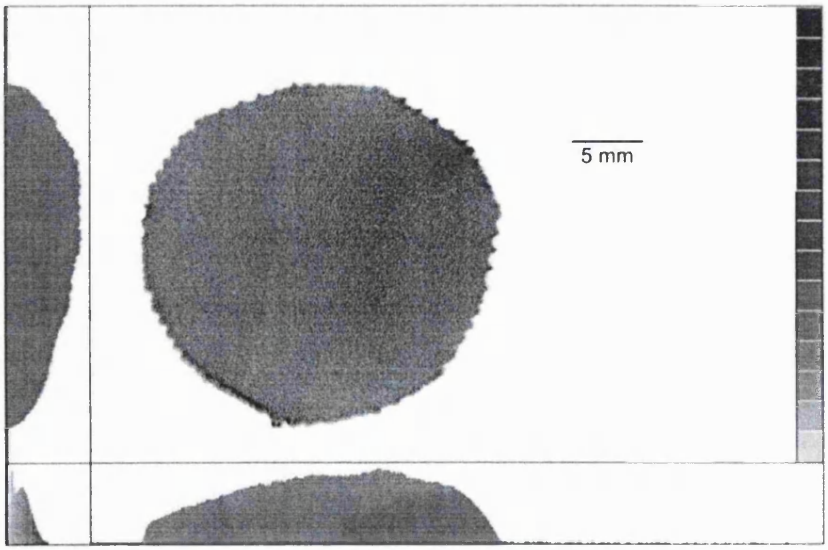

Figure 4-18. The absence of modulation in the final detector configuration.

WSA Position Resolution

The detector was fitted with a pinhole array mask consisting of 42μm diameter pinholes in a rectangular pattern with a spacing of 0.5 mm in both x and y axes to measure the position resolution and linearity. The illuminated area on the MCP from a single pinhole was calculated to be 64μm after broadening due to the collimation and diffraction. Due to practical limitations the mask could not be placed in contact with the MCP and light scattered in the gap caused a substantial but uniform background level. Figure 4-19 shows a central area of the image of 604k events at high magnification taken with an MCP to WSA voltage of 200 V, an MCP to WSA gap of 7.94 mm and a WSA pitch of 600 μm using 0.5 diameter MCP end-spoiling. Measurement of the 15 central pinhole images gave an average position resolution of 78 and 77 μm FWHM with a standard deviations of 3 and 3.2 μm in the x and y axes respectively. The mean gain of the MCP stack for this data was 1.8 x 10^7 electrons. The results were in good agreement with the predicted overall resolution of 75 μm FWHM, calculated from the quadratic sum of the electronic noise, partition noise and effective pinhole size, which were 34 μm, 21 μm, and 64 μm respectively. This large size of the mask pinhole component in this calculation however, makes the determination of the intrinsic detector resolution, in this case 40 μm FWHM, subject to a large degree of uncertainty.

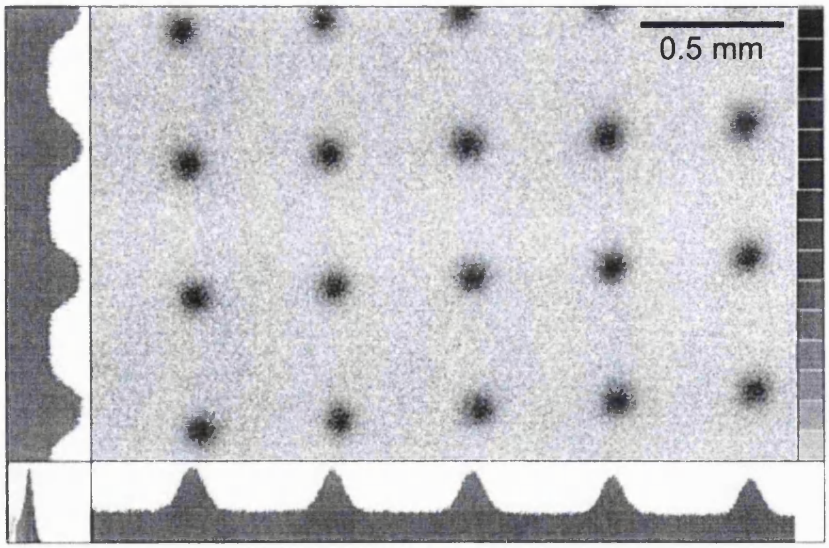

Figure 4-19. A pinhole mask image indicating resolution of 77 μm FWHM.

WSA Position Linearity

The pinhole mask used for the resolution experiments was also used to assess detector linearity at MCP to WSA voltages of 200, 400, 600 and 800 V. Each dataset contained one million events and the detector operating configuration was unchanged. Figure 4-20 shows an image of the entire detector illuminated through the pinhole mask, used to determine the image linearity.

The main features of the images could be summarized as follows :-

1. The image scale diminished with increasing MCP to WSA voltage. This was thought to be a result of the geometry of the lower MCP contact. The degree of deflection imposed on the MCP output electrons by the radial field distortion produced by the MCP contact being dependent on the absolute field strength between MCP and anode.

2. At low MCP to WSA voltages the pinholes near the MCP perimeter were smeared radially. This was attributed to either, a) the differing effect of the radial field distortion at low field strength on events with different pulse heights and thus different mean electron energies [134], or, b) distortions due to pulse height related variation in the charge cloud footprint. This would cause the footprint to fall off the edge of the pattern, to greater or lesser extent depending on the event pulse height, resulting in a corresponding pulse height dependent centroid error. The effect would be accentuated because of the enlarged footprint at low field strength.

3. The image linearity progressively developed an elongation towards the +x;+y direction with increasing MCP to WSA voltage. This nonlinearity was seen with the first sealed tube device and has been identified with other WSAs using the same pattern.

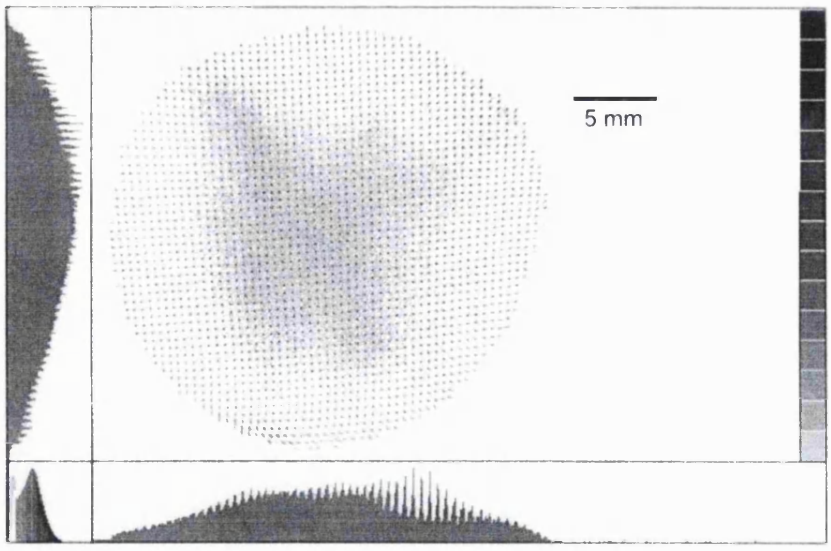

Figure 4-20. A pinhole mask showing the WSA linearity. This data was taken at an MCP to WSA voltage of 400 V.

A series of experiments were undertaken in parallel to investigate causes of non-linearity in MCP detectors using charge division readouts (described in the following chapter). At the time of this work, one cause was thought to be charge redistribution after the arrival of the electron cloud on the anode, due to the emission of secondary electrons. These electrons have a much lower energy (typically 0-20 eV) than the primary electrons, and are more influenced by local electric field distortions such as electrode differential voltage. They could also be sensitive to transient electrode voltage differentials, if present, during the pulse arrival. Two patterns were constructed

using copper electrode material 150% thicker than standard, in order to reduce electrode resistance and lower potential transient voltages. The initial results were surprising. Figure 4-21 shows two pinhole mask images produced using readouts having the same pattern but 150% thicker copper. The WSA use for the left-hand data used a matt finish substrate, while WSA for the right-hand image was manufactured on a polished substrate. The linearity of both devices improved drastically after they had been cleaned using a light plasma etch.

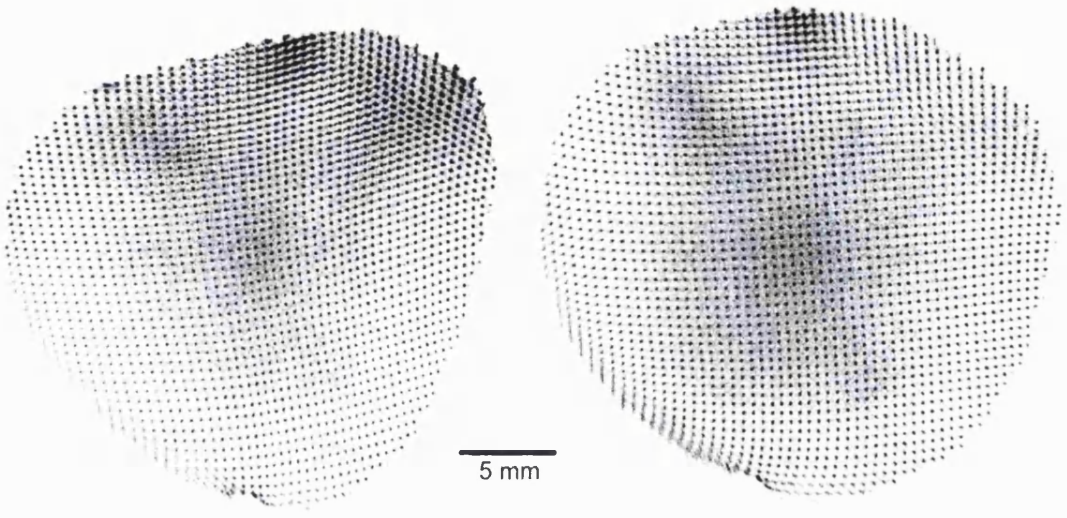

Figure 4-21. Highly distorted pinhole mask images caused by surface effects. These WSAs were manufactured on different substrates with thicker conductor.

The gross distortions present before cleaning were completely unexpected and were postulated to arise from the increased heating effect, and electrode and substrate disruption, during the laser machining of the thicker copper. The recovery after cleaning showed that this type of device was highly sensitive to its surface properties.

The MCP to WSA distance was reduced from 7.94 to 5.84mm to minimize radial nonlinearity caused by field non-uniformities near the perimeter of the field of view. This was felt to be an acceptable compromise with regard to the onset of image modulation, owing to the large contingency built into the original 7.94mm MCP to WSA dimension. This was borne out by datasets at MCP to WSA voltages of 160, 200, 300, 400, 600, 800 and 1000V which were taken with the finalised WSA pattern construction and detector geometry. Image modulation was apparent only at the last two voltage levels.

Rate Dependent Position shift

It was already known that WSAs could exhibit rate dependent position shifts [135] which depended on the resistance of the electrode DC bias resistors. The cause of this position shift is due to secondary electron mediated charge redistribution, driven by inter-electrode voltages generated by the mean signal current in the bias resistors.

In order to measure this effect, it was accentuated by increasing the bias resistors to the nominal 100MΩ of the preamplifiers, as supplied. The rest of the imaging data had taken with 15MΩ bias resistors on both wedge and strip channels, and 7.5MΩ on the Z channel to minimize the position shift.

Figure 4-22 shows the position shift of the pinhole array image, referenced to the position at a count rate of 200Hz, both at the centre, and high *x*, high *y* corner of the image. At low rates the shift varies approximately linearly with count rate but the effect saturates at higher rates (as can be seen by the distance from the origin of the 8kHz point compared to the others). The scale of offset was also seen to be larger at the centre than the edge of the readout. N.B this data represented the worst case due to the large value of the bias resistors used to accentuate the effect.

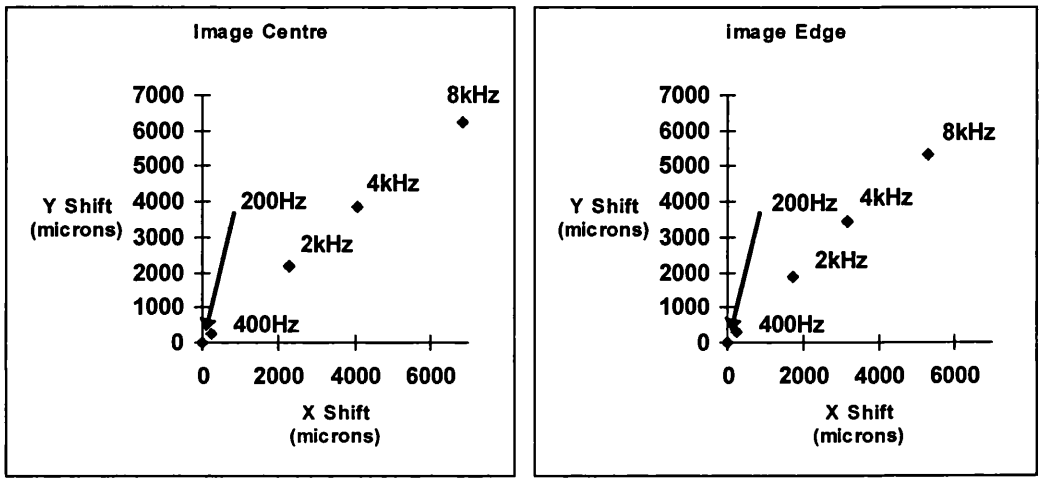

Figure 4-22. WSA image shift versus count rate for the centre and edge of the FOV.

MCP to WSA Voltage Dependent Position Shift

The position shift caused by variation of the MCP to WSA voltage was also characterized using the pinhole mask data. Figure 4-23 shows two plots of the position shift as a function of MCP to WSA voltage referenced to the position at 800V for the centre and edge of the detector field of view. In this case, the form of the curve was similar between centre and edge, but the scales were drastically different. This was due to the diminishing image scale as MCP to WSA voltage was increased.

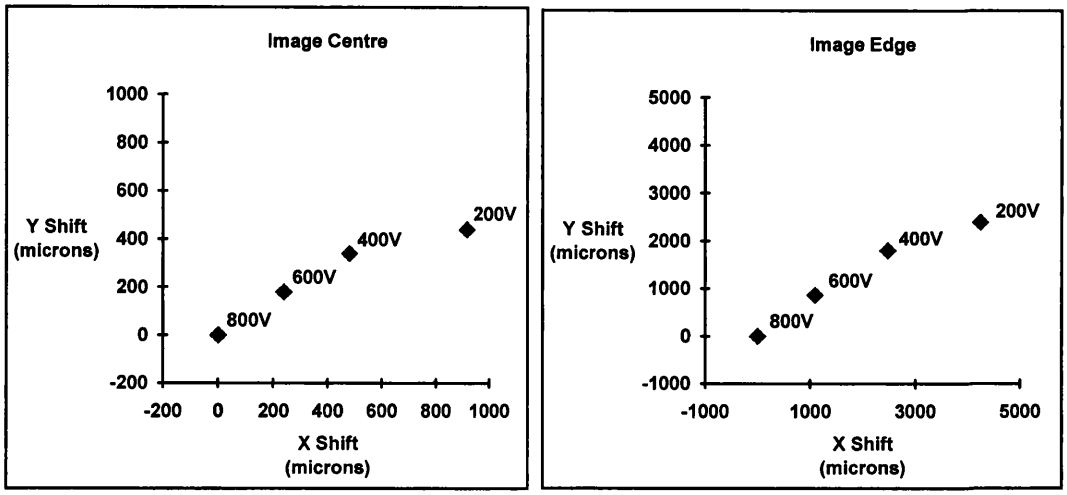

Figure 4-23. WSA image shift vs. MCP to WSA voltage at the centre and edge of the FOV.

Image Scale - Dependence on MCP-WSA voltage

The variation of image scale with MCP to WSA voltage, as discussed earlier, is presented graphically in Figure 4-24. The data was taken from the same images used for the voltage dependent shift measurements.

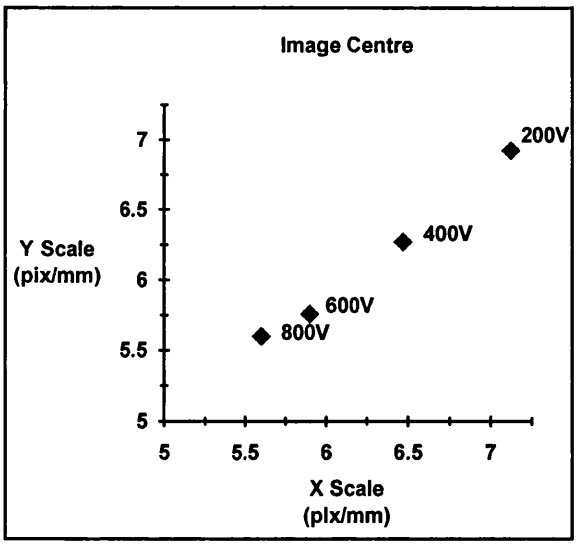

Figure 4-24. The variation of image scale with MCP to WSA voltage.

Image Stability with Time

Image data using the pinhole mask was taken 20 days apart using identical detector configurations and illumination. The pinholes in the centre of the image did not move position but an image scale change took place displacing pinhole position at the edge by 0.5mm radially inwards. All detector parameters were identical apart from the MCP gain, which had dropped by 16% between the two measurements. The cause of the scale change was not identified at the time but is suggestive of the output electron energy being reduced.

Effect of MCP output coupling to ground

One concern was that changes in the electrical coupling between the rear MCP electrode and ground could influence the imaging behaviour due to induced signal on the WSA. Two datasets were taken under identical conditions apart from a change to the capacitive coupling to ground from the output face of the MCP. The usual 6nF capacitor coupling the MCP to ground was removed for the second data set, leaving only stray capacitance of <100pF. Comparison of the images showed no discernable difference for this particular detector geometry.

MCP and WSA Relative Pulse Amplitude and Distribution

Some detector configurations use the pulse from the rear MCP contact to provide information for purposes such as event timing or windowing, etc. A charge sensitive preamplifier was attached to the MCP output electrode and the combined anode electrodes to determine the correspondence between this signal and the sum signal from the WSA electrodes. Analysis of the shaped signals showed that the MCP and WSA charge levels were not proportional.

Figure 4-25 shows the MCP and WSA pulse height distributions respectively. The mean MCP signal was measured to have an amplitude of 32% of the mean of the sum of WSA signals, and the pulse height distributions were significantly different in shape.

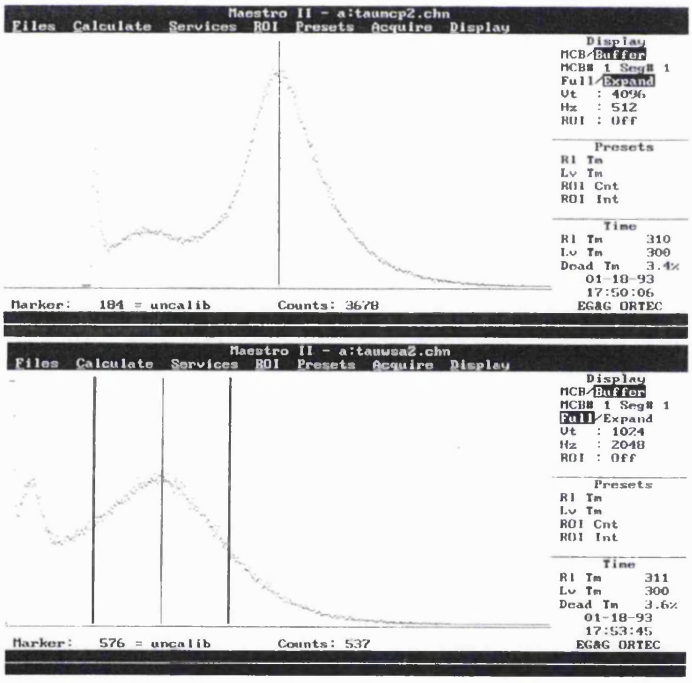

Figure 4-25. The pulse height distribution from the MCP (top) and WSA (bottom). The horizontal scales are different. The relative amplitudes are given by the marker positions of 184 & 576 respectively.

Results using a secondary electron control grid

The breadboard detector was reconfigured with a conductive grid interposed between the MCP and anode. The grid was made of electroformed Nickel having a ~60 % open area ratio and a pitch of 17 μm. A spacing between grid and anode of 900 μm was used. With the anode at a high

positive voltage with respect to the grid, ~60 % of primary electrons pass through the grid while the remainder collide with the grid and can produce secondary electrons, some of which may reach the anode. A high field between the grid and anode was used to suppress the range of anode secondary electrons, which owing to their relatively low energies, could be well controlled.

Figure 4-26 shows an image of a 0.5 mm × 0.5 mm pitch pinhole mask and a graph of its linearity respectively. The image was taken with the grid at -200V with respect to the anode. In this regime, the non-linearity of the WSA was dramatically reduced, except near the pattern perimeter due to MCP and readout edge effects.

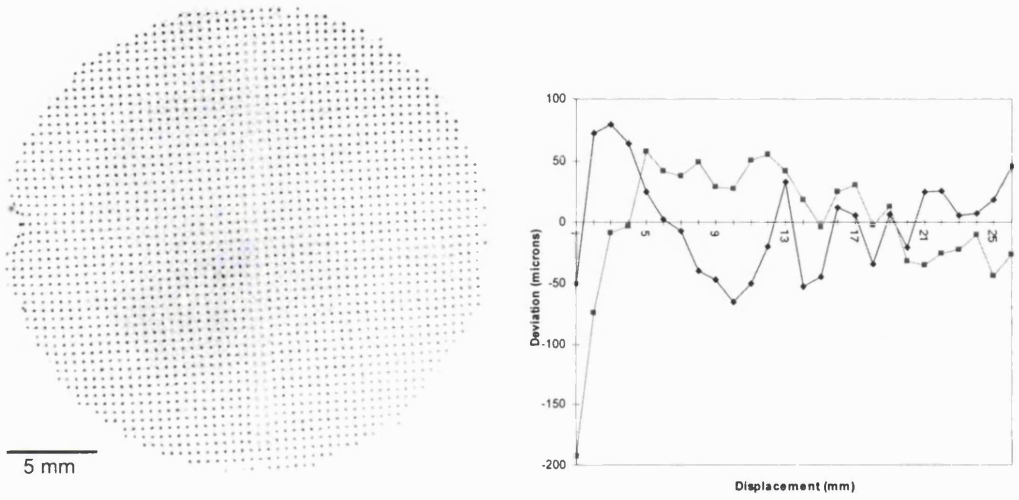

Figure 4-26. Data showing the improved linearity gained using an electron control grid.

The spatial resolution of the breadboard WSA detector with the secondary electron grid is shown in Figure 4-27. The detector was illuminated via a resolution test mask with UV light from a low pressure mercury discharge lamp. The six smallest test patterns are 15.8, 13.0, 11.2, 8.1, 6.3 and 5.0 line pairs per millimetre (lp/mm) respectively. The detector resolution was measured at ~70 μ m FWHM. Some residual modulation is present in this image which can be seen in the *y* histogram which can be removed by modifying detector configuration as described previously.

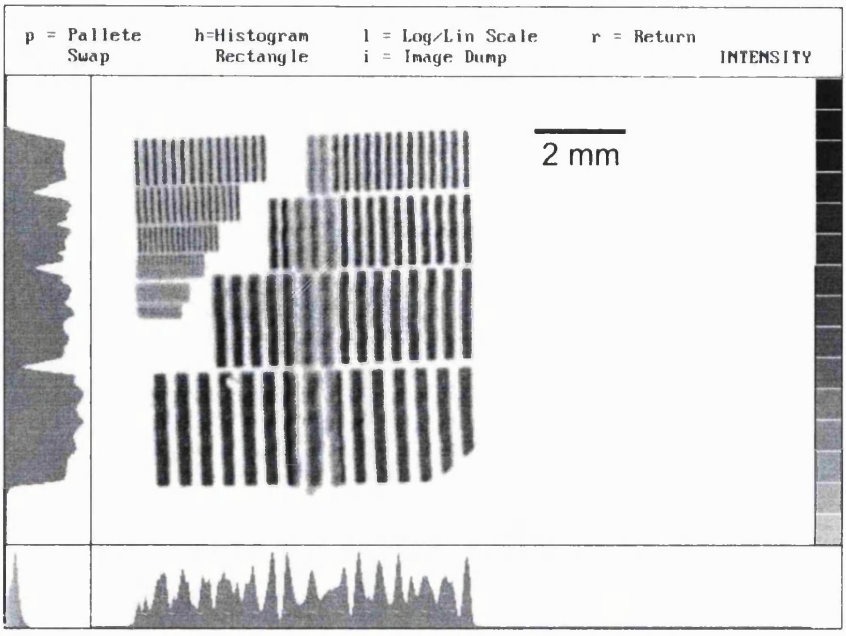

Figure 4-27. A bar mask taken with the WSA detector with a control grid.

The MCPs in this detector were well used. The detector had been illuminated for a long period through a slit placed in a vertical orientation for another experiment. This had scrubbed these areas of the MCPs and reduced their gain. The degraded resolution in this area shown by the WSA at reduced gain is particularly noticeable in Figure 4-26 and Figure 4-27.

Chapter 5

Investigations into Physical Processes and New Techniques

This chapter is divided into four sections, the first two of which describe experiments undertaken to characterize detector parameters and physical processes which influence the performance of detectors using charge division anodes, the remaining two describing techniques to overcome some of the limitations of existing devices and improve performance.

The first section describes a technique to experimentally measure the distribution of the charge footprint collected by a charge division readout device. In section 2, the effects produced by secondary electrons emitted from the readout are investigated and a scheme to mitigate them discussed. Section 3 introduces a novel, computationally economic technique to simulate the operation of a charge division readout pattern using a realistic charge distribution and practical pattern design. The image charge technique described in section 4 overcomes several limitations of the charge division devices previously discussed. It functions by inducing the event charge on to the readout device, thus avoiding the problems associated with direct charge collection and also offers several operational advantages.

5.1 Measurement of Radial Charge Distribution

Various types of position readout are used in conjunction with MCPs in imaging, photon-counting detectors [93][76][136][60]. Each of them requires a particular size and shape of electron cloud to achieve optimum imaging performance. This section describes an experimental technique [137] which was developed to measure the spatial distribution of the charge cloud footprint from the MCP collected on a planar, charge division anode.

The split-strip anode, developed during this research work, was designed specifically for the purpose of measuring the spatial distribution of the charge cloud from an MCP stack as it is collected by the anode (see Figure 5-1). It employs the geometric charge division technique with four electrodes to encode two charge cloud parameters, allowing event position and charge cloud dissection to be determined simultaneously. The two event parameter decoding algorithms

perform a measurement of the position of the charge centroid (in one-dimension) together with a measurement of the fractional charge falling to one side of the split, the central divide in the pattern. These measurements are carried out on the charge cloud from every event. A data set combining the measurements from several thousand events can be used to calculate the average spatial distribution of the electron cloud.

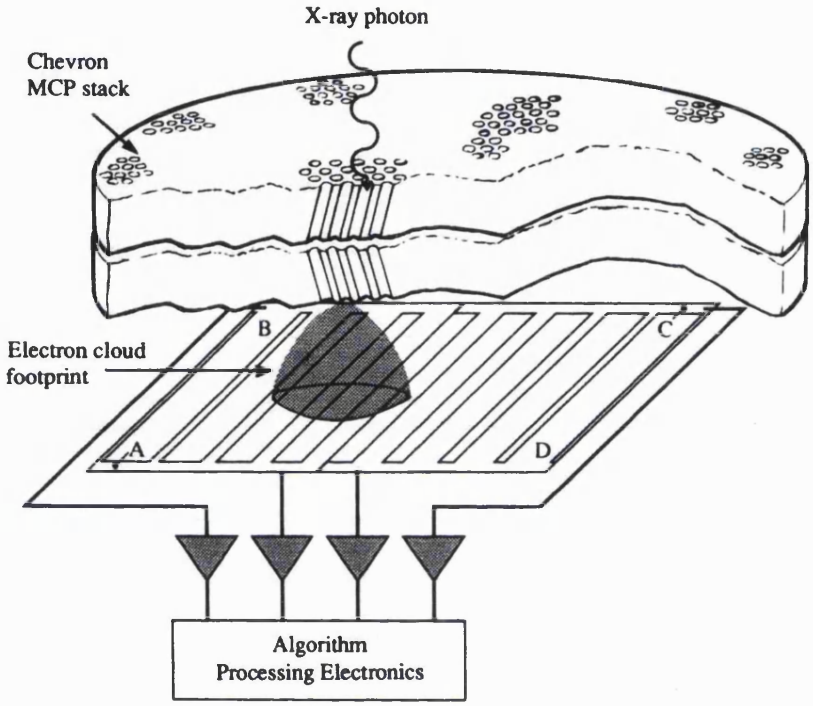

Figure 5-1. A schematic of the split-strip anode. In this instance it is being used to measure the charge footprint distribution from a chevron MCP stack [113].

The split-strip spatial charge measurement technique is applicable to situations where :-

1. the existing anode is planar and can be replaced with a Split-Strip Anode without altering the charge collection environment.
2. the repeat pitch of the Split-Strip Anode can be made fine enough such that image modulation, caused by too small a charge cloud, does not result. In practice, this is not a problem since, if the charge cloud to be measured is small, then the anode itself can be smaller.

5.1.1 Split-strip operation

The Split-Strip Anode consists of four isolated electrodes. The electrodes are paired in two ways to produce two charge division configurations. With the A+D and B+C electrodes summed, the combined electrodes resemble two interlocking strips with linearly varying widths, the discretely sampled analogue of the Backgammon or wedge-wedge anode. This allows determination of the charge centroid position, *cp*, using the following algorithm :-

$$(5\text{-}1)\quad cp = \frac{Q_A + Q_D}{Q_A + Q_B + Q_C + Q_D}$$

With the electrodes paired as A+B and C+D, a similar algorithm decodes the fraction of the total charge collected on one side of the split or divide in the pattern which separates electrodes A and B from C and D.

The fractional charge, *fc*, is given by

$$(5\text{-}2)\quad fc = \frac{Q_C + Q_D}{Q_A + Q_B + Q_C + Q_D}$$

If a simple distribution consisting of a disc of charge is considered, as long as the disc is large enough to avoid position modulation effects, it will behave as follows :-

1. When the disc centroid is to the left of the split and none of it overlapping electrodes C and D, the fractional charge will be zero.
2. As the centroid moves to the right and the disc crosses the split, the charge collected on C and D will rise from zero, the rate of increase of charge on C and D increasing to a maximum at the point where C+D = A+B. At this point both *cp* and *fc* will be equal to 0.5 owing to the charge cloud symmetry.
3. As the centroid moves further right, the fractional charge, *fc*, will increase beyond 0.5, but the rate of increase of *fc* will again reduce.
4. The fractional charge will reach unity once the disc no longer overlaps the split.

When the event centroid positions, *cp* (*x* axis) are plotted against the fractional charges, *fc* (*y* axis) the characteristic split-strip data is produced, known as the S-curve. If the distribution has mirror symmetry about the *fc* axis, the S-curve will be symmetric about its centre, at [0.5,0.5]. Since each event supplies only one data coordinate on the S-curve, and the whole S-curve dataset is required to calculate the charge distribution, the S-curve data represents an average charge distribution. However, the width of the S-curve, i.e. the distribution of *fc* values for a given *cp*, is itself a measure of the variation in the charge distribution from event to event. In general this width is small, implying that variation in the distribution is correspondingly small.

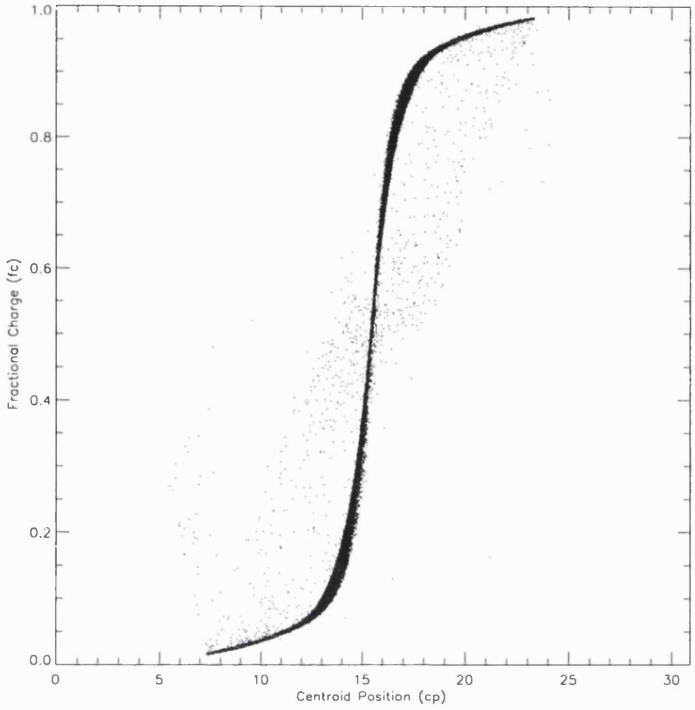

Figure 5-2. The characteristic form of the data from Split-strip anode, known as the S-curve.

The MCP geometry leads to the expectation that the charge cloud to be azimuthally symmetric. This symmetry can be investigated by comparing data taken with various MCP chevron plane orientations, all other detector parameters being the same. The differential of the S-curve shown in Figure 5-2 directly gives a one-dimensional distribution corresponding to the charge cloud integrated over the axis parallel to the split. It has been shown by Edgar [138] that these data sets verify the azimuthal symmetry assumption, to first order, allowing the distribution to be modelled using a radial function.

The analysis method described by Edgar [138] follows from this symmetry. Trial radial functions are transformed into basis functions in the S-curve domain where their success is determined by a least squares fit to the experimental data. The reduced χ^2 of the fit is used to determine the most successful radial scale length parameters for a given set of basis functions, using an iterative procedure. Edgar found that the charge cloud has a radial distribution which, in general, can be expressed as the sum of two exponentials.

5.1.2 Instrument Design

The initial spilt-strip device was manufactured in 1/8 oz. copper on a 12.5 μm Kapton substrate to reduce interelectrode capacitance and electronic noise. This was required to enable small pitch patterns to be used so that modulation could be avoided even for narrow charge cloud distributions. The pattern was constructed using conventional photolithographic techniques and

wet chemical etching. Results were obtained with two patterns, 27 × 27 mm^2 with a pitch of 630 μm, and 13 × 13 mm^2 with a pitch of 315 μm, used in an MCP detector with MCP-anode gaps of the 6.2mm and 3mm respectively.

The MCPs and anode were assembled in a demountable stack manufactured in stainless steel and ceramic. Geometry changes were carried out by replacement of ceramic spacers without disturbance of the MCP chevron alignment. The MCP chevron alignment itself was accurate to ±10° with respect to the anode strip (or position) axis. The detector was mounted in a large vacuum chamber and stimulated with *Al-K* X-rays (~1.5 keV) from a collimated source.

The charge clouds measured were produced by a pair of 36mm diameter, 80:1 *L/d* ratio MCPs in a chevron configuration. The MCPs each had a bias angle of 13° and pore diameter of 12.5 μm with an end-spoiling of half a pore diameter. The two MCPs were separated, in one case, by a 50 μm conductive shim, and secondly, by an insulating spacer 80 μm thick. The latter allowed us to examine the effect on the charge distribution of interplate accelerating or retarding voltages. For these experiments, the Split-Strip Anode was placed at two different distances from the MCPs, 6.2mm and 3mm.

The MCP stack was illuminated via a slot mask designed to exclude all but background events from non-active regions of the pattern. Both the mask and the front of the stack were held at high negative voltage with respect to ground. A resistive divider in conjunction with two high voltage supplies was used to vary the overall voltage across the stack. The interplate voltage was controlled by a potentiometer within the divider chain. The anode electrodes were held at ground potential.

The charge collected on each electrode was measured using four identical electronic channels. A charge sensitive preamplifier was attached to each electrode and its output amplified and filtered using quasi-gaussian, unipolar shaping amplifiers. A peak detecting ADC was used to digitize the pulse amplitude and a PC used to record the four digital data words from each event and perform the data decoding. A software routine is used to vertically slice the data and calculate a mean *fc* coordinate corresponding to a given *cp* coordinate.

5.1.3 Data Reduction Techniques

5.1.3.1 Method 1

Edgar et al. [138] showed that the spatial charge cloud distribution is azimuthally symmetric to a first order approximation and could be reasonably represented by a radial distribution, *N(r)*. The S-curve, *S(cp)*, (i.e. fractional charge as a function of centroid position), generated by such a distribution is given by

$$(5\text{-}3)\quad S(cp)=\frac{2\pi\int_0^{cp} rN(r)dr+2\int_{cp}^{r_{limit}}\left[\pi-ar\cos\left(\frac{cp}{r}\right)\right]rN(r)dr}{2\pi\int_0^{r_{limit}} rN(r)dr}$$

where r_{limit} is the radius containing all of the charge. In the analysis, this radius is taken to be the width of the anode.

The radial charge distribution was modelled as the sum of n terms

$$(5\text{-}4)\quad N(r)=a_1N_1(r)+a_2N_2(r)+\ldots+a_nN_n(r)$$

where $a_1,a_2,\ldots,a_n$, are the weights of the components which make up the radial charge distribution. Substitution of Equation (5-4) into Equation (5-3) yields

$$\begin{aligned}S(cp)=\;&a_1\left\{\frac{2\pi\int_0^{cp} rN_1(r)dr+2\int_{cp}^{r_{limit}}\left[\pi-ar\cos\left(\frac{cp}{r}\right)\right]rN_1(r)dr}{a_1 2\pi\int_0^{r_{limit}} rN_1(r)dr+a_2 2\pi\int_0^{r_{limit}} rN_2(r)dr+\ldots+a_n 2\pi\int_0^{r_{limit}} rN_n(r)dr}\right\}\\(5\text{-}5)\quad&+a_2\left\{\frac{2\pi\int_0^{cp} rN_2(r)dr+2\int_{cp}^{r_{limit}}\left[\pi-ar\cos\left(\frac{cp}{r}\right)\right]rN_2(r)dr}{a_1 2\pi\int_0^{r_{limit}} rN_1(r)dr+a_2 2\pi\int_0^{r_{limit}} rN_2(r)dr+\ldots+a_n 2\pi\int_0^{r_{limit}} rN_n(r)dr}\right\}\\&+\ldots+a_n\left\{\frac{2\pi\int_0^{cp} rN_n(r)dr+2\int_{cp}^{r_{limit}}\left[\pi-ar\cos\left(\frac{cp}{r}\right)\right]rN_n(r)dr}{a_1 2\pi\int_0^{r_{limit}} rN_1(r)dr+a_2 2\pi\int_0^{r_{limit}} rN_2(r)dr+\ldots+a_n 2\pi\int_0^{r_{limit}} rN_n(r)dr}\right\}\end{aligned}$$

For an exponential term, the radial charge distribution which satisfies the required normalization condition is of the form

$$(5\text{-}6)\quad N_{\exp}(r,r_0)=\frac{1}{2\pi r_0^{\,2}}e^{-\frac{r}{r_0}}$$

or for a gaussian it is

$$(5\text{-}7)\quad N_{gau}(r,\sigma)=\frac{1}{2\pi\sigma^2}e^{-\left(\frac{r}{\sigma}\right)^2}$$

Only two exponential terms were used, as this was found to provide a good description of the radial distribution. The general form of the radial charge distribution was given by

$$(5\text{-}8)\quad N(r)=\frac{a_c}{2\pi r_{0c}^{\,2}}e^{-\frac{r}{r_{0c}}}+\frac{a_w}{2\pi r_{0w}^{\,2}}e^{-\frac{r}{r_{0w}}}$$

where a_c is the weight in the centre component, a_w is the weight in the outer or wing component, $a_w = 1 - a_c$, and r_{0c} and r_{0w} are the corresponding component scale lengths. For any given pair of values for r_{0c} and r_{0w}, the weights and the χ^2 of the fit were evaluated. The values of the scale parameters r_{0c} and r_{0w} were varied in an iterative procedure to find the pair of values that corresponded to the global minimum of the χ^2 surface.

The iterative procedure was also used to determine the value of the centre channel that, combined with the pair of scale parameters, produced the minimum χ^2. The centre channel corresponds to the point about which the basis functions were all symmetric. This symmetry arises from the original assumption of the azimuthal symmetry of the charge cloud.

Originally a manual search through three dimensions was carried out. This was a very long and tedious process but it demonstrated that the χ^2 surface was smooth and continuous, without localized minima. An automated search algorithm was later developed and used, though even using this the procedure took several hours of CPU time to complete.

Measured spatial resolutions

The spatial distribution of the MCP output electron cloud was measured in several operating regimes, and in most cases was best modelled by a radial charge distribution consisting of two exponential terms.

Data sets were taken over a variety of detector operating conditions. The parameters varied were as follows :-

1. The overall MCP operating voltage was set at 2.65 kV, 2.80 kV, 2.90 kV and 3.00 kV. These voltages correspond to gains of 0.6×10^7 e^-, 1.4×10^7 e^-, 4.8×10^7 e^- and 1.1×10^8 e^- respectively. The gains increase by approximately 30-40 % between anode voltages of 100 V and 800 V.
2. The interplate voltage (i.e. that across the 80 μm gap between the two MCPs) was varied from +30V to -30V. Note that the measurements taken with the MCP-anode gap of 6.2mm were with an interplate gap of 50 μm and zero interplate voltage.
3. The accelerating voltage between the MCPs and Split-Strip Anode was varied from 50V to 800 V.
4. The MCP-Anode spacing was alterable. Data was taken with spacings of 3.0 mm and 6.2 mm.

A sample of some of this data is shown in Figure 5-3; plots of the r_{0c}, r_{0w} and a_c parameters as a function of varying MCP interplate voltage. The MCP voltage was kept constant at 3.0 kV and the MCP-Anode gap voltage was 400 V. A plot of modal gain versus interplate voltage is also shown in this figure. In the central portion of the plot, near 0 V, the variation of size of the central component corresponds closely with the variation in the modal gain. This suggests that the gain is

the factor driving the size of the charge cloud. The variations of r_{0w} and a_c have a similar form to that of r_{0c} but they are offset by approximately 5 V. This may be due to a difference in the properties of the populations of electrons that make up the central and wing components of the distribution (i.e. the energy and angular distributions at the microchannel pore exit). Space charge effect, causing expansion of the charge cloud, provides a likely explanation for the correlation between modal gain and charge cloud size.

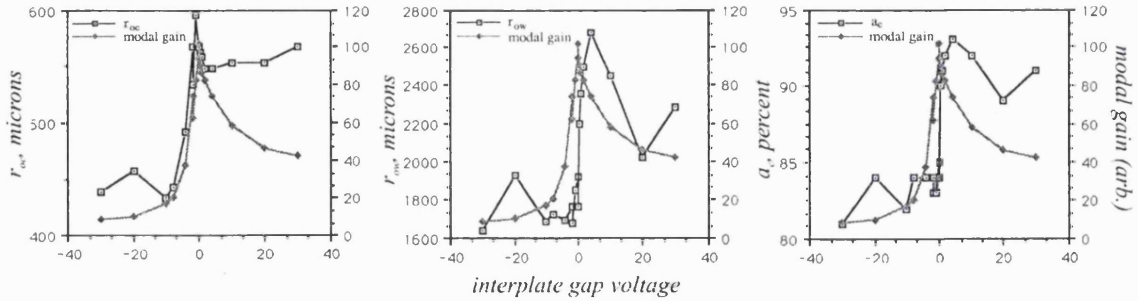

Figure 5-3. Variation of the radial distribution fit parameters with MCP inter-plate voltage.

5.1.3.2 Method 2

The split-strip experiment was revisited to analyze the charge footprint distribution and its temporal variation when induced on to a WSA readout, using the image charge technique described in section 5.4. In this instance, an accurate, numerical description of the radial distribution was required, as opposed to the previous solution, which had provided the best fit parameters of a limited number of simple mathematical terms, such as exponential or gaussian distributions.

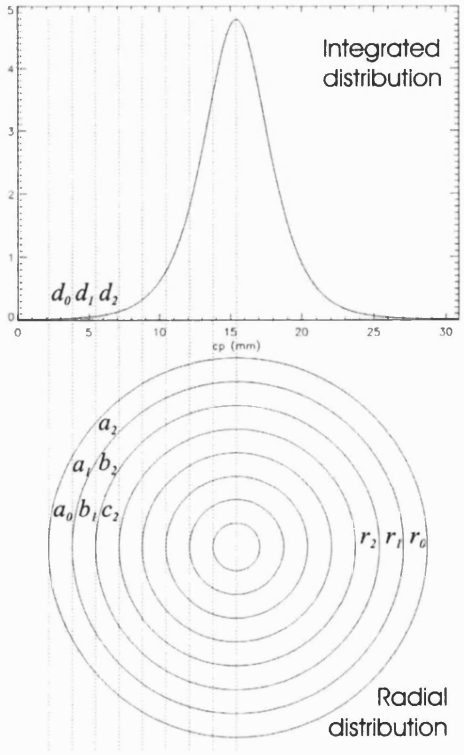

Figure 5-4. The calculation of the radial distribution from the integrated distribution.

Figure 5-4 shows smoothed, integrated distribution obtained directly from the differentiated S-curve, This particular data was obtained in collected charge mode using an intermediate grid with an MCP to grid voltage of 100 V and a grid to anode voltage of 10 V. It can be seen from Figure 5-4 that the outermost radial charge density value, r_0, can, in principle, be determined by the value of the outermost bin, d_0, of the integrated distribution, given by $d_0 = a_0 r_0$, where a_0 is the area of the annular element at r_0 subtended by the bin, d_0. The full set of simultaneous equations which can be solved to determine the radial distribution are given by :-

$$(5\text{-}9)\quad d_0 = a_0 r_0,\ d_1 = a_1 r_0 + b_1 r_1,\ d_2 = a_2 r_0 + b_2 r_1 + c_2 r_2,\ \ldots$$

This leads to a description of the S-curve data given by :-

$$(5\text{-}10)\quad fc_0 = a_0 r_0,\ fc_1 = (a_0 + a_1) r_0 + b_1 r_1,\ fc_2 = (a_0 + a_1 + a_2) r_0 + (b_1 + b_2) r_1 + c_2 r_2,\ \ldots$$

Examination of Figure 5-4 shows that the contribution of the charge distribution at a radius, r_0, to the bin of the integrated distribution, d_i, and given by the series of weights $a_0, a_1, a_2, \ldots a_i$, decreases monotonically as the distance between d_i and the centre of the integrated distribution decreases. Given the presence of noise in the data, the improvement in the signal to noise ratio of the r_i th component in the set of simultaneous equations relating the S-curve to the radial distribution decreases from the outermost equation containing an r_i component, working inwards. The diminishing returns gained from using a larger set of equations to determine a value of r_i was used to justify the use of a method which solved a local subset of these simultaneous equations, beginning at the outermost radii and working inwards, to solve for r sequentially. An iterative method was used to solve for each pair of adjacent r values, by finding the best fit to the reduced S-curve data. The reduced S-curve data was determined by finding the optimum value of fc for each cp bin. Several methods were used, including centre of gravity, the position of the median, and position corresponding to the maximum value of the fc distribution for each cp bin. The latter method produced the most reliable results for the majority of S-curve data.

There were several problems with this initial method. Firstly, events near either end of the anode, where fc was close to zero or unity were not detected, owing to the electronics which used four independently triggered ADCs to digitize the event pulse levels and required a pulse height above the noise threshold on every channel for ADC conversion to take place. The effect this produced can be seen in Figure 5-2, where the S-curve does not quite reach the two asymptotes at $fc = 0$ and $fc = 1$.

The nature of the electronics also introduced an uncertainty into the values of fc at these asymptotes, since crosstalk, caused by the finite ratio of the pre-amplifier dynamic capacitance to the inter-electrode capacitance, prevents the measured fc every reaching zero or unity. However this could be measured electronically and taken into account.

On the subject of crosstalk and analogous effects, the split-strip anode, when used in charge collection mode, is also susceptible to charge redistribution. This equates to a physical crosstalk which is mediated by means of secondary electrons, and driven by inter-electrode voltages. Qualitatively it acts in similar manner to electronic crosstalk, moving the S-curve asymptotes closer together, but does not guarantee the linear scaling of the *fc* axis that occurs with electronic crosstalk. Significant nonlinear scaling of the *fc* axis would distort the radial distribution determination in an unpredictable fashion. Since the experiment was primarily performed to investigate charge distributions with the image charge technique (see section 5.4), charge redistribution was not of concern. Charge redistribution is discussed in the following section.

The lack of data at the crucial values of *fc* near the asymptotes, which determine the power in the wing component of the charge distribution, coupled with the uncertainty of exactly where the asymptotes should be, compromised the ability to fit successfully to the empirically measured S-curve. The solution found was to fit a suitable series of functions to the S-curve, which themselves corresponded physically realizable radial distributions (an arbitrary S-curve not does necessarily have a physical radial representation). A hyperbolic tangent proved a suitable function for this purpose, especially since much of the S-curve data could be well approximated using a small number of fit components.

The most suitable fitting function for the S-curve data with sufficient but not excessive degrees of freedom was found to be :-

$$(5\text{-}11)\quad F = A_4\left(A_5 \tanh\left(A_0\left(x - A_3\right)\right) + A_6 \tanh\left(A_1\left(x - A_3\right)\right) + \left(1 - A_5 - A_6\right)\tanh\left(A_2\left(x - A_3\right)\right)\right)$$

This function is defined for all x and reaches asymptotes at zero and unity as desired, but at an x value of ±infinity. This function cannot accurately represent a charge distribution of finite size. However, for this case, another solution was to define the asymptotic limits using a free parameter. The S-curve generated by the fit was truncated when it reached *fc* values of zero and unity. This method produced a discontinuity in the S-curve which resulted in some error in the calculated radial distribution at large radii. Figure 5-5 shows the difference between the two methods of fitting the radial distributions. The solid curve represents the calculated radial distribution obtained by forcing the fitted S-curve to asymptotes at 0 and 1, the dotted curve is the same with free asymptotes and the S-curve truncated. Both distributions show errors where there is a discontinuity, either as a result of the limit of the S-curve array (with the first method at 14.75 mm) or due to truncation (with the second method at 12 mm). For radii smaller than the S-curve discontinuities, they produced very similar results. The first method produced significantly smaller errors at the discontinuity and consequentially was used in preference.

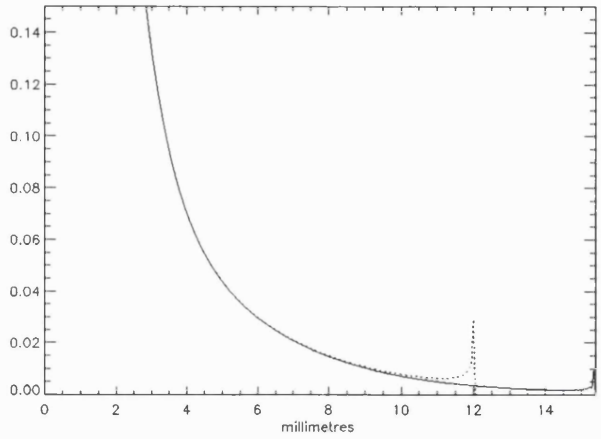

Figure 5-5. Differences between the two radial distribution calculation methods.

5.1.3.3 Results

This software technique was used to investigate the variation in the radial charge footprint with voltage for several detector configurations. Sanderson [154] measured the radial charge distributions for detectors using collected charge mode with and without an intermediate grid (described in sections 5.2.3 and 7.4.2.2). Figure 5-6 shows the calculated radial distributions obtained using a variety of detector configurations, with and without an intermediate secondary electron control grid.

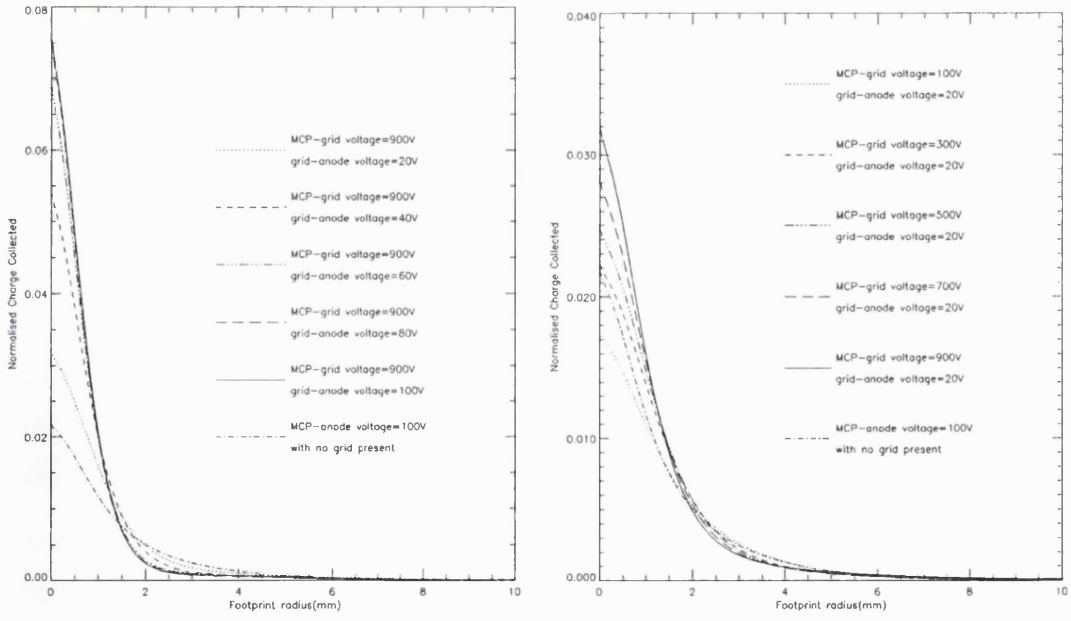

Figure 5-6. The radial charge distributions for a variety of detector configurations [154].

The split-strip anode was instrumental in demonstrating and characterizing the unexpectedly large charge footprint found in the particular operating regime, using a high MCP to grid voltage and low grid to anode voltage, as shown in Figure 7-26. This particular configuration was used to great effect to achieve MCP pore limited imaging with the Vernier anode (described in 7.4.2.2).

5.2 Secondary Electron Processes

Secondary electron emission plays a crucial role in the operation of position sensing anodes used in imaging MCP intensifiers. Secondary electrons emitted from the anode have the ability to influence both the size and shape of collected charge cloud distribution, and also to mediate charge redistribution between the anode electrodes. Charge redistribution, in particular, can significantly degrade the performance of position readouts using charge division.

This experiment was designed to study the secondary electron emission process from a charge division position readout using an intermediate grid between the MCP and anode to control the trajectories of the secondary electrons emitted from the anode. Configuration of the grid and anode voltages in several modes allowed a variety of physical processes occurring within the detector to be measured, including the secondary emission coefficients for both the anode and grid materials. The benefits of controlling secondary electrons were demonstrated by the improvement in imaging performance, particularly the linearity, obtained with the grid in place.

5.2.1 Introduction

The successful operation of geometric charge division readout devices relies on the division of the charge cloud produced, for example by an MCP intensifier, between several electrodes so that the electrode geometry accurately defines the charge division ratio. Since every point on the pattern corresponds to a unique ratio of electrode areas, the measured charge ratio from an event can be used to uniquely determine the event centroid position. Any mechanism which distorts this ratio will cause a corresponding position distortion.

The probability that secondary electrons played an important role in determining the imaging performance, particularly the linearity, had already been indicated by experiments using modified WSA readouts, as described in chapter 4. Figure 4-21 shows two images of a pinhole mask taken with an MCP-based WSA detector using identical configurations apart from small differences in the WSAs, which were manufactured on the same substrate material with different surface finishes. The left-hand image was obtained using a quartz readout substrate with a pattern surface ground using 1 μm diamond paste, whilst for the right-hand image, the substrate was optically polished.

It was difficult to conceive how the energetic primary electrons from the MCP would be affected by mechanical and chemical properties of the anode, unless severe substrate charge-up was occurring. It seemed much more plausible that the differences in surface finish, which is known to affect the secondary electron emission coefficient, energy spectrum and angular distribution [139], gave rise to the differences in image distortion by means of the effect on the production of secondary electrons. Surprisingly, the ground substrate which demonstrated the gross distortion was expected to produce a lower number of secondary electrons from both its electrode and insulator areas, since this surface quality generally reduces the secondary emission coefficient.

Possible non-uniformity in the surface finish, not present in the polished substrate, could have been to blame.

In an MCP detector, the primary electrons arrive at the anode with a mean energy of typically ~500 eV, the sum of their output energy and energy imparted from the field in the MCP to anode gap. The secondary electron emission coefficients of the majority of conductors also peak around this energy with a typical peak value of 0.75-1.5, the mean energy of the secondary electrons being a 0-20 eV [139]. Thus the cloud of high energy primary electrons colliding with the readout rapidly transforms into a cloud of secondary electrons of similar magnitude constrained by their low energy to remain in close proximity to the readout.

The very nature of geometric charge division readouts, being finely divided patterns of electrically isolated conductors, leads to the potential for secondary electrons to cause problems. Being comprised of isolated conductors, the opportunity for non-zero inter-electrode voltage exists. The situation is compounded by the charge sensitive pre-amplifiers generally used for accurate charge measurement, which require the impedance provided by the pattern to be as high as possible [107]. This requires that the DC bias of the pattern electrodes must be defined using high value resistors in order to keep the input impedance high and the electronic noise low. Since the event charge collected on the readout electrodes must be discharged through the DC bias resistors, the net result is that each bias resistor drops a voltage dependent on the size of the bias resistor and the mean value of the event current for the relevant electrode. In general terms, the centroid of the ensemble of events making up an image will define the mean electrode current ratio which determines the various inter-electrode voltages. For a WSA the inter-electrode voltages are only zero for the one specific image centroid location equivalent to $Q_W=Q_S=Q_Z$, assuming that the bias resistors are all of the same value and the MCP gain is not position dependent.

The finely-divided nature of the geometric charge division pattern, with all the electrodes folded together relatively closely with respect to the charge cloud size, allows a seemingly small spatial redistribution of charge, produced by electrons crossing an insulating gap of ~40 μm, to have considerable effect on the collected charge ratio.

5.2.2 WSA position shifts

Evidence of the role played by secondary electron emission is given by the effect of count rate dependent image drift seen with the WSA and measured in chapter 4. When the detector is illuminated, an offset voltage is developed on each electrode across its bias resistor, due to the current flow produced by events, as described above. These voltages are proportional to the electrode area ratios at the centroid of the image. For a uniform image with its centroid at the nominal WSA centre, $Q_Z = 2Q_W = 2Q_S$, the offset voltage results in the Z electrode becoming negative with respect to the W and S, causing any inter-electrode voltage driven charge

redistribution effect to diminish the Z charge in favour of the wedge and strip electrodes. The increase in charge on the wedge and strip electrodes results in a diagonal drift of the entire image, which can have a magnitude of several millimetres in each axis. At low rate the drift is approximately proportional to total event current, and thus overall count rate. Figure 4-22 shows the dramatic measured position shift for a WSA as a function of count rate when using 100 MΩ bias resistors. At a count rate of 8 k count s^{-1} and an MCP gain of 10^7, a differential voltage of 320 mV is produced between the Z and W,S electrodes. The gross position shift can be improved, but never completely eradicated, by lowering these resistances.

The effect could be explained in two ways :-

1. Firstly, it could be produced as the result of deflection of primary electrons (i.e. those produced by the MCPs) by the non-parallel field close to the anode. This does not require the physical charge centroid to be shifted, instead, charge is deflected from the more negative electrode(s). The resulting charge ratio produces an apparent position centroid shift. A simple ballistic model using the longitudinal field in the MCP to anode gap, and a transverse field defined by the inter-electrode voltage and spacing of the electrode centres assumed to be constant across the MCP to anode gap, shows that the transverse position shift of the electron is insufficient to produce the required image shift. In reality this model is highly conservative since the field distortion produced by the inter-electrode voltages is highly localised, and its magnitude will be greatly diminished at the MCP output.
2. The production of secondary electrons from primary electron impact on the anode offers a more plausible explanation of the apparent position shift. Their low energy (0-20 eV) makes them much more amenable to deflection by differential electrode voltages and their large number (the secondary emission coefficient is 0.75-1.5) makes them capable of producing significant charge redistribution and resulting image position shifts.

This charge redistribution effect is not limited to the WSA. It is exhibited by all charge division devices which directly collect electrons. Though it can be reduced by careful design, it will always be present at some level, causing rate and image dependent charge ratio distortion, which result in image instability and nonlinearity. The image charge technique described later provides an elegant method of avoiding these problems and offers other advantages.

5.2.3 Secondary electron control

The energy spectrum of secondary electrons [139] can be divided into three components: elastically scattered primary electrons, having the same energy as on collision, inelastically scattered primaries, produced over a wide range of lower energies, and true secondary electrons whose energies are typically less than 20 eV. The numbers of the latter, low energy, group of electrons predominate, so the majority of the secondary electron population can be controlled by

applying an electric field in a narrow region above the anode [141]. In an initial test to assess the extent to which secondaries affected imaging, a conductive, transparent grid was placed above and parallel to the anode, in close proximity to it. This enabled a large field to be generated above the anode, with the aim of suppressing the range of secondaries produced from it, and thus limiting their potential for redistributing charge among the electrodes. The empirical success of this technique is demonstrated by the image in Figure 4-26 showing the much improved linearity. This data was obtained with same detector format as Figure 4-20 but including the secondary suppression grid.

5.2.4 Experimental Technique

The detector used for this experiment consisted of a demountable detector body housing three 33 mm diameter MCPs having 8 μm pores, the uppermost with a 40:1 length to diameter ratio and separated from the lower two MCPs by a 50 μm conductive shim. The lower MCPs both had an 80:1 length to diameter ratio. The separation between the MCP and anode was 6.8 mm. A grid of electroformed nickel was placed 0.9 mm above the anode. The grid had a pitch of 17 μm, and an open area ratio of 60 %. The anode itself was a wedge and strip device manufactured in copper on a polished quartz substrate.

Four charge measurement electronic channels were used, one attached to the grid and the other three to the wedge, strip and Z electrodes of the readout anode. Anode images and pulse height distributions for both grid and anode were taken over a variety of operating conditions.

The MCP stack was operated at the same voltages throughout, producing a gain of 2×10^7 electrons with a saturated pulse height distribution. The MCP-grid voltage, V_{MCPg}, and the grid-anode voltage, V_{ga}, were used to define three distinct modes of operation, as follows :-

Mode 1: The voltages V_{MCPg} and V_{ga} established electron accelerating fields from the MCP to grid, and grid to anode respectively. Data was taken over voltage ranges of V_{MCPg} from 25 V to 800 V and V_{ga} from 0 V to 800V.

Mode 2: V_{MCPg} range was as mode 1. The V_{ga} voltage ranged from 0 V to $-V_{MCPg}$, such that electrons were accelerated away from the anode. The magnitude of V_{ga} does not exceed that of V_{MCPg}.

Mode 3: The V_{MCPg} range was as mode 1. The V_{ga} voltage ranged from $-V_{MCPg}$ to $-(V_{MCPg} + 150\ V)$.

5.2.5 Results

The data was analysed by measuring the percentage of the total event charge collected on the grid and anode. The typical form of the data, for a fixed accelerating voltage of 400 V between MCP and grid, is shown in Figure 5-7. The horizontal axis represents the grid to anode voltage, a

positive value indicating that the anode is positive with respect to the grid. The vertical axis is the negative charge collected on the grid and anode as a percentage of the total MCP output charge. Thus data points below the x axis represent a positive charge signal.

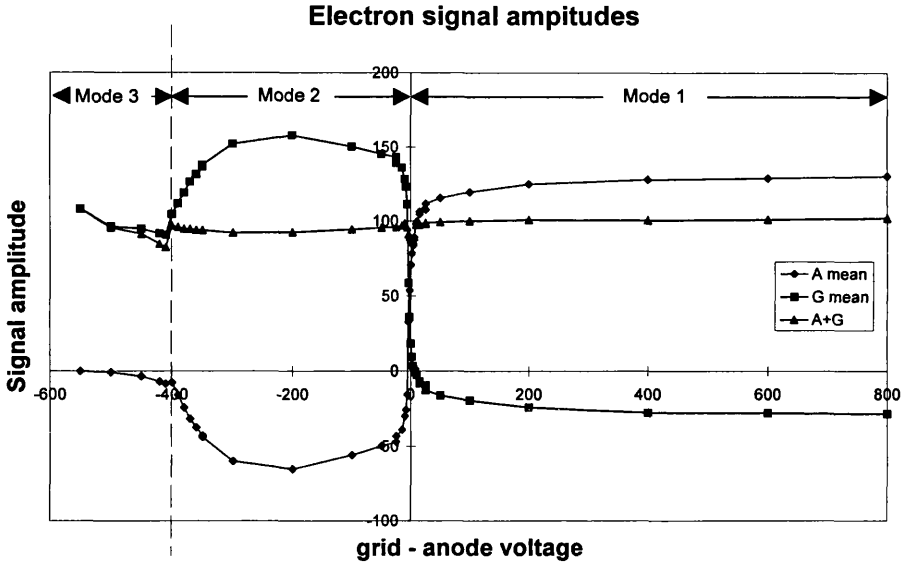

Figure 5-7. 1 of 10 data sets showing the grid, anode and summed signal amplitudes. This plot represents the magnitudes of the grid, anode and grid+anode signals over the entire range of V_{ga} for a fixed V_{MCPg} of 400 V.

The grid signal in mode 1 was always positive due to the secondary electron emission coefficient of the grid being greater than unity, and the sense of the anode field causing removal of the secondary electrons produced from the anode.

For each V_{MCPg} , the grid signal approached an asymptote with increasing V_{ga} because the energy of electrons colliding with the grid remains constant (equal to V_{MCPg}) and the efficiency of removal of secondary electrons from the grid increases asymptotically towards 100 % as V_{ga} is increased. The value of the asymptote was used to measure the secondary emission coefficient of the grid. The increased size of anode signal reflected the gain in charge resulting from the secondaries produced by the grid. The sum of grid and anode signals was constant as expected, being equal to 100 %, equivalent to the MCP output charge. The variation in the grid signal with V_{MCPg} showed that the secondary emission coefficient reached a maximum when the energy of the primary electrons was approximately 200 V.

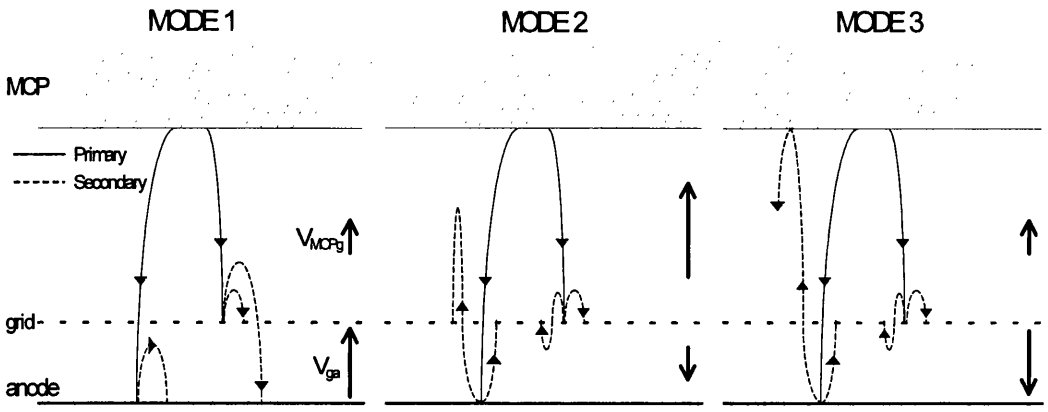

Figure 5-8. The simplified electron trajectories for mode 1, mode 2 and mode 3. This approximation ignores elastic and inelastically scattered primary electrons.

The reversal of the anode and grid signals does not quite coincide with the transition from mode 1 to mode 2. Instead, it occurs when V_{ga} is slightly negative. This may be due to either the leakage field from V_{MCPg} through the semi-transparent grid, or charge up the insulating gaps in the anode pattern which would be positive owing to the high secondary emission characteristic of insulators. Both effects would tend to cancel the small negative V_{ga} field and retain the electron signal on the anode.

In mode 2, the secondaries produced from the anode are collected by the grid. This reverses the signal polarities observed in mode 1. As the V_{ga} field increases negatively, the energy of electrons reaching the anode decreases and thus an asymptote is not seen since the emission coefficient varies with input energy. The magnitude of the positive anode signal decreases as V_{ga} approaches V_{MCPg} because the emission coefficient drops rapidly as input energy is reduced below 100V.

As mode 3 is reached, the positive anode signal at V_{ga} equal to $-V_{MCPg}$ results from the output energy distribution of the MCP. Electrons from the MCP have an initial energy over and above that gained or lost from the fields defined by V_{MCPg} and V_{ga} allowing them to reach the anode and produce secondaries which are removed by the grid, leaving a net positive charge. This feature allows the energy distribution of the MCP output to be measured by using the anode signal present for V_{ga} greater than $-V_{MCPg}$ in mode 3, as long as the secondary emission coefficient of the anode is known. The dip in both grid and grid + anode signals at $V_{ga} = -V_{MCPg}$ is due to electrons having enough energy to return to the MCP and be collected by the MCP back face. When V_{ga} becomes even more negative, these electrons can cause secondary emission from the back face of the MCP which is then collected by the grid resulting in a net increase in the grid + anode signal.

The measurements of secondary emission coefficients are compromised to some extent by the MCP energy distribution itself (since the primary electron energy is not single valued) and the fact that some electrons reaching the anode are secondaries produced from the grid. In addition it is assumed that all secondary electron energies are much less than V_{MCPg} or V_{ga} , ignoring the contribution of elastic and inelastically scattered primary electrons which constitute a minority,

~20-30% of the total. The simplifications to the allowed electron trajectories are shown graphically in Figure 5-8. These simplified trajectories are used to compute the secondary emission coefficients for each mode. The measured emission coefficients are shown in Figure 5-9.

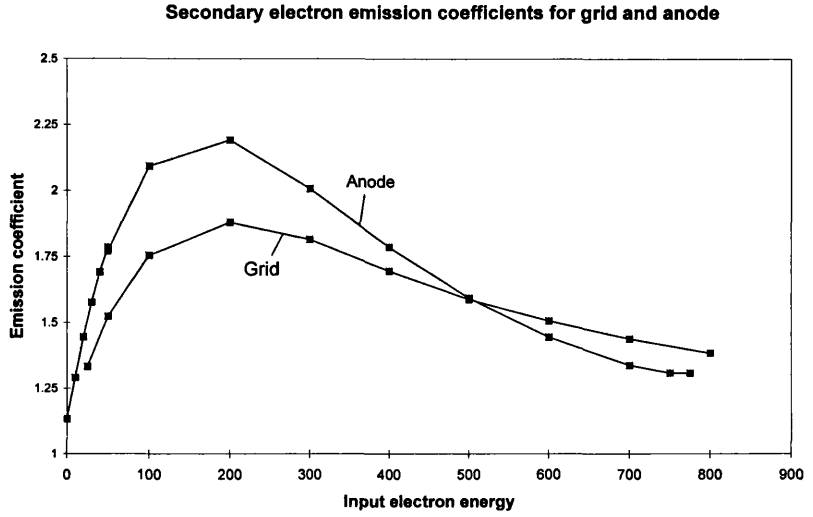

Figure 5-9. The calculated secondary emission coefficients of the grid and anode.

The experimentally measured secondary emission coefficients are larger than reported by other researchers for pure nickel and copper, the grid and anode materials [139]. Apart from the simplifications and approximations described above, there are a number of factors which could cause this :-

1. The grid cross-section has a complex geometry and the primary electron impact cannot be characterized as a simple normal incidence interaction, the mode commonly utilized for emission measurements. In fact secondary electron emission increases with incident angle [139][140]. This is due to the fact that interactions which occur at high angles of incidence produce higher emission due to the combination of shallower electron absorption and escape depths, the same mechanism which produces an analogous result in photoelectric emission.

2. The measurement for the grid secondary emission coefficient assumes that the grid geometrical open area ratio accurately represents the grid transmission whereas electrons are influenced, depending on their energy, by the field line geometry, in particular by the relative numbers of field lines from the MCP and ending on, or passing through, the grid. Depending on the electric field strengths above and below the grid, this can either increase or decrease the effective grid open area ratio, affecting the secondary electron emission calculation. For example, reducing the grid open area ratio from 60% (the actual geometric value) to 30% would reduce the calculated maximum value for the grid emission coefficient from 1.87 to 1.50. However when this change in open area ratio is applied to the calculation of anode emission coefficient, its maximum value would increase from 2.19 to 3.38.

3. The incident angle of electrons reaching the anode is close to zero so the angle of incidence does not explain the higher than expected result in this case. However a high values for the anode emission coefficient may not be unreasonable for two reasons. Firstly a significant fraction of the anode area is exposed fused silica, between the copper electrodes, a material with a high emission coefficient. Secondly, the copper electrodes become noticeably tarnished during detector operation, possibly due to oxidation enhanced by action of the electron flux on the residual atmosphere in the vacuum system. The build-up of such a thin insulating film is likely to increase the secondary emission coefficient.

5.3 Imaging Performance Simulation

The two dominant mechanisms by which the charge footprint distribution affects the imaging performance are image modulation, resulting from a small charge footprint distribution, and edge distortions due to the interaction of the charge footprint with the perimeter contact electrodes. In practice the two effects interact because of the inevitable compromise between detector size which limits the maximum size of the WSA, and the pitch size whose reduction is limited by manufacturing and electronic noise constraints. The pitch size sets the footprint size required to avoid modulation, and though in principle the pattern can be manufactured large enough to ensure the charge cloud is always collected on the active, geometrically representative readout area, this is often not practically possible. A larger readout also reduces the spatial resolution, which is proportional to pattern size, yet another reason to accept some level of edge distortion caused by the footprint falling off the edge of the active region of the pattern.

The invention of the split-strip anode made it possible to measure the radial distribution of the footprint with reasonable accuracy. What was required next was the ability to use the measured radial distribution to predict the modulation and edge distortion characteristics of a given readout design. A suitable computer simulation would enable the pattern design to be iteratively optimized, a process which would not be viable by experimental means.

Image modulation has been simulated [108][142] using techniques based on two dimensional Fourier transforms and numerical integrations. Whilst these techniques provided useful information for idealized patterns without edge connections and with simply modelled charge distributions, i.e. gaussian, exponential and uniform, they could not be used to realistically simulate the image linearity or modulation using an arbitrary measured radial distribution falling on to a practical pattern design with external contact electrodes and pads.

One obvious way to simulate readout operation would be to generate a two dimensional array representing the amplitude of the two dimensional charge footprint distribution, and deposit this on another array representing the simulated pattern. Since the minimum electrode width and inter-electrode gap are typically ~0.001 of the pattern size, and the array size of the simulation would

need to adequately over-sample these structures if it were to be realistic, it is easy to see that the necessary array size, even for the charge cloud alone, let alone the whole pattern area, is computationally unmanageable on a desktop computer.

A simpler solution was sought, making use of azimuthal footprint symmetry to reduce the computational effort. This technique was primarily developed to model the performance of image charge WSAs whose charge footprint is azimuthally symmetric and can to first order be mathematically defined, since it is induced through a thick substrate on to the readout, a near continuous electrode surface, from what can be approximated as a point charge.

5.3.1 Simulation technique

An azimuthally symmetric charge footprint distribution allows the problem to be addressed one-dimensionally, reducing the computational task by the square root of the number of two dimensional array elements necessary to over-sample the readout pattern. Whereas the radial charge distribution is straightforward to represent as a one dimensional array, it is not intuitively obvious how to reduce the dimensionality of the two-dimensional WSA pattern.

The problem was addressed by determining the area of each electrode as a function of radius from the event position, *P*, being simulated i.e. from the centre of the charge footprint. Each pattern electrode was defined as a simple, closed polygon. A function, which can be defined as the 'radial area', was calculated for each line segment (e.g. *AB*) of the polygon. The radial area, RA_{AB}, for line segment *AB* is an r,θ plot which represents the triangle *PAB* as a polar expression. The value of θ is given by the angle subtended by the triangle *PAB* at a given radius, *r*, centred at *P*. The area of *PAB* can be calculated from this polar representation by the integral :-

$$(5\text{-}12)\quad Area_{PAB} = \int_0^{r_0} RA_{AB}(r) r.dr$$

where *RA (r)* is the angular extent of the arc at radius, *r*, and r_0 is the maximum radius at the outermost vertex of triangle *PAB*.

The order of the points in the line segment *AB* can be used to define the sign of the angle, generating an area which is also signed. The sign depends on the direction of rotation of the line segment *AB* around the centre, *P*. Figure 5-10 shows a simple polygon, *ABDEF*, and an arbitrarily positioned point, *P*. Simple inspection of Figure 5-10 shows that the signed areas of the triangles generated by each line segment *AB,BC,CD,...* of the polygon and the point, *P*, (sign being indicated by the direction of the fill in each triangle) can be used to determine the area of the polygon, a parameter which is independent of *P*. This works so long as the correct cyclic order of polygon vertices is followed, and is calculated as follows :-

$$(5\text{-}13)\quad Area_{ABDEF} = Area_{PAB} + Area_{PBD} + Area_{PDE} + Area_{PEF} + Area_{PFA}$$

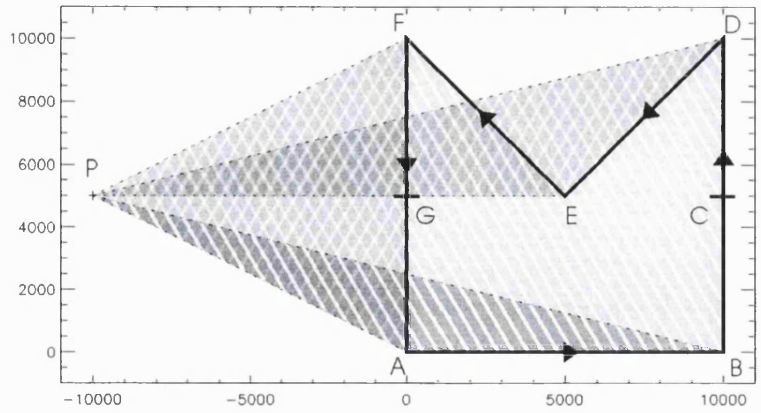

Figure 5-10. The calculation of the area of the polygon, ABDEF. This can be determined using the sum of the signed areas of the five shaded triangles.

Rather than calculate the scalar triangular areas and add them to calculate the area of the polygon, the signed radial areas corresponding to each line segment can be added to generate a signed radial area for the polygon. Figure 5-11 illustrates how this is calculated. The five curves with horizontal components represent the signed radial areas of the five triangles shown in Figure 5-10. The horizontal sections of each of these correspond to the constant angles subtended by all the triangles at increasing radius from point *P*, until the first of the outer two triangle vertices is reached. The horizontal section is followed at larger radius by a curved section which represents the angle subtended by the triangle between the outer two vertices. This diminishes as the radius increases, reaching zero at the radius of the outermost vertex. The bold, shaded region is the sum of these five curves and represents the radial area of the polygon *ADDEF*. The form of this function is dependent on the location of *P* but the area calculated using equation (5-13) is independent of *P*. The points C and G have been included, though not actually polygon vertices, to indicate the correspondence between the two figures.

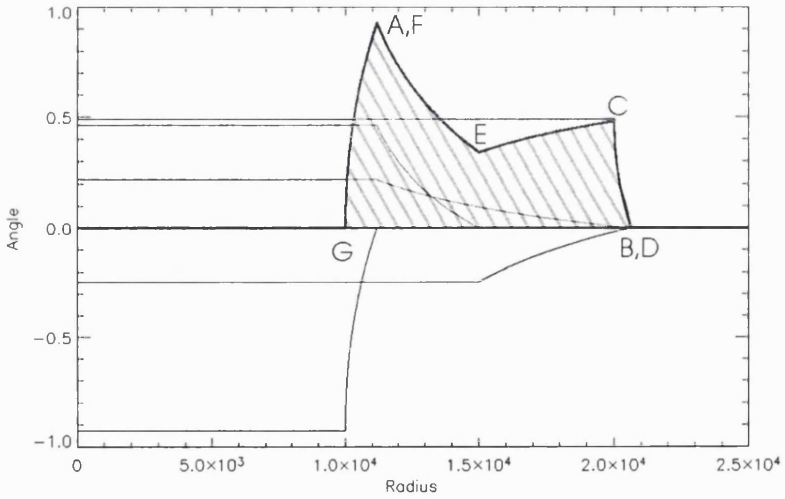

Figure 5-11. The radial area of the polygon *ABDEF*, in *r,θ* space.

The radial area of the polygon can be used, in combination with the radial charge footprint distribution, to directly determine the charge collected on the polygon. In practice, a one dimensional floating point array was used to manipulate and store the radial area calculation

numerically. The radial scale of each element of the array was chosen to substantially over-sample the pattern structure, and a test procedure was also used to establish the accuracy of the area calculation which was carried out with a numerical integral. Figure 5-12 shows the error in the calculation of the area of polygon *ABDEF* for a range of positions, *P*, from [0,0] to [-1000,-1000], with an radial bin size of 1. The maximum error in the measured area (nominally 7.5×10^7) of 1.3×10^{-4} % with a standard deviation of 2.9×10^{-5} % are relatively insignificant but could be further improved by refinement of the numerical integration.

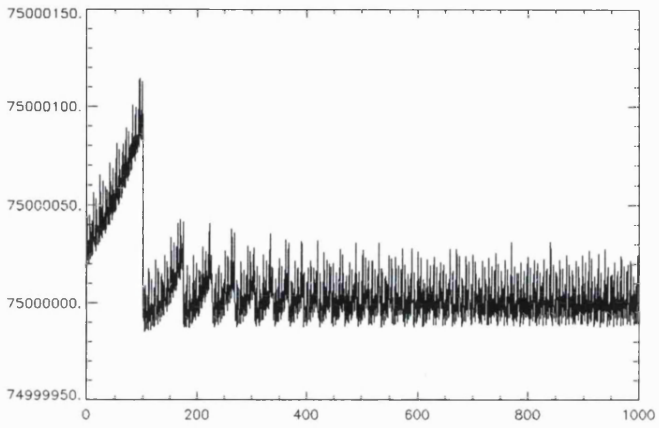

Figure 5-12. The numerical calculation error of the area of polygon *ACDEF*. The area of *ACDEF* was calculated for a range of *P* positions and the maximum error was 1.3×10^{-4} %.

This example uses a very simple polygon, but for simulation of the WSA, the polygons defining the wedge, strip and Z electrodes can be used to directly calculate their radial areas with respect to a given event position. This information, in combination with the radial charge distribution, either calculated or measured using the split-strip anode, enables the charge collected per electrode to be determined.

The charge collected on an electrode as a function of radius from the event position is given by the array multiplication of radial area × radial charge distribution, and the total charge is simply the sum of the elements of the resultant array. The simulated measured charges are applied to the position decoding algorithm, and the simulated position coordinate calculated. Comparison with the event position enables the linearity of an actual, practical pattern design to be simulated without cutting metal.

This technique is applicable to any charge division pattern since arcs or any curved electrode can be generated using sufficiently small line segments. Since the polygon definitions can be the ones used for pattern manufacture, which include the outer contact electrode and pad definitions (in this case an AutoCAD DXF file), this technique can genuinely simulate the realistic operation of the pattern. In addition, the radial area technique allows an arbitrary radial charge distribution to be used without any computational penalty, whereas other techniques using gaussian or

exponential fits would require multiple terms to even approximately fit a measured radial distribution.

5.3.2 Results

This technique was used to iteratively optimize the design of a WSA used in Image Charge mode (see section 5.4). Time and resources prevented performing an experiment with a split-strip anode to actually measure the true radial charge distribution. However, a detector using the Image Charge technique does not require a charge spreading region in order to provide a suitably large footprint necessary to prevent image modulation. The charge induced on the readout electrodes through the substrate has a spatial distribution defined by the convolution of the footprint distribution collected by the Image Charge resistive layer with the induced radial charge distribution generated by a point charge [143]. The latter is given by :-

$$(5\text{-}14)\quad \sigma_r \propto \frac{1}{(r^2 + a^2)^{3/2}}$$

where a is the substrate thickness

In practice, there are several advantages to proximity focusing the charge on to the Image Charge resistive layer, and letting the induced charge distribution function dominate the distribution perceived by the image readout electrodes. The detector was operated in this mode so that equation (5-14) provided a close approximation to the distribution on the readout, enabling the operation of the pattern to be accurately simulated.

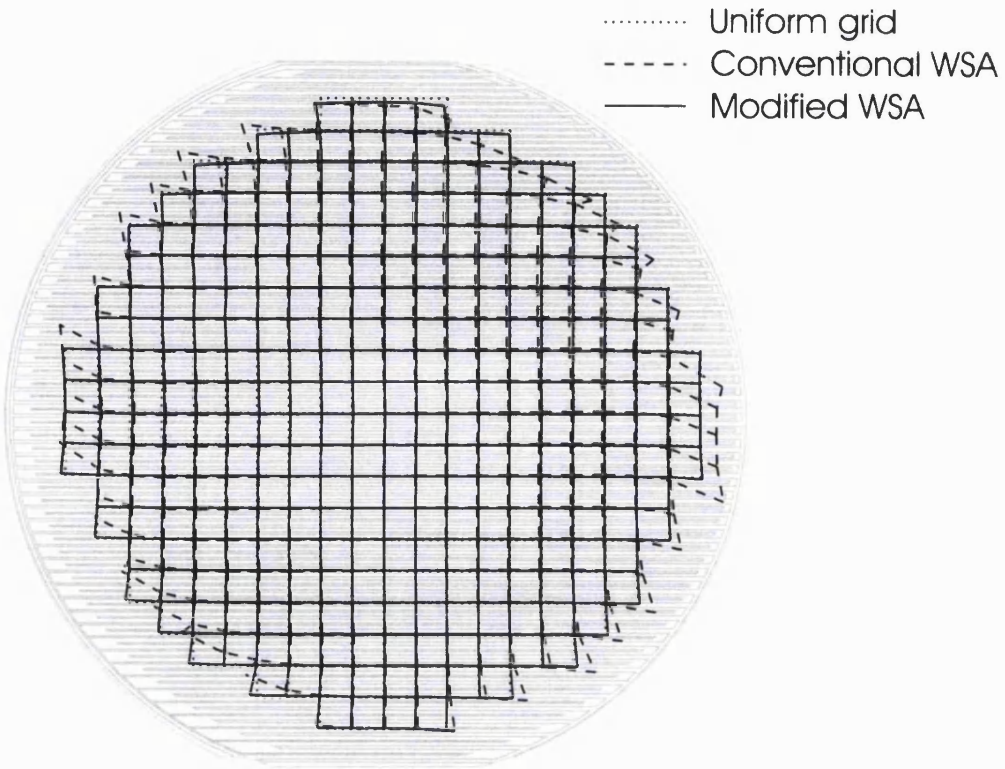

Figure 5-13. Linearity comparison of a conventional WSA and a modified design. The vertices of the 3 grids represent input event coordinates (dotted) and the resulting output position as determined by a conventional WSA (dashed), and the modified WSA (solid).

Figure 5-13 shows the simulated linearity of the redesigned WSA pattern versus that of an unmodified pattern in response to a uniform array of input point sources. Three sets of grids can be seen superimposed on the modified WSA pattern design. The vertices of the uniform grid marked with dotted lines show the coordinates of the event positions input to the simulation, which are in a regular square array with a spacing of 2×2 mm^2. The vertices of the highly distorted grid marked with a dashed line represent the output from a traditional WSA using a typical boundary electrode design which was optimized to minimize edge non-linearity. The vertices of the minimally distorted grid marked using a solid line are the outputs from the simulation for the modified WSA design.

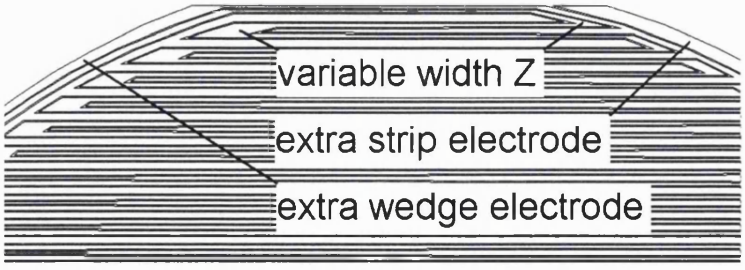

Figure 5-14. Modifications to improve the WSA linearity. This figure shows the upper half of a WSA pattern showing modifications which allow significant linearity improvement.

The modifications included the addition of two extra narrow sickle shaped wedge and strip electrodes to the right and left of the main pattern, together with position dependent variation of

the Z electrode area where it connects pitch to pitch at the perimeter. Figure 5-14 shows a region of the WSA pattern with these features indicated.

The simulated rms deviation of all the points within the entire 40-mm diameter detector FOV was 43 μm and 45 μm in the x and y axes, respectively, for the new design, 3-4.5 times better than the unmodified design that had deviations of 119 and 192 μm for x and y axes, respectively. These figures represented the overall rms deviation, however near the perimeter the improvement in linearity was visibly better.

Thus far, no opportunity has arisen to compare the simulation data with experimental results obtained with a modified pattern. This full circle demonstration will provide the acid test for the technique. In order to be a realistic test, the charge distribution would also need to be empirically measured using the split-strip anode, to avoid the approximation of calculating the induced charge distribution, which does not include the effects of the actual charge distribution landing on the image charge surface, or the conductor-less areas, the insulator gaps, in the readout pattern.

5.4 Imaging using Induced Charge

5.4.1 Introduction

The image charge technique, first suggested by Battistoni [144], and developed by Jagutzki [145], uses a resistive layer, commonly made of Germanium, to collect the charge cloud produced by an MCP resulting from a detected event. Figure 5-15 shows a schematic of an MCP detector using the image charge technique with a WSA position readout. The Germanium layer acts as the anode, collecting the MCP charge in place of the conventional readout pattern. Unlike the resistive anode, which is a position sensing device in its own right, the Germanium layer acts solely to localize the charge, allowing it to capacitively couple to the readout electrodes from the position of its arrival, which represents the event coordinate. The readout is manufactured on the reverse side of the anode substrate. The signal arrival generates an induced charge on the readout electrodes, the rising edge of which is sensed by charge sensitive preamplifiers used for charge measurement. The resistance of the Germanium layer is chosen such that the time constant for event charge dissipation is significantly longer than the time constant of the charge measurement electronics. The charge begins to spread as soon as it arrives on the Germanium, and the increase in size of the charge footprint as a function of time can be measured with the split-strip anode by using a range of electronic shaping time constants. Figure 5-16 shows the measured radial distributions for a range of shaping time constants. The longer the time constant, the more the charge can spread out, resulting in a larger measured footprint. The last data set shows the even larger footprint produced when the MCP to anode voltage is reduced, the extra charge spread occurring in this instance in the MCP to anode gap. This data was taken by Sanderson [154] and the radial distributions determined using the software described in section 5.1.3.2.

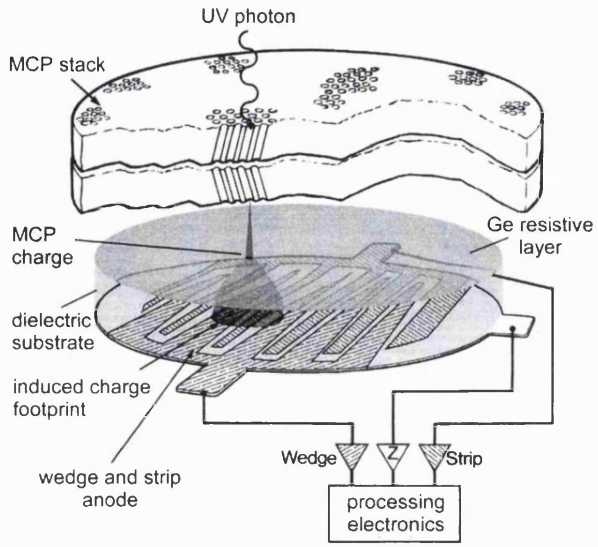

Figure 5-15. A schematic of the image charge technique used with a WSA.

In practice it is beneficial to define the detector geometry so that the anode is effectively proximity focused making the footprint of the collected charge small, and the Germanium time constant is significantly longer than the electronic shaping time constants. In this situation the major factor determining induced charge footprint size is the thickness of the substrate between the Germanium anode and the position readout. The slow charge leakage from the Germanium to ground is equivalent to the signal discharge of the WSA electrodes through the DC bias resistors in charge collection mode, since in both cases the pre-amplifiers are AC coupled. This slow signal component is filtered out by the fast pulse shaping electronics.

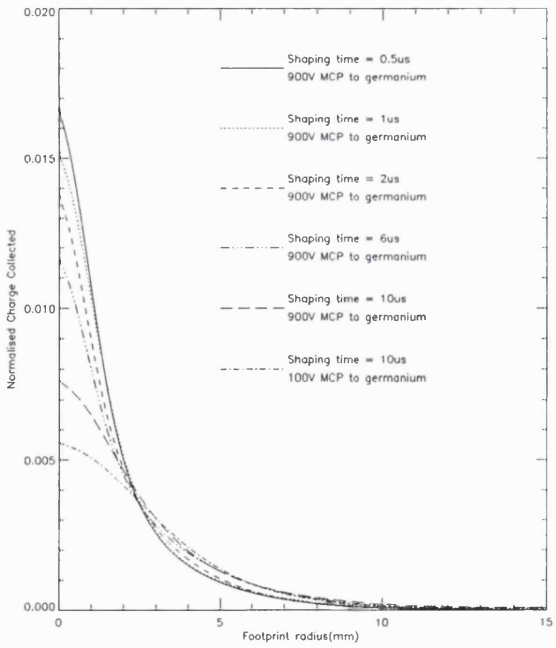

Figure 5-16. The radial charge footprint distribution measured in image charge mode. The shaping times measure the charge footprint at different times after arrival, indicating the charge spread.

Since the charge is spatially localized during the time it is measured, and the footprint primarily results from the geometry of the coupling dielectric, a charge division anode detects the true capacitance ratio as determined by the electrode geometry i.e. as charge division is meant to work. The electrode ratio distortions caused when secondary electrons are produced during charge collection, and giving rise to image instability and non-linearity, are not present.

Position resolution is also enhanced because of the following factors. Firstly, the charge division readout is not degraded by partition noise. This noise occurs in collected charge mode and results from the statistical errors due to division of a finite number of electrons among a small number of electrodes. This statistical noise is physically represented by the random spatial distribution of the collected charge cloud. Secondly, a magnified charge centroid error resulting from an initially inhomogeneous charge distribution which is allowed to expand to match the requirements of a charge division anode used in collection mode, is avoided because the charge cloud can be proximity focused to the anode in image charge mode. N.B. the hypothesis that the charge centroid from an MCP is inhomogeneous, and the effect this would have on position resolution, is discussed in chapter 7.

The image charge technique has major benefits for practical applications. The capacitive coupling allows the readout to be electrically isolated from the MCP detector and independent of the detector voltage configuration and grounding scheme. The readout electrodes can be operated at ground potential, resulting in improved noise immunity and eliminating the risks associated with operating them at high voltage. Image charge requires only a simple capacitively coupled interface between detector and readout pattern. The readout can be manufactured on a separate substrate from the image charge anode in the detector body and capacitively coupled via contact allowing readouts to be interchanged with ease to suit different requirements. This has enormous advantage for sealed intensifier tubes, where a "generic" tube design can be used for many applications. In addition to the flexibility this offers, the sealed tube does not contain the readout device or require extra UHV electrical feedthroughs, with major manufacturing and operational advantages.

The image charge technique does have features which restrict its operation. A fraction of the collected charge is induced on to electrodes in the detector i.e. the MCP output contact, etc. This leads to a small decrease in the charge sensed by the readout, which is typically 76% of the collected charge, resulting in a small degradation of the signal to noise ratio. The pulse height distributions for collected and induced charge are plotted in Figure 5-17. The resistance of the Germanium must be sufficiently high to localize the charge during measurement, but must not allow charge up at high count rates. Readouts designed for high rate applications require a lower Germanium resistance than those for lower rates using longer shaping times. This feature is analogous to the requirement placed on the DC bias resistors which drain the signal current in a conventional WSA where charge is collected. These too have to be reduced in value for high rate operation. These limitations are insignificant compared with the advantages offered.

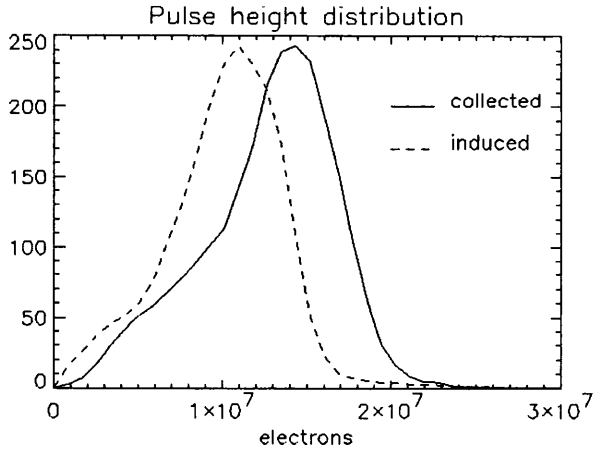

Figure 5-17. The pulse height distributions for collected and induced charge. These distribution were measured using identical MCP configurations and voltages.

5.4.2 Results using a WSA in image charge mode

Initial experiments to assess the viability of the image charge technique were carried out using a WSA, and manufacture and operation of an image charge WSA was reasonably straightforward. An existing WSA pattern was used, which had been manufactured using the laser machining process. It consisted of copper conductors on a 2 mm thick fused silica substrate. The WSA pattern had a pitch of 980 μm and active area of 40 mm diameter. The resistive layer was manufactured by sputter coating with germanium. Initially RF sputtering was used which produced a satisfactory surface resistivity for the first device of ~400 MΩ/□. DC sputtering has also been evaluated, but the generally high deposition rate this produces is difficult to attenuate sufficiently to achieve a high enough resistivity.

The detector utilized a chevron stack of Photonis MCPs, each with a length to diameter ratio of 120:1. The configuration allowed the same WSA to be used for electron collection, and induced charge imaging, allowing direct comparison of their performances.

The detector produced very promising results immediately, despite an un-optimized substrate geometry. A pinhole mask was imaged and a position resolution of better than 40 μm FWHM obtained, without deconvolution of the pinhole size. This represented an image format of ~1000 × 1000 pixels, an excellent result for a WSA especially since the MCP gain was only 10^7 electrons. There was also an obvious improvement in linearity and image stability. Analysis of the data showed the position shift with count rate to be ± 5μm up to 4×10^4 cts^{-1}, insignificant with respect to the position resolution.

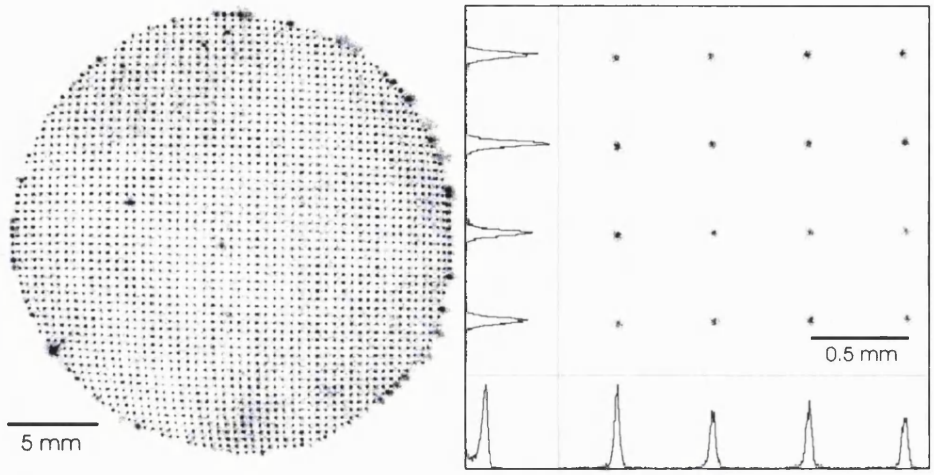

Figure 5-18. A pinhole mask image using a WSA in image charge mode. The right-hand figure shows the zoomed central area.

Figure 5-18 shows an image of the pinhole mask taken at a count rate of 400 count s^{-1} with the detector in the image charge configuration. The right-hand plot shows the zoomed central region of the image. The pinhole mask for this experiment had a pinhole size of 19 μm diameter on a 0.5 mm pitch.

This and other data were used to compare WSA performance between collected and induced charge collection. The left hand plot of Figure 5-19 shows the position resolution versus input count rate for data taken in both modes. The resolution at higher count rates degraded mainly because of a combination of pulse pile-up in the electronics, and gain depression from the localised high count rate in the MCP. Even so, the resolution versus count rate graph shows that spatial accuracy is little more than 100 microns FWHM even at 150 k count s^{-1}. Results using electron collection at lower rates are shown for comparison. No pile-up rejection was used and only a small fraction of events were collected owing to limitations of the computer interface.

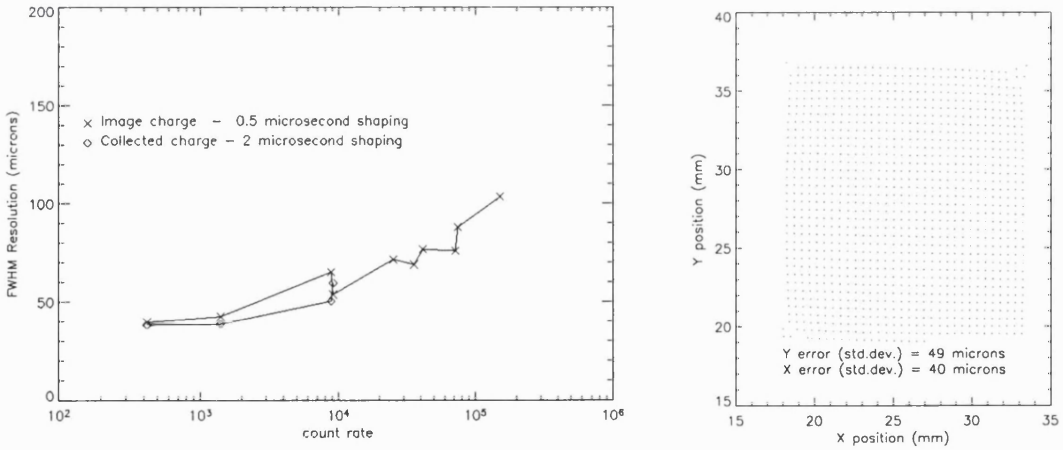

Figure 5-19. WSA image resolution versus count rate and linearity measurements. The resolution data on the left was taken for electron collection and image charge modes. The linearity data on the right was taken using and image charge WSA.

Image resolution is very similar in both modes; the loss of induced signal in the image charge mode being compensated for by the absence of both partition noise and possible centroiding errors caused by inhomogeneity in the charge cloud. The positions of the central pinhole images from Figure 5-18 are plotted in the right-hand image of Figure 5-19. For this experiment, the anode could not be proximity focused in the image charge mode, owing to the in-built geometry required for electron collection mode, and the electrostatic distortion caused by the lower MCP contact intruded into the imaging area owing to the unnecessary 6 mm drift region between MCP and anode. The distortion would have diminished if the anode had been proximity focused using a smaller gap. The measured linearity, given by the rms deviations of the pinhole positions for the central region shown in Figure 5-19, is 40 μm and 49 μm for x and y respectively. Over the whole image, the rms deviations are 81 μm and 70 μm for x and y respectively.

5.4.3 Image charge Vernier anode results

It was more difficult to achieve an immediate result from an image charge Vernier anode, because of its greater sensitivity to the charge footprint. An over-large charge footprint on the Vernier anode caused reduction in the electrode dynamic range, resulting in reduced resolution, so proof of the Vernier image charge performance awaited optimization of both substrate thickness, and Germanium resistance, both factors influencing the charge footprint dimension. A Vernier anode was manufactured on a 1mm substrate to reduce the size of the induced charge footprint through the substrate. The germanium coating process was revised to produce a higher surface resistivity, slowing down the charge spread on the anode. These two factors enabled the image resolution to be improved.

The linearity data shown in Figure 7-25 was the first data taken using image charge with the Vernier and shows a pinhole array with a pitch of 0.5 mm. The image wrap-over at the perimeter of the field is due to an electrostatic distortion at the lower MCP contact face caused by the contact edge, which lies inside the anode field of view. The measured position error over the central 23 × 36 pinholes is 13.2 μm rms. and 12.4 μm rms. in x and y respectively, significantly better than ever achieved using the Vernier readout in electron collection mode. Figure 7-29 is an image produced by illuminating a 0.5 mm diameter area of the detector without a mask. The pore structure of the upper MCP is clearly visible, indicating that the Vernier anode can achieve a similar position resolution in image charge as in collected charge mode.

5.4.4 Removable readout devices

A demountable version of the Photek IPD [146], modified to use the image charge technique, was used to demonstrate operation of a removable readout pattern. The intensifier was welded into a vacuum flange and the substrate supporting the resistive Germanium layer also acted as the vacuum enclosure wall. This enabled a readout pattern manufactured on a separate substrate to be brought into contact with it, outside the vacuum chamber used to operate the detector. For these

demonstrations a wedge and strip readout was simply held in contact with the germanium substrate and was easily removed. The germanium substrate was attached in place using an o-ring seal to enable easy removal so that the effect of variation of Germanium resistance could be measured. The performance proved to be insensitive to the germanium resistance over the range of count rates tested, up to 300 k count s^{-1}.

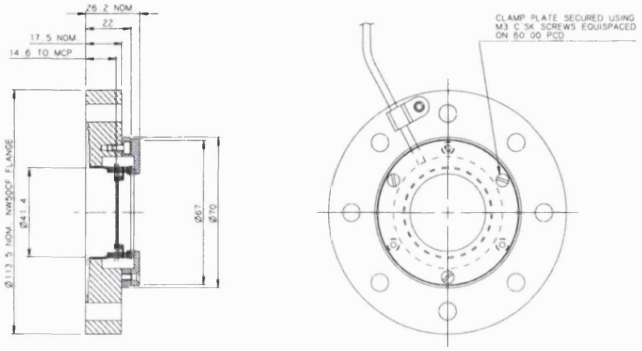

Figure 5-20. The demountable image intensifier with removable WSA. This was used to investigate Germanium anode resistance and to demonstrate operation of a removable readout pattern.

Figure 5-21 shows data representing the response of the demountable detector described above. The image on the left was obtained using uniform illumination of the MCP with UV radiation from a Pen-ray lamp at a count rate of 240 kHz. The image on the right was taken using the same configuration with the addition of a pinhole mask close to the input surface of the MCP. The collimation provided by the illumination geometry was insufficient to prove the image resolution to better than 100 μm FWHM for this particular experiment.

It can be seen that the pulse height distribution of the MCP is not well saturated and not ideal for optimal imaging performance. In addition, there are non-linearities near the edge of the field of view, which result from the non-uniform electric field behind the MCPs as a result of compromises made in the demountable design. No pile-up rejection was used for the high rate measurement, and the scattered noise outside the nominal edge of the detector field of view results from severe electronic pulse pile-up.

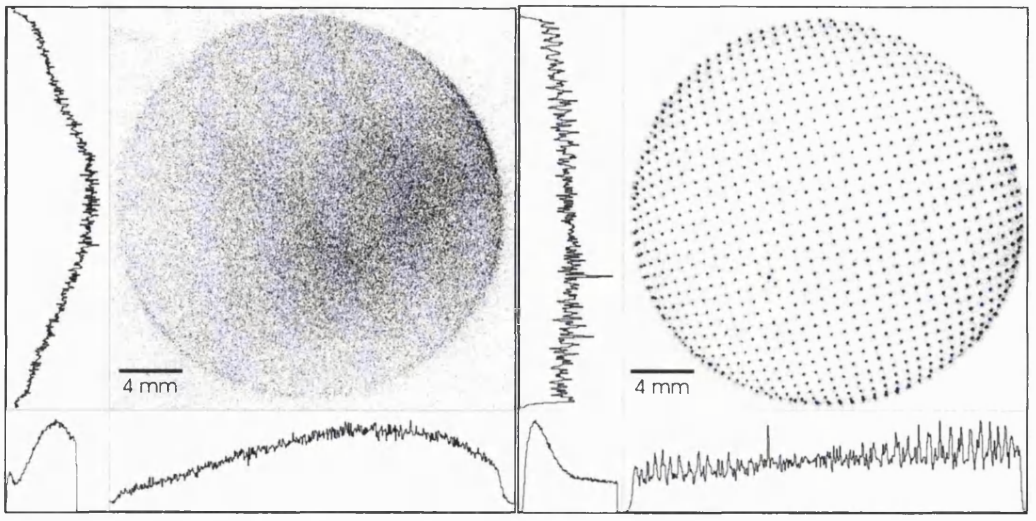

Figure 5-21. High count rate images taken using the demountable detector. The left-hand image shows response to uniform illumination at 240 k event s^{-1}, while the right-hand image is the same configuration with a pinhole mask in place.

Despite these design and electronic compromises it can be seen that the detector with its image charge readout, and detachable WSA, performed more than adequately, even at very high input count rates. As the proof of concept for an intensifier tube design with the major advantage of using an independent, external electronic image readout device, this experiment provided a very successful demonstration.

Chapter 6

New designs for charge division readouts

6.1 Introduction

In the field of space-based astronomy improvements in all aspects of instrumentation, from dramatically improved resolution of modern telescope optics to the miniaturization and vastly increased capabilities of digital data processing electronics, have created the requirement for detector systems with much higher performance. Position resolution and maximum count rate are two of the major factors which characterize this performance. Amongst the alternative readouts available, we have already shown that existing designs of charge division readouts offer relative simplicity, format flexibility, a low electronic channel count and come in a variety of designs each optimized for a particular count rate-to-resolution trade-off. The traditional two dimensional WSA provides moderate position resolution and count rate capability (conservatively 512 × 512 pixels at 50 kHz). This chapter describes a new generation of pattern designs which extend the available performance envelope to high resolution (up to 4000 pixels and beyond) or higher count rates.

The development of these readout designs was instigated by the requirement for a high resolution large format UV photon counting detector for spectroscopy; a detector system for the Grazing Incidence Spectrometer on the SOHO mission [147]. Detectors combining MCPs with charge division readouts are well suited to this sort of application. Large format MCPs are readily available and UV sensitivity can be achieved by coating the MCPs with a suitable photocathode. The charge division readout can easily be designed to accommodate high aspect ratio rectangular image formats with differing resolution requirements in each axis. However the position resolution of the WSA was insufficient for this application which required 2000 resolution elements along the dispersion axis.

6.1.1 Limitations of Linear Readout Designs

In common with virtually all readouts performing serial event detection using analogue measurements, the charge division image readout, as exemplified by the WSA, has its

performance fundamentally limited by the trade-off between position resolution and maximum count rate. The analogue electronic processing time has to be reduced in order to increase the maximum event rate. Practically, this means that the signal shaping time,τ, must be shortened. This can only be achieved by increasing the signal bandwidth which in turn results in an increase in the electronic noise, a major component of which is proportional to the square root of the bandwidth (see equation (3-12)). The resulting noisier charge measurement degrades position resolution.

The ultimate position resolution of the linear designs such as the WSA is fundamentally limited by the linear one-to-one mapping of the range of fractional charges collected on the relevant electrode to the encoded position range on the pattern (fractional charge being defined as charge collected on one electrode divided by the total collected charge for a particular event). The fundamental implications of linear mapping on performance are:-

1. The linear nature of the readout is essentially finite in extent since the relevant electrode varies from small to large area along the encoded axis. Repetition of the pattern to increase the active length cannot occur without discontinuity in the electrode first derivative. Such discontinuities have infinite spatial bandwidth and cannot be accurately represented using the charge division technique which is utilizes the low spatial frequency filtering provided by the charge footprint to eradicate the effect of the pattern fine structure. For a given spatial resolution, the noise sets the required linear variation or slope of the relevant readout electrodes i.e. the variation of area versus position, thus setting the maximum number of resolution elements which can exist within the fractional range of the electrode.

2. The maximum theoretical fractional range of each electrode, 0.0 to 1.0 (or 0.0 to 0.5 for the WSA due to its design) is reduced typically by a further 50% owing to the practical constraints of pattern design, for example the active pattern must be larger than the imaging area to accommodate the charge footprint, and electrodes cannot have zero width owing to the requirement that they have sufficiently low resistance. These factors further reduce the number of resolution elements along the axis.

3. As a rule of thumb. the practicalities of pattern design together with additional constraints imposed by the detector, for example the accommodation of pulse height distribution which may have widths of up to 100% FWHM for an MCP stack, typically cause the spatial resolution to be significantly less than the charge resolution for these simple linear devices. i.e. a signal-to-noise-ration of 1:1000 will in general result in a lot less than 1000 useable resolution elements (see section 3.3.1.1)

There are limited enhancements possible for these linear designs, such as pattern capacitance reduction to reduce electronic noise, improved designs with enhanced electrode fractional range such as the tetra-wedge anode [80], and geometry optimizations for circular perimeter patterns to

extend the effective electrode dynamic range. These techniques have been described in chapter 3. Attempts have also been made to join several WSA readout patterns together to cover a larger area. The effective the position resolution is improved by virtue of concatenation of the resolution elements of the independent pattern used but there are several downsides, the major ones being :-

1. The unavoidable discontinuities at the pattern boundaries cause image nonlinearity at the boundaries of order 50-100 μm.
2. The centroid calculation for events near the anode perimeters is pulse height dependent, due to variation of the charge footprint distribution with gain,
3. The number of electrodes required increases as the square of the increase in size of the active pattern.

6.2 Progressive Geometry Patterns- the Vernier and Spiral Readouts

Most of the charge division patterns described so far utilize linearly varying electrodes which, as noted, are by their very nature, finite in extent, a feature which fundamentally limits their performance. An alternative approach is to choose an electrode form which doesn't have this limitation. An obvious solution is to use cyclically varying electrode areas, the simplest and most obvious of which is the sinusoid. In this chapter a family of new charge division readout designs are described employing sinusoidal and quasi-sinusoidal electrode forms. These new patterns can offer a performance advantage over the wedge and strip due to the combination of two techniques: -

1. The use of a set of electrodes whose ratios vary cyclically for position measurement, as opposed to the linear variation of a WSA electrodes. This scheme, although running into ambiguities every cycle, can essentially be infinite whereas their linearly varying counterparts exhaust their dynamic range in a finite length.
2. A Vernier-like technique can be used to overcome position ambiguity. Whereas the normal Vernier technique uses the alignment of two coarse scales to define a fine scale, this complementary scheme uses two fine scales to define a coarse scale. The low beat frequency between the different spatial frequencies of two cyclic sets of electrodes is used to provide the coarse position measurement necessary to uniquely encode a large range of electrode cycles.

When combined, the two techniques provide a means of measuring position to an accuracy many times greater than the precision of the charge measurement on each electrode.

6.2.1 Design History

This section, which precedes the description of the new design of readout, is a narrative describing the chronological evolution of concepts which led to these developments. This is felt to be useful since it provides a logical and reasoned route through to various ideas which were melded to generate the Vernier concept.

6.2.1.1 The Split-strip anode - a precursor

The family of devices whose invention is described here was inspired by ideas generated from an experiment to measure the spatial distribution of charge clouds. This experiment, described in chapter 5, was designed to characterize the spatial distribution of the electron clouds produced by an MCP as they are collected on a charge division anode. This distribution is important in determining the ideal pattern geometry, particularly the pitch and active size, in order to minimize image modulation and edge nonlinearity while maintaining performance. The Split-strip anode [137] shown in Figure 6-1 was specifically designed to determine two parameters of the charge cloud when collected: the position in one dimension, centroid position, *cp*, given by :-

$$(6\text{-}1)\quad cp = \frac{A+D}{A+B+C+D}$$

and the division, in terms of fractional charge magnitude, *fc*, around a central division in the pattern orthogonal to the position axis, given by :

$$(6\text{-}2)\quad fc = \frac{C+D}{A+B+C+D}$$

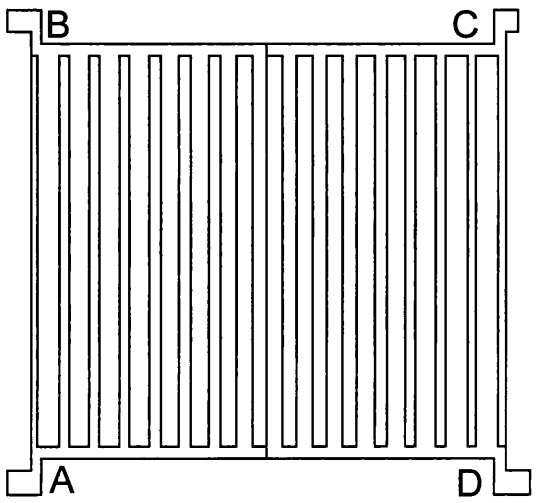

Figure 6-1. A schematic of the Split-strip anode.

Figure 5-2 shows a typical plot of data collected by the split strip anode. Each point represents a single event. The small spread in *fc* for a given position, *cp*, implies that the charge cloud distribution is reasonably stable. The general form of this data, the aptly named S-curve, is

independent of the actual distribution for the usual, monotonic distributions. Simple examination of this data shows that, in a region centred around the pattern division between A+B and C+D, there is a limited extent where the fractional parameter, *fc*, has an approximately linear variation with centroid position, *cp*. The high gradient of the data in this region also indicates that *fc* is more sensitive to position than *cp*, or in terms of performance, *fc* alone would provide enhanced position resolution. The position determination provided by *fc* depends solely on the area division provided by the electrode grouping A+B and C+D and does not require the repetitive structure of linearly modulated strip widths provided by the electrode combinations of A+D and B+C.

The enhanced position resolution available in the region surrounding the split-strip division has a two-dimensional analogue in the quadrant anode (see Figure 2-13). This device consists of four simple electrodes tiled around a central cruciform intersection. Position is determined in an analogous way to the fractional Split-strip parameter, *fc*, and provides relatively coarse imaging over most of its area, with a region of high resolution around its centre. Both the fractional charge axis of the Split-strip design and the quadrant anode offer a simple means to attain high resolution (in one and two dimensions respectively) albeit over a small area. If this potential was to be developed into a one dimensional high resolution readout of greater extent, the next step would be to find a technique to increase the length of the linear region, or, to increase the number of linear regions while arranging them to overlap. A pattern of successive electrode strips of equal width can be envisaged with divisions between electrodes orthogonal to the axis of position measurement. Let us assume that the collected charge cloud is of finite extent with a well defined boundary. In this situation it can be appreciated that in order to achieve continuous sensitivity, the charge cloud extent must be larger than the electrode width, otherwise all events with centroids located at the midpoints of electrodes will cause charge to be collected on that electrode only. A larger charge cloud will at these same points, be collected on a minimum of three electrodes. A simple linear ratio of two electrode amplitudes is ineffective at dealing with the events at electrode midpoints, where the linearity is diminishing and where there exists a boundary at which one member of the chosen pair changes. It is more efficient to make use of the symmetry of charge collection on three electrodes and provide continuous sensitivity with position, by using a three parameter centroiding algorithm. There are analogies with other readout systems here [148] [149].

6.2.1.2 The minimum number of electrodes

Charge must be collected on a minimum of three electrodes for continuous position sensitivity. A pattern consisting of repetitions of the same three electrodes will have ambiguities owing to uncertainty of the electrode cycle in which the event lies. To overcome this, more than three electrodes could be used. For instance, a one dimensional imaging readout employing six electrodes as shown in Figure 6-2 can theoretically be organized such that coarse position is determined by identifying which of the three electrodes collecting the charge for any event. Since

there are 120 unique permutations of three out of six, and each permutation covers a range equal to half an electrode width, the pattern could, in principle, consist of up to 60 electrodes arranged to sequentially exploit these combinations, without ambiguity, if such an ambiguity-free arrangement exists.

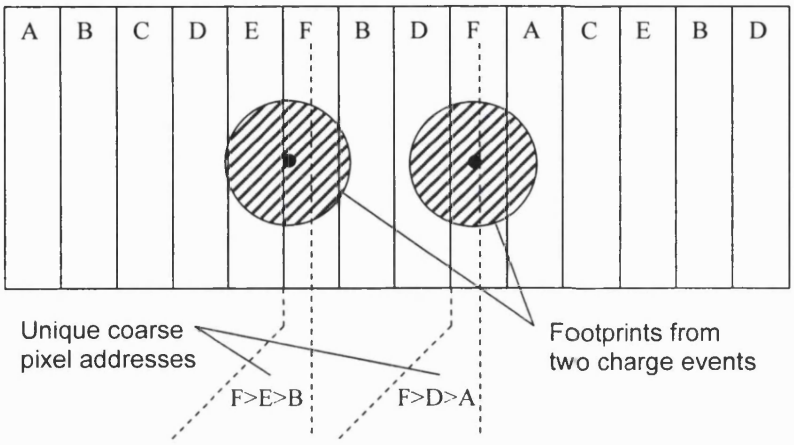

Figure 6-2. A possible scheme for one-dimensional imaging using 6 electrodes.

The advantages offered by this scheme over existing designs can be summarized as follows.

1. There is no fundamental limit to its extent since charge collected on any electrode varies cyclically with position and not linearly.
2. Since the charge collected on any electrode can cycle through the available dynamic range of the electrode several times within the pattern, the spatial resolution is not directly limited by the charge measurement accuracy; a feature of linear charge division readouts.
3. It uses relatively few electrodes given its potential for high resolution
4. The scheme outlined in Figure 6-2 is of simple design with no fine structure required.

There are also several drawbacks to such a one-dimensional scheme of simple electrodes:

1. It is not easily adapted to a two dimensional readout, at least as a planar electrode pattern. It could be realized perhaps as two orthogonal wire planes arranged such that charge is shared equally among both planes.
2. Non-ideal (i.e. realistic) spatial charge distributions would give rise to cyclic non-linearities. Even if the distribution is constant in form, and there exists a suitable centroiding algorithm which gives near perfect linearity, it could well prove to be impractical to implement without simplification and performance degradation.
3. Since detectors often produce charge distributions which vary from event to event, there may be no algorithm which provides a perfectly linear response.
4. The scale of these cyclic nonlinearities could be significant compared to the electrode (i.e. collecting element) dimension. The scale of the errors are quite small for CCDs in

centroiding applications [148], where there are many pixels (acting as collecting elements) along each axis, and the ratio of the sizes of collecting element to resolution element is not so large. It might pose more of a problem for the design in Figure 6-2 where this ratio would be larger.

6.2.1.3 The application of geometric charge division

The imaging concepts described above have only been considered theoretically, but some of the features discussed played a large part in the development of the concepts which led to the final readout designs. In order to explain the next stage in the design evolution it is useful to compare the operation of two different one-dimensional readout schemes; a simple two adjacent electrode device, as characterized by the A+B and C+D electrode combination of the Split-strip, and the Backgammon or wedge-wedge device. Both patterns achieve a linear variation of charge with position over at least part of their extent (the former being non-linear away from the central divide in the pattern). The linear response in each device results from two alternative but complementary mechanisms. The "adjacent electrode" device relies on the form of the spatial distribution of the charge cloud causing the collected charge to vary linearly with position, at least over a small region where the centroid is near the electrode division. More precisely, it relies on the fact that the derivative of the distribution integrated across one axis, corresponding to the rate of change of charge collected on one of the electrodes, is near constant. If an arbitrary distribution could be chosen whose derivative is truly constant over a longer range, then this region could be extended. For example, a square and uniform distribution (though practically unrealizable) would provide a linear response at all locations where it is divided amongst the two electrodes. The design of the Backgammon readout seeks to mimic the operation of such a distribution by moving the responsibility for the linearity of the charge division from the charge cloud distribution to the pattern itself. The pattern is constructed as a series of fine pitches and the widths of the electrodes in each pitch are modulated so that their average areas vary linearly with position.

The same technique of electrode modulation can be applied to the scheme of Figure 6-2, where collected charge magnitudes vary cyclically. The limitation on linearity previously described, imposed by variation of the charge cloud distribution can be side-stepped by modulating the electrode areas locally on a fine scale with a non-linear cyclic function, defined during pattern manufacture. The cyclic variation of charge with position is then not a function of the charge cloud, but of the pattern itself, and is thus constant. As with the multiple electrode pattern of Figure 6-2, division of the event cloud among at least three electrodes is necessary to provide continuous and uniform position sensitivity. This is an absolute requirement since a pattern consisting of two cyclically varying electrodes must have repeated positions where the rate of change of both electrodes with respect to position is zero (the maxima of one electrode must coincide with the minima of the other). Position resolution at these points tends to infinity since

the rate of change of collected charge with position is zero. The presence of a third electrode completely eliminates this problem.

Practically realizable patterns have other requirements than just number alone. Other major requirements for the electrode form are :-

1. The sum of the electrode widths must be a constant, which is equivalent to disallowing areas of exposed insulator larger than that required by the fixed width electrode insulator gaps. The pattern is divided into pitches of equal width, whose dimension is equivalent to the sum of the electrode widths and the required insulator gaps.
2. The electrodes must not have discontinuities. Discontinuities cannot be faithfully represented in the variation of collected charge with centroid position owing to their infinite spatial frequency bandwidth, as discussed earlier with respect to mosaic WSAs.
3. Similarly, the pattern should not have discontinuities in the derivatives of the function describing the electrode as these will also be distorted by this same process.

6.2.1.4 A cyclic position metric using three sinusoidal electrodes

The most simple and obvious cyclic three electrode geometry that meets the above criteria consists of three sinusoids, *A*, *B*, and *C* of identical amplitude with relative phases of 120°, defined by:-

(6-3) $A = o + a\sin(\theta)$

(6-4) $B = o + a\sin\left(\theta + {}^{4\pi}/_{3}\right)$

(6-5) $C = o + a\sin\left(\theta + {}^{4\pi}/_{3}\right)$

where: o is the offset necessary to produce a positive electrode area at all positions
a is the electrode sinusoidal amplitude (equivalent to half of the electrode dynamic range)
θ is the triplet phase co-ordinate (proportional to displacement along the image axis)

Figure 6-3 is a schematic showing a single pitch of a pattern comprising three electrodes with this arrangement. Like all charge division readouts, the size of the charge cloud footprint is chosen to smooth out fine electrode structure and collected charge magnitudes are proportional to the mean local electrode areas. The sum of these electrode areas is a constant and given by the following expression :-

(6-6) $\left(o + a\sin(\theta)\right) + \left(o + a\sin(\theta + {}^{2\pi}/_{3})\right) + \left(o + a\sin(\theta + {}^{4\pi}/_{3})\right) = 3o = const.$

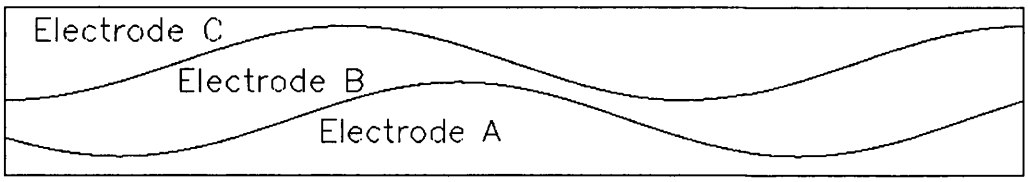

Figure 6-3. A single pitch of a pattern using 3 sinusoidal electrodes.

When the offset, *o* equals *a*, the theoretical maximum electrode dynamic range is thus two thirds of the total electrode area. In practice *o* must be greater than *a* to allow all the electrodes to be continuous as required for electrical continuity. The physical arrangement of the electrodes will be discussed in a later section. The ratio of the three charges collected, resulting from an event at any position within one wavelength, uniquely determines a phase between 0 and 2π which varies linearly with centroid position.

Visualization of this electrode scheme

The operation of this scheme and the advantages conferred by the cyclic non-linear electrode designs can be usefully visualized by examining the 'charge domain' space. In this space, every event has a unique co-ordinate directly defined by the charge amplitudes collected on the electrodes. Both this scheme and the WSA use decoding algorithms whose inputs are the amplitudes of charges collected per event on three electrodes. These values define a three dimensional co-ordinate, Q_i, Q_j, Q_k, for each electrode triplet, which may be simply visualized as point within the three dimensional volume of charge domain space. Since, in the majority of applications, the pulse height (or total charge per electrode triplet, $\sum Q_i$), is not known and varies between events, no positional information can be encoded by the axis normal to $\sum Q_i = const$. For a given pulse height, the charges collected on the i^{th}, j^{th} and k^{th} electrodes is either the total charge (in the case of the WSA) or a constant fraction of the total charge (for instance if several triplets were used). Therefore $Q_i + Q_j + Q_k = Q_{pulse}$ has a constant value. This condition is satisfied by a series of parallel planes, normal to the line defined by $Q_i = Q_j = Q_k$ in the charge domain volume. Figure 6-4 shows how the two dimensional image space of the wedge and strip pattern maps on to this plane.

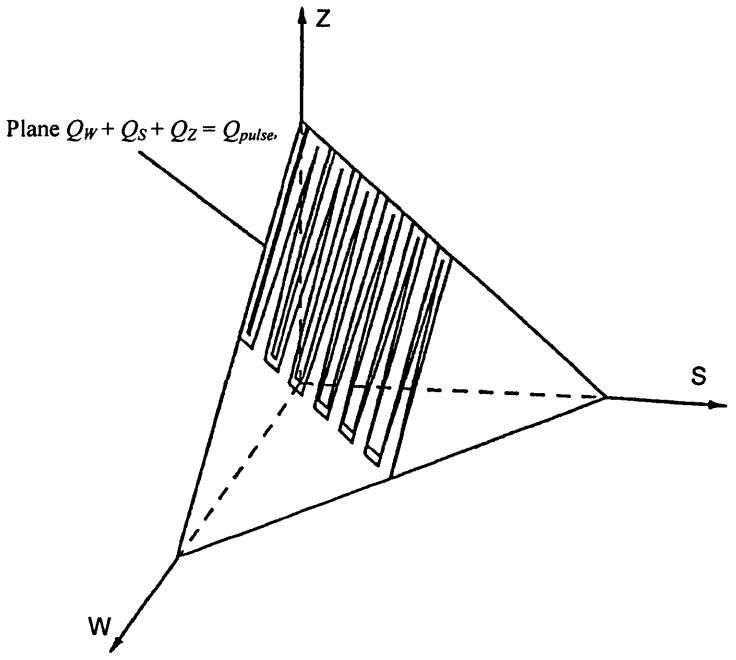

Figure 6-4. The mapping of 2-D WSA image space on to the charge domain.

The values of the charge co-ordinates allowed in the new scheme caused by the variation of the three sinusoidal electrodes with position, define a conical surface whose apex lies at the origin. The cross-section of this surface in each plane of constant pulse height is a circle. While the charge measurement is analogue, the set of planes is effectively infinite in number, but after digitization of the charge amplitudes, the number of planes becomes finite. The pattern phase at any co-ordinate is the angle subtended between the radius from the circle centre (defined by the intersection point of the line $Q_i = Q_j = Q_k$ and the plane), and the radius defined at $\theta = 0$, an arbitrary position. This geometry is shown graphically in Figure 6-5.

Decoding the phase co-ordinate

The phase value for an event co-ordinate is determined using two steps. Firstly, a co-ordinate transformation is used to rotate the co-ordinate axes so that the two of the new axes, X and Y, lie in the plane $\sum Q_i = const$, the third orthogonal axis thus lying along the line $Q_i = Q_j = Q_k$.

The equations defining the transformed co-ordinates in the plane are :-

$$(6\text{-}7)\quad X_{i,j,k} = \frac{(Q_j - Q_k)}{\sqrt{2}}; Y_{i,j,k} = \frac{(2 \times Q_i - Q_j - Q_k)}{\sqrt{6}}$$

where: Q_i is the charge collected on the i^{th} electrode

X and Y are the new axes lying in the plane of constant charge, shown in Figure 6-5

Conversion to polar co-ordinates then provides position decoding information and event discrimination. The phase of an event co-ordinate can now be determined using the equation :-

$$(6\text{-}8)\quad \theta = \arctan\left(\frac{Y}{X}\right)$$

X and Y allow determination of a unique phase co-ordinate between 0 and 2π which is used for event position determination. Unlike many other charge division designs, position determination does not require any normalization with respect to the total collected charge.

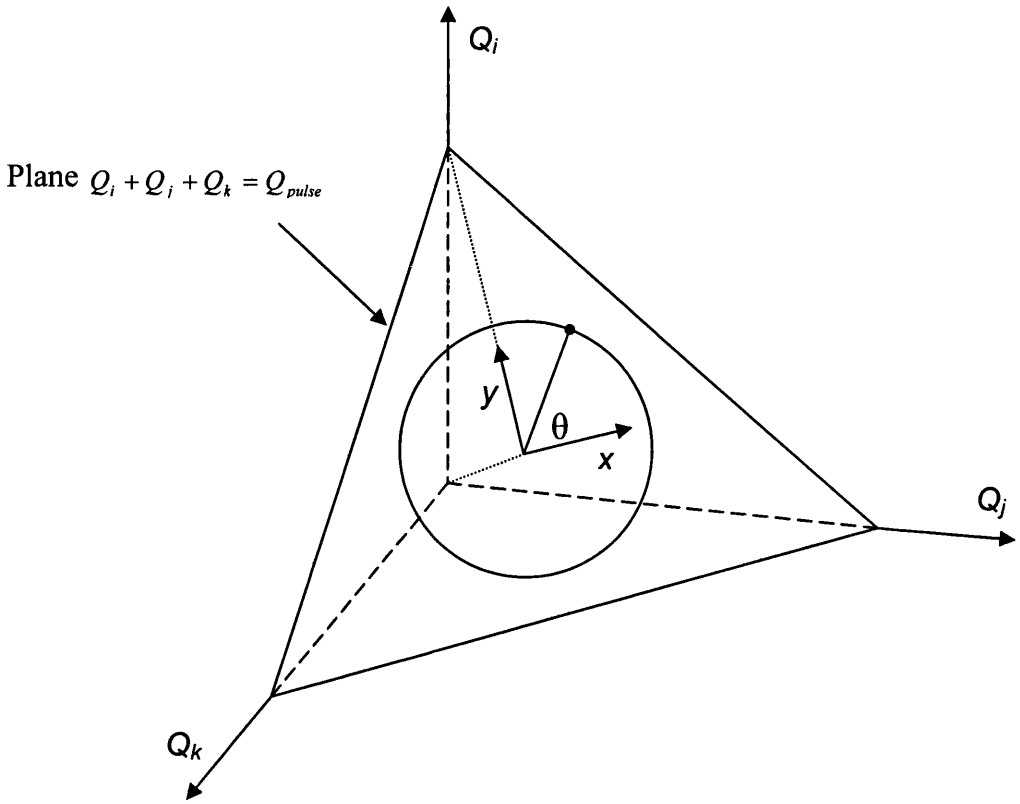

Figure 6-5. The locus of allowed charge ratios for three sinusoidal electrodes.

For certain applications described later the normalized radius of the event co-ordinate is required. Since the allowed values of the event co-ordinate lie on a conical surface with its apex at the origin, the absolute radius is proportional to the total charge or pulse height. Calculation of the normalized radius may be carried out, if required, using the following equation :-

$$(6\text{-}9)\quad r_{norm} = \frac{\sqrt{X^2 + Y^2}}{\sum Q_i}$$

Knowledge of the radius can be used to disqualify events having invalid charge co-ordinates i.e. those which lie outside the acceptable envelope surrounding the conical surface. Signal errors from several sources can produce excursions from the nominal charge values. An envelope encompassing the acceptable range can be used to discriminate events with larger errors which are likely to also have invalid phase values. The errors may be caused by pulse pile-up, events occurring near the edge of the active pattern (where electrode geometries are not representative), or very small pulse heights (when the signal to noise is too low).

One pattern described later, the Spiral anode, uses modulation of the radial co-ordinate to supply coarse position information to overcome phase ambiguity, supplementing the fine knowledge of position gained from the phase coordinate.

Position Resolution

Progressive charge division readouts are operationally similar to the WSA in that each triplet of the Vernier anode uses three electrodes, and the representation of the electronic noise, limiting the accuracy of measurement of the three charges in the charge domain, is the same for both devices. In the charge domain volume, whose coordinates are defined by the three electrode charges, the Gaussian electronic noise is represented by a three dimensional probability distribution, $P_{x,y,z}$, described by the equation (3-1) for a charge ratio at position x_0,y_0,z_0.

The larger the charge footprint compared to the electrode wavelength, the more it will smooth out the sinusoidal modulation, reducing it to zero when the footprint becomes much larger than the wavelength. Thus it is important to optimize the footprint size, since the effective sinusoidal amplitude, a, is crucial in defining the spatial resolution.

The effective sinusoidal amplitude defines the radius coordinate of events in the charge domain space as shown in Figure 6-5, the complete circle representing one whole electrode wavelength. Since the scale of electronic noise is constant in this plot, the effective resolution of triplet phase is the ratio of the azimuthal noise width to the circumference.

The importance of the effective sinusoidal amplitude can be demonstrated by a quantitative noise study. Differentiating equation (6-8) gives :-

$$(6\text{-}10)\quad \delta\theta = \frac{X\delta Y - Y\delta X}{X^2 + Y^2}$$

For the triplet with electrodes A, B, and C :-

$$(6\text{-}11)\quad X = \frac{B - C}{\sqrt{2}} \text{ and } Y = \frac{2A - B - C}{\sqrt{6}}$$

$$(6\text{-}12)\quad \therefore \delta X = \frac{1}{\sqrt{2}}(\delta B - \delta C) \text{ and } \therefore \delta Y = \sqrt{\frac{2}{3}}\,\delta A - \frac{\delta B}{\sqrt{6}} - \frac{\delta C}{\sqrt{6}}$$

Substituting (6-11) and (6-12) into (6-10) gives :-

$$(6\text{-}13)\quad \delta\theta = \frac{\sqrt{3}}{2}\left(\frac{(B - C)\delta A + (C - A)\delta B + (A - B)\delta C}{A^2 + B^2 + C^2 - AB - BC - CA}\right)$$

If the definitions of A, B, and C from equations (6-3), (6-4), and (6-5) are used, it follows that :-

$$(6\text{-}14)\quad \delta\theta = \frac{\sqrt{3}}{2}\left(\frac{\sqrt{3}a\cos(\theta)\delta A + \left(-\frac{3}{2}a\sin(\theta) - \frac{\sqrt{3}}{2}a\cos(\theta)\right)\delta B + \left(\frac{3}{2}a\sin(\theta) - \frac{\sqrt{3}}{2}a\cos(\theta)\right)\delta C}{\frac{9}{4}a^2}\right)$$

Electronic noise

If we use this equation to consider electronic noise, each term, $\frac{\delta A}{a}$, $\frac{\delta B}{a}$, and $\frac{\delta C}{a}$ is independent and equivalent to an electronic noise source $\frac{\delta Q}{Q_a}$, where δQ is the noise charge and Q_a is the sinusoidal amplitude in terms of charge, the three terms of equation (6-14) add quadratically to give :-

$$(6\text{-}15)\quad \delta\theta = \sqrt{\frac{2}{3}}\frac{\delta Q}{Q_a}$$

The number of resolution elements, N_{res}, per triplet wavelength is therefore given by :-

$$(6\text{-}16)\quad N_{res} = \frac{2\pi}{\delta\theta} = \sqrt{6}\pi\frac{Q_a}{\delta Q} \cong 7.7\frac{Q_a}{\delta Q}$$

The electronic signal to noise ratio, *SNR*, is given by ratio of the maximum electrode charge, Q_{max}, to the noise, δQ :-

$$(6\text{-}17)\quad SNR = \frac{Q_{\max}}{\delta Q} = \frac{Q_{a+0}}{\delta Q} \cong \frac{3Q_a}{\delta Q}$$

if, as typically is the case, $o = 2a$, where a and o are the sinusoidal amplitude and the offset.

$$(6\text{-}18)\quad \therefore N_{res} \cong 2.6SNR$$

This calculation, using realistic pattern parameters, shows the power of the Vernier readout technique. Each cycle of a pattern triplet provides phase resolution equivalent to ~2.6 *SNR*, more than two passes of the entire electronic dynamic range, whereas a typical WSA uses only 0.5-0.75 of this range over the length of the encoded axis.

One of the great benefits of the Vernier sinusoidal electrode form is that it provides uniform resolution irrespective of the phase coordinate, when electronic noise is being considered. This is demonstrated by equation (6-15), where $\delta\theta$ is independent of θ.

The number of position resolution elements follows from the phase resolution, depending on the configuration of the Vernier fine and coarse pixel schemes.

Partition noise

A similar method to that used for the WSA in section 3.3.1.1 can be used to calculate the magnitude of the partition noise limited position resolution, using equation (6-13), and the condition that $\delta A + \delta B + \delta C = 0$. In this case however, a general solution for all θ is not easily forthcoming, so we shall solve it the simple case where $C - A = A - B$,which using equation (6-6) occurs for $\theta = 0$. Solving equation (6-13) gives :-

$$(6\text{-}19)\quad \delta\theta = \frac{\sqrt{3}}{2}\left(\frac{(B-C)\delta A + (C-A)(\delta B + \delta C)}{A^2 + B^2 + C^2 - AB - BC - CA}\right)$$

Using the conditions $\delta A + \delta B + \delta C = 0$ and $C - A = A - B$, it follows that :-

$$(6\text{-}20)\quad \delta\theta = \frac{\sqrt{3}}{2}\left(\frac{(A+B-2C)\delta A}{A^2 + B^2 + C^2 - AB - BC - CA}\right)$$

If the definitions of A, B, and C from equations (6-3), (6-4), and (6-5) are used, it follows that :-

$$(6\text{-}21)\quad \delta\theta = \frac{\delta A}{a}, \text{ at } \theta = 0$$

Using the standard deviation of a binomial distribution from equation (3-9) :-

$$(6\text{-}22)\quad \delta\theta = \frac{\sqrt{f(1-f)N}}{a}$$

where, f, is the fractional value of A, and N, is the total charge in terms of a.
From equations (6-3) and (6-6), at $\theta = 0$, $f = 1/3$ and if $o = 2a$ as before, $N = 6a$.

$$(6\text{-}23)\quad \therefore \delta\theta = \frac{2}{\sqrt{3a}} = \frac{2\sqrt{2}}{\sqrt{Q}}$$

This value of $\delta\theta$ is correct for θ = 0, and 120° and 240° by pattern symmetry. If this was constant for all θ it would correspond to a number of FWHM phase resolution elements given by :-

$$(6\text{-}24)\quad N_{phase} = \frac{2\pi}{2.36.\delta\theta} = \frac{\pi\sqrt{Q}}{2.36.\sqrt{2}} \cong 2970$$

at Q = 10^7 electrons, equivalent to ~1.7 μm FWHM for a 5 mm coarse pixel dimension. Though the general solution has not been found, the variation of $\delta\theta$ with θ, as with the electronic noise, is not expected to vary dramatically from this figure.

Other possible geometries

The simple sinusoidal electrode shape is not the only solution which meets the constraints for geometric charge division discussed in 6.2.1.3. There are alternative geometries. One, for example, using $\sin^4\theta$ electrode variation, is described by the following equation which evaluates the total electrode area at all positions as the sum of the three electrode components :-

$$(6\text{-}25)\quad \left(o + a.\sin^4(\theta)\right) + \left(o + a.\sin^4(\theta + \frac{2\pi}{3})\right) + \left(o + a.\sin^4(\theta + \frac{4\pi}{3})\right) = \frac{9}{8}a + 3o$$

It can be seen that this satisfies the requirement that the sum of the triplet electrodes is constant. The locus of point, P travelling along the position axis is no longer a circle in charge domain space, but has lobes with a three-fold symmetry. If equation (6-13) is evaluated to determine the position resolution using the new electrode forms from (19), $\delta\theta$ is found to be a complex function of θ, given by :-

$$(6\text{-}26)\quad \delta\theta = -8\sqrt{\frac{2}{3}}\frac{\delta Q_A}{Q_A}\left(\frac{1}{\sqrt{256\cos(\theta)^6 - 384\cos(\theta)^4 + 144\cos(\theta)^2 - 25}}\right)$$

Thus position resolution varies cyclically with phase. For this reason together with its sensitivity to charge cloud footprint, discussed in the following section, this pattern, together with all others not using pure sinusoids, is not ideal.

Spatial frequency analysis of the electrode structure

Qualitative study of the primary spatial frequency components of the electrode variation for any particular design can usefully predict the sensitivity to variations in the charge footprint. The effective geometry of the readout is given by the convolution of the pattern electrode geometry with the charge footprint distribution. In spatial frequency space this corresponds to a multiplication of corresponding spatial frequency distributions. The sinusoidal pattern can be described in two dimensional frequency space as a delta function close to the origin, representing the fundamental sinusoidal frequency, accompanied at higher frequencies (i.e. further from the origin) by a complicated two dimensional function representing the pattern fine structure. The azimuthally symmetric and monotonic charge footprint distribution is represented by an azimuthally symmetric, though not necessarily monotonic, spatial frequency distribution whose radius scales inversely with its physical size. Pattern modulation will occur if the nominally low frequency charge footprint function has significant power at frequencies represented by the fine structure, i.e. if it is more peaked (smaller in physical extent) or has edges. This will cause their product at the fine structure frequencies to be finite, and modulation will become apparent. If charge footprint is large enough so that no modulation occurs, then changes in the footprint size, whose width varies inversely with the width of the distribution in frequency space, modify the effective pattern geometry solely by attenuating to a greater or lesser extent the delta function at the fundamental pattern frequency. This is equivalent to reducing the amplitude of the pattern sinusoid: the broader the footprint, the narrower it's width in frequency space and the greater the attenuation of the sinusoid amplitude.

If one considers the $\sin^4$ pattern, it will be represented by a number of discrete sine functions at the fundamental frequency and at higher harmonics :-

$$(6\text{-}27)\ \sin^4(\theta) = \frac{3}{8} - \frac{\cos(2\theta)}{2} + \frac{\cos(4\theta)}{6}$$

It is immediately obvious that even without modulation, changes in the footprint size will cause varying degrees of attenuation to the different frequency components of the pattern, causing the pattern form to be, not merely attenuated, but distorted. This would impact severely and irrecoverably on the decoding algorithm. This example serves to illustrate the unique property of the sinusoidal solution, making it by far the most suitable cyclic function to use for the electrode variation.

Exploiting the cyclic phase coordinate

The Vernier anode and its derivatives use the same basic technique of charge division amongst discrete electrodes combined with charge measurement as does the WSA. However they differ fundamentally from the WSA in the way in which the real position domain maps onto the multi-dimensional space defined by each unique charge ratio. Whereas the WSA maps 2-D position space on to the two dimensional plane defined by $Q_W + Q_S + Q_Z = constant$, each of the Vernier anode triplets of electrodes map only 1-D position space. The line representing the encoded position axis in charge domain space is continuous, curved and bounded (see Figure 6-5). This means that the triplet electrode pattern can be repeated ad infinitum. Thus, a given ratio of charges will correspond to an x position unique only within the 2π radians of a single revolution around the bounded axis. However, if more than one wavelength of the pattern is used, it is impossible to predict on which cycle the encoded event has been detected using one electrode triplet alone. Several practical pattern designs which use multiple sets of triplets to overcome this ambiguity are now described.

6.2.1.5 Methods to overcome cyclic position ambiguity

The Vernier scheme

For simplicity we will begin by considering a one dimensional readout. One solution to overcome the cyclic position ambiguity is to use a further triplet of electrodes, the charge cloud being collected on six electrodes in total. In this scheme, the second triplet is also used to encode a phase co-ordinate which varies in the same axis as the co-ordinate generated by the first triplet. The wavelength of this second triplet differs from the first, so that the difference between the two phase co-ordinates varies slowly with position and is unique for a large number of wavelengths, over a range equalling the lowest common multiple of both wavelengths. This technique allows determination of a coarse position for an event, eliminating the ambiguities which occur beyond a one wavelength range with a single electrode triplet. Coarse and fine position information are combined to generate a continuous, linear position co-ordinate extending over the unique encoded range of the two triplets.

This principle of operation is analogous to the Vernier technique used to enhance the accuracy of measurement scales, but in a reciprocal sense. The standard Vernier technique relies on the alignment of two coarse scales, each with the same number of divisions, n, but with slightly different pitches, $p \times \frac{n-1}{n}$ and p, to provide a fine interpolated measurement with resolution of $\frac{1}{n} \times p$. The Vernier readout design described here uses the alignment (provided by the phase difference measurement) of two fine scales, whose pitches are represented by the triplet wavelengths, to determine a coarse position, i.e. the position of the particular wavelength in which the fine scale alignment occurs.

The 1D Vernier scheme (six electrodes)

The simple Vernier scheme as previously described can be immediately used as a one dimensional image readout consisting of six electrodes, arranged as two triplets, each providing a phase co-ordinate. In practice, the anode layout is essentially similar to the WSA, being comprised of a series of repeating elements with a pitch of typically 1 mm of less. Each element is divided into two halves, each half being subdivided into the three electrodes making up one triplet.

The 2D Vernier scheme (twelve electrodes)

In two dimensions the same technique could be used for both axes. This requires an extra six electrodes for the second axis. The event charge cloud is shared among all twelve electrodes which are repeated in every pattern pitch. One pair of triplets behaves and can be constructed identically to their counterparts in the one dimensional six electrode Vernier pattern. The extra pair of triplets is arranged so that the mean electrode ratios which define the two phases vary in an orthogonal direction.

Figure 6-6 shows a schematic of a possible pattern design which makes use of the same mechanism used by the WSA to encode the second dimension, namely discrete sampling. Whereas the widths of the electrodes encoding the first position axis vary continuously, the orthogonal axis is encoded by similarly continuous electrodes arranged parallel to those of the first axis, but having constant widths. These widths represent the unique ratios of the two second axis triplets, and vary from pitch to pitch. This technique is analogous to the operation of the strip axis of the WSA where the strip widths vary linearly from pitch to pitch, effectively a discrete sampling of a virtual wedge electrode along the direction of the strip axis. The widths of the electrodes encoding the Vernier discrete axis similarly represent the ratio of electrode amplitudes of a virtual six electrode pattern, which varies continuously along the discrete axis, sampled at discrete points separated by one pitch dimension.

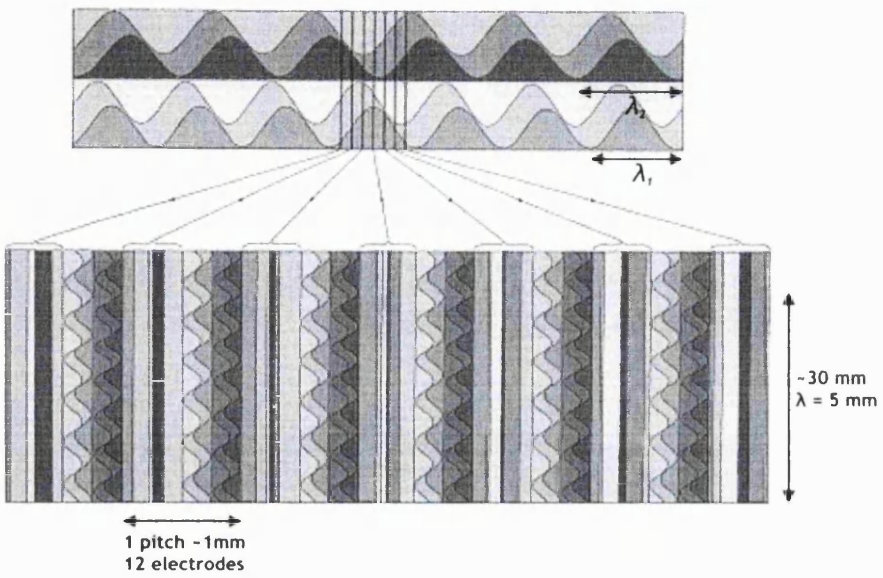

Figure 6-6. A schematic of the 12 electrode two dimensional anode. The readout pattern shown in the lower diagram has six electrodes in the y axis which vary continuously whereas those for the x axis discretely sample the nominal electrode ratios shown above. The y axis scale has been shrunk for clarity.

The size of the charge footprint collected by the anode pattern is set by the requirement that the pattern fine structure, i.e. the high spatial frequency of the repeating electrode elements, in every pitch is smoothed out, and the discretely sampled second axis is smoothly interpolated.

The Spiral scheme

The Spiral Anode is an offshoot of the Vernier Anode, developed for applications requiring simpler electronics and smaller image formats. It shares some of the features of the basic Vernier concept but uses an alternative technique to determine the coarse pixel position which requires only three electrodes per axis. Fine position determination is based on the same principle as the Vernier, relying on the phase calculated from the ratio of the charge collected by the electrodes triplet. Unlike the Vernier, however, the coarse position, which corresponds to the determination of the particular electrode cycle in which the event lies, is also parameterized by the same three electrodes. This is accomplished by the varying the sinusoidal electrode amplitude, and causing the radius as measured in the charge domain space, to vary linearly with position. The radius of an event can thus be used to uniquely identify the coarse position. Because the radius changes the electrode variation is only quasi-sinusoidal and both the electrode amplitudes and wavelengths vary linearly with position. The pattern is not cyclic and in the charge domain, the representation of the possible charge ratios is an Archimedean spiral c.f. the circle produced by one triplet of the Vernier pattern.

A plot of the locus of possible charge ratios in the charge domain for all positions along one axis of this pattern is shown in Figure 6-7. This pattern variant was named the Spiral anode (or SPAN) after its graphical representation in the charge domain. This spiral represents the mapping of the

one dimensional position axis on to the volume within the charge domain defined by the three electrode collected charge amplitudes. Using this particular mapping the Spiral Anode utilises the large number of the pixels with which the WSA addresses the two position dimensions, over one dimension alone. As with the Vernier Anode, the position resolution can greatly exceed the charge measurement accuracy.

While in principle, the form of the spiral curve and the mapping of position space on to this arc could be arbitrary so long as every encoded position defined a unique charge ratio, the earlier discussion of qualitative spatial frequency analysis indicates that the electrode form should be chosen to minimize its spatial frequency components. Thus discontinuities or high frequency electrode variation (high curvature in the charge domain representation) were avoided. An Archimedean spiral with the form $r \propto \theta$ was used in order to make best use of the available charge ratios, and to ensure that the likelihood of coarse position miscoding remained constant by maintaining constant arm separation. The mapping of position axis, x is arranged so that $\delta x \propto r.\delta\theta$ to ensure that position resolution is constant across the readout.

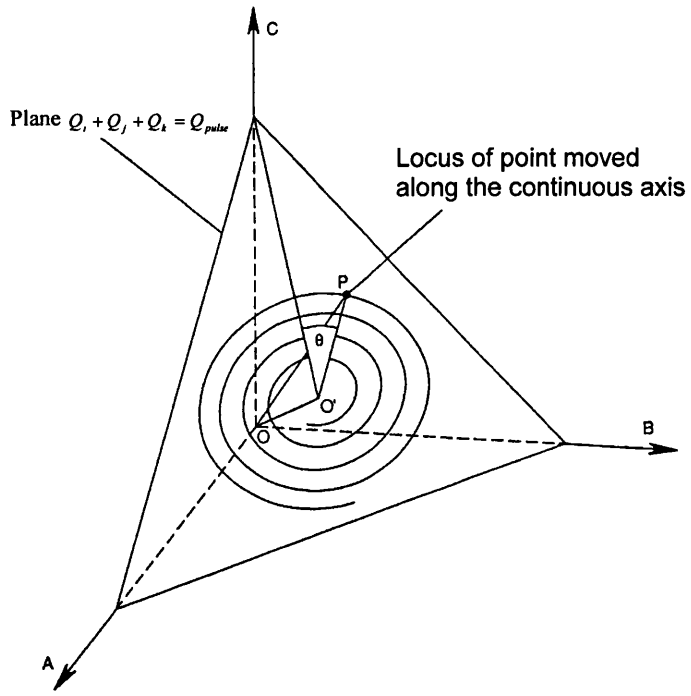

Figure 6-7. The locus of allowed charge ratios for one SPAN electrode triplet. The spiral represents one axis of the pattern.

The Spiral anode definitions leading to the variation of the electrode width, *y*, along its length, x, are as follows :-

$$r = f\theta$$

$$r\frac{d\theta}{dx} = c$$

$$y = r\sin(\theta) \quad (6\text{-}28)$$

$$\therefore y = \sqrt{2cfx}\sin(\sqrt{\frac{2cx}{f}})$$

It should be noted that the requirement $\delta x \propto r.\delta\theta$ is only an approximation to $\delta x = \delta s$ since the arc length element δs is not quite tangential, having a small radial component as well. This is neglected since it results only in a second order variation in resolution and is taken account of in the decoding algorithm thus having no effect on linearity.

6.3 Practicalities of pattern design and implementation

The progressive geometry readout concepts have been described thus far mainly in terms of qualitative definitions indicating how the mean electrode areas should vary in order to encode the position co-ordinate. Adaptation of these schemes into physically realizable and practical, working charge division readouts, requires certain criteria to be met, which are common to virtually all charge division readout patterns.

Table 6-1 defines the meaning of the pattern parameters necessary to describe practical designs and which are referred to in the following discussion.

The most generic form in which charge division readouts are realized is as a conductive pattern of planar electrodes deposited on an insulating substrate on which a charge cloud may be either collected or induced. Multiple wire planes are also sometimes used, but these are not as amenable to geometric division by means of modulated areas, a requirement for the progressive geometry devices described here. The prime characteristics of these charge division readouts can be summarized as follows :-

1. The charge division principle is based on the assumption that the collected charge per electrode is proportional to the mean local area of each electrode.
2. The electrode pattern divides the charge cloud such that it is shared among all the electrodes constituting the pattern.
3. Charge division among all electrodes at every position is accomplished by using a fine structured pattern consisting or repetitive or pseudo-repetitive pitches. Every electrode is represented in each pitch and every pitch has the same width.
4. The pattern is designed so that the ratio of mean local electrode areas at any position, as represented by the relative charge levels on each electrode, is unique.

5. Charge collected by each electrode is measured serially, per event, and a position encoding algorithm used to determine the position co-ordinates of each event.

These generalized rules apply to most such readouts though there are some exceptions, for example :-

1. The graded density anode consists of a wire array, connected as two groups, where the collection area corresponding to each group varies linearly with position. This readout also has a dimension analogous to the 'pitch' of a planar pattern equal to the extent of the smallest region bounded by a transition from group A to group B in a fixed direction.
2. The electrodes need not always be represented in every pitch. This exception applies in the mosaic WSA. However this device could be regarded as several adjacent patterns.
3. The Vernier pattern itself does not exactly comply with the 'electrode charge proportional to local area' requirement in the strictest sense, owing to the non-linear electrode function allied with the finite extent of the charge footprint, causing reduction in the effective sinusoidal amplitude.

Image axis	The encoded position axis in the output image.
Electrode pitch	One repeat of the electrode structure, the minimum area containing one element of each electrode.
Pitch direction	The direction along the length of the electrodes, parallel to pitch boundaries.
Electrode triplet phase	The phase defined by the relative amplitudes of the three electrodes constituting a triplet, and visualised in the charge domain.
Phase variation direction	The direction normal to lines of constant phase, along which the rate of change of phase is a maximum.
Phase wavefront	A line joining points of constant phase, normal to the phase variation direction

Table 6-1. Definition of practical pattern parameters

The idealized pattern algorithm, such as that already defined for the Vernier anode or SPAN for instance, may be used to construct a physical pattern design by applying it in reverse to determine the correct ratio of electrode areas at any point on the two dimensional electrode pattern. The electrode widths normal to the pitch direction can be calculated using the fractional ratio of electrode areas provided by the algorithm, and the pitch dimension. The widths represent the

electrode ratio for points lying along the centreline of the particular pitch (or sub pitch) of the pattern.

The traditional layout, used in the WSA, uses a pitch direction parallel to one of the image axes. Thus, in the WSA, one electrode will be physically parallel to its axis of linear variation, producing a wedge shaped profile which is identical from pitch to pitch. The electrode encoding the orthogonal axis does not vary in the pitch direction, but orthogonal to it. Called the strip, this electrode does not change width in the pitch direction, but varies linearly in width between pitches.

In its practical implementation, the Vernier anode, whether one dimensional (six electrode) or two dimensional (twelve electrodes), has much in common with the WSA. One of the early practical realisations of the 12 electrode Vernier anode structure is shown in Figure 6-6. Whereas the six electrodes of the y axis vary continuously, those of the x axis do not vary along their length but their widths represent the notional x axis electrodes widths, sampled at a discrete point. The x axis is known as the 'discrete axis' and is analogous to the Strip axis of the WSA whose width discretely samples a notional wedge. The twelve electrode structure is repeated every pitch and, like the WSA, the charge cloud must spread over several pitches to filter out the pattern fine structure.

Whereas the continuous axis continuously maps the triplet phase co-ordinate as a circular locus on to the plane in charge domain space, the discrete axis maps its co-ordinate only at discrete but regularly spaced points. The charge cloud footprint, which is collected over several discrete samples, causes the pattern to linearly interpolate the charge centroid position between these discrete samples. With eight discrete samples per revolution, the interpolation will cause the discrete position axis to be mapped as an octagonal locus with rounded vertices; the vertices corresponding to the sample positions and the straight edges representing the interpolation between samples positions. If the charge cloud footprint size is increased, the locus approaches a circle but of reduced radius, thus reducing resolution. The two axes produce slightly different curves in the charge domain.

There is no essential reason why the pitch direction needs be aligned so as to provide 'continuous' and 'discrete' electrodes for either the wedge and strip or for any other pattern of similar operation. If an arbitrary pitch direction is used, the wedge and strip is transformed into a pattern with two wedges and a Z electrode. The gradient of the wedges and their offset between pitches depends on the pitch direction chosen. An arbitrary pitch direction can also work with the Vernier and SPAN designs and this has been used to gain certain advantages.

6.3.1 Practical Implementation

The traditional pattern layout using continuous and discrete axes is not ideal due to differences in behaviour between the axes. An alternative pattern layout has been devised which eliminates the

static sampling points of the discrete axis in order to avoid the non-ideal behaviour this creates, especially for progressive geometry readout designs. For SPAN the axis of the continuous electrodes, the pitch direction, is arranged at 45° to the orthogonal position co-ordinate axes as shown in Figure 6-8. For patterns using independent sets of electrodes for each axis, it has the advantage that the two electrode sets are identical in shape, apart from being mirrors of each other. The curve described by the pattern in the charge domain is identical for both axes, and this introduces the possibility of multiplexing one 'position look-up' table (should that be the method used to implement the decoding algorithm).

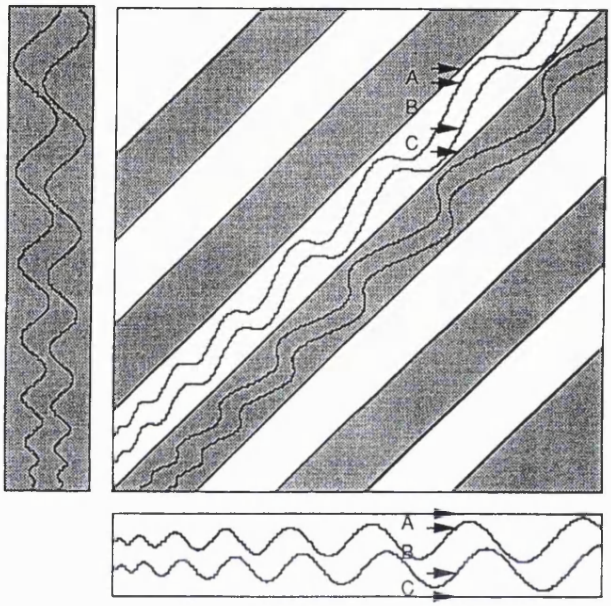

Figure 6-8. A schematic of the projected two dimensional SPAN readout.

The modified pattern layout can be applied to all variants of both the Vernier and Spiral anodes. For all patterns where the phase variation directions are parallel to their respective axes, the pitch structure of the pattern is arranged at 45° to the two dimensional image axes. Since the pitch direction is at 45° to the phase variation direction, the spatial frequency of the sinusoidal variation in the pitch direction is $\sqrt{2}$ times lower. Control of the phase variation direction is achieved by offsetting the phase of electrodes by a length equal to the repeat pitch every pitch, so that the phase variation direction is parallel to the encoded axis.

In the general case, it can be seen that by choosing the correct physical electrode wavelength and phase offset between pitches, the phase variation can be generated in any arbitrary direction. In such a pattern, the electrodes will still vary continuously, albeit at lower or higher spatial frequencies, depending whether the angle is increased or reduced. In the special case where pitch direction is orthogonal to the phase variation direction, the wavelength of the electrode sinusoidal variation becomes infinite. This equates to the electrode widths being constant and occurs in the discrete axis of the traditional pattern arrangement.

Since the charge footprint is collected over several pitches, the centre of gravity of the charge collected on each pitch will determine the phase for that charge contribution, and its magnitude will determine the weight applied to that contribution. This is carried out implicitly on the anode itself, since all corresponding electrodes in every pitch are connected.

6.4 Advances in pattern design

The simple one dimensional six electrode Vernier is capable of a theoretical resolution equal to the product of the numbers of fine and coarse resolution elements. Practically, the number of the fine resolution elements is given by the wavelength divided by the FWHM position resolution. The number of coarse resolution elements is simply the number of uniquely distinguishable pattern wavelengths determined using the difference between the two fine position (or phase) measurements. Since the fine position is used to determine the coarse position, the number of coarse resolution elements must always be significantly less than the number of fine resolution elements to avoid the possibility of coarse position ambiguity. Even if the coarse to fine resolution element ratio was chosen conservatively to be 1:10, and the fine resolution was 500 pixels per wavelength, the theoretical overall resolution would be $50 \times 500 = 25000$. However, this potential is not readily achievable since practical considerations come into play. As previously discussed, the practical minimum electrode wavelength is set by the charge footprint size, which itself is defined by the pattern pitch dimension. There are a number of practical factors limiting the minimum pitch size :-

1. Inter-electrode capacitance increases as the pattern pitch is reduced. This increases the electronic noise which degrades the position resolution.
2. Mechanical errors in the pattern geometry increase proportionately as the pitch is reduced. The laser machining technique used for pattern production would be unsuitable below a mean electrode width of ~50 microns.
3. The practicalities of making electrical interconnections using wire bonding techniques limit the average electrode width to ~ 75 microns using currently available equipment.

In practice, the pitch size (typically no less than 200 microns per triplet) sets the wavelength, which itself sets the size of the coarse resolution element. Thus for a given readout format, only a limited number of the possible coarse position elements can be used. Even if the pattern format required is very large, enabling use of a greater proportion of the available coarse resolution, the increased electrode capacitance, approximately proportional to readout area, eventually places an upper limit on the resolution due to the increase in electronic noise. The trade-off between all these factors is complicated and specific to each application. Despite the fact that the full theoretical resolution of the Vernier anode cannot be realised in practice, the available fraction still provides a large improvement in resolution over competitive charge division devices.

The two dimensional Vernier pattern so far described is an inefficient use of resources because it requires twelve electrodes but is able to utilize only a small fraction of the available resolution. This prompted the development of a modified two dimensional Vernier scheme, using a lower number of electrodes combined with a more efficient use of the available resolution, to provide equal imaging performance with fewer resources.

Instead of operating the pattern as two independent axes (with two extra triplets to provide two independent coarse position determinations), the coarse position can be determined directly as a two dimensional coordinate using only one extra electrode triplet in addition to the two required for fine resolution. Thus the modified pattern consists only of three electrode triplets or nine electrodes in total. This scheme is initially described in a simple version which uses two triplets to provide fine position resolution in orthogonal axes, whilst the third provides two dimensional coarse position.

6.4.1 The Simple Nine Electrode Vernier Scheme

Three electrodes triplets can be arranged to define three phases which vary across the two dimensional pattern area as shown in Figure 6-9. This figure uses a vector representation where vector angle and magnitude represents the triplet phase directions and wavenumbers normalized with respect to the coarse pixel size. The phases A and B vary orthogonally and the respective phase values constitute the respective fine x and y co-ordinates of an event within a coarse pixel boundary. The phases A and B alone provide insufficient information to determine in which coarse pixel an event lies. Coarse pixel determination requires an additional phase, C which varies slowly across the pattern in the direction shown. Although a single value of phase C can be measured in several coarse pixels, the co-ordinate A,B,C uniquely defines both the fine and coarse position in two dimensions. Figure 6-10 shows the mapping of the readout plane at all positions, (x,y) into the phase domain volume defined by A,B,C; the three dimensional phase co-ordinate produced by the three electrode triplets from an event.

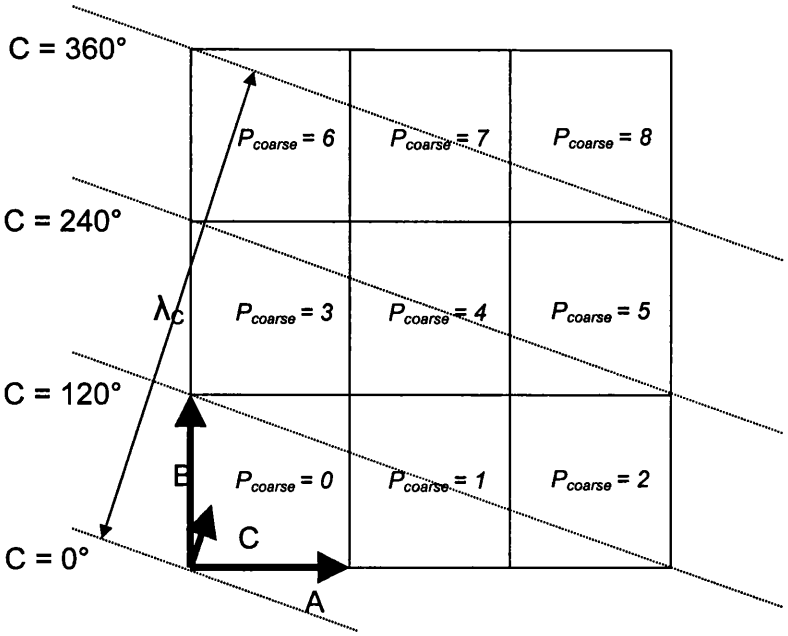

Figure 6-9. The simple 9 electrode Vernier readout vector plot. The vectors represent the directions and wavenumbers of the three phases. This readout scheme uniquely encodes all x,y positions within the 3 × 3 arrangement of coarse pixels.

The position is decoded by an algorithm consisting of two components. The Cartesian position co-ordinate in each coarse pixel is simply that given by the phases of triplets A and B (A,B). The coarse position co-ordinate (the coarse pixel number) is calculated by comparing the measured phase C to an artificially phase C′ generated from the fine position co-ordinate (A,B). Though Figure 6-9 shows a 3 × 3 coarse pixel arrangement, any square or rectangular format is possible. For a pattern of N coarse pixels, the difference C - C′ can only be one of N discrete values, each corresponding to a unique coarse pixel address, following the order shown in Figure 6-9. The coarse pixels can be arranged in square or rectangular formats simply by modifying the wavelength and direction of phase C. The coarse pixels themselves could be rectangular if phase directions and wavelengths of A and B were also modified to suit. For a pattern with m × n coarse pixels, the coarse position decoding algorithm can be described mathematically as :-

$$(6\text{-}29)\quad P_{coarse} = \frac{(m \times n)}{2.\pi}.(C - \frac{A}{m \times n} - \frac{B}{n})$$

where: *A, B,* and *C* are the triplet phases in radians

m and *n* are the numbers of unique coarse pixels in the x and y axes respectively

P_{coarse} are consecutive integer values identifying each coarse pixel uniquely

In practice, P_{coarse} varies around the expected integer value owing to noise sources associated with charge measurement and phase calculation. Its correct value is selected by choosing the nearest integer. Phases A, B and C are calculated directly in pixel units such that $2.\pi$ radians are represented by the number of pixels, n_c, desired per coarse pixel in the final two dimensional

image. The normalizing factor, 2π, is accordingly replaced by the value n_c. The equations determining the final x and y coordinates are as follows :-

$$(6\text{-}30)\quad P_{coarse} = \mathrm{int}\left(\left(\frac{m \times n}{n_c}\right) \times \left(C - \frac{A}{m \times n} - \frac{B}{n}\right) + 0.5\right)$$

$$(6\text{-}31)\quad X = x_{coarse} + x_{fine} = (P_{coarse} \bmod n) \times n_c + A$$

$$(6\text{-}32)\quad Y = y_{coarse} + y_{fine} = \mathrm{int}\left(\frac{P_{coarse}}{m}\right) \times n_c + B$$

The maximum number of coarse pixels in the pattern is limited by the phase resolution of C. This determines the number of uniquely encoded coarse pixels which may be unambiguously identified by the decoding algorithm.

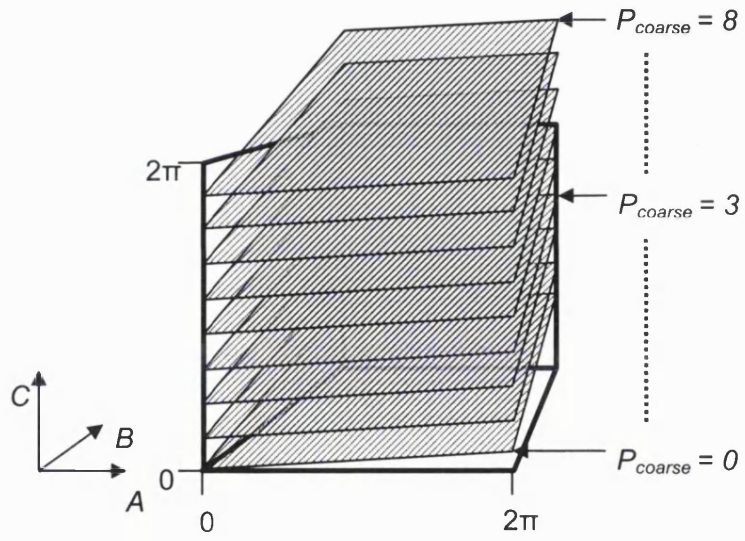

Figure 6-10. The phase domain volume for the simple 9 electrode Vernier readout. This schematic shows how the coarse pixels are stacked up vertically as a series of parallel, inclined planes.

This device has several advantages over the twelve electrode Vernier readout which can be summarized as follows :-

1. It uses nine electrodes instead of twelve, reducing the electronic complexity by 25%.
2. It achieves comparable resolution, since it uses the potential resolution of the Vernier technique more efficiently, with less wastage.
3. The smaller number of electrodes allows a smaller pitch to be used. In turn this permits use of a shorter electrode wavelength and corresponding smaller pixel size for a given electronic resolution.

4. The average charge collected per electrode is increased by 33%, increasing signal to noise ration and dynamic range.

One drawback of this scheme is the presence of fixed pattern noise, which is completely absent in the standard Vernier scheme. Fixed pattern noise is a result of natural alignment of digital pixels in particular directions within the charge domain. It manifests itself as small regions of the position axis where event co-ordinates, instead of being uniformly distributed, are quantized into a small number of discrete values. It occurs in this design because only one triplet is used to generate the fine co-ordinate, unlike the original Vernier anode, in which the fine co-ordinate for one axis can be more accurately calculated when both phase values are used. The use of both phases in the original Vernier design eliminates fixed pattern noise since pattern geometry can be chosen ensure that co-alignment of fixed patterning between phases never occurs.

6.4.2 A Modified Nine Electrode geometry

The phase geometry described in Figure 6-9 need not be arrived at by using phases generated by the three electrode triplets directly. Instead, these can be generated as the resultants of simple arithmetical combinations of the real triplet phases. The arithmetical combinations used are as follows :-

$A = A' + B'$; $B = B' + C'$; $C = A' + C'$, where A', B', C' are the real electrode triplet phases. For a given pattern geometry, defined by the arrangement of coarse pixels (i.e., m × n) in the uniquely encoded position range, there is only one solution for the wavelength and direction of the three real triplets, A', B', C'. This solution is shown graphically in Figure 6-11 using a vector representation where vector angle and magnitude represents the triplet phase directions and wavenumbers normalized with respect to the wavenumbers of A and B. This vector representation was chosen because it obeys the rules regarding the addition of two phase values to correctly determine the resultant phase direction and wavenumber. Thus the vector sum A'+B' generates a resultant vector that predicts the correct phase for the resultant A.

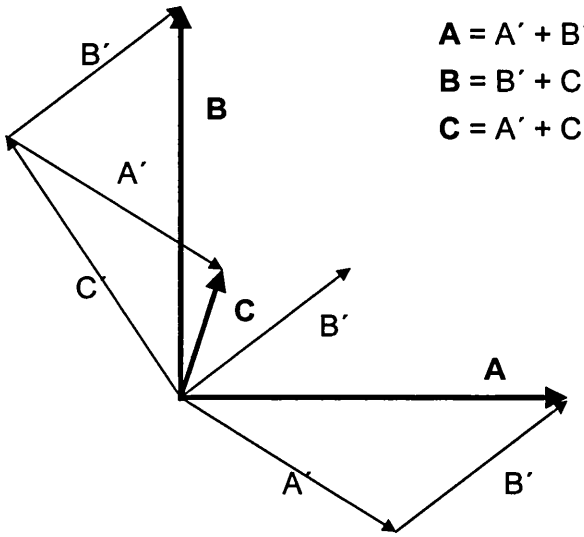

Figure 6-11. The vector representation of the modified nine electrode geometry.

Whilst this method requires three extra parallel addition steps in the position decoding algorithm, it has several benefits for performance :-

1. Fixed pattern noise is virtually eliminated because the fine position co-ordinate is generated from the addition of two phases whose directions are unaligned. This will be discussed in more detail later.
2. The three real triplet wavelengths are longer and closer in value than the resultants A, B and C. For a given resolution this results in a significant increase in the smallest electrode wavelength, reducing the constraint of charge cloud footprint size and pitch dimension with ensuing benefits.

The practical implementation of this pattern uses the technique described earlier whereby the electrode wavelength and phase offset between pitches is determined to generate a phase change with required wavelength and direction for the A′, B′ and C′ electrode triplets. For simplicity, the pitch direction is chosen to lie along the position co-ordinate x axis with the phase directions disposed at their specific angles, all close to 45°, to this direction. The specific angles depend on the coarse pixel number and layout, whether square or rectangular. Equations (6-33), (6-34) and (6-35) show how the required geometry determines the angles and magnitudes of the wavenumber vectors for a readout using m × n coarse pixels, each coarse pixel being square. The wavenumber vector co-ordinates are given by :-

$$\vec{A}' = \frac{(m.n+1)}{2.m.n}, -\frac{(n-1)}{2.n}$$

$$(6\text{-}33)\quad \therefore \lambda_A = \sqrt{\left(\frac{2.m.n}{(m.n+1)}\right)^2 + \left(\frac{2.n}{(n-1)}\right)^2}$$

$$\therefore \theta_A = \tan^{-1}\left(-\frac{m.(n-1)}{(m.n+1)}\right)$$

$$\vec{B}' = \frac{(m.n-1)}{2.m.n}, \frac{(n-1)}{2.n}$$

$$(6\text{-}34)\ \therefore \lambda_B = \sqrt{\left(\frac{2.m.n}{(m.n-1)}\right)^2 + \left(\frac{2.n}{(n-1)}\right)^2}$$

$$\therefore \theta_B = \tan^{-1}\left(\frac{m.(n-1)}{(m.n-1)}\right)$$

$$\vec{C}' = -\frac{(m.n-1)}{2.m.n}, \frac{(n+1)}{2.n}$$

$$(6\text{-}35)\ \therefore \lambda_C = \sqrt{\left(\frac{2.m.n}{(m.n-1)}\right)^2 + \left(\frac{2.n}{(n+1)}\right)^2}$$

$$\therefore \theta_C = \tan^{-1}\left(-\frac{m.(n+1)}{(m.n-1)}\right)$$

The physical electrode wavelengths are given by $\frac{\lambda_i}{\cos(\theta_i)}$, where λ_i is the triplet wavelength, and θ_i is the angle between the pitch direction and the phase direction. Figure 6-12 shows a schematic of the modified 9 electrode Vernier readout. The electrode triplet defining phase A is drawn in bold, and the dashed line represents a line of constant phase A. The linear phase offset per pitch is used to define the direction of the phase change.

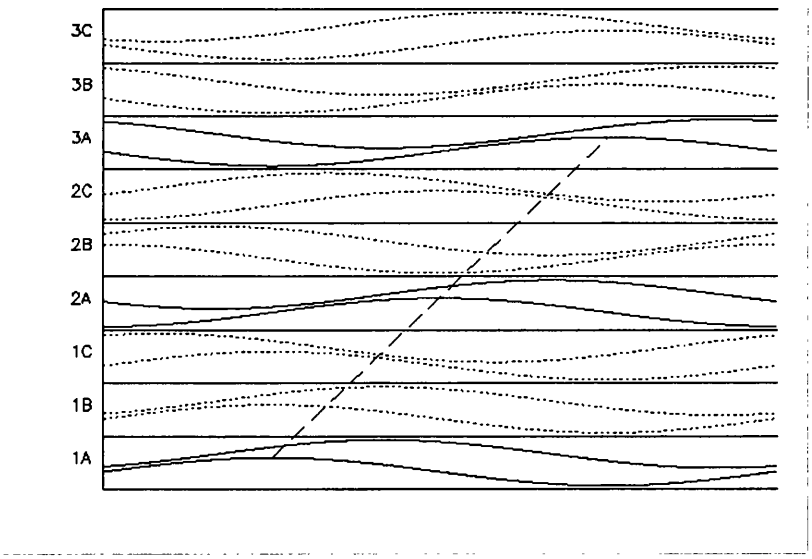

Figure 6-12. A schematic of the 9 electrode Vernier anode showing three pitches.

The two dimensional position co-ordinate is determined using the same algorithm as the simple nine electrode Vernier, with the addition of three initial calculations required to generate the intermediate phases A, B and C, which are equivalent to those of the simple nine electrode Vernier pattern.

$$(6\text{-}36)\ A = (A' + B') \bmod n_c$$

(6-37) $B = (B' + C') \bmod n_c$

(6-38) $C = (A' + C') \bmod n_c$

(6-39) $P_{coarse} = \text{int}\left(\left(\frac{m \times n}{n_c}\right) \times \left(C - \frac{A}{m \times n} - \frac{B}{n}\right) + 0.5\right)$

(6-40) $X = x_{coarse} + x_{fine} = (P_{coarse} \bmod n) \times n_c + A$

(6-41) $Y = y_{coarse} + y_{fine} = \text{int}\left(\frac{P_{coarse}}{m}\right) \times n_c + C$

The phases shown in Figure 6-13 are combined to produce three resultants, A = A′+B′, B = B′+C′, and C = A′+C′. The vectors describing the wavelength and direction of each phase variation are chosen so that A and B are normal and have equal wavelengths. These two resultant phases represent the fine 'x' and fine 'y' position. The C phase varies across the *x,y* plane in such a way that that P_{coarse} varies discontinuously in steps. Each step corresponds exactly to the unambiguous range of the A and B phases and the result is depicted in the last plot on Figure 6-14. The steps define the coarse x and y co-ordinates.

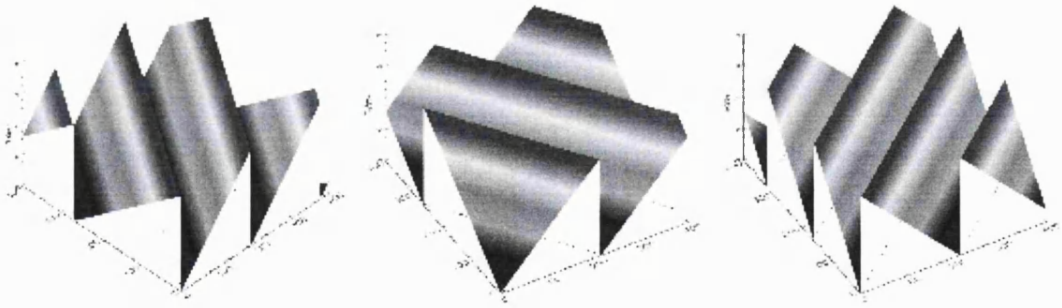

Figure 6-13. The variation of the phases A′, B′, and C′ in the pattern x and y co-ordinates. The z axis in these plots represents the phase coordinate which is cyclic.

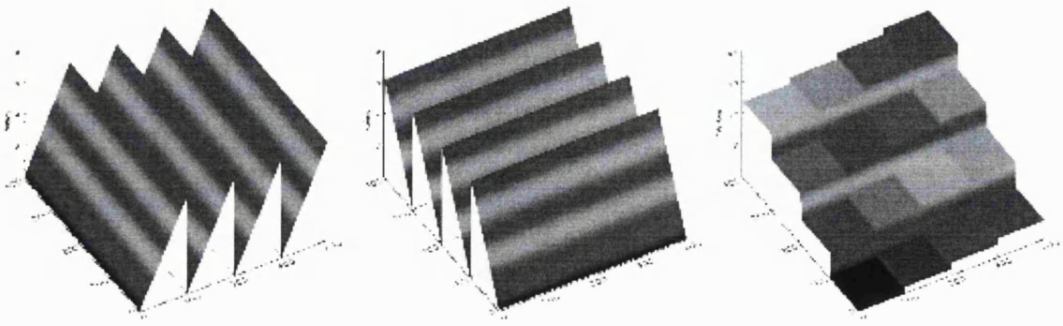

Figure 6-14. The variation of the resultants X, Y and P_{coarse} with position.

A significant practical advantage of the cyclic nature of the electrodes, which applies to all the Vernier schemes, is that it allows the pattern to be extended beyond the unambiguous active area while maintaining its correct geometry. The full unambiguous pattern area can be used for imaging, the pattern being extended outwards to capture the whole charge footprint from events at the edge. This makes the best possible use of the electrode dynamic range and resolution potential.

The Vernier readout is highly immune to the fixed pattern noise exhibited by linear devices such as the WSA. This noise results from digitization of the individual electrode values, and occurs at spatial coordinates corresponding to particular alignments of the discrete pixels in the three dimensional charge domain space. It is a permanent feature of any device using charge division and digital charge measurement, but its scale is usually much smaller than the noise limited position resolution which sets the sensible image pixel size, and thus it smoothed out and not apparent in the data. However, at low pulse heights, when the effective digitization of the readout electrode dynamic range is undersampled, and its scale becomes comparable to the electronic noise limited resolution, it can become visible. If this occurs, a larger pixel size can be used to reduce the fixed pattern noise, but only at the expense of position resolution. The nature of the cyclic electrode structure of progressive geometry readouts means that the dynamic range of the charge measurement electronics is exploited many times over the range of the pattern axes. Thus the degree of oversampling provided, even using 12-bit ADCs, is generally more than adequate to virtually eliminate fixed pattern noise at scales comparable with the readout resolution, irrespective of pulse height. The use of resultant phases to define A, B and C, further reduces the fixed pattern effects.

Fixed patterning in the Vernier anode occurs because at certain phase angles, the discrete pixels (generated by digitizing the electrode signal) become aligned radially. Near these regions, which occur at particular angles defined by the three dimensional symmetry of the charge domain, the phase increments discretely. However, by using resultant phases to generate the X and Y coordinates, the pattern geometry both scales down the feature size (because the triplet phase directions are angled with respect to the encoded position axis), and prevents the simultaneous occurrence in both x and y, of fixed pattern noise, thus minimizing its impact. Figure 6-15 shows a plot of event data from one triplet in the charge domain. The small event radius and low amplitude of these signals has caused them to be digitized with low accuracy, accentuating the fixed pattern noise, which is visible as radial patterning specific angles, predominantly every 60°. The position coordinate is calculated from the sum of two such phase determinations, and only the occurrence of simultaneous fixed pattern noise in both phases gives rise to such noise in the actual image, and then, only in one position axis.

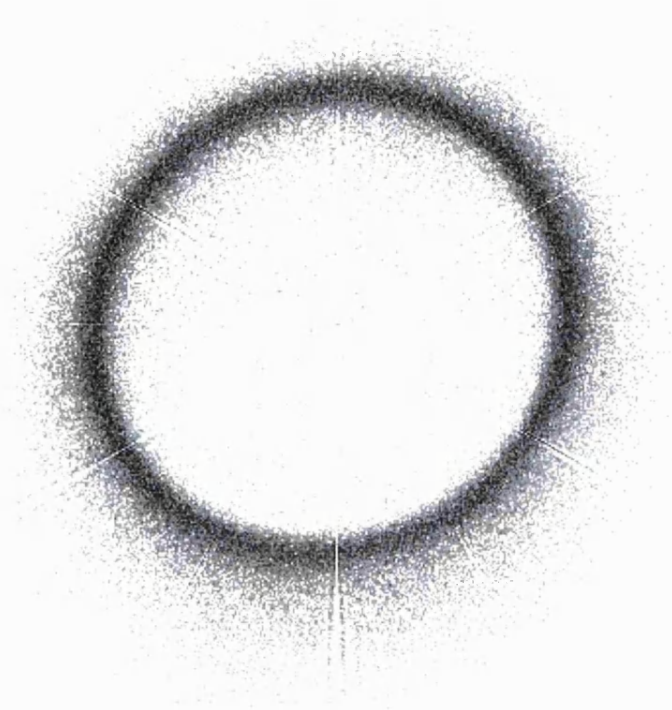

Figure 6-15. Event data from one electrode triplet plotted in the charge domain. This data was taken using a large charge footprint which exaggerates the scale of the fixed pattern features.

The possibility of coarse position miscoding as a result of charge measurement error was simulated for a pattern with a 4 × 4 coarse pixel layout, using a conservative estimate of 512 fine resolution elements per coarse pixel. In order for the coarse addresses to be unambiguously defined, the P_{coarse} co-ordinate must resolve the correct discrete value from the sixteen values available. Since both the A and B fine position co-ordinates require 512 resolution elements per coarse pixel, and the C phase will have a similar resolution, the simulation showed that this would pose little problem. Figure 6-16, Figure 6-17, and Figure 6-18 show simulations of the onset of failure of the coarse pixel addressing, albeit produced by introducing large phase errors in the initial A′, B′, and C′ phase values. The coarse addressing error is characterized by ghosting of events into the preceding and following 'x' coarse pixels, and is best shown in Figure 6-18. In fact, no ghosting occurs as long as the error per phase is less than ± 4.3 degrees. This would only occur if the noise increased to the extent that there were only 42 resolution elements per coarse pixel, an order of magnitude below the conservative estimate of 512. This simulation indicated that, even using a conservative estimate for the expected electronic noise, coarse position encoding would not be a problem.

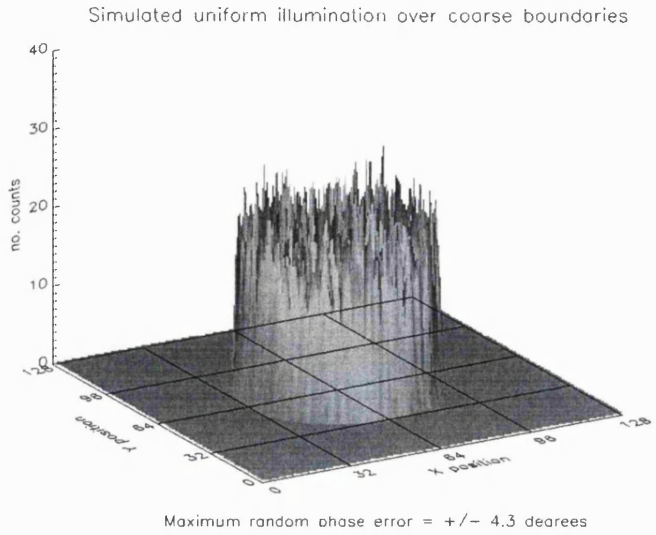

Figure 6-16. Simulated data showing no coarse pixel miscoding. A plot showing uniform random illumination across the centre four coarse pixels with a phase error of ±4.3°. No position miscoding is present at this error.

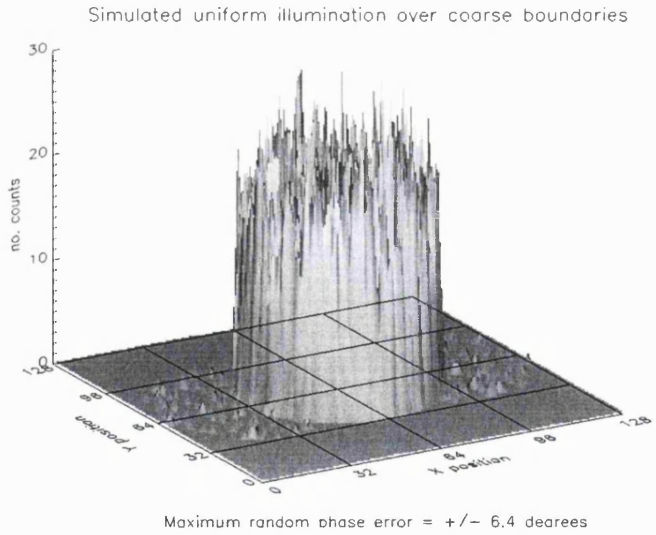

Figure 6-17. Simulated data showing the onset of coarse pixel miscoding. A plot showing uniform random illumination across the centre four coarse pixels with a phase error of ±6.4°.

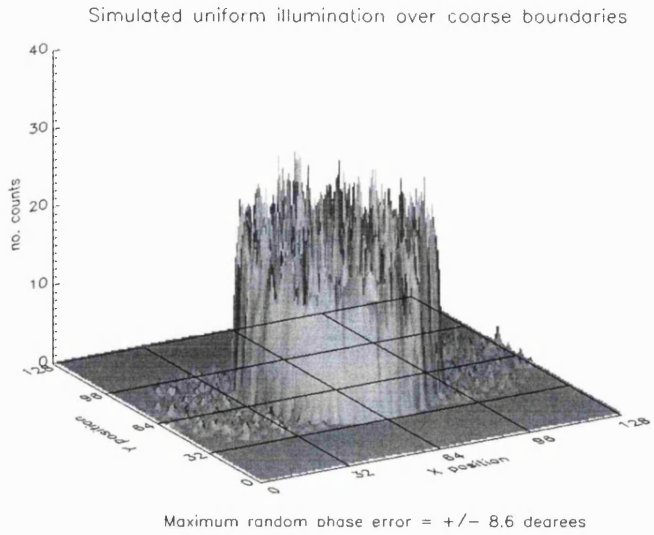

Figure 6-18. Simulated data showing significant coarse pixel miscoding. A plot showing uniform random illumination across the centre four coarse pixels with a phase error of ±8.6°.

6.5 Putting Theory into Practice - First Experimental Results

6.5.1 SPAN

The choice of which progressive geometry readout to manufacture first was driven primarily by the availability of suitable charge measurement electronics. The Spiral anode, or SPAN as it became known, was the simplest device to operate and construct, and could be proven in two dimensional form using only six electronic channels. It was also the most demanding of the patterns in that it used non-sinusoidal electrodes, which were expected to have sensitivity to the charge footprint due to the utilisation the radial event coordinate to encode coarse position, making for a significantly more complicated position decoding algorithm which would have to take account of the charge footprint. If SPAN performed as predicted, this would provide a high level of confidence in the simpler Vernier design.

The very first SPAN device was manufactured on a copper coated thin kapton substrate using hand soldered electrode interconnects made with fine copper wire. This device was of a fairly coarse design with a pitch of 1.25 mm, too large to provide the best resolution performance, and was seen only as a crude proof of concept. However some very basic imaging using an MCP stack indicated that even this less than optimal device was capable of reasonable results.

This original pattern was generated, as with previous wedge and strip patterns, using a coordinate table produced mask, together with a photolithographic process requiring wet etching. Even though its geometry was coarser than optimal, the manufacturing difficulties of making such a

fine pattern resulted in a low yield in the small scale, non-continuous production mode used in the research environment. This was the stimulus to develop the laser micromachining approach which has the advantage of directly cutting the pattern in the coated substrate and requires no intermediate mask. Manufacture of the first pattern with a realistic design capable of meeting the projected performance targets had to wait until the commissioning of the laser micromachining facility which was purchased primarily to produce progressive geometry readout patterns for upcoming project opportunities, SOHO-GIS AND XMM-OM.

6.5.1.1 Laser Manufacture

A FORTRAN programme was written to define the SPAN pattern for manufacture using the laser micromachining facility and techniques described in chapter 3. Since the quasi-sinusoidal form of the electrodes is not amenable to a solution using a Bresenham-type local difference algorithm [114], the sequence of coordinate steps, at a step spacing equal to the coordinate table used for manufacture, was determined and stored as an array. The indices of the intersections of this array with the perimeter electrodes were also calculated. The standard Bresenham algorithm routines were used to drive the coordinate table for the line and arc segments of the pattern, whilst lines defining the active electrode edges were drawn by sending the predetermined step array to the coordinate table in a real-time mode. The pattern drawing software enabled all pattern dimensions to be easily modified as required. The SPAN pattern was drawn sequentially and uni-directionally in a particular orientation to minimise drawing errors. In this way the table manufacturers' quoted bidirectional repeatability were vastly improved upon.

The very first patterns were manufactured in ~2 μm thick aluminium sputtered on to fused silica with a chromium inter-layer to enhance adhesion. This material, though very easy to laser machine, was quite fragile due to the softness of the aluminium layer. Any accidental mechanical contact could cause smearing of the aluminium resulting in electrical shorts between electrodes. This is especially problematic with fine patterns such as SPAN where the interelectrode insulating gap length can easily exceed 10 m. Later patterns used copper electrodes, which while more problematic to laser machine and wire bond, proved very durable. Wire bonding was used to connect all the corresponding electrode segments from pitch to pitch, using 25 μm diameter aluminium wire. Fused silica was the preferred substrate material due to its low dielectric constant, keeping the interelectrode capacitance as low as possible. This is important in order to minimise the capacitive loading of the preamplifiers which has a direct bearing on the electronic noise and the signal rise-time. Typically, the capacitance of a 36mm SPAN pattern is 120pF per electrode on a fused silica substrate. A photograph of the first SPAN device is shown in Figure 6-19.

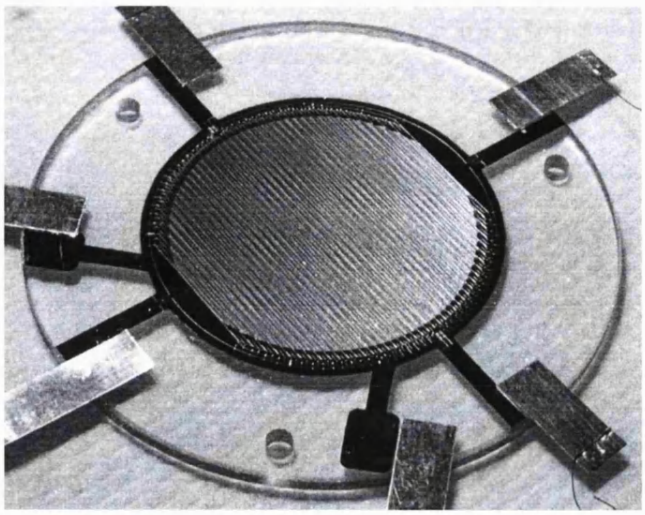

Figure 6-19. A photograph of an early SPAN device.

6.5.1.2 Practical pattern design

For a given electronic charge resolution and detector gain, the position resolution is dependent on the arc length of the spiral. This length can be maximized by choice of the best pattern and detector geometry. The major variables are :-

1) the repeat pitch. This parameter controls both the inter electrode capacitance and the spiral arc length/position conversion factor, and hence pixel size. The minimum electrode wavelength (i.e. the position displacement between points of equal phase in the spiral plane) should be no smaller than 8 times the pitch otherwise the convolution of the charge cloud with the electrode structure will reduce the spiral amplitude unacceptably, degrading the resolution. On the other hand, capacitance and thus electronic noise increase as the pitch is reduced. Reducing the pitch not only increases capacitance, but reduces the electrode dynamic range since a minimum electrode width is always required to ensure a sufficiently low electrode resistance, important to minimize exaggerated electrode ratio distortion due to secondary electron redistribution driven by dynamic electrode charge up. The first 25 mm active area two dimensional SPAN had a pitch of 680μm. The six electrodes were separated by an insulating gap of 23 μm and the maximum and minimum electrode amplitudes were 160 μm and 20 μm respectively. The optimum pitch is also related to the number of electrode wavelengths or spiral rotations as discussed below.

2) The number of wavelengths, equivalent to the number of revolutions of the spiral. Two factors limit the number of wavelengths used in the pattern. Firstly, the pitch imposes a minimum limit on the wavelength, which in turn impose a maximum number of wavelengths for a given pattern size. Secondly the radial noise of the spiral imposes a minimum value for the radial arm separation. Without the ability to distinguish the spiral arms with reasonable certainty, ghosting appears in the image at positions displaced from the true position by a distance equivalent to the electrode wavelength. The radial noise is a combination of electronic and partition noise together with any non-correctable element of the radius/pulse height variation, the latter being due to

variation of charge footprint with pulse height. The spiral pattern cannot be used at its centre owing to the very short wavelength this would dictate. Normally, the pattern runs from 6π to 16π i.e.5 rotations (assuming the centre to be 0π). The first 25mm SPAN pattern had a minimum wavelength of 4.6mm.

3) The MCP - anode gap and voltage. This size of this gap and the voltage applied control the charge cloud footprint. These parameters are chosen to allow the electron cloud to spread sufficiently to avoid image modulation due to the pattern fine structure, without significantly reducing the electrode dynamic range. The latter occurs when the charge footprint extent becomes a significant fraction of the electrode wavelength. The optimal drift gap parameters depend on MCP characteristics such as gain and depth of endspoiling, and on the anode geometry. Typically, the drift gap dimensions are 3-5mm with an applied voltage of 200 - 700 V.

The pitch and wavelength cannot be reduced arbitrarily in order to maximize the arc length and thus image resolution. Apart from increasing the difficulty of manufacture, it would increase the pattern capacitance. This would increase both crosstalk and noise. Crosstalk would cause the spiral size to be reduced, resulting in reduction of the arc length and more closely spaced spiral arms, reducing the resolution and increasing the possibility of spiral arm selection ambiguity. Increased electronic noise would further compound the latter.

6.5.1.3 Electronic requirements

Once the detector configuration and pattern geometry were fixed an estimate of the required electronic signal to noise ratio could be made by calculating the arc length of the spiral position coordinate locus in the charge domain with respect to the scale length of the charge resolution element in this domain. Though the pattern was drawn with a maximum quasi-sinusoidal amplitude of 70 μm and a maximum electrode amplitude of 160 μm, the effective amplitude was expected to be reduced because of the charge footprint smoothing out the quasi-cyclic variation. Instead of using the theoretical maximum quasi-sinusoid amplitude of 70/160 of the peak electrode signal, a conservative figure of 0.25 based on experimental results was used. The signal to noise ratio, SNR, can be defined as the number of charge resolution elements corresponding to the maximum electrode signal. Thus the maximum radius of the spiral was conservatively estimated to be $0.25\times SNR\times\sqrt{1.5}$, in terms of charge resolution elements ($\sqrt{1.5}$ is due to the projection on to the plane of constant charge). The spiral arc length, S, was then calculated, using the equations of the spiral anode, in terms of charge resolution elements. While not as comprehensive as the electronic noise calculation performed for the Vernier triplet shown above, this method provides a rough estimate of the number of position resolution elements as a function of SNR :-

$$(6\text{-}42)\quad S = \int_{5\pi}^{16\pi} f\theta d\theta = 110\pi^2 f$$

$$(6\text{-}43)\quad f = \frac{r_{max}}{\theta_{max}} = \frac{0.25SNR\sqrt{1.5}}{16\pi}$$

$$(6\text{-}44)\quad S = \frac{0.25SNR\sqrt{1.5} \times 110\pi^2}{16\pi} = 6.6SNR$$

Using this conservative estimate of radius, an electronic noise limited resolution of 1000 pixels per axis would require a signal to noise ratio of ~150:1 assuming there was no variation in the total height pulse height. Given a conservative MCP modal gain of 10^7 electrons, and the capability to image with nominal resolution at 0.25 of nominal pulse height, this signal to noise level would be required at a charge per triplet of 1.25×10^6 electrons. Since the maximum fractional electrode amplitude was 4/9 of the triplet (a figure defined by the 0.25 estimate of quasi-sinusoid amplitude / peak amplitude), the required SNR corresponded to a noise level of ~3700 electrons FWHM, or ~1570 e^- rms.

The above calculation did not take account of partition noise, which was estimated using the method described for the Vernier anode, to be < 3.0 μm FWHM at a modal gain of 10^7 electrons, and thus totally inconsequential.

Fixed patterning due to the digitization of the electrode charge levels becomes a problem when the scale of the structure it imposes on the image approaches that of the position resolution. This sort of fixed patterning can, in general, be avoided by ensuring that the analogue noise is sufficiently oversampled. The maximum charge level expected per electrode sets the range of the digitization. Using the estimate of a modal gain of 10^7, a maximum event charge of 2×10^7 was set, defining the maximum charge per electrode to be 4.44×10^6 electrons. At 14-bit digitization, each step would therefore correspond to 271 electrons, or 7.3 % of the FWHM noise requirement. Even at 12-bit digitization the step size would be only 29% of the noise, still providing adequate oversampling.

From these calculations we could conclude that a resolution of at least 1000 × 1000 should be achievable at a moderate MCP gain of 10^7 electrons, and that fixed pattern noise would not be a problem with the 14-bit digitization which was employed.

Laboratory testing of the SPAN detector was undertaken using a set of NIM based charge measurement electronics. Each of the six identical electronic channels consisted of an Ortec 124B charge sensitive preamplifier, having suitably low noise characteristics to easily achieve the required noise specification above, followed by an Ortec 572 shaping amplifier, nominally set for 2 μs unipolar shaping. The shaped pulses were digitized using Canberra 7077 14-bit ADCs, acting independently and using their in-built peak sense and digitize mode. A PC was used to correlate the six event ready signals generated by the ADCs to determine whether they arrived within a narrow, preset time window and thus represented a valid event, otherwise they were discarded.

The position decoding algorithm was implemented in a PC based DOS Program written in C [151]. A coordinate transformation and normalization was performed on the three digitised charge levels from each triplet to calculate the Cartesian event coordinates on the normalized plane of constant charge in the charge domain (as shown in Figure 6-7). A Cartesian to polar transformation was used to obtain the event r,θ coordinates, an example of such data is shown plotted in Figure 6-20. The spiral fit on to this plane is a series of parallel lines and each photon event coordinate must lie within a suitable band, close to the optimum fit, or it is discarded. The position coordinate corresponding to the electrode ratio for each event was computed, and the two dimensional event position was either directly plotted, or used to increment a 2d image histogram for larger integrations. This computationally intensive method, while suitable for laboratory testing, was not feasible for a flight application. A different scheme using a combination of ratiometric ADCs to avoid the requirement for digital division, and look-up tables to replace the algorithm computation was devised [150] for the SOHO Coronal Diagnostic Spectrometer SPAN detector.

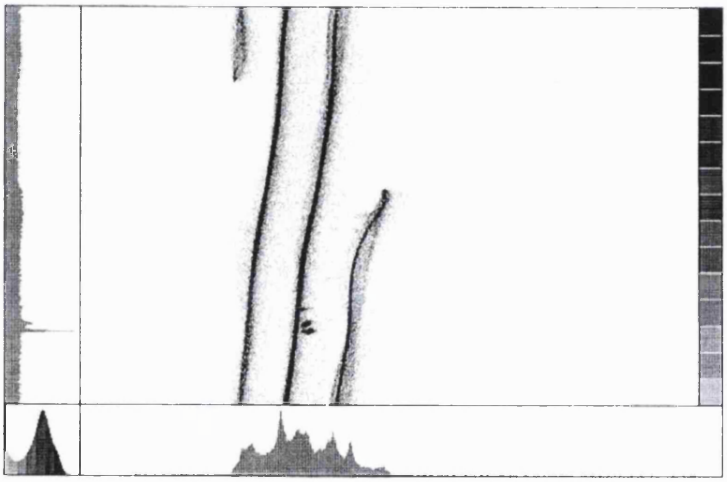

Figure 6-20. Event data from the SPAN detector plotted as radius (x) versus theta (y).

6.5.1.4 Imaging Performance

Initial imaging tests were undertaken with the open faced of the prototype detector, which had an imaging area of 25 mm diameter and used the 36 mm diameter SPAN readout described earlier. The detector used a double thickness chevron MCP stack with a gain of ~1.4 x 10^7, mounted in a demountable, open faced detector and illuminated with a Pen-Ray UV light source. Image resolution and linearity were measured using a range of test masks mounted close to the front surface of the MCP stack. A brief summary of the major results is given below. A more comprehensive set of experiments to optimize the SPAN detector were undertaken and reported on by Edgar [151].

Figure 6-21 shows an image of an 8 x 8 mm^2 square resolution test mask. The finest bars of the mask have a repeat dimension of 63μm. The distortions at the centre of Figure 6-21 and in the two finest sets of bars in Figure 6-22 are the result of high level illumination of the MCP via a pinhole

and annulus respectively, during gain depression experiments. Not only has this produced lasting long range gain depression, but it has also caused image distortion (the shape of the illuminated annulus can be discerned – shown by the dotted circle in Figure 6-22). Figure 6-23 shows an image at further zoom of the fine bars.

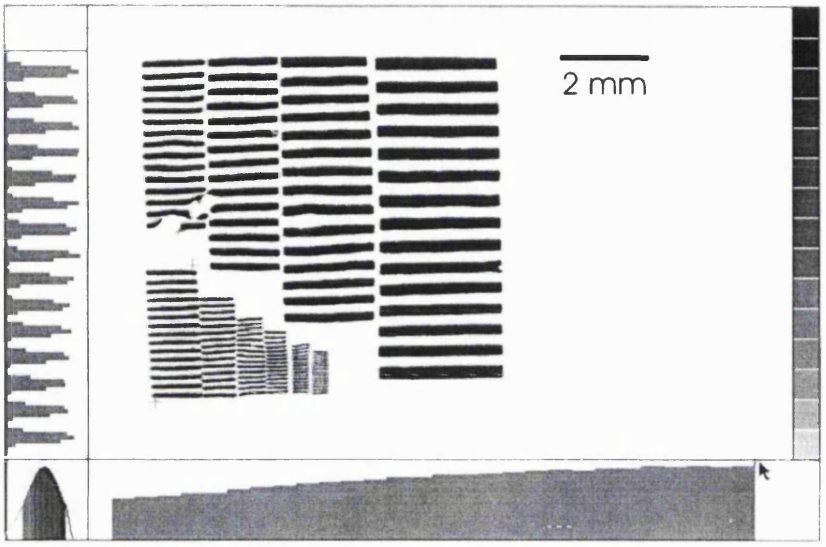

Figure 6-21. An image of a resolution test mask over an 8 × 8 mm^2 area.

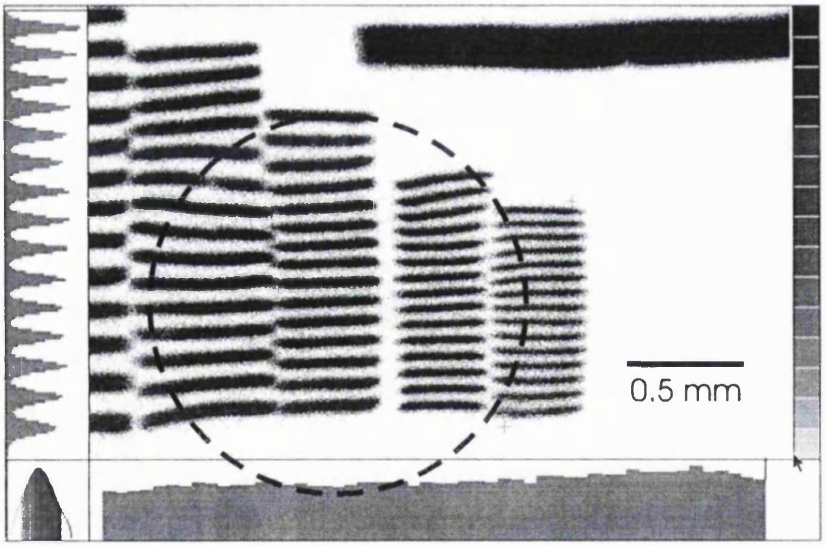

Figure 6-22. A zoomed image of a resolution test mask showing the finest bars. The dotted circle indicates the position distortion caused by long term illumination via an annulus.

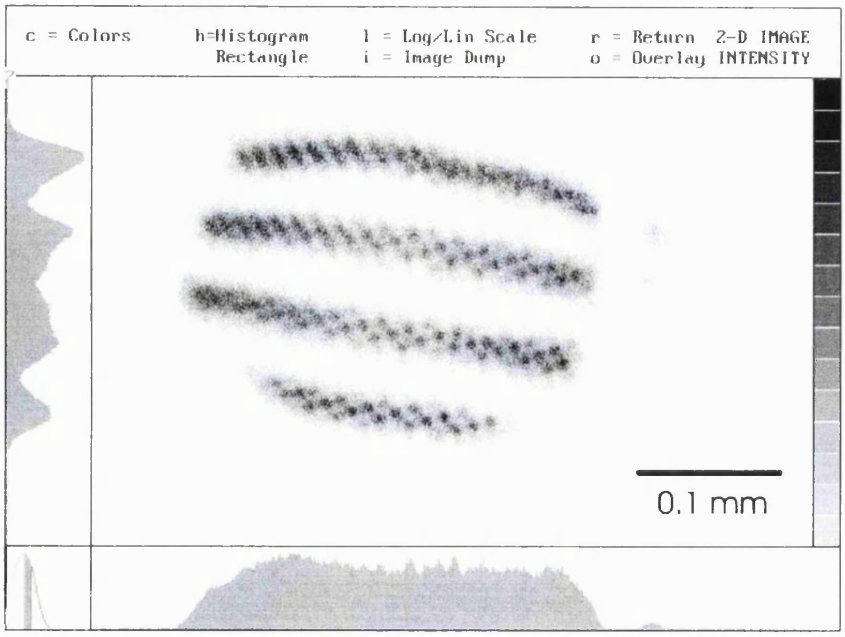

Figure 6-23. A SPAN test mask image showing the MCP pore structure.

The data shown in Figure 6-23 was a breakthrough in the development of progressive geometry patterns because it was the first evidence of the underlying high resolution, which had been predicted but was elusive to demonstrate. This image at last showed that SPAN could achieve one of its goals, that of creating a readout which was not the limiting element in the detector. Figure 6-23 demonstrates this with an image of a bar mask, having a centre-centre spacing of 74μm. The hexagonally packed pattern is produced by the pores of the front MCP. Analysis of the width of the pore images indicated an intrinsic readout resolution of 18μm FWHM, the best SPAN result so far, and below the goal of 25 μm which had been predicted.

However, performance was still far from perfect. The distortion of the bars and poorer resolution at the circumference was thought to be due to electrostatic lensing at the MCP output, maybe resulting from the same phenomenon producing long range gain depression [152]. Similar distortions are also seen to occur at the edge of brightly illuminated regions of the MCP. The pore images were only distinct with the narrow pulse height window shown in the left lower corner. Wider pulse height windows produced a smearing of the pore images in one particular direction owing to a pulse height dependent position shift. At the time, two possible causes were suggested :-

1. Collimation due the bias angle of the lower MCP (13 degrees in this particular case). Less saturated events have higher energy electrons which travel from further up the pore. They are more highly collimated along the pore bias angle and their trajectories less influenced by the drift field than the lower energy electrons produced in highly saturated events. The centroid of the charge footprint of a less saturated event would be closer to the pore bias axis than that for an event showing more saturation.

2. The spatial size of the electron cloud at the anode is pulse height dependent. It is possible that the effective electrode ratio (i.e. that measured after convolution of the charge cloud with the two dimensional electrode structure) varies with pulse height in such a way as to produce this effect. The change in spiral radius produced by a change in charge cloud size could also be accompanied by a small phase shift and consequent position shift. In SPAN this distortion would be symmetric in both axes and the shift would be along the diagonal between the axes. The answer to this problem was not resolved at the time since it was only visible at the sub 10μm level and required direct imaging of MCP pores to detect. It should not occur with the true sinusoidal form of the Vernier electrode.

Another pulse height related effect was more generally apparent. The charge footprint varied with event pulse height causing the spiral radius to change due to the effect of nonlinear electrode structure. This effect was seen to be markedly different depending on the MCP stack used, being almost undetectable in the optical intensifier described later, but very apparent with the open faced detector. A simple modification to the decoding algorithm was used to correct for its effect :-

$$R' = R + \sigma Z \quad \textbf{(6-45)}$$

where R was the old radius, R', the corrected radius, Z, the pulse height, and σ, the fit parameter

It was found that very low level events, such as those produced by MCP hot-spots or extremely bright point source illumination causing severe MCP gain depression, produced events whose radial coordinate lay significantly far from the expected radial value creating ghost images. These were eliminated by using a lower level discrimination on the electrode sum signal.

6.5.1.5 Linearity

The dominant effect producing image nonlinearities in the SPAN readout was the sensitivity to variations in the spatial charge cloud distribution which in turn affected the spiral radius. The fixed variation in cloud size with pulse amplitude together with fixed distortions in the *r,theta* plot (i.e. deviations from linear) could be relatively easily and successfully accommodated by using a fitting routine to choose the best spiral fit parameters. However, the dynamic changes in gain produced by changing the image morphology and count rate were accompanied by a change in the spatial charge distribution. In consequence the best spiral fit parameters required to make the transformation from the *r,theta* spiral plot to the position axis would also alter. This effect was seen at its worst when using the high resistance MCPs in the open faced 25mm detector (6 GΩ per square cm). One way to avoid the problem would have been to increase the spiral arm separation but this unfortunately would have degraded the resolution.

Despite this variability, the intrinsic linearity of the SPAN readout was reasonably good. Figure 6-24 shows a pinhole array across the entire active area of the open faced 25mm detector. The standard deviation of the pinholes in the central 20 mm from their expected positions is 30μm.

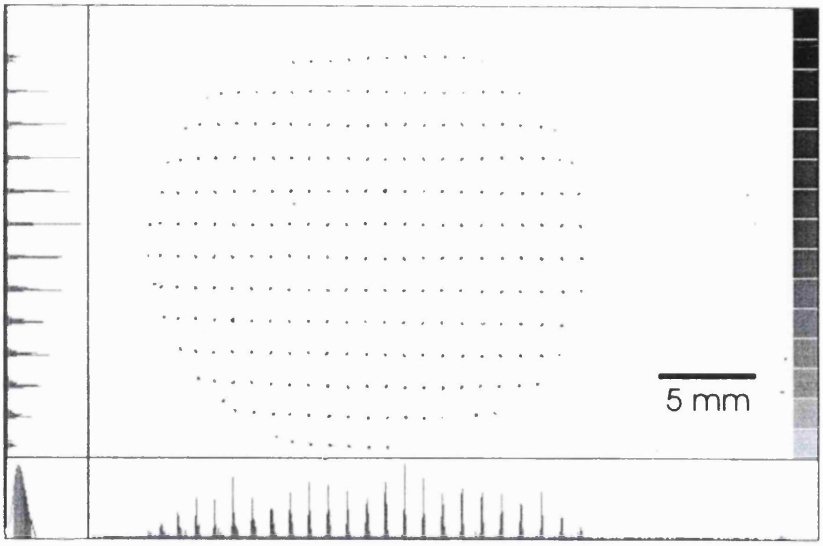

Figure 6-24. A SPAN image of a pinhole array showing linearity of 30 μm rms.

6.5.1.6 SPAN Optical Intensifier Prototype

A sealed tube intensifier version of the SPAN detector, using an optical S20 photocathode, was manufactured as a prototype for the XMM Optical Monitor instrument. Unfortunately the delivered tube was only capable of low gain operation as a result of excessive MCP scrubbing during manufacture. The low gain precluded measurements of the predicted high resolution performance, and also produced image ghosting owing to the degraded signal to noise ratio which caused ambiguities in the coarse position decoding.

Figure 6-25 and Figure 6-26 show images of a bar mask placed against the window of the intensifier tube, illuminated with daylight via a 25μm pinhole at a distance of 50cm. The overall count rate on the tube is ~10 kHz. Figure 6-25 shows the entire mask which has a side of 8mm. Figure 6-26 shows the smaller set of bars at higher magnification. Both images were taken with the pulse height window limits at the full width, half maxima of the distribution. The three coarser groups are resolved; these have widths of 100μm, 79μm and 60μm respectively. The finer bars cannot be resolved. The detector exhibited good positional linearity within the central 90% of the image area. Despite the apparent poor performance due to low gain, the position resolution was actually as predicted, given the tube operating gain of ~3 x 10^6.

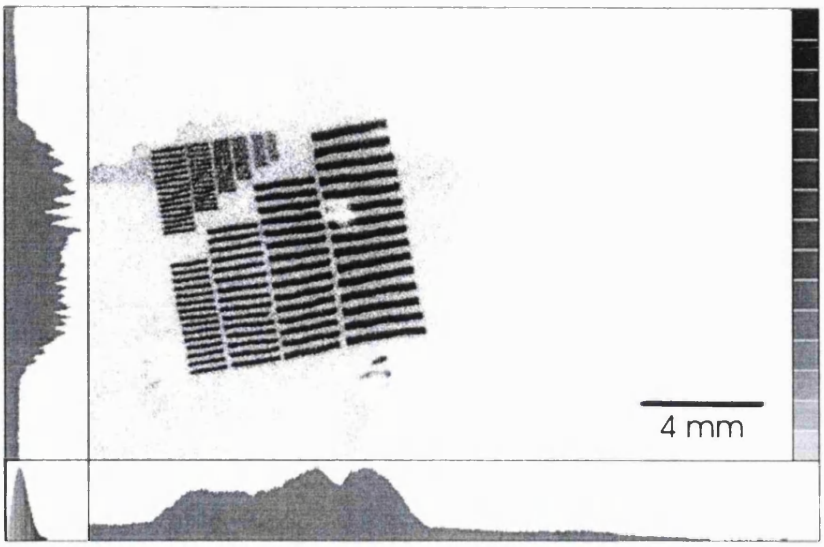

Figure 6-25. The full resolution test mask imaged with a SPAN sealed tube intensifier.

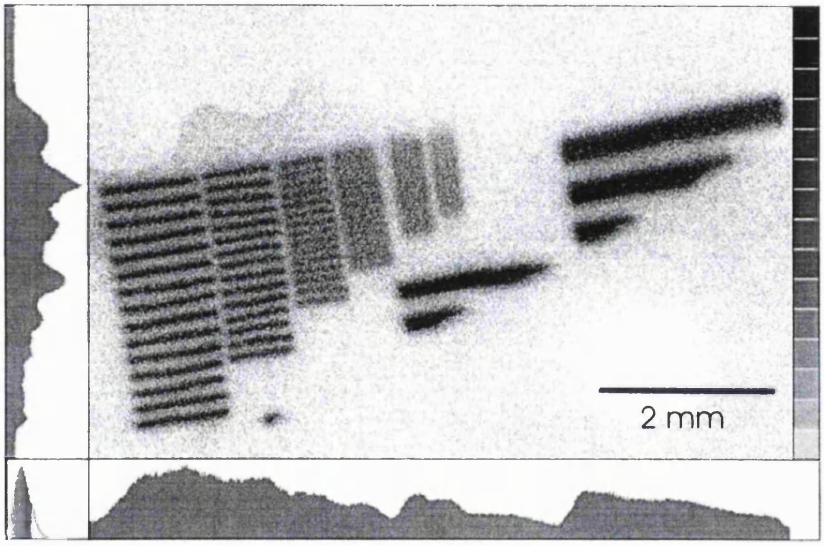

Figure 6-26. A zoom of the fine bars imaged with the SPAN sealed tube intensifier.

Chapter 7

Realizing the Potential of the Vernier Readout

Whilst the preliminary experimental results from the first progressive readout manufactured, the SPiral ANode (SPAN) were being taken, as described in the conclusion of the previous chapter, the concept of the nine electrode Vernier anode had just been devised. A comparison of both readout techniques was important in order to prioritize the overall readout development plan. Whilst they are both variants of the progressive geometry readout family they each offer distinct strengths and weaknesses.

SPAN requires the least number of electrodes, making it the least complicated pattern to design and manufacture, and requiring corresponding fewer electronics channels. However its more complicated and partially empirical decoding algorithm and its reliance on charge footprint stability to encode coarse position (discussed more fully later) make it more vulnerable to operational problems. The Vernier, particularly the latest nine electrode variant, whilst needing 50% more electrodes and electronics that SPAN, is fundamentally simpler in operation, having a more straightforward decoding requirement as well as being much less sensitive to charge footprint variations. The latter factor was always a bugbear to a varying extent until alleviating techniques such as the introduction of an intermediate grid between MCP and readout, or image charge were applied. The greater robustness of the Vernier coarse position encoding also allows a larger number of coarse pixels to be encoded without ambiguity, for a given noise and digitization level. This results in higher ultimate spatial resolution. Whereas the SPAN is only quasi-cyclic (the modulation of the radius being linear and thus of finite extent), the Vernier pattern is truly cyclic which allows the full extent of the unambiguous pattern to be used for the illuminated detector active area. The active surrounding pattern can repeat as required to provide full charge collection of the extended charge footprint. The Vernier is also less susceptible to fixed pattern noise; the obligatory but serendipitous misalignment of the three phase axes serves to diminish this to negligible levels.

The choice of the SPAN readout for the SOHO GIS detectors was primarily driven by simplicity, SPAN only needing three electronic channels for one dimensional imaging, whereas the Vernier

would need six for this format. SPAN was selected for SOHO-GIS at an early stage in the development of these readouts and suffered from problems resulting from the variations of the charge footprint distribution as a function of gain, count rate and image distribution. Charge cloud variability caused radial variations in the intermediate r,θ coordinate producing noise in the coarse position determination, which manifested itself as image ghosting. These problems were overcome but only by trading some performance. SPAN was also proposed as a detector system for the Optical Monitor instrument on ESA's X-ray Multi-Mirror mission (XMM-OM). However delays in the manufacture of the prototype sealed intensifier, and non-optimal operational gain of this tube once delivered which limited the demonstrable performance, made its choice too risky. In the meantime the modified nine electrode Vernier readout had been designed. With significant advantages over the original SPAN design it was an obvious candidate for the J-PEX mission, a sounding rocket experiment comprising a UV spectrometer with a requirement for a very high resolution detector.

This chapter describes the evolution of the Vernier progressive geometry readout, beginning with pattern design, manufacturing and electronic measurement techniques, followed by the first results and then moving on to the development of the Vernier readout used for the J-PEX sounding rocket mission. The full potential of the Vernier readout was achieved only after a variety of investigations into effects limiting resolution and causing nonlinearities were undertaken and remedies found. In conclusion the J-PEX mission and the performance of the flight detector are described, ground calibration is discussed, and flight data and mission results are presented.

7.1 Pattern Design and Manufacture

An essential element in the production of a working readout anode is the pattern definition. The initial proof-of-concept one-dimensional Vernier anode used a FORTRAN routine to define this. The much more complicated two dimensional, 45 degree, projected nine electrode Vernier pattern selected for J-PEX, was coded in C and uses 1157 lines of code to generate the coordinates and arrays of step sequences necessary to define the readout pattern. The software is written to allow the user to input all physical pattern dimensions such as size, pitch, insulting gap width, and coarse pixel arrangement. From these it then calculates the required triplet vector parameters, implementing them automatically in the pattern. Figure 7-1 shows a schematic, drawn using the pattern drawing software, but using coarse pitch for clarity.

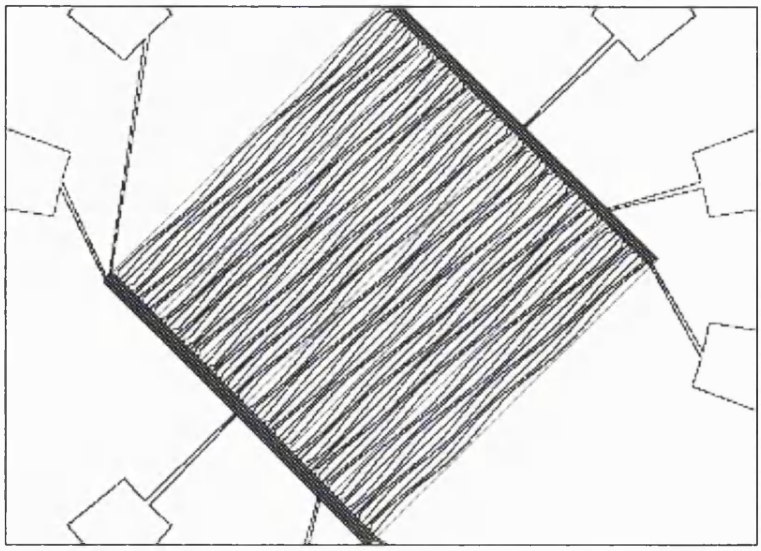

Figure 7-1. A schematic of the Vernier 9 electrode readout.

The actual pattern pitches are oriented along the readout x axis. This is a particular arrangement used with the modified 9 electrode Vernier in order that all the triplets may be drawn in continuous (as opposed to discrete mode). It can be seen from Figure 6-11 that the triplet vectors for this pattern are arranged at approximately 45° to the pattern x axis and their ratios can be projected on to this pattern orientation in a manner shown in Figure 6-8.

To complicate matters further, the pitches are orientated at 45° with respect to the pattern drawing coordinate table axes to avoid backlash and minimize the impact of differential nonlinearity in the stepper motors of the laser micromachining facility (discussed in chapter three). The mechanical slack in the worm gear drive between stepper motor and table screw results in a backlash, effectively offsetting the pattern each time the table direction alters. Backlash can be particularly problematic for the cyclic electrode structures found in all progressive geometry readouts. If the pattern were drawn with the pitches parallel to either axis of the coordinate table, the orthogonal cyclical electrode modulation would cause that axis to be driven in alternately positive and negative directions. If the pitch axis of the pattern is drawn at 45° to the table, both table axes are driven constantly in one direction for each line segment and backlash is totally avoided.

This drawing arrangement also minimizes the effect of the cyclic differential nonlinearity found in stepper motors which use fractional stepping as a way of achieving fine resolution. The coordinate table used has a table increment of 80 μm per motor pole and the fractional stepping technique is used to create up to 1000 fractional steps in each increment by using pulse width modulation of the two motor pole currents. Though the positional errors for each step may be fractions of microns, the Vernier sinusoidal amplitude is only ~70 μm for J-PEX and so the percentage error can be significant. If the pitch is drawn parallel to the table axis, this error has a low spatial frequency since it's distributed over the length of a pattern wavelength and thus sensed by the charge footprint. However if the pattern is drawn at 45° to the table, though the

positional error is still present, its spatial frequency is at $80\sqrt{2}$ μm and is integrated out by the charge footprint in the same way as the pitch structure.

The original nine electrode Vernier pattern was drawn with a 890 μm pitch, but it was later realized that the J-PEX Vernier would require a smaller pitch of 636 μm pitch, making it even more sensitive to machining inaccuracies. One technique that was used to improve precision further was to draw every line segment in the same direction, thus avoiding diagonal table offsets between lines drawn in the x,y = (+ve,+ve) and x,y = (-ve,-ve) directions. This practice can double the length of time it takes to draw the pattern from typically three to six hours, accentuating the problem of thermal drift between the coordinate table and the laser head. Thermal drift was found to give rise to a small position offset, typically 20 μm, which varied with time. To avoid this problem the laser facility was cooled using forced air ventilation and made to reach thermal equilibrium by drawing a dummy pattern, with the laser Q-switch off, before beginning actual pattern manufacture. Even so, it was important to ensure that the pattern was drawn consecutively, so that thermal drift errors were integral and not differential i.e. the order of line drawing progressed linearly from one end of the pattern to the other. The point at which the starting line joined the end was made to occur within the non-active perimeter region where electrode areas do not influence operation.

The patterns were manufactured on a 1 mm thick polished fused silica substrate. Though it would have been possible to manufacture the pattern directly on the multilayer substrate (see Figure 7-2 for a photograph and substrate drawing) which provides the vacuum sealing, electrical feed-throughs and mechanically defines the readout position, there are two major reasons why this was avoided. Firstly, the fused silica substrate has lower dielectric constant and produces a lower capacitance pattern. Secondly, once lased this part would not be reusable, posing a problem since only a limited quantity was available. The use of a thin substrate brings its own problems to laser machining. The slow laser optics have a large focal depth and, because fused silica is transparent to the laser wavelength (1064 nm) once material has been ablated, the transmitted beam can reflect off the opposite surface of the substrate and once again impinge on the underside of the electrode layer, somewhat out of focus but with sufficient intensity to cause further ablation and a ragged insulator gap. This was avoided by using a further transparent substrate beneath the pattern substrate, which was optically coupled to minimizing the reflection at the boundary.

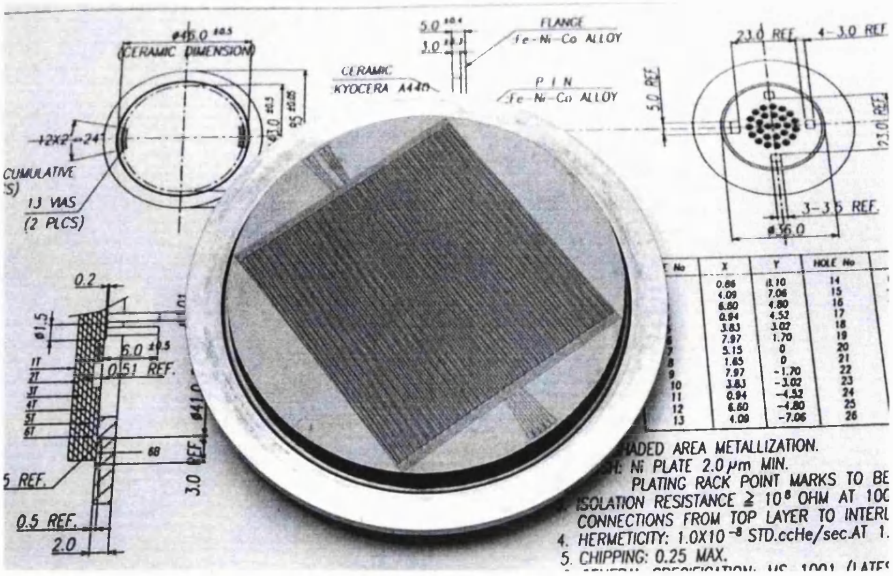

Figure 7-2. The Vernier readout manufactured on a ceramic multilayer substrate.

Copper was used as an electrode material mainly because of robustness and economy. It was deposited using a magnetron sputter coating plant dedicated primarily to pattern manufacture. Having two magnetrons and a plasma cleaning facility it is ideally suited to this task, providing the facility to clean the substrate and coat two different layers without breaking vacuum. Though fused silica is an ideal substrate in terms of its rigidity and electrical parameters, it is notoriously difficult to obtain coatings with good adhesion, an essential requirement for wire bonding. The use of plasma cleaning and a chromium 'glue' layer beneath the copper, both coatings deposited using sputtering, in general produced very good conductor adhesion.

Manufacture of the pattern using the laser micromachining facility was carried out as described in chapter 3, with the additional requirements of establishing thermal equilibrium and machining in one direction only as described above. One crucial step in the manufacturing process is pattern cleaning, which takes place between lasing and wire-bonding. This is the only stage when the pattern can be thoroughly mechanically polished to remove debris from the lasing process. If not carried out this debris can give rise to the effects described in chapter 5 which result from insulating deposits and pattern charge-up. Once the wirebonds have been attached the pattern cannot easily be cleaned using solvents or mechanical methods.

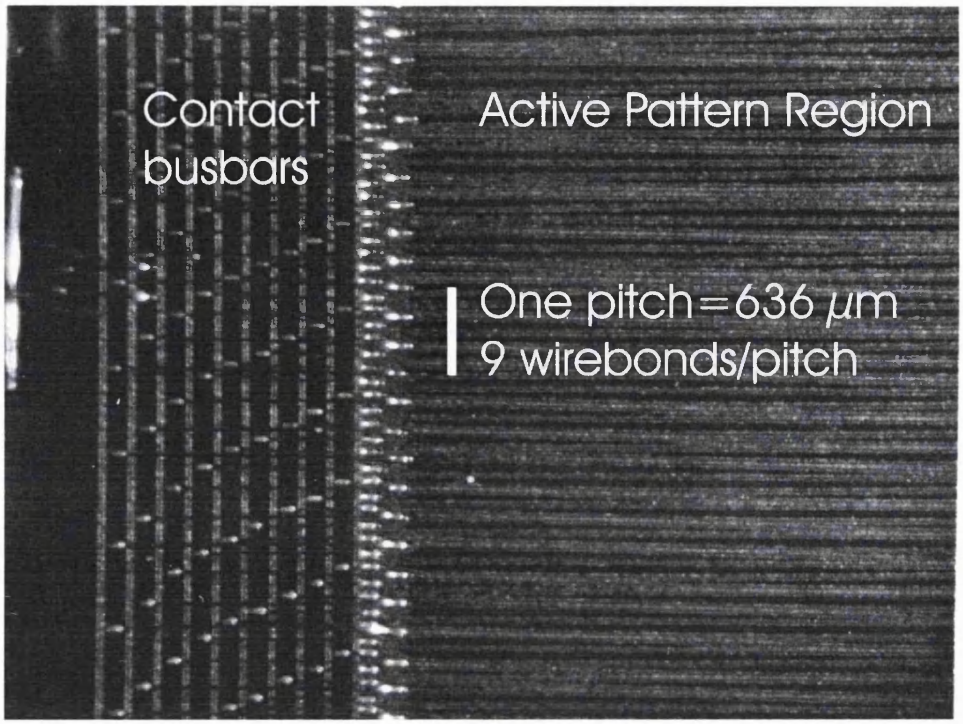

Figure 7-3. A photograph showing the wire-bonds used to connect the Vernier electrodes.

Ultrasonic wire-bonding is used for the electrode interconnects using the techniques described in chapter 3. The flight anode uses a wire bond at both ends of every electrode for redundancy, as an insurance particularly against bond breakage during the high level of vibration experienced at launch. The J-PEX anode has 47 pitches, each requiring 18 wire bonds, plus 36 external connections making a grand total of greater than 880 per pattern. Each bond is individually positioned and made, the entire process taking more than one hour for an entire pattern. Despite the large number of bonds and the manual dexterity and precision required to perform this task, it is remarkably problem-free once the manual skills have been grasped.

Figure 7-3 is a photograph of the pattern showing 9 pitches of the pattern and 81 wire bonds made using 25 μm diameter wire. The electrode contact pads are staggered in two rows for ease of bonding so that the 9 bonds are not all side by side. The outer row has 6 bonds per pitch while the inner row has 3, with average spacings of 106 and 212 μm respectively.

7.2 One-dimensional Vernier

An initial test of the practicality of manufacturing a 12 electrode 45° two dimensional Vernier pattern was undertaken before the 9 electrode Vernier design was conceived. Whilst this proved that manufacture was possible, testing was limited by the lack of availability of a sufficient number of charge measurement electronic channels. Thus the first experiments were limited to imaging using the 6 available channels of the SPAN electronics. A one dimensional 6 electrode Vernier anode was manufactured specifically for these tests.

7.2.1 Hardware Description

This prototype detector was based on the demountable design used for the WSA development work described in chapter 4, and was modified to include a nickel grid between the MCP stack and anode in order to continue investigations into effects due to anode secondary electrons.

The detector configuration for these experiments was as follows. The MCP stack was illuminated directly with a low pressure Mercury UV lamp via a variety of masks positioned near the MCP input face. The detector comprised an MCP Z-stack with a front MCP of 40:1 length to diameter (L/d) ratio. A 25 μm spacer separated the input MCP from two further 80:1 L/d MCPs which were held in contact. The MCP gain in this format was typically 1.5×10^7 electrons. The gap between the output face of the MCP stack and the anode was 6.9 mm. The conductive grid between the MCP and anode was made of electroformed Nickel with a ~60 % open area ratio and a pitch of 17 μm. The spacing between the grid and anode was 750 μm.

For these experiments the anode was held at a high positive voltage with respect to the grid. In this mode ~60 % of the electrons from the MCP pass through the grid while the remainder collide and produce secondary electrons from the grid, some of which also reach the anode. The thinking behind this mode of operation was that the high field between the grid and anode would suppress the range of secondary electrons produced on the anode, especially since they have a relatively low energy.

7.2.2 Preliminary Imaging Results

The six electrodes of the one dimensional Vernier readout are organized as two pairs of three, producing two phase outputs. These are combined to produce a coarse and a fine x co-ordinate which are then concatenated. The active region of this 1D Vernier was 25 × 25 mm^2. The following figures show a series of the one dimensional image histograms obtained with this detector and which provided preliminary experiment results for the performance characteristics of the Vernier technique.

Figure 7-4 shows an image produced by the detector when illuminated with UV through a linear pinhole array, with a spacing of 1.6mm and pinhole diameter of 25 μm. The central portion of the array has extra pinholes at closer spacings (down to 50 μm) and an image of this region is shown in Figure 7-5. Figure 7-6 shows one end of the array with five pinholes visible. Appreciable non-linearity is present only at the first pinhole position which is at the very edge of the pattern and there is no noticeable fixed pattern noise. The satellite peaks either side of each pinhole image were a source of conjecture. Since this was one dimensional data, integrated across the orthogonal axis, they were too well defined to be a halo effect caused by photoelectrons ejected from the MCP web. They were more likely to be caused by reflection of UV in front of the mask causing the pinhole to see multiple sources.

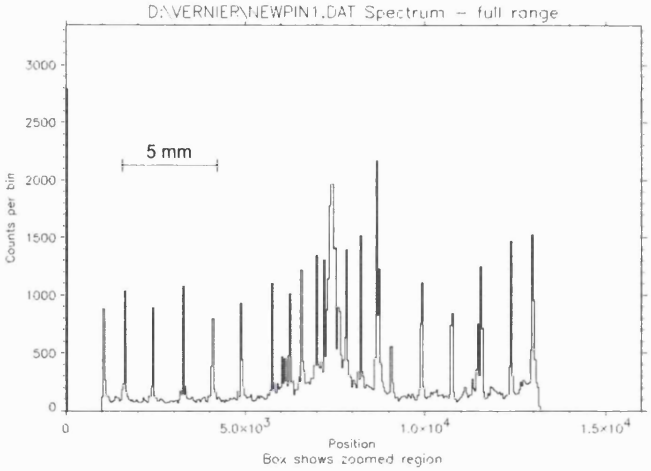

Figure 7-4. A one dimensional Vernier image of a pinhole array with 1.6 mm spacing. The central portion has several closely spaced pinholes. The random peaks are caused by MCP hotspots.

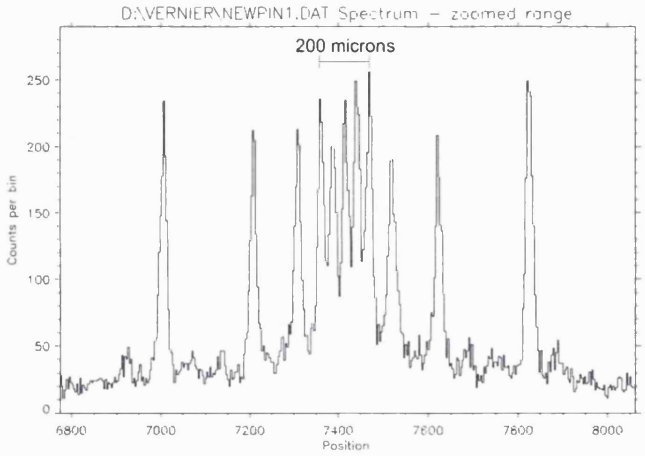

Figure 7-5. A zoomed image of the central portion of Figure 7-4. The minimum pinhole separation is 50 μm.

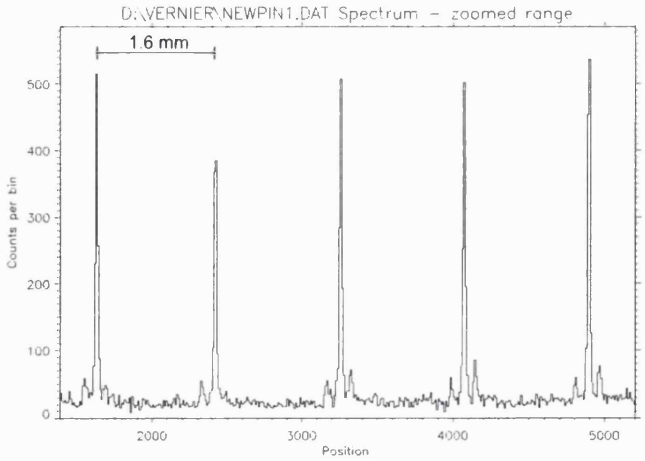

Figure 7-6. A zoomed image of the left-hand end of Figure 7-4. The pinhole separation is 1.6 mm.

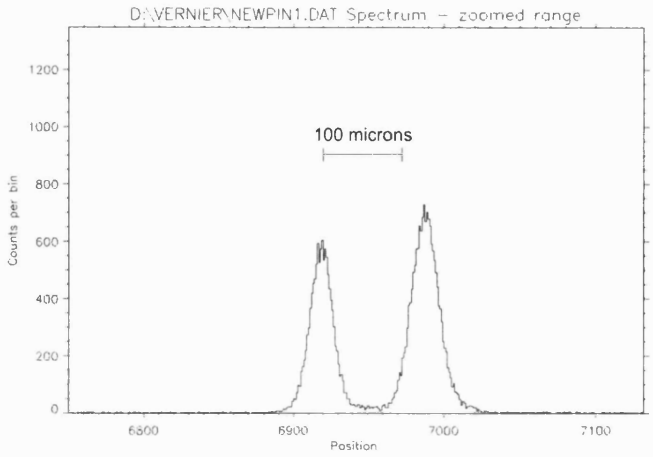

Figure 7-7. An image of two MCP hotspots with 0.125 of the nominal gain. The left hand peak has a FWHM of 32.6μm.

The mean FWHM of the pinhole image is 28.1 μm compared with the projected size of the pinhole, which is ~27.5 μm after taking into account the collimation of the source. It was not useful to deconvolve these numbers because of the large errors involved, but these results suggested a detector resolution of less than 10 μm FWHM. The rms deviation of pinholes from their expected position was 20.9 μm over the central 90% of the active area. The demountable tube and MCPs used for this demonstration were well used in a previous development programme and had several hotspots. However, these hotspots exhibited low gain and were useful in showing the relative insensitivity of the Vernier anode resolution to pulse height. The image in Figure 7-7 shows two hotspots having gains ~2 × 10^6 electrons. The left peak has a FWHM of 32.6 μm, which, if one assumes that the resolution is electronic noise limited, would correspond to a readout resolution of ~4 μm FWHM at nominal gain.

7.3 Two Dimensional Vernier

The nine electrode Vernier readout design was conceived as alternative to SPAN that would offer similar or better resolution without the drawbacks described in the last chapter. Quite early on in its development it was proposed as a very high resolution image readout for a MIDEX mission, which though unsuccessful, paved the way for its proposal on a substitute sounding rocket programme led by the Naval research Laboratory, and named Joint Plasma Experiment (J-PEX).

7.3.1 Prototype Pattern Geometry

This first pattern had an active area of 25.8 × 25.8 mm^2, a pitch of 890 μm, a sinusoidal amplitude of 99 μm, and an insulating gap width of ~20 μm. The encoding scheme had a 5 × 5 coarse pixel geometry with a coarse pixel size of 5.3 mm, leading to wavelengths of triplets A, B, and C of 8.08, 8.49, and 6.90 mm respectively, the physical wavelengths of electrode sinusoids being 10.20, 11.05 and 11.05 mm respectively. The pitch dimension was chosen to fulfil the criterion

that the pitch should be approximately 1/8 of the triplet wavelengths. This figure was estimated as the optimum trade-off between reduced effective sinusoidal modulation and pitch size. A larger pitch size would require a corresponding larger footprint, which in turn would reduce effective sinusoidal amplitude, and smaller pitch size would increase electrode capacitance and thus electronic noise, and introduces practical manufacturing difficulties. This criterion was later to be revised in the light of the results from this first prototype.

7.3.2 Preliminary Imaging Results

The very first image captured using this pattern, in the same demountable detector used with the one dimensional Vernier anode, is shown in Figure 7-8. The imaging area of the MCPs was the same size as the pattern, and so the charge footprint at the perimeter overlapped the contacts surrounding the active readout area, resulting in imaging errors: some ghosting and nonlinearities. This was used to assess the extent of edge effects to determine the pattern oversize necessary to produce the required linearity over the full detector field of view and was expected to disappear when a pattern larger than the detector field of view was used.

Figure 7-8 shows the entire field of view of the detector illuminated through a mask of 40 μm diameter pinholes at 0.5 × 0.5 mm^2 spacing. Analysis of events lying in the central region of the pattern showed the coarse pixel boundaries to be well separated.

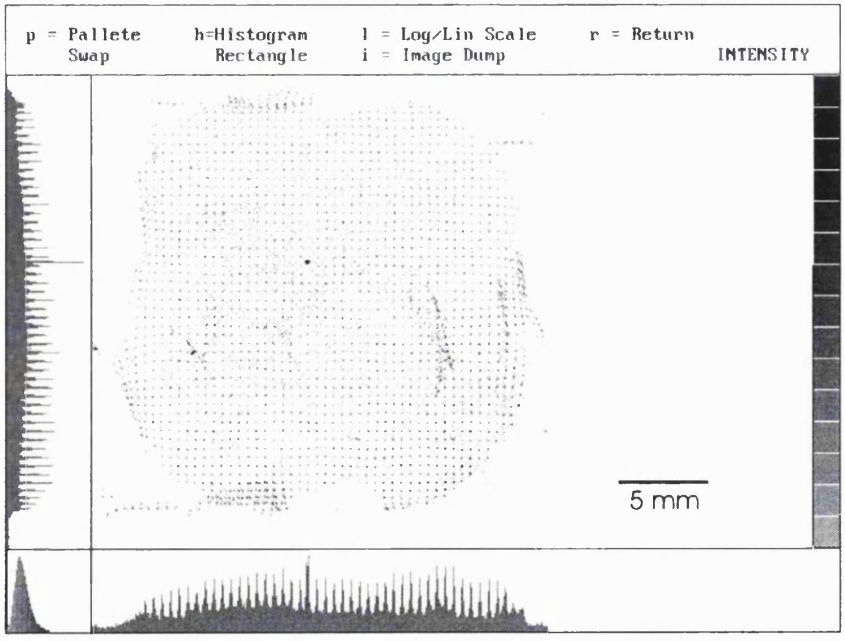

Figure 7-8. The first image from the nine electrode two dimensional Vernier anode. The image artefacts are a result of the field of view of the MCP overlapping the edge of the active readout area, and producing ghosting.

7.3.3 Linearity

As we have discussed in previous chapters, traditional charge division readouts used in MCP detectors, such as the WSA, can suffer from positional nonlinearities and instability in absolute positioning. These effects occur because the ratio of charges collected on the individual electrodes does not accurately represent the electrode geometry, and is primarily caused by redistribution of secondary electrons produced from the anode surface amongst the anode electrodes.

The Vernier anode, being a charge division readout, is no exception to this and so in order to exploit this performance to the full and produce a device with absolute position stability, the problem of secondary electron redistribution had to be overcome.

We set out to determine the physical processes producing charge redistribution and to make modifications to the detector, the anode pattern design and data acquisition software to diminish the effect. These modifications are also applicable to other anodes relying on analogue charge division and provide improvements in absolute positional stability and linearity.

The satisfactory performance of any charge division depends on the faithful replication of the ratios of the electrode geometry in the collected charge ratios. The advantage in resolution offered by the Vernier anode is gained by the use of cyclic electrode structures which enable the dynamic range of the electrodes to be used several times over the length of the pattern. Errors in the collected charge ratios due to non-localized effects such as pattern errors and charge redistribution tend to cause a cyclic position error in the image. Figure 7-9 shows an early image from the Vernier readout of a pinhole array with 0.5 mm spacing and these cyclic position errors can be clearly seen.

In order to analyze the effect, a software tool was written which utilized the distorted image data of the pinhole array to determine the positional and electrode triplet phase errors for every pinhole position. These were used to generate correction factors which were then applied to the position decoding algorithm, and more fundamentally, to determine the causal mechanisms and enable the hardware to be redesigned to avoid these effects at source.

In its initial form, the analysis tool first used user input to coarsely fit a uniform grid to the image data. Then a user-defined threshold intensity was applied to the two dimensional image histogram to select 'bright' pixels representing the pinhole positions. The threshold level was adjusted to select all the pinhole but minimize false identification due to noise, a task very much dependent on the total number of events in the image and the uniformity of the illumination and MCP response. Once the 'brightest' selected pixel closest to the expected pinhole position (defined by the user-fitted uniform grid) had been chosen, the pinhole position in the real image data was determined by centroiding using a 3 × 3 pixel area. The array of image positions was used to generate a simulated image with Gaussian pinhole distributions, and the correlation with the real image was calculated. The geometry of the simulated image (angle, scale, x and y offset) was

altered iteratively to maximize the correlation with the real image data. The pinhole centroids from the best fit simulated image were compared with the pinhole centroids from the real image to calculate the x and y position errors together with the three Vernier triplet phase errors. This method relied on the use of a pinhole mask whose geometry was well known.

A later incarnation of the software used a kernel which was initially defined by the user, who would interactively select a number of image features with nominally the same structure (e.g. pinholes or grid intersections, etc.). The convolution of this user-defined kernel with the image was used to search for points of maximum correlation, whose coordinates corresponded to the array of features in the real image, and used to calculate the various error parameters. This solution was very flexible with respect to the image content and remarkably insensitive to noise. It used to measure and correct non-linearities in the J-PEX Vernier anode using the repeller grid image (see Figure 7-34), when circumstances prevented the use of a pinhole mask.

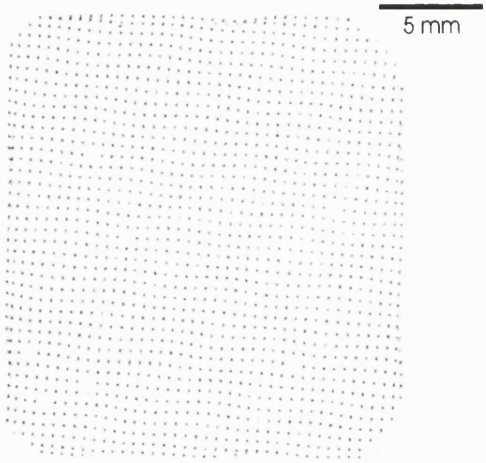

Figure 7-9. A 20 × 20 mm^2 pinhole mask image showing cyclic nonlinearities. The mask had a pinhole spacing of 0.5 mm. This image was taken with the Vernier anode and the linearity was uncorrected.

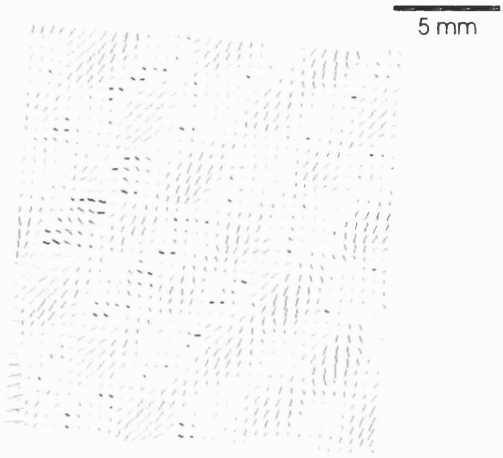

Figure 7-10. A vector plot of the position error for the image in Figure 7-9. The vector magnitudes have been magnified by a factor 5 for clarity.

Figure 7-10 is the output of the analysis software showing a vector plot of pinhole position errors over a 20 × 20 mm^2 imaging area. These position error vectors are used to calculate the x and y position errors which are shown in Figure 7-11. In the Vernier, the x and y co-ordinates are generated by the sum of triplet phases A+B and B+C respectively. The parallel stripes Figure 7-11 indicated immediately that the cyclic errors correlated perfectly with the three phase directions and wavelengths. Figure 7-12 shows the position errors of each pinhole plotted against the expected values of the three phases used to generate them. Each point in the plots represents a single pinhole and the noise in the data is due to the error in the other, uncorrelated phase (each co-ordinate is generated by the sum of two phases). The noise is removed by binning and the cyclic error is characterized by fitting with a sinusoid and selected harmonics.

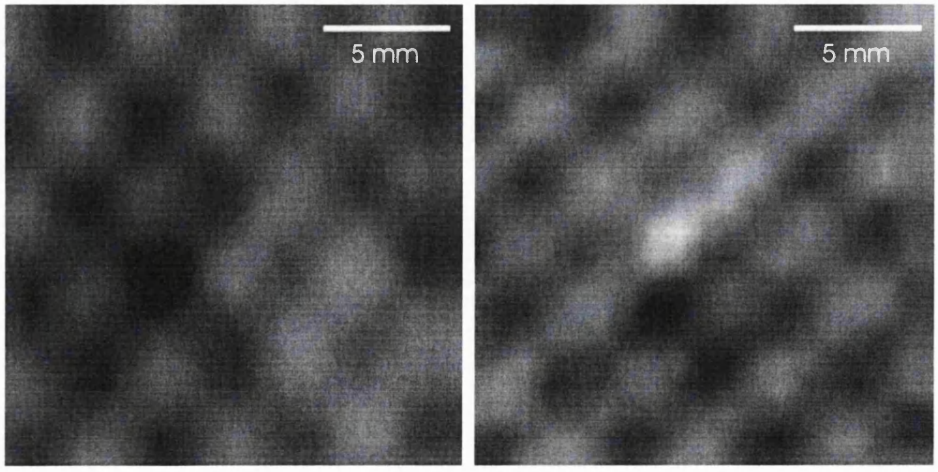

Figure 7-11. Plots of the x and y pinhole position error over the entire pinhole array. The linear structures are parallel to the triplet phase wavefronts and are cyclic, having the same wavelength as the triplet phases.

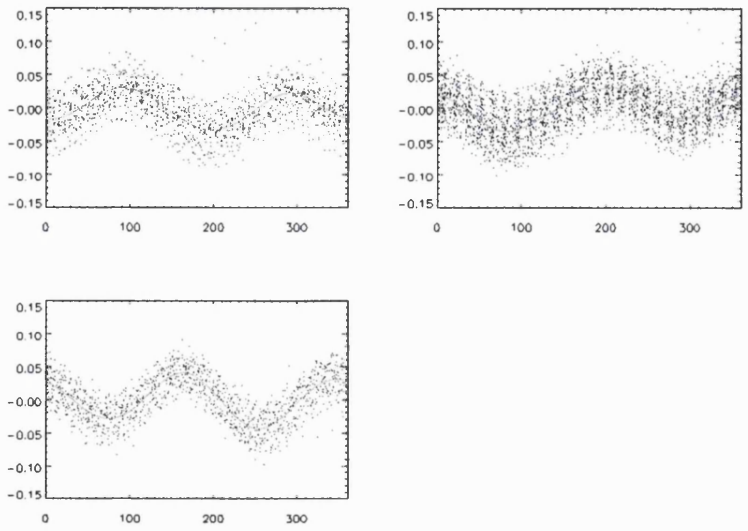

Figure 7-12. A plot of pinhole position errors versus phase for the Vernier anode. The plots represent; the x position error versus expected phase A, the x+y position error versus expected phase B and y position error versus expected phase C, respectively. The fit to the data is also shown.

The simplest method to introduce correction factors into the position decoding algorithm was to modify the phase of each triplet. This was achieved by calculating the phase error of each triplet and generating a set of error terms to correct the measured triplet phase to its expected value. The functions used to characterize the error were sinusoids at the fundamental triplet frequency (i.e. the phase wavelength) and its harmonics. The dominant errors were found to be in the sin(θ), sin(2θ) and sin(3θ) terms and were parameterized as follows :-

$$(7\text{-}1)\quad \delta\theta = a\sin 2(\theta+\alpha) + b\sin 2(\theta+\beta) + c\sin 3(\theta+\chi)$$

These values were implemented in the position decoding algorithm to correct the image distortion in real time. Figure 7-13 shows the same pinhole image as Figure 7-9 with phase correction parameters implemented in the decoding algorithm. Figure 7-14 is the pinhole position error vector plot of the image run through the data acquisition software with corrections implemented, showing the remarkable improvement made to the image linearity.

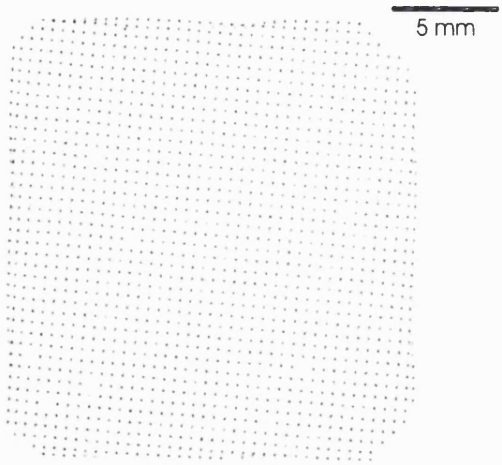

Figure 7-13. The image from Figure 7-9 after correction factors have been implemented.

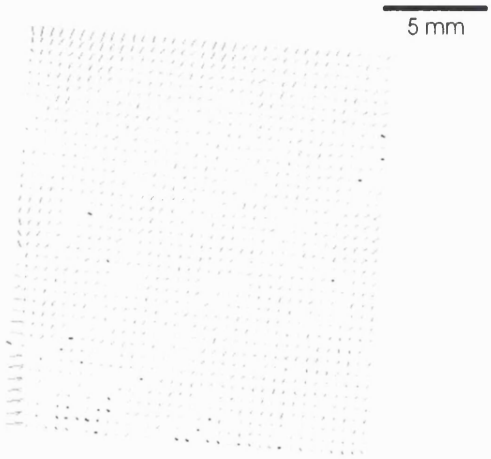

Figure 7-14. The corrected pinhole position error vector plot (c.f. Figure 7-10).

7.3.4 Resolution

Early resolution measurements using the 890 μm pitch Vernier anode were limited by two effects. Firstly, the MCP stacks used for these tests produced a pulse height dependent position shift, which though not problematic for a low resolution readout, degraded the potential high resolution of the Vernier anode. Figure 7-15 shows an image of a test mask consisting of 14 μm slits separated at a 63 μm pitch. Note the image is not an intensity plot; the colours represent the pulse height of the last event to land in a particular pixel and clearly show the pulse height dependent position shift which was found to be aligned with the bottom MCP pore bias angle. This effect is also reported by Tremsin [153].

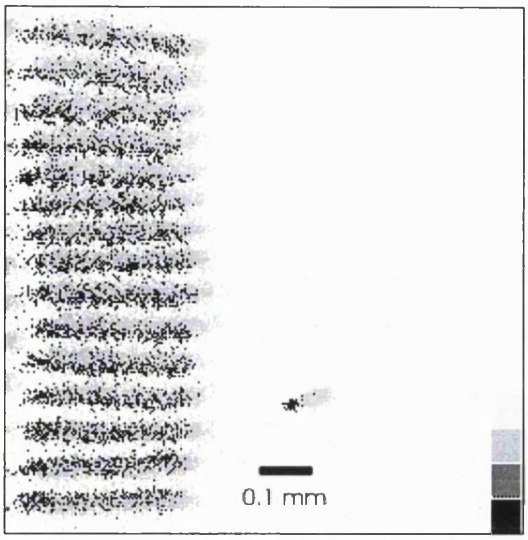

Figure 7-15. A Vernier anode image of the fine bars of test mask. The bars are 14 μm wide on a pitch of 63 μm. The pixel grey scale is used to designate the pulse amplitude for each event showing the pulse height dependent position shift.

The mean width of the slits in this image was measured to be 23 μm FWHM. If the 14 μm width of the slits is deconvolved from this figure, the intrinsic resolution is predicted to be 17 μm FWHM. This sharply contrasted with the predictions from electronic noise measurements which suggested that the readout resolution would be ~6 μm FWHM and the overall detector resolution would be restricted by the MCP pore spacing of 12 μm centre to centre.

The pulse height dependent position shift was probably brought about by a combination of high end-spoiling, which would increase the collimation of the MCP output electrons, and low drift a field, which would accentuate the event position error caused by variation of the electron mean energy as a function of pulse height. A low gain event occurs at lower MCP saturation. Its mean electron energy will be higher, and its effective last dynode position (which determines the degree of collimation along the pore axis) will be further up the MCP pore, than a high gain event. The differences in collimation and transverse momentum between events of differing gains, accentuated a longer time of flight due to the low drift field, produces a pulse height dependent position offset.

The second, more fundamental factor limiting the measured resolution was the reduction in the electrode effective sinusoidal amplitude. The initial criterion that the pattern pitch should be ~1/8 of the electrode sinusoid wavelength was found to be too large. If the footprint was made small enough so as not to reduce the effective sinusoidal amplitude significantly, the image was modulated due to the electrode pitch structure being too coarse with respect to the footprint distribution. There are two solutions to this problem; either to increase the coarse pixel size and decrease the resolution, or to reduce the pitch size and increase the difficulty of manufacture. Since the Vernier readout was being developed to achieve highest possible resolution the latter path was chosen.

7.4 A Vernier Readout for J-PEX

At this stage in its development the Vernier readout was selected for the Joint Plasma Experiment (J-PEX), a sounding rocket mission led by the Naval Research Laboratory, Washington D.C. The J-PEX instrument is an EUV spectrometer using multilayer coated gratings to deliver high spectral resolving power requiring a correspondingly high spatial resolution MCP detector, the latter being the responsibility of two British groups in collaboration, namely Leicester University and MSSL.

7.4.1 Experimental Setup

The development of the Vernier anode was now focused towards meeting the required specification which was initially set at 15 μm FWHM over 30 × 30 mm^2 field of view. The first task was the manufacture of a finer pitch pattern to address the sinusoidal amplitude issue previously described. In order to prepare for this early flight opportunity, the devices manufactured early on in the development phase were made as flight representative as possible. The first J-PEX 9 electrode Vernier readout was manufactured directly on multi-layer ceramic substrate itself (see Figure 7-2), left over from a previous research programme. Later devices used a fused silica pattern substrate glued to the multilayer which, though less elegant, was easier to manufacture, had lower inter-electrode capacitance, and consequently had better performance.

The J-PEX detector used an existing detector body design originating from the ROSAT WFC, modified to accommodate the Vernier anode where necessary to provide the higher resolution required for J-PEX. The existing demountable Vernier prototype detector was initially used for development before the scheduled mating of the MSSL Vernier readout with the Leicester MCPs and detector. It was modified to accommodate a used set of triple thickness, 12.5 μm pore MCPs donated by Leicester University, as well as the multilayer ceramic mounted Vernier anode. This detector was operated in the same regime as the prototype, using a grid interposed between MCP stack and anode.

The Vernier readout manufactured as a J-PEX prototype used the original software written for square pattern production, and utilized a 5 × 5 coarse pixel format , to prove the performance of the 636 μm pitch device as shown in Figure 7-2. The actual J-PEX detector specification required a rectangular image format and the manufacturing software was modified for later patterns and a 6 × 4 scheme was adopted. This final design used for flight had dimensions of 20 × 29.73 mm^2, a coarse pixel size of 5.00 × 5.00 mm^2, a pitch of 636 μm and a sinusoidal amplitude of 35 μm. The insulating gap width was ~ 20 μm. The A, B, and C triplet phase wavelengths were 7.56, 7.81 and 6.59 mm respectively, generated using physical electrode wavelengths of 9.73, 10.29, and 10.29 mm respectively.

Three sets of charge measurement electronics were used during the J-PEX detector development. The lab based system utilized nine identical channels each comprising an Ortec 142B

preamplifier, Ortec 572 shaping amplifier and Canberra 8077 analogue to digital converter (ADC) with a resolution of up to 14 bits. Two sets of flight electronics were constructed, having different preamplifier circuit designs. The Mk1 design was developed by Jason Tandy at MSSL from a five channel system used with a WSA equipped proportional counter on a previous sounding rocket experiment, while the Mk2 design was used to explore the possibilities of miniaturization using surface mount components. All three systems used the same PC based software for data acquisition. The original DOS based application program was written in C, and the final incarnation used for the J-PEX flight was an IDL software suite, comprising integrated electronic calibration, data acquisition, and analysis tools.

The lab system used a LeCroy HV4032B multi-channel high voltage power supply to control each detector voltage independently, allowing great flexibility but in hindsight having the danger that individual channels could trip singly resulting in an over-voltage of detector components. The flight HV system was developed at MSSL from a design conceived for the "blue' detectors on the XMM-OM mission.

Unless otherwise indicated all data was taken using illumination from a low pressure Mercury Pen-Ray lamp, having its major output at 254 nm. The UV source was mounted ~1.5 m away from the MCP on an optical bench outside the vacuum system housing the detector. UV entered the vacuum system via a fused silica window. The MCPs were uncoated and no repeller grid was used in front of the detector. Most of the images were taken using masks constructed in thin metal shim placed either close to, or in contact with the front MCP, which was uncoated.

7.4.2 Readout Optimization

7.4.2.1 Image nonlinearity

The analysis software had been used with the prototype Vernier anode to characterize the readout distortions in terms of triplet phase errors, which were then applied to a modified image decoding algorithm to correct the image distortions. This empirical method, though a powerful technique to improve performance, was not the ideal solution. The factors causing image distortions, time dependent effects, and limiting resolution are influenced by a large number of disparate elements including MCP related effects such as spatial charge distribution, readout pattern design, secondary electron redistribution, substrate charge-up, and calibration of measurement electronics. Results from experiments with the prototype Vernier had shown that these factors vary significantly depending on detector operating parameters, such as the MCP-grid-anode geometry, the MCP-grid-anode voltage configuration, time from high voltage turn-on, and presence or absence of the grid. Experiments were carried out by Sanderson [154] over a large range of the available parameter space in order to untangle the physical causes of these unwanted effects and arrive at solutions which would improve the uncorrected imaging performance,

reducing or removing the requirement for correction factors and enabling the decoding algorithm to be simplified. Additional data from the same Vernier based detector operated in the image charge mode provide powerful evidence to further distinguish and identify the causal agents.

Mechanisms to explain features of the image distortion data have already been proposed by Lapington [155] and Sanderson [154]. The following section provides a review of previous work and proposes refined explanations based on the entire dataset taking into account the important evidence from the image charge mode data. In this mode of operation, some of the physical processes which can cause distortion when charge is directly collected are absent :-

1. While secondary electrons will certainly be produced from the image charge resistive layer to some degree, the only charge redistribution effect arising from their production will be modification the radial footprint distribution by convolution; each element of the primary spatial distribution giving rise to a secondary electron distribution of recollected electrons, which to first order will be azimuthally symmetric and constant. The only effect on the readout will be an altered, but still azimuthally symmetric charge footprint.
2. Substrate charge-up is clearly not relevant in this mode of operation since the image charge resistive layer is uniform and no substrate material is exposed to electron bombardment.

The following analysis of image distortion is divided up into subsections based on the potential causal factors.

Electronic Calibration

A custom software utility was written for the J-PEX development programme and flight operations to automate electronic calibration. Electronic calibration is required since the gains and offsets of the highly sensitive charge measurement electronics drift independently with time. If uncorrected, this results in charge measurement errors on the nine electronic channels used to measure the Vernier anode outputs, which propagate into image nonlinearities and degrade position resolution due to pulse height dependent position shifts.

The basic technique uses a PC to digitally drive a precision digital to analogue converter (DAC) and generate an accurately known voltage. This drives the reference input of a precision tail pulse generator whose output is used to stimulate the charge measurement electronics either via internal preamplifier test capacitors (the default option) or an external reference test capacitor (used to establish the ratio of internal preamplifier test capacitors). The PC is used to compare the digital output from the electronic channel under calibration with the originating digital amplitude. The PC performs this comparison a user defined number of times at several different amplitudes to allow the gain and offset of each channel to be calibrated, either relatively, using the internal test capacitor, or absolutely, using a calibrated external test capacitor.

During this process the electronics are connected to the detector as during detector operation. The software was designed to allow each channel to be calibrated independently to avoid the crosstalk problems (owing to coupling of preamplifiers input via the pattern capacitance) which had caused inaccuracies in the previous calibration technique. The DAC and tail pulse generator linearities were also verified by independent methods as a precaution against inbuilt systematic error.

Figure 7-16 shows a series of screens from the calibration software which display the various textual and graphical output formats. The leftmost purely textual screen displays gain, offset, optional quadratic fit parameters, the X^2 success of fit parameter, together with the electronic noise for each channel. The graphical displays show the input/output linearity plot, followed by two plots of the integral nonlinearity using a two term linear fit, and a three term quadratic fit.

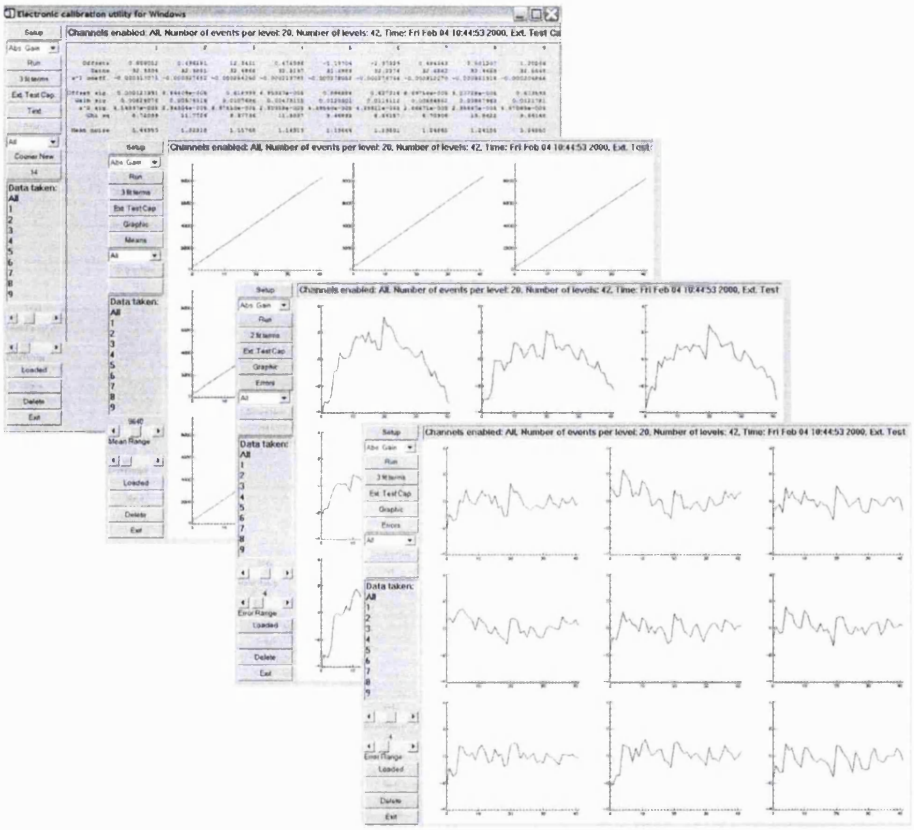

Figure 7-16. Four display screens from the electronic calibration software. These views show the textual and graphical output formats of the gains and offsets, linearity and integral noise performance for the nine channels of the Vernier charge measurement electronics.

The calibration software was used for both the lab NIM-based electronics and both sets of J-PEX flight electronics for which it proved invaluable. It interacted directly with the PC based data acquisition software, used for lab experiments and J-PEX flight operations, to set the gain and offset parameters without the need for human interaction. The software was future-proofed in as much as it was able to handle a user-defined number of channels. This software greatly facilitated calibration allowing it to be performed every day.

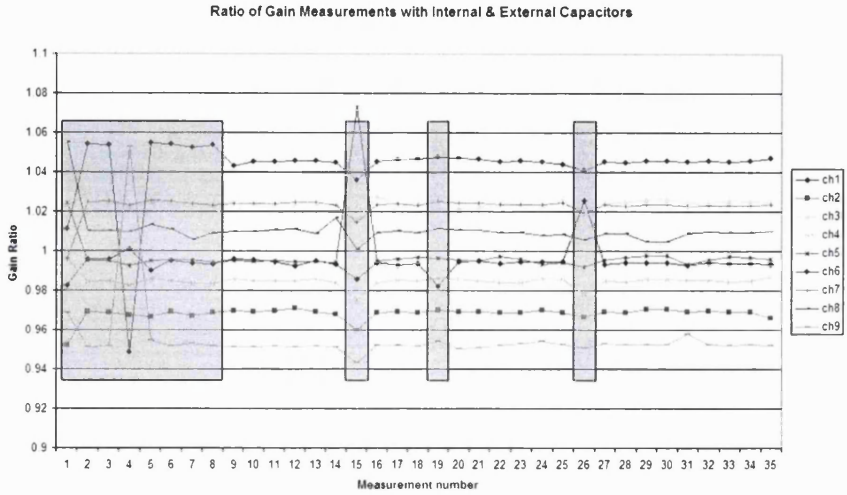

Figure 7-17. The variation in the electronic gains over a 6 month period. This graph shows the ratio of the gains as measured using internal and external test capacitors taken 35 times over a period of 6 months. Excluding the shadowed points which show systematic or operator error, the mean of the standard deviations for the each channel is 0.0011 indicating the stability of the electronic calibration with time.

Figure 7-17 shows a graph of the ratio between the external reference and all nine internal test capacitors from a series of measurements taken over the course of six months. It can be seen that occasional systematic errors are present (which for instance could be caused by grounding /termination changes), even operator error in the early measurements (e.g. in measurements 1 and 4 the channels have obviously been swapped). However if one excludes the erroneous data points shown in shadow, the mean of the standard deviations for each channel is 0.0011 i.e. a variability of just over one part in one thousand. This data indicates the accuracy and stability of the electronic calibration available using this technique so long as erroneous data is recognized and replaced. At this level of inaccuracy it is unlikely that error in the electronic calibration can give rise to the nonlinearity features observed. Simulation of the effect of a normalized gain offset of 0.0011 in one of the three triplet channels shows that it produces a first order sinusoidal phase error ($\sin 2\theta$) with an amplitude of 0.00037, an order of magnitude lower than that observed.

Readout Design Approximations

The first nine electrode Vernier anode initially suffered from an unexpected level of image ghosting due to coarse pixel miscoding. This was quickly diagnosed as a pattern design feature and was due to the fact that the areas of all nine electrodes (at a given x coordinate along the pitch dimension) in each pitch were drawn as if they corresponded to the ratios defining a single point at coordinate x along the pitch. The correct solution should have recognized the differing y coordinates of each triplet (for the same given x coordinate) and the ratios for each triplet should have corresponded to these differing y values. This was easily rectified, initially by a simple algorithm change, but later the correction was built into the pattern. This correction is in itself is

an approximation since the electrodes in every pitch are arranged sequentially in the pattern y axis and their areas should in principle be defined using a different y coordinate for each electrode. However this is not practically realizable since the width of each electrode triplet, given by :-

$triplet_{width} = 3.(a+o) + a.(\sin(\theta_{x,y1}) + \sin(\theta_{x,y2} + \frac{2.\pi}{3}) + \sin(\theta_{x,y3} + \frac{4.\pi}{3}))$ is only constant if $y1 = y2 = y3$ since phase varies with y for all three triplets.

One solution, involving a change to the pattern, would be to shift the phase of the two outermost electrodes, which define the edges of each triplet, so that their new phase more closely corresponds to their actual location with respect to the ideal triplet phase. This has the effect of modifying the amplitude of the third central electrode, so that the original triplet symmetry is destroyed. A better solution would be to leave the pattern alone modify the algorithm so that instead of assuming the three electrodes are offset by 120° from each other, they are offset by $120°+\delta\theta_1$, $120°+\delta\theta_2$, and $120°-\delta\theta_1-\delta\theta_2$, respectively, where $\delta\theta_1$ and $\delta\theta_2$ are the effective offsets of the two outermost electrodes from their nominal expected phase. In fact $\delta\theta_1$ and $\delta\theta_2$ are equal since the phase varies linearly and are proportional to the particular triplet wavelength. Even this correction would be an approximation since the local centre of gravity of all the electrodes follows an undulating sinusoidal path as opposed to a straight line and thus $\delta\theta$ is not constant along the length of the pitch. However, as an approximation, the constant phase angle associated with the mean of this sinusoidal oscillation could be used to set $\delta\theta$.

This algorithm modification could be simply accomplished by changing transformation matrix that converts triplet electrode amplitudes to intermediate Cartesian coordinates, prior to polar transformation.

The J-PEX pattern parameters were used to calculate the real values of the individual electrode phase offsets and the phase error calculated. The analysis in Figure 7-18 shows the calculation of the phase error for triplet A, which was found to be a very close approximation to a first order sinusoidal of the form $\theta' = \theta + \alpha\sin(2\theta)$. The amplitudes of the phase errors for all three triplets were calculated to be A: 0.021, B: 0.022, and C: 0.029, and the phases of the errors in radians were given by A: 2.03, B: 0.57, and C: 1.13. These figures show a striking resemblance with linearity data obtained using image charge, and their relevance is described later in the section.

Unlike SPAN, for which the electrode structures were drawn projected as discussed in section 6.3.1, the J-PEX electrodes were drawn as sinusoids rotated, as opposed to projected, from the phase direction to lie along the pitch direction. Sanderson [154] discusses the potential error that this causes. However, the only major difference between the two schemes is the choice of orientation of the two dimensional axes along which you choose to integrate to arrive at the overall areas under a given charge footprint, the final integrals being comparable. The significant practical difference between the two schemes is that the phase offsets of the individual electrodes

has to be calculated differently; the rotated scheme having two phase error components corresponding to lengthways and vertical offsets of the electrodes (with respect to the pitch axis), whereas the projected scheme only has a phase error corresponding to the vertical offset of the electrodes.

If we use the calculated electrode phase errors for triplet A :-

$off_a := -0.018501738$

$off_b := -0.055505215$

$off_c := -0.092508692$

These modify the electrode definitions :-

$$a(\theta) := \alpha \cdot \left(\sin\left(\theta + off_a\right) + 2\right)$$

$$b(\theta) := \beta \cdot \left(\sin\left(\theta + \frac{2}{3}\cdot\pi + off_b\right) + 2\right)$$

$$c(\theta) := \gamma \cdot \left(\sin\left(\theta + \frac{4}{3}\cdot\pi + off_c\right) + 2\right)$$

If the standard transformation calculation is used (assuming 120 degree offsets :-

$$X(\theta) := \frac{b(\theta) - c(\theta)}{\sqrt{2}} \qquad Y(\theta) := \frac{2\cdot a(\theta) - b(\theta) - c(\theta)}{\sqrt{6}}$$

Then the circle in the charge domain is distorted :-

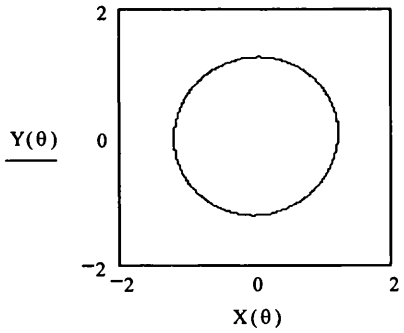

The error in θ is given by :-

$$\delta\theta(\theta) := \operatorname{mod}\left[\left(\theta - \operatorname{atan}\left(\frac{Y(\theta)}{X(\theta)}\right)\right) + \frac{\pi}{2}, \pi\right] - \frac{\pi}{2}$$

which can be plotted and a fit found (shown dotted) :-

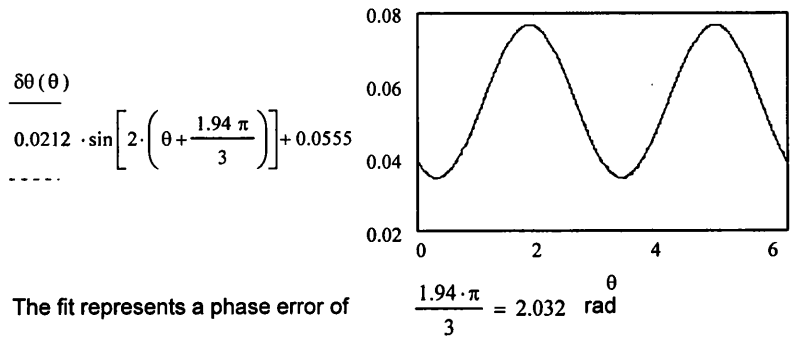

The fit represents a phase error of $\frac{1.94\cdot\pi}{3} = 2.032$ rad

Figure 7-18. Calculation of the phase error due to the individual positions of electrodes. A Mathcad spreadsheet showing the charge domain circle distortion and calculation of the phase error due to the electrode position offsets for triplet A.

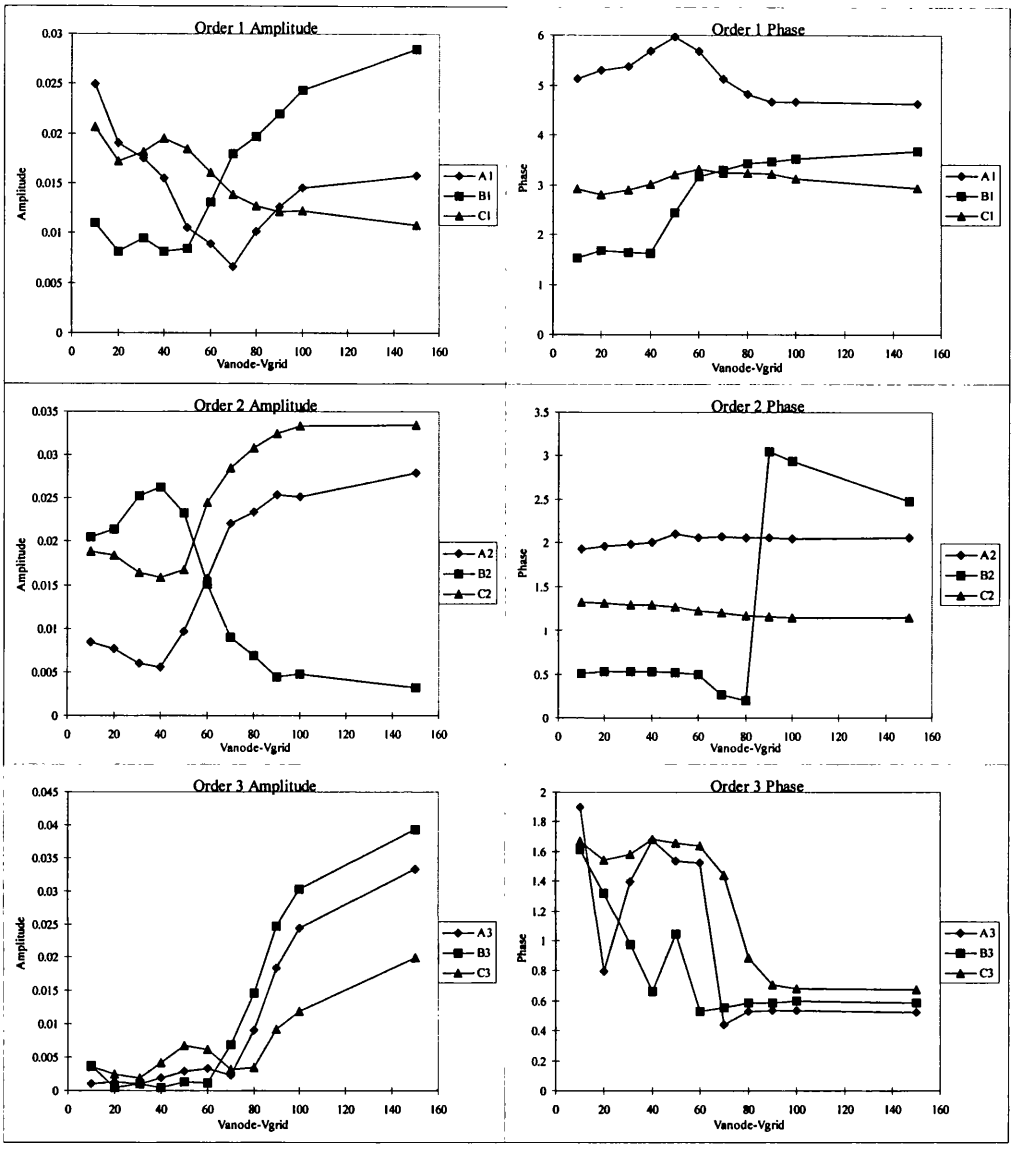

Figure 7-19. The variation of phase error fit parameters with grid to anode voltage. This data represents a constant grid to MCP voltage of 260 V, using sin(θ),sin(2θ) and sin(3θ) fit terms. The detector is operating with electron accelerating fields between MCP to grid, and grid to anode.

There is some evidence from the collected charge mode that points to these small phase offsets of individual electrodes being a significant factor causing image distortions. The pattern manufacture was simplified by organizing all three triplets in the same way. The electrode order in all three is 1,3,2 in the positive x direction and triplets A and C are drawn in the same sense using positive phase offsets between pitches in the positive y direction to generate the required phase directions. The opposite sense of phase C is introduced in the polar conversion in the algorithm. Triplet B uses a negative phase offset between pitches to generate its required phase direction. The order of increasing individual electrode phase offsets in the direction of positive phase is thus 3, 2, 1 for both A and C, while for B it is 1, 2, 3. This asymmetry between the operation of electrodes B and A, C is reflected in many of the sets of linearity data. Figure 7-19 shows a plot representing the variation in the fit parameters with the grid to anode voltage at a constant MCP to grid voltage.

There is a noticeable difference of behaviour between the zeroth and first order fit amplitudes for triplet B versus those for A and C.

Charge Footprint Distribution Sensitivity

Though in theory the Vernier readout linearity should, like the WSA, be independent of charge footprint size and distribution so long image modulation and edge effects do not occur, evidence points to the contrary. Data obtained using the Vernier readout in image charge mode from Sanderson [154] is important in assessing how the charge cloud footprint size and distribution affect image distortions.

Figure 7-20 shows an equivalent series of linearity fit plots similar to Figure 7-19 but with the Vernier readout operating in image charge mode. All terms are effectively constant, or noise limited as in the case of the second order phase, except for the zeroth order amplitude, which diminishes as MCP to anode voltage is increased. The primary effect of this increase in voltage is to reduce the size of the charge footprint landing on the anode, limiting the charge footprint on the Vernier anode to that produced by the induction process (see equation (5-14)) through the substrate and whose scale varies with substrate thickness.

Since we have demonstrated the accuracy of the electronic calibration, and other effects such as charge redistribution, and substrate charge-up are not applicable to image charge mode, this data is evidence that :-

1. The variability of the zeroth order phase error ($\sin(\theta)$) term in this mode is caused by the change in size of the charge footprint alone.
2. All the other terms are static and can be attributed to errors in the pattern geometry.

Note that second order distortion is effectively absent. This component is strongly sensitive to grid to anode voltage in the collected mode and its cause will be discussed later.

One obvious explanation of the zeroth order variability seen in Figure 7-20 is an offset of the origin in the charge domain space used to calculate the phase angle. This would be caused by inequality in the mean values of each electrode and would give rise to a phase error growing larger as the circle size becomes smaller, which occurs as the MCP to anode voltage reduces. This effect could result from either a pattern error, or from some feature of the charge induction mechanism causing an offset in the measurements.

Analysis of the circle radius shows that it is significantly smaller than the typical values obtained in the charge collection mode. This small radius has a number of implications Firstly, the image charge Vernier is not operating in an optimum configuration and resolution will be degraded. Secondly, the smaller radius is caused by an overly large charge footprint, and given the fact that the induced charge footprint is infinite in extent, it will have some power outside the active pattern region. This charge will be induced on the contact pads, particularly the bus-bars (see

Figure 7-3) surrounding the active pattern area, whose geometry is likely to give rise errors which cause offsets of the circle origin. As the MCP to anode voltage is reduced, the footprint grows in size inducing more charge on external electrodes, and the circle size diminishes enlarging the relative offset, both effects compounding to increase the zeroth order the phase error.

Qualitative analysis of the circles of events in the charge domain space for each triplet shows that while the data is reasonably circular, limited by the first order distortion which is apparent as an elliptical distortion, they are visibly offset from the nominal origin as expected.

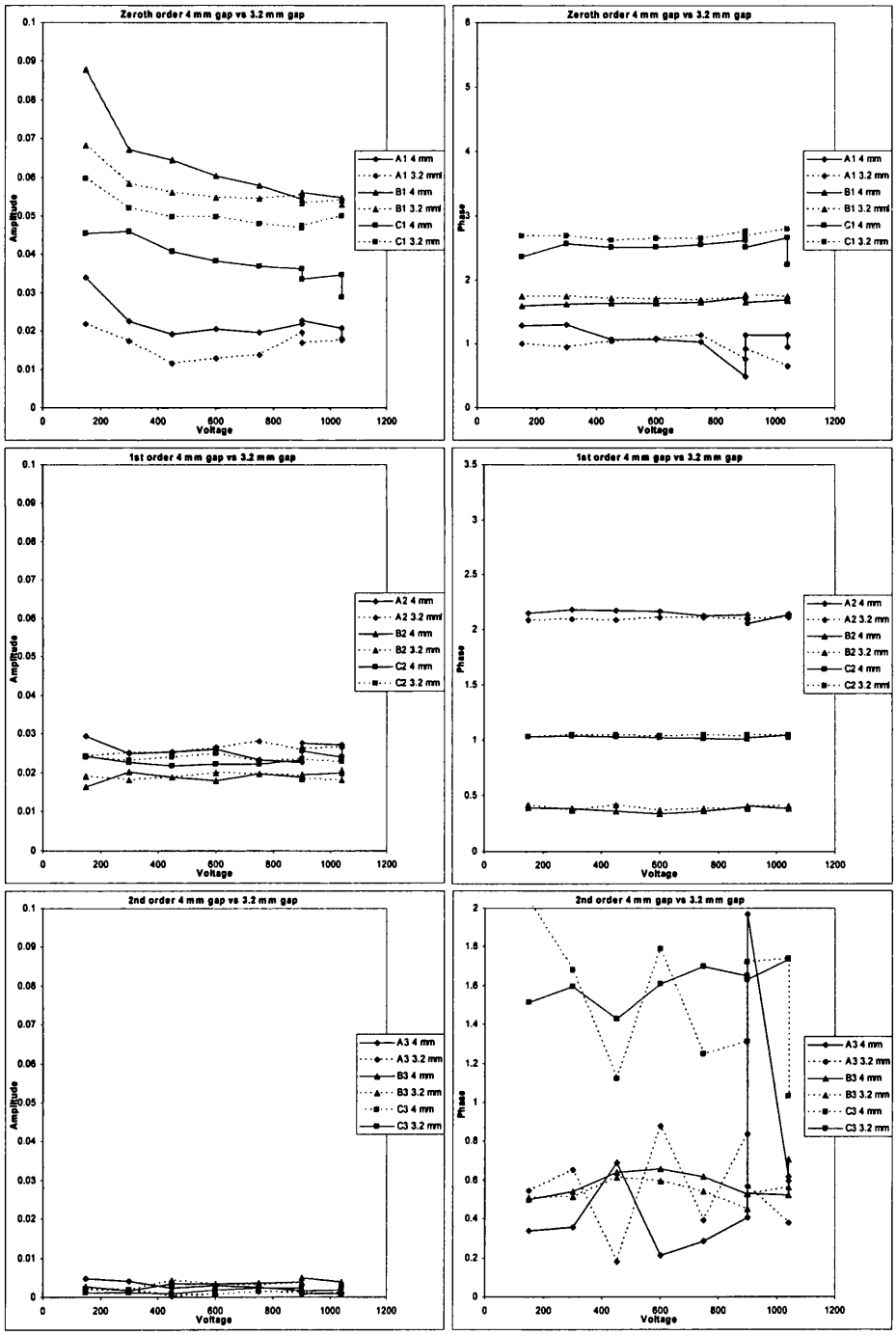

Figure 7-20. Linearity fit data in image charge mode for varying MCP-anode voltage.

The data from the simulations of the effect of the electrode offsets due to their position within each triplet presented in the previous section shows remarkable correlation, in both predicted

amplitude and phase for all three triplets, with the first order distortion measurements in image charge mode, shown in Figure 7-20. From this we can conclude that the major component of the first order error is due to this pattern feature. As discussed previously, it is easy to correct, requiring a simple change in the transformation matrix used to convert the three electrode values to a Cartesian coordinate on the normalized charge domain plane, prior to the polar transformation which generates the triplet phase coordinate.

Secondary Electron Redistribution and Substrate Charge-Up

One of the major characteristics of secondary electron production in the WSA is rate dependent position shift caused by differential electrode voltages (see section 5.2.2). This symptom straightforwardly indicates the effect in the WSA, however the behaviour of the Vernier readout is more complicated. Firstly, because of the sensitivity of the electrode sinusoidal amplitude to charge footprint size, the difference in mean signal currents which generates the differential voltages is footprint size dependent, unlike the WSA where it is independent because of the WSA's linearly changing electrodes. Secondly, whereas the centre of gravity of the image distribution predicts the differential voltages directly for the WSA, no such simple answer applies to the Vernier. The use of a fine pinhole mask should minimize the extent to which small repositioning affects mean signal currents and thus differential voltages, however something as simple as fluctuation in the illumination intensity over the mask would change the behaviour unpredictably. Thus the linearity data obtained in collected charge mode, where secondary electron distribution occurs, has to be given lower status than the image charge data. Though the Vernier anode used as low value bias resistors as was practical, without significant noise increase, to minimize differential voltages, this mechanism could well lie behind the anode to grid voltage dependent variation in the error fit parameters shown in Figure 7-19.

Much of the collected charge data is awkward to interpret conclusively. For instance, it is been suggested that the asymmetries between triplets in the zeroth and first order amplitudes could correlate with a pattern design feature. It is difficult to identify anything more substantial about these data apart from the fact that nothing else has been identified which can provide this correlation. However the second order data is more interesting, displaying obvious symmetry between all electrodes, with a distinct change of mode at between 60V and 80V grid to anode voltage when the distortion suddenly becomes much larger.

The second order error parameters are highly correlated with distortion of the circular form of the event loci in the normalized charge domain plane. This circle takes on a triangular distortion whose apexes lie either at the phase associated with maximum or minimum electrode area depending on the mode of operation of the detector. If the grid voltage is positive with respect to the anode and secondary electrons are removed from the anode, leaving a net positive charge on the pattern electrodes, the sense of the distortion is opposite to that when the field is reversed and secondary electrons are collected on the anode.

Figure 7-21 and Figure 7-22 show the distortions in the circle radius for a range of MCP to grid, and grid to anode voltages, with the anode both positive and negative with respect to the grid. The enlarged circle diameter in Figure 7-22 is a result of the induced negative charge on the anode from the grid (which is collecting secondary electrons from the anode) which diminishes the positive electrode signals by a constant offset determined by the capacitive coupling.

The fit parameters corresponding to the data in Figure 7-21 and Figure 7-22 are shown in Figure 7-23 and Figure 7-24 respectively. These data sets show that the reversal of the circular distortion corresponds to a change of 60 degrees in the second order phase parameters. In addition, for the case where the anode is positive with respect to the grid, the 2nd order amplitude rapidly rises for anode to grid voltages above 60 V. This is just above the voltage at which the secondary emission coefficient of quartz rises above unity (30 ~ 50 V) [139]. All other fit parameters show a marked change above this voltage, which suggests that substrate charging is playing an important role.

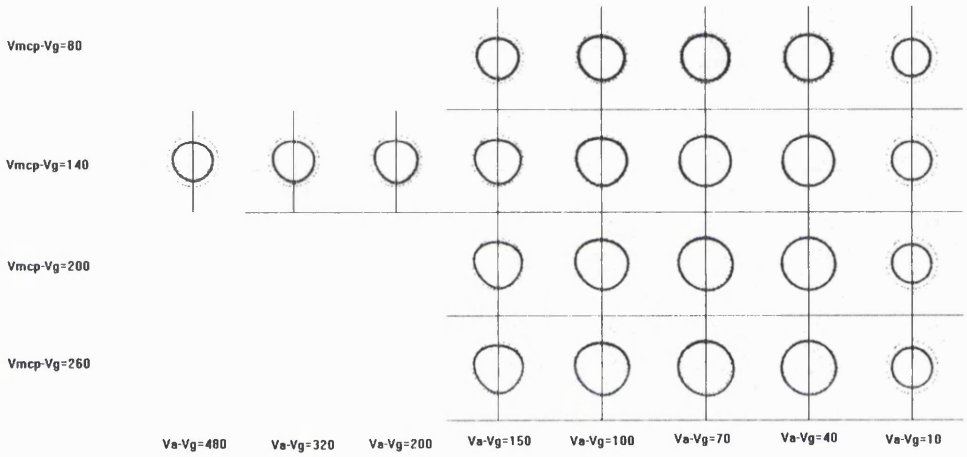

Figure 7-21. The normalized charge domain circle size versus voltage (mode 1). This data was taken over a range of MCP to grid, and grid to anode voltages. In all cases the anode is positive with respect to the grid.

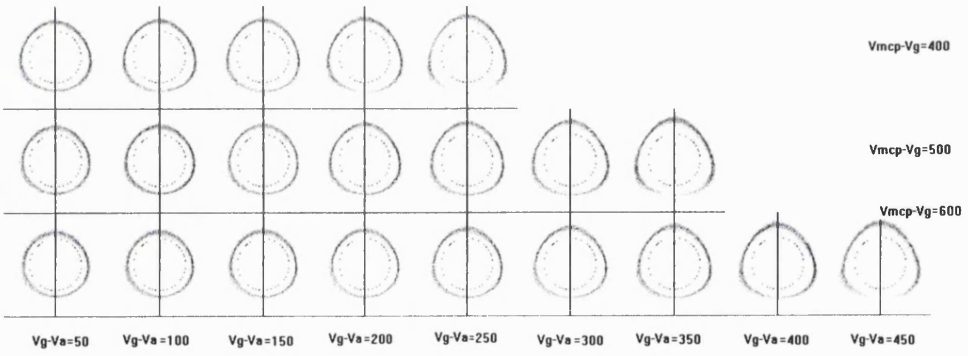

Figure 7-22. The normalized charge domain circle size versus voltage (mode 2). This data was taken over a range of MCP to grid, and grid to anode voltages. In all cases the anode is negative with respect to the grid.

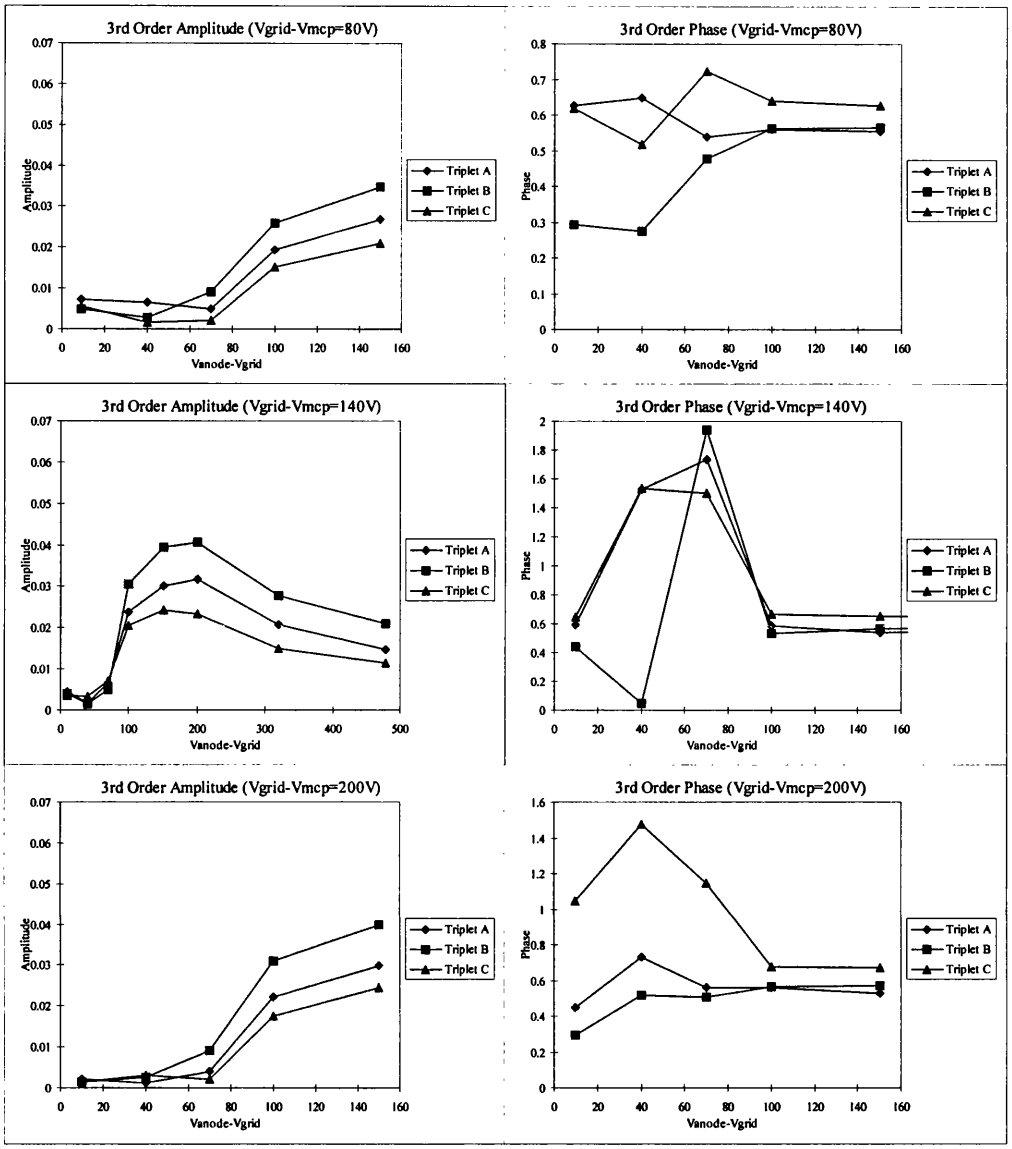

Figure 7-23. The second order phase error characteristics for mode 1. The amplitude and phase parameters corresponding to data in Figure 7-21, with the anode positive with respect to the grid.

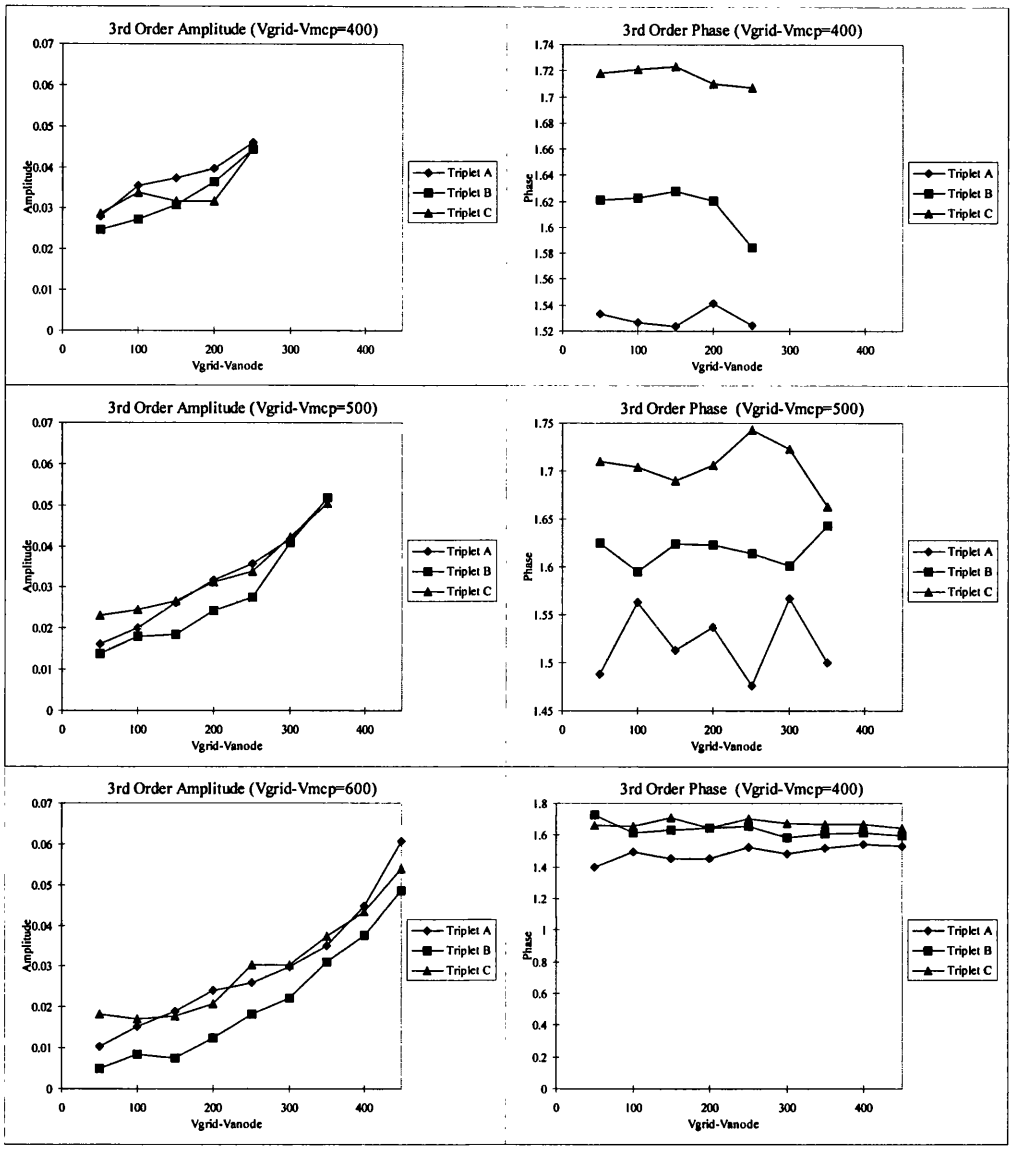

Figure 7-24. The second order phase error characteristics for mode 2. The amplitude and phase parameters corresponding to data in Figure 7-22, with the anode negative with respect to the grid.

This effect can be explained as follows :-

At anode to grid voltages below 50V, Primary electrons from the MCP, and accelerated by the MCP to grid field, have enough energy to produce several secondaries, and thus charge the insulator positive. However, for the secondaries produced from the grid and attracted towards the anode (and particularly towards the now positively charged insulators), the secondary electron emission coefficient of the insulator is less than unity, and these electrons do not have sufficient energy to produce surplus secondaries themselves. They simply are able to discharge the positive charge created in the insulator by the primary MCP electrons, which arrive first due to their higher energy. Thus the insulator is discharged and its potential remains near that of the anode electrodes.

If the anode to grid voltage is greater than 50 V, the emission coefficient is greater than unity for all incoming electrons, and any electrons hitting the insulator cause positive charging. There is

nothing to prevent the insulator gap charging positive, apart from secondaries produced from the anode, which are now more constrained by the higher grid to anode field. In the areas of the pattern where the insulator makes up a large proportion of the local area, such as around the electrode minima, the attraction of positively charged insulator will be greater, and will soak up more of the locally produced secondary electrons. The electrode minima will be depleted of secondaries and appear to be smaller relative to the remaining electrode, producing lobes at the phases of the electrode minima. This is supported by the distortions of the circle shown in Figure 7-21 which appear relatively quickly above 50 V anode to grid voltage.

Further evidence of insulator charge up is given by the temporal variation in the second order amplitude parameter, which changes from close to zero when the insulator is fully discharged and lies on the anode equi-potential surface, rising to its nominal value after charge-up in timescales of tens of minutes after initial turn-on [154].

Summary of Vernier linearity performance

The development of the linearity analysis software was crucial in allowing the nonlinearities to be quantified and characterized. The electronic calibration software provided an accurate and ergonomic means to set up the gains and offsets, which were then automatically propagated to acquisition software. This technique has been shown to minimize the effects of electronic nonlinearity to sufficiently low levels to be insignificant to readout performance. Readout pattern design has been investigated and some corrections to the pattern and algorithm have already been applied successfully to minimize the associated distortions. Simulations of the nonlinearities due to further pattern features correlate well with image data using an image charge detector indicating that first order ($\sin 2\theta$) errors are primarily pattern related. Though in principle the Vernier should be insensitive to the charge footprint distribution, evidence from the image charge mode shows a zeroth order correlation. This is very likely due to the over large footprint falling on to the external contacts. The image charge technique allows an ingenious solution to this problem. Since the pattern does not collect charge, and the capacitive coupling is through the substrate, wire bond interconnects between electrodes can be made in the active pattern region and external electrode structures removed altogether.

A comparison, of the linearity data between image charge and collected charge modes shows the extent to which both secondary electron redistribution and substrate charge-up degrade performance in the latter. The physics of the electron interactions in the volume between the output face of the MCP, the electron control grid, and the readout anode is highly complicated and a comprehensive model would have proved exhaustively time consuming. The variation of the zero and first order distortions with detector parameters in the collected charge mode indicate the complexity of the problem. Many factors influence these linearity data, including image dependent interelectrode voltages, secondary electron coefficients, energies and distributions, electrode and substrate material properties, MCP electron energies and distributions, substrate

charge-up, etc. making it very difficult to analyze or model. The second order term has a more predictable behaviour. Its voltage sensitivity in collected charge mode strongly suggests that it is caused by substrate charge-up alone, a conjecture supported by its effective absence in image charge mode.

The collected charge mode of operation can still provide reasonably good linearity if these effects are mediated by the use of a control grid operating in the correct voltage regime. Despite the variability of the linearity data, the stability of a fixed point in the parameter space i.e. a given detector configuration enables us to correct linearity to a significant degree. Typical linearity, measured as the standard deviation of pinhole position errors across the image is in the range 16-24 μm. The linearity correction achieved in the image charge mode is even better.

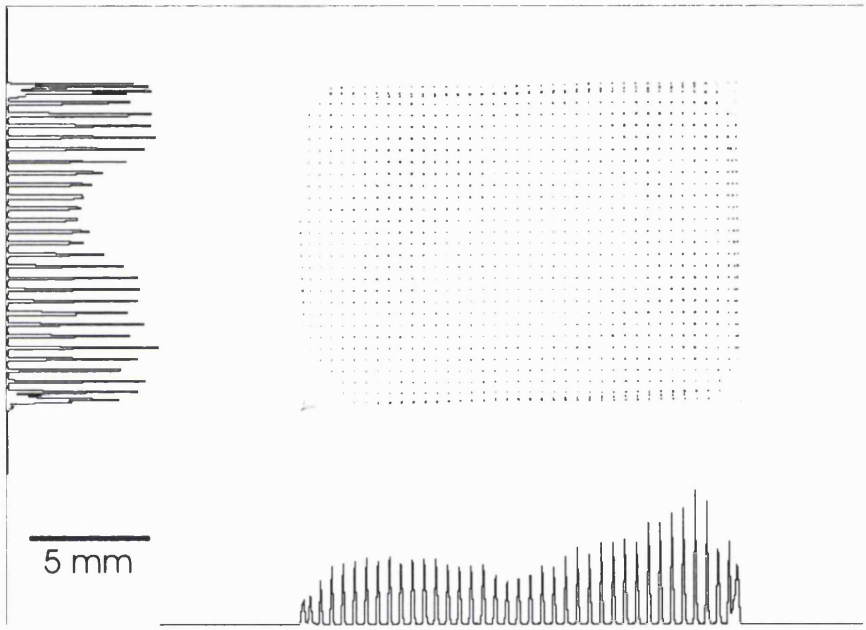

Figure 7-25. A 0.5 mm pitch pinhole mask image in image charge mode. The position error over the central 23 × 36 pinholes is 13.2 μm rms. and 12.4 μm rms. in x and y respectively. The image wrap-over at the perimeter of the field is due to electrostatic distortion at the lower MCP contact face.

Figure 7-25 shows data taken using image charge of a pinhole array having a pitch of 0.5 mm. The measured position error over the central 23 × 36 pinholes is 13.2 μm rms. and 12.4 μm rms. in x and y respectively.

Modification of the algorithm to correct the first order pattern produced distortion, together with optimization of the image charge Vernier pattern and detector configuration, to reduce footprint size and eliminate external contacts, is expected to correct the zeroth order distortion, leaving the detector essentially distortion free.

7.4.2.2 Image resolution

The image resolution of 17 μm FWHM achieved by the prototype two dimensional Vernier anode, while by no means a poor result, was disappointing compared with the expected value of less than 10 μm FWHM calculated using measured electronic noise, calculated partition noise and taking into account the lower than ideal charge domain circle radius. This led us to consider other factors which could cause degradation within the detector, such as the discrete nature of the MCP itself, and the possibility that noise is introduced into the event centroid as charge propagates firstly through the MCP, and then the drift gap where it spreads out on to the readout.

One limitation of any MCP based detector, which has become a major factor as higher resolution readouts have become available, is the image quantization due to the pore spacing in the first MCP. The prototype detector used MCP with pore spacing of 12 μm in the standard hexagonally packed format and for the J-PEX prototype the pore spacing increased to 15 μm. Though this essentially limits the overall detector image resolution, it is actually useful for characterizing the intrinsic resolution and differential nonlinearity of the readout if the individual pores of the first MCP can be resolved. This is possible for events initiated from a single photoelectron since only a single pore in the first MCP can be stimulated. This situation is the norm when illuminating bare MCPs with longer wavelength UV from a Penray lamp; the experimental arrangement. Only with higher energy photons and a more efficient photocathode would you start to expect to see multiple photoelectrons [156].

The Inter-plate Gap

To maintain resolution, the accuracy of the charge centroid needs to be retained as it progresses through the MCP stack. Once a single pore in the first MCP has been fired, the resulting electron cloud exiting from the bottom of the pore is used to stimulate the next MCP. The first and most significant source of centroid noise is this interface. It would be virtually impossible and extremely impractical to consider matching geometries between MCPs to achieve one to one pore position correspondence. Therefore with the MCPs butted together there is the possibility, even likelihood, that low frequency Moiré fringing causes positional variation of the distribution of lower MCP pores excited, altering the local gain and image centroiding accuracy [157]. In addition, the difficulty of achieving good MCP surface flatness (probably due to the stress relieving effect of the pore etching process), causes positionally variable gaps between MCPs further accentuating this problem. The positional variability with which the lower MCP is stimulated can be alleviated by physically separating the MCPs and using this inter-plate gap to allow some degree of spread, improving the statistical distribution of the charge and increasing overall MCP gain by firing more, lower MCP pores. However there can be problems with this approach. There is some evidence that high energy secondary electrons produced from the lower MCP web can travel significant distances laterally through the gap and give rise to satellite events around the main event, distorting the charge centroid. This may certainly be a problem when the

nature of the device requires a conductive shim be used (i.e. a sealed tube that cannot accommodate thin polymer insulators). However evidence from the J-PEX prototype indicates that this effect is not apparent when an accelerating voltage is applied across this small gap.

The detector was initially configured with the MCPs butted together, later modified by the insertion of a 12.5 μm conductive shim. This modification was made primarily to increase the initially low MCP gain (by virtue of increasing the number of lower MCP pores excited), and to avoid the potential Moiré fringing effects as referenced earlier. The conductive shim was later replaced by a 100 μm thick component manufactured of double side copper clad kapton which allowed an inter-plate field to be applied. Using a test mask, resolution was found to be degraded at very low accelerating voltages, reaching a soft minimum at a voltage of 100-200 V. This empirical result was used to fix the inter-plate voltage at 200 V from then on.

The role of the intermediate grid

Having minimized the centroiding degradation through the MCP stack, the next major influence on Vernier anode resolution was the collected charge footprint, which controls the amplitude of the electrode sinusoidal modulation, directly driving the readout resolution. The initial concern was simply to optimize the footprint distribution and maximize electrode dynamic range without causing image modulation. This optimization was being carried out in a detector configuration using an intermediate grid between MCP and anode, which had been shown to reduce position non-linearities as described in the previous section.

In its original concept the grid had been perceived as a way of applying a high field region just above the anode which could control the trajectories of secondary electrons produced on the anode and limit their lateral travel, with the aim of reducing the possibility of their being captured by a different electrode and thus mediating charge redistribution. However, an alternative configuration was used which simultaneously improved both linearity and resolution.

The improved configuration used a high MCP-grid field, and low grid-anode field. The detector had an MCP to grid spacing of 5 mm, and a grid to anode spacing of 0.7 mm. The nominal operating regime producing the best results used an MCP-grid accelerating voltage of 900 V and a grid-anode accelerating voltage of 20 V.

This alternative solution was discovered by Sanderson [158] while exploring the entire envelope of possible operating regimes and at first sight seems counter intuitive. The high field between MCP and grid has been demonstrated experimentally to produce a very small footprint size which would certainly give rise to image modulation. The low field between grid and anode would not be expected to significantly alter the distribution of high energy primary electrons passing through the grid. Secondary electrons produced from the grid would be initially influenced by the stronger field above the grid. Coupled with the leakage of this field through the grid, and the grid to anode field, they would have their lateral motion highly constrained, especially since the grid-anode

dimension is relatively small and the vast majority of the secondaries have low energies [139]. Given this, there appears to be no mechanism for adequate charge spread, though the experimental evidence shows that this does occur since image modulation is not present.

This serendipitous empirical result was then investigated to determine its modus operandii. Figure 7-26 shows the radial charge distribution measured using the slit strip anode for following :-

i) the charge footprint reaching the grid, simulated by measuring the footprint using a grid-less drift region with an MCP-anode voltage of 900V

ii) The charge footprint as collected by the Vernier anode at nominal voltages of 900 V between MCP and grid, and 20 V between grid and anode, measured by simply replacing the Vernier with the Split strip anode.

iii) the charge footprint as collected by the Vernier anode in a grid-less configuration using 200 V between MCP and anode, the optimal voltage for this mode of operation.

iv) the charge footprint as collected by the Vernier anode in a grid-less configuration using 100 V between MCP and anode, the optimal voltage for this mode of operation.

For easy comparison of data Figure 7-26 has been normalised for equal area under the radial distribution as opposed to equal charge.

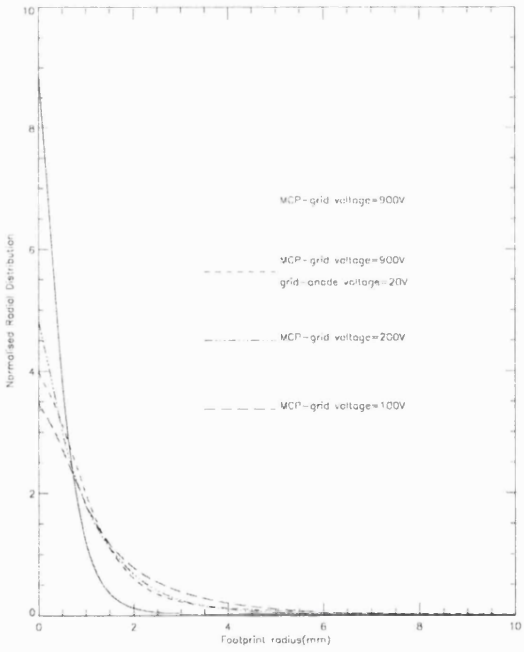

Figure 7-26. The radial charge distributions using several operating modes. This data used collected charge mode in three operating regimes, (i) MCP:anode = 900 V(no grid), (ii) MCP:grid:anode = 900:20V, (iii) MCP:anode = 200 V(no grid), and (iv) MCP:anode = 100 V(no grid). N.B distribution (ii) undergoes significant enlargement between grid and anode.

Figure 7-26 shows that, as expected, the charge footprint produced by a grid-less configuration with a 900 V MCP to anode accelerating voltage is small. This footprint corresponds to the

footprint arriving at the grid in the nominal mode of operation with the grid in place. However the distribution collected by the anode in the nominal mode of operation is significantly broader, and quite similar in scale to that produced using a grid-less configuration with a low accelerating voltage of 100-200V. The grid itself must be providing a mechanism to spread the footprint to the size necessary for satisfactory modulation-free operation of the Vernier anode.

Possible mechanisms for the footprint enlargement include the lateral spread of secondaries, or electrostatic lensing by the grid. Given the low energy of the secondaries, it seems unlikely that they could provide sufficient spread, but this requires further investigation. Another possibility is electrostatic lensing due to the grid bars. The grid used for this experiment was rather fine with a pitch of 17 μm and an open area of ~60 % and thus all primary electrons pass within at least 6.7 μm of a grid bar. The ratio of field strengths above and below the grid was 6.3. An electrostatic lensing effect similar to that found in the output region of an MCP pore could be present. This mechanism would cause primary electrons passing close to the grid bars to have their near-normal trajectories given a horizontal component resulting in a transverse shift.

For either mechanism the net result would be convolution of the small charge cloud reaching the grid, with the footprint enlargement function. This could provide an explanation for the marked improvement in position resolution which occurred as soon as this mode of operation was implemented, immediately showing that the Vernier could indeed produce MCP pore-limited image resolution. Figure 7-27 shows a small part of a test mask image, consisting of 50 μm bars at 180 μm centres. The MCP pores suddenly became visible.

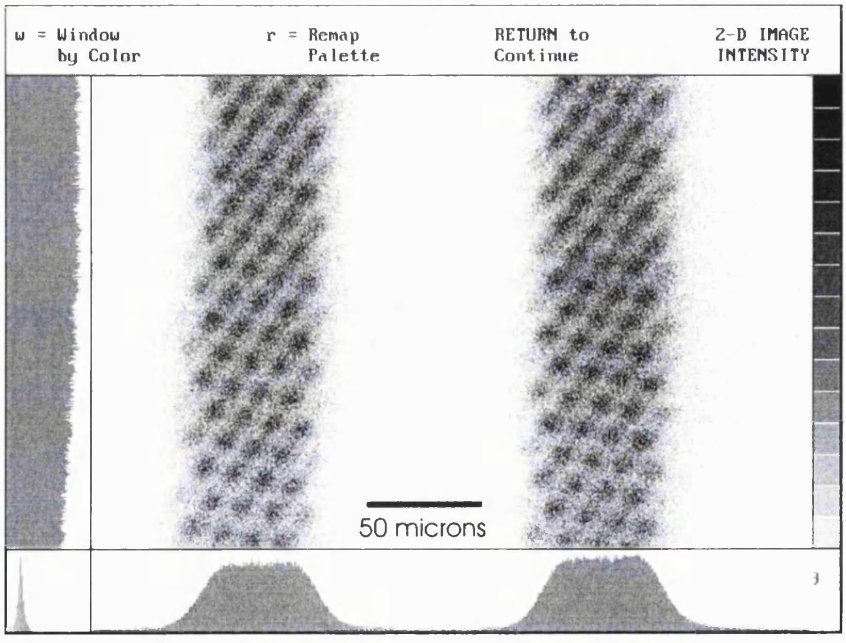

Figure 7-27. An image of 50 μm wide bars of a resolution test mask showing MCP pores. The hexagonal structure in each bar is the MCP pore arrangement in the top MCP.

The normal mode of operation of most charge division devices uses a drift field to allow the charge footprint to expand to a suitable size for the anode requirement. If inhomogeneity exists in

the MCP output charge distribution, then depending on how it is manifested in the electron energy/angular distribution, it could be reflected in a corresponding inhomogeneity in the collected footprint distribution, whose size depends on the expansion allowed by the drift field. The centroid error produced by the inhomogeneity could scale with the footprint size. If instead, the charge footprint scale is kept small, and is followed by a mechanism characterized by azimuthally symmetric convolution which produces the footprint magnification, the centroid error will correspond only to the initial expansion process, not the convolution. An azimuthally symmetric convolution retains the centre of gravity of each point about which it is performed, and thus maintains the centre of gravity of the entirety of the data set convolved.

This hypothesis is supported by evidence from intensified CCD detectors [159], where images of the MCP pore structures are readily obtained (when using pixel centroiding techniques), and higher resolutions are readily achievable in designs using proximity focused MCP output stages.

MCP Pore-limited image resolution

The best image resolution previously measured using the prototype, which utilized a grid but still relied on charge expansion in a relatively low drift field, had been 17 μm FWHM after deconvolving the mask and windowing in energy to remove the effect of the pulse height related position shifts due to the MCPs. Once the modified grid voltage regime was applied, the Vernier anode resolution improved dramatically reducing to 10 μm FWHM. The MCP pore structure was now the factor limiting resolution, and the readout could now easily resolve individual pores in the front MCP together with the boule boundaries, missing and damaged pores, and a hint of the boule boundaries in the lower MCP. Figure 7-28 shows an image of a 1 mm diameter illuminated area on the detector.

Figure 7-28. A Vernier anode image showing clearly resolved MCP pores. A 1 mm diameter illuminated area of the JPEX flight Vernier anode and electronics using 12.5 μm pore MCPs. The Vernier readout easily resolves the pores and boule boundaries in the top MCP. This data represents a readout resolution of 10 microns FWHM. The electronic noise was measured at 4 μm FWHM.

Resolution using Image Charge

The image charge technique had clearly provided superior linearity, even given the improvements obtained by reconfiguration of the collected mode grid operating regime. Although too late to use this for the first J-PEX mission, it was decided to investigate its image resolution. A series of experiments using the J-PEX Vernier design in image charge mode are described by Sanderson [154].

One of the aims of the image charge experiments was to provide further evidence to support the hypothesis regarding charge cloud inhomogeneity. Since the charge footprint could be enlarged sufficiently using induction process through the substrate thickness alone, the MCP could, in principle, be proximity focused to the image charge layer, which would reduce any charge centroid errors even further.

In practice it was more difficult to achieve an immediate result from an image charge Vernier because the charge footprint could not be made small enough, without resorting to pattern geometry changes or using awkwardly thin substrates. Even using a 1 mm thick substrate resulted in an over-large charge footprint on the Vernier anode causing reduction in the electrode dynamic range, and degrading resolution. The circle size was more than two times smaller than for the same pattern in charge collection mode. The potential resolution was degraded further by a reduction in the effective MCP gain by 25 %. Some degree of gain loss is inevitable in the image charge mode owing to signal which is induced through capacitances other than those to the readout pattern. The major component of this loss is to the rear MCP and this effect limits the extent to which the readout can be proximity focused.

Despite these negative factors, the readout resolution was still sufficient to image the MCP pores and boule structure, as can be seen in Figure 7-29, which shows an image produced by illuminating a 0.5 mm diameter area of the detector without a mask. The image intensity has been inverted for clarity. The relatively small number of counts in this image limits quantitative analysis. Qualitatively, the resolution is at least on a par with that obtained in collected charge mode i.e. 10 μm FWHM. Given that charge footprint optimization is likely reduce the electronic noise limited resolution by at least a factor two, the potential resolution of the image charge Vernier will be close to the figure of 5 μm FWHM predicted by noise measurement and simulation.

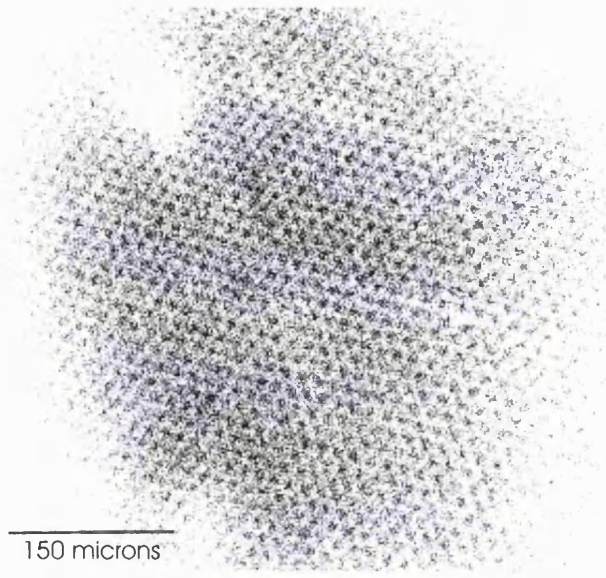

Figure 7-29. An image taken with an image charge Vernier showing MCP pores. A boule boundary in the upper MCP is visible in the upper right hand corner; a lower MCP boule boundary is visible in the centre. The upper light spot is due to local gain depression.

Development of the image charge Vernier was adjourned at this time due to the demands of the J-PEX flight programme. Whilst the Vernier anode had been clearly demonstrated to have suitable intrinsic resolution to provide pore limited resolution using MCPs with pore spacing of 15 μm, the performance of the overall detector was obviously unsatisfactory owing to the quantization generated by the MCP itself. The next step was to integrate the now proven Vernier anode into the J-PEX detector and demonstrate the improvement in overall resolution gained from using smaller pore MCPs.

7.5 J-PEX – the Joint Plasma Experiment

The Joint Plasma Experiment or J-PEX [20] is a high throughput, high resolution EUV spectrometer operating in the wavelength range between 225 Å and 245 Å aimed at investigating the photospheric composition of hot white dwarf stars. White dwarfs are separated into two groups whose compositions are dominated either by hydrogen or helium. The detection of helium abundance in the hottest white dwarfs is made difficult by confusion with the large numbers of lines from heavier elements. A major feature of the J-PEX instrument is its high spectral resolution which coupled with high sensitivity allow these lines to be distinguished during the short duration of a rocket flight. The scientific objective of J-PEX was to search for the presence of helium and determine whether its location is the photosphere or interstellar medium. This aim of this measurement was to aid understanding of the evolutionary paths of white dwarf stars.

7.5.1 Instrument Design

The J-PEX instruments exploits developments in high reflectance multilayer-coatings operated in normal incidence to deliver a compact instrument with high resolving power of $\frac{\lambda}{\Delta\lambda} \approx 5000$ in a high throughput format. The instrument, shown in the engineering drawing in Figure 7-30, consists of a collimator to restrict the field of view, through which incident light passes towards the four single reflection optics. Each optic comprises a multilayer-coated grating, operating in normal incidence, and serving to collect and disperse the UV light. The four spectra produced by the gratings are suitably aligned to lie side by side (see Figure 7-37) on the 16 × 26 mm^2 active area of a single open-faced MCP detector with a caesium iodide photocathode, positioned adjacent to the collimator. The detector has its own vacuum enclosure and door. The whole instrument is contained within a double skinned tube which serves as the external payload skin and a vacuum enclosure. The optical bench which maintains the alignment of the gratings with the detector consists of three invar tubes to accurately define the distance between the gratings and detector. An optical telescope with a CCD camera is used for attitude correction, and as a backup, a multilayer EUV mirror is used to image the target star directly on the MCP detector alongside the spectra.

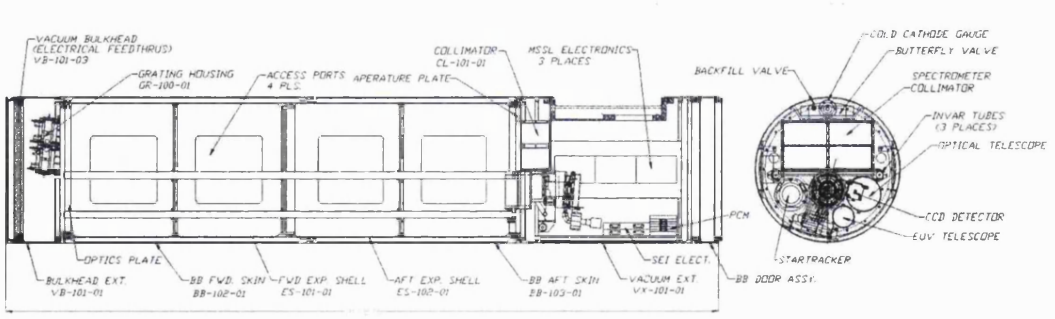

Figure 7-30. An engineering drawing showing the layout of the J-PEX flight payload.

The exceptional resolving power of the gratings placed a demanding requirement on the detector spatial resolution. The initial design of the detector utilized two 6 micron pore triple thickness MCPs in order to over sample the data and achieve a genuine 10 micron FWHM spatial resolution. This required a matching resolution capability from the image readout. The image format of 1600 x 2600 pixels was not realistically achievable using traditional readouts such as the RDA or WSA and so the Vernier anode was chosen for this role. For efficiency and economy, the existing and well-proven Rőentgen Satellite (ROSAT) Wide Field Camera (WFC) MCP detector design was used, after modifications to accommodate square format small pore MCPs and the Vernier anode.

The heritage of the J-PEX flight detector electronics stemmed from the XOGS sounding rocket experiment described in chapter 4. During early preparations for the second flight of XOGS, a scheme to equip the imaging proportional counter with a SPAN readout to replace the WSA was

shelved due to lack of development time, but not before a six channel electronic charge measurement prototype was constructed by Jason Tandy at MSSL. The Vernier flight electronics developed for J-PEX extended this by three channels, a block diagram of which is shown in Figure 7-31.

The nature of sub-orbital sounding rocket experiments, their short flight time and robust methodology, places less constraints on instrument power, mass and telemetry budgets than the stringent requirements for orbital missions. Since the Vernier anode was still under development when selected for J-PEX, and sufficient telemetry data rate was available, it was decided to telemeter the raw charge measurement information to the ground, rather than relying on an onboard algorithm to decode event position which would not be able to accommodate last minute changes. This gave us the ability to modify the position decoding algorithm as necessary, up to and after launch. In hindsight, this capability was unnecessary and the decoding parameter algorithms were unchanged from a date long before the first J-PEX flight, such was the stability of the image readout characteristics.

Electronics Block Diagram

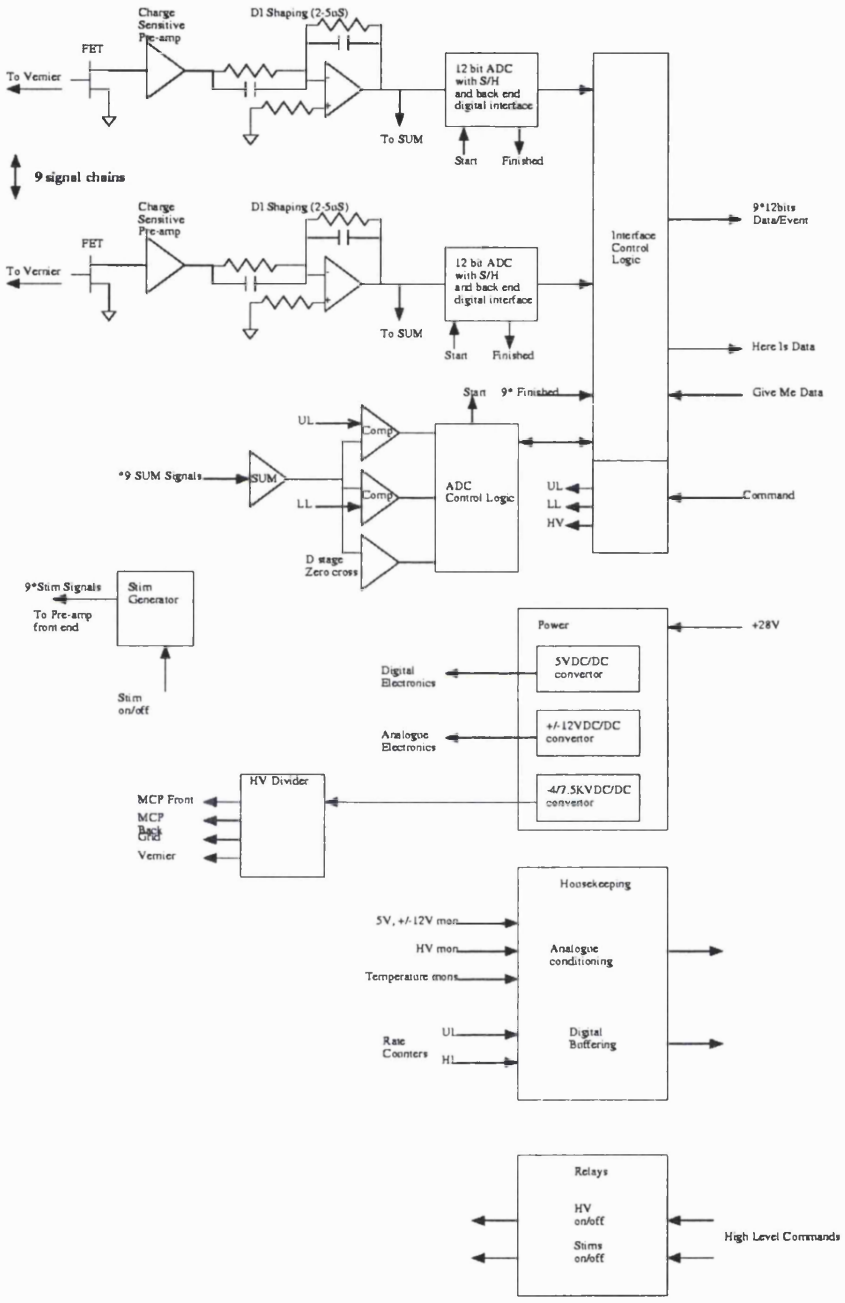

Figure 7-31. A block diagram of the J-PEX flight electronics [161].

7.5.2 Detector Performance

The time available for experimentation to determine the optimum geometry and voltage configurations for the Vernier readout within the existing WFC detector was limited owing to the JPEX project timescale and financial restrictions. The 6 μm pore MCPs were left over from an ESA technology research programme and experimental results showed that they were not of

optimal design for the Vernier readout. We inferred from the triplet event radius that the MCPs produced an overly large charge cloud footprint for the Vernier anode, probably caused by low endspoiling, which proved difficult to correct given the project constraints. This compromised performance, degrading the resolution somewhat and leaving us unable to image the MCP pores as had been expected. We were further hampered by the difficulties of measuring high spatial resolution with the WFC detector. Mask placement close to the MCP face was impossible because it reduced the detector outgassing path making it more prone to HV breakdown, and source collimation was the limiting factor when using a practical mask position.

The J-PEX Vernier readout had already been demonstrated with MCP pore-limited resolution using the J-PEX flight electronics at MSSL albeit using 12.5 μm pore MCPs. Since it was not possible to modify the experimental setup at Leicester University to enable a definitive resolution measurement, it was decided to use a spare set of 6 μm pore MCPs in a modified MSSL detector for this task. Figure 7-32 is an image of a resolution test mask taken using this detector with an MCP modal gain of 2.6 pC. Both MCPs were operated at 1600V with an interpolate voltage of 200 V. The MCP to grid separation and voltage were 2.85 mm and 600 V respectively, the grid to anode parameters being 0.9 mm and 60 V respectively. The reduction of the MCP to grid gap had been made as small as practically possible to try to offset the over-large charge footprint.

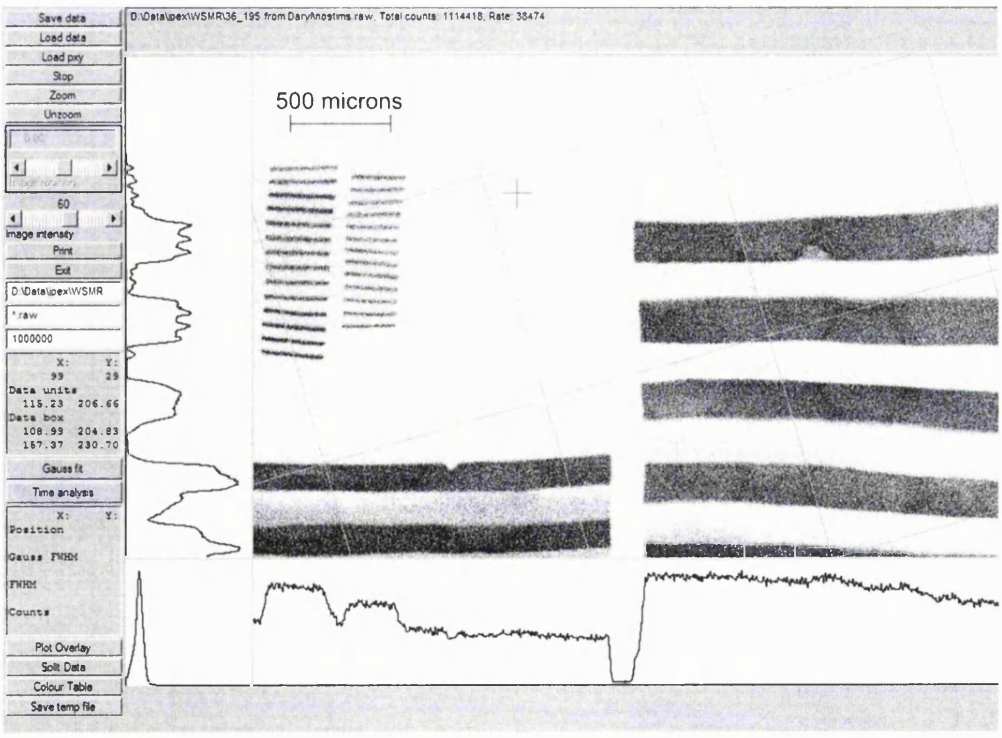

Figure 7-32. A test mask image using the TRP MCPs with the Vernier anode. The boule structure of the MCPs is visible in the illuminated regions of large bars. Resolution measurements were taken using the small set of bars.

The image could not be corrected for linearity because the schedule precluded imaging using a pinhole mask. A tripped HV supply caused the MCPs to be severely damaged by breakdown,

putting a halt to the measurements. Correction parameters were applied post-facto from data taken later using the same readout. The correction these provided was unsatisfactory and these images should not be used to assess linearity performance. The image data was taken at a count rate of 4 kHz in order to collect sufficient data before the MCP current rose above an acceptable level. During the data collection the MCP current rose from 50 to 160 μA and continued to rise at ever faster rate, eventually causing the HV problem described earlier. This effect, due to the negative temperature coefficient of resistance of MCPs (a feature of glass MCPs), was accentuated by the thermal shielding provided by the proximity focused test mask and the low resistance of these particular plates which, at ~30 MΩ, constituted a 0.1 W internal heating element. This problem did not occur before the test mask was fitted when they reached thermal equilibrium, and a current level of 65 μA was maintained.

Owing to the non-linearity present in the bar mask image, and a positional drift with time caused by anode charge up due to the non-optimal conditions, the bar mask image was histogrammed using windowing in both the x and time axes. The mean of the FWHM value for the 13 smallest bars was taken for each window, and the mean of means computed. Figure 7-33 shows one of the histogrammed windows with the gaussian fit used to measure the FWHM superimposed. The mean value of the small bar width was measured at 17.2 μm FWHM. Deconvolution of the 14 μm wide mask top hat function indicates a detector resolution of 14 μm FWHM. The electronic noise contribution for these measurements (albeit with the high voltage supply off - thus missing one noise source) was 7 μm FWHM.

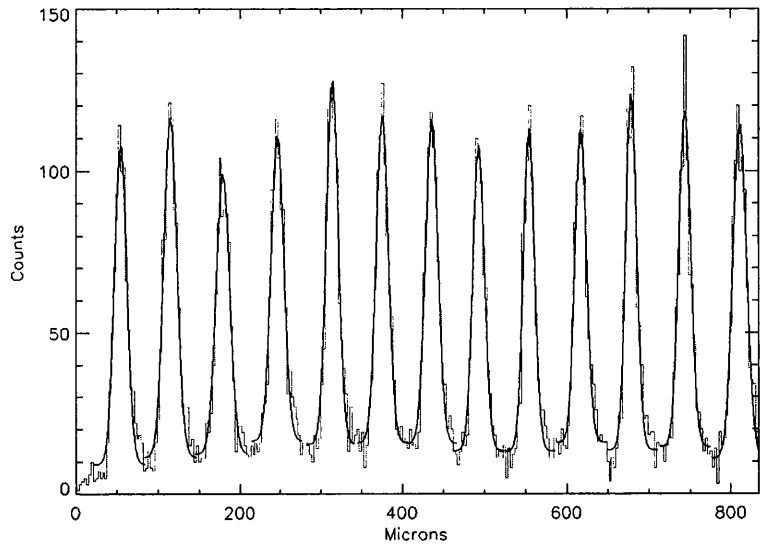

Figure 7-33. A bar mask histogram used for position resolution analysis. The data is overlayed with fitted Gaussians used to improve the FWHM measurement statistics.

The position resolution demonstrated using the 6 μm pore MCPs, though worse than predicted by previous experiments, was adequate for the J-PEX imaging requirements. However, they seriously underperformed in the area of quantum efficiency, both when bare and photocathode-coated. This phenomenon has been generally observed [160] as a feature of MCPs manufactured

over approximately the last decade. Since sensitivity was a key issue for J-PEX, several alternative MCPs were tested to find an immediate, cost effective solution to this problem, and a batch of Russian MCPs available at Leicester was chosen as a preferable alternative. The detector was reconfigured with a circular 9 μm pore Russian MCP at the input face. At this stage in the project, it was too late to conduct further position resolution measurements so electronic noise measurement and direct imaging of detector hotspots were utilized to demonstrate a maximum limit to the resolution of 15 microns FWHM measured in the flight configuration.

The modified linearity error fitting software, employing correlation of a user defined kernel in this case constructed from the mesh intersection points, was used to measure image linearity in situ with the support mesh of the flight UV filter.

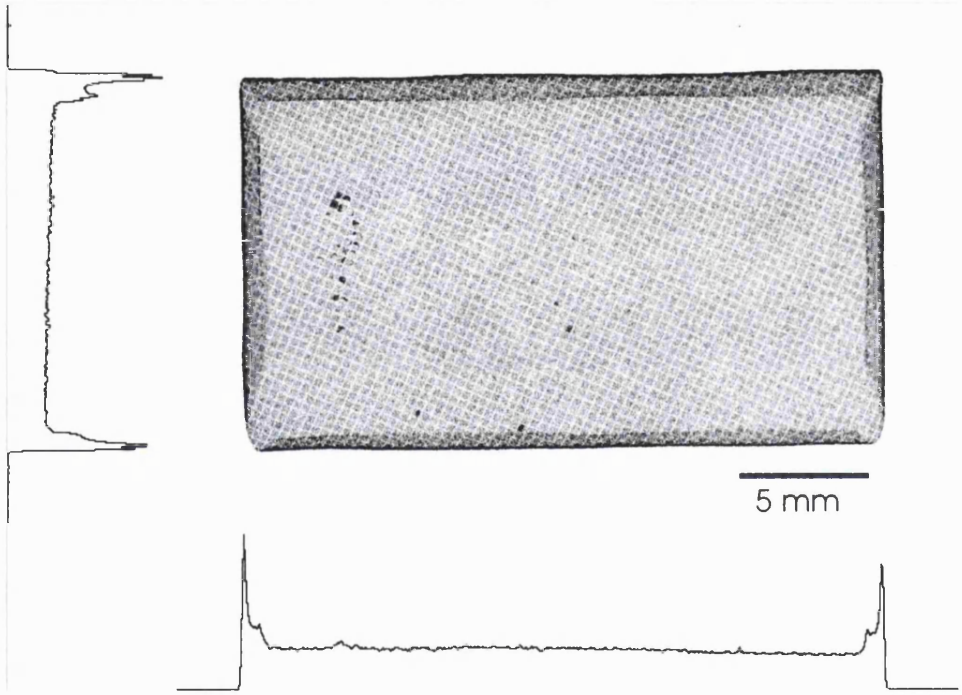

Figure 7-34. Uniform illumination of the JPEX detector showing the filter support mesh. The mesh was used to generate the linearity correction parameters and to measure the resulting linearity. The edge shows image wrap-around due to the electrostatic distortion caused by the contact at the lower MCP output face. This filter obviously has a few holes!

Figure 7-34 is the linearity corrected image taken with the J-PEX detector using uniform illumination of a 16 × 26 mm^2 area of the detector. The shadow of the filter support mesh has been used to generate the linearity correction terms and to measure the subsequent image linearity. Despite some distortion in the mesh itself, and a somewhat noisy image, the measured standard deviation of the mesh intersections from a linear grid across the entire field of view is 20.6 μm and 24.7 μm in the x and y axes respectively.

7.5.2.1 Calibration

Several weeks were spent at the Naval Research Laboratory calibrating the J-PEX instrument prior to both J-PEX launch campaigns. The calibration involved illuminating the complete flight payload with a collimated UV beam of correct wavelength range, which was initially used to position and focus the four grating spectra, and finally to calibrate the instrument response.

Since the J-PEX instrument is a EUV spectrometer using an open-faced MCP detector, the entire calibration system comprising the beam collimator and the payload had to be evacuated in order to operate the instrument. The high spectral resolution of the instrument required that the collimator and payload were maintained in accurate alignment during tests. This was achieved by mounting the entire system on a large, air-supported optical bench to free it from external disturbances. A large vacuum tank was used to house the collimator which comprised a Penning EUV source and at one end, an off-axis paraboloidal mirror producing a parallel beam along the chamber axis and exiting through the opposite end. The complete payload was attached to this end of the chamber and the entire calibration system and payload was pumped down to pressures of typically 10^{-6} mmHg using a combination of turbo and cryo-pumps, the latter used for the payload to maintain the cleanliness required for the delicate UV gratings and detector photocathode.

The position of the UV source and pinhole was adjusted to provide a parallel beam whose collimation was verified by illuminating the pinhole with visible light and observing with a telescope, previously set in focus at infinity (the accuracy of the latter procedure was later a cause for discussion). The parallel beam consisting mainly of line radiation was used to illuminate the instrument aperture, though in practice it wasn't possible to illuminate all gratings uniformly at once.

The task of positioning, focusing and calibrating the four grating spectra was made more onerous by practical constraints, which dictated that each grating had to be set up individually, with vacuum on the whole system being broken between each run.

The detector and electronics behaved almost flawlessly for both series of calibrations. The major noise source limiting the success of the calibration tests was mechanical thermal drift in the payload. This problem was accentuated by the low intensity of the beam which required integration times of ~ 2 hours to obtain satisfactory data. The IDL based data acquisition software was modified to provide a facility to time bin the data and calculate the thermal drift parameters to an accuracy limited by statistical noise from the limited counts per spectral line. This was then used to provide "attitude correction" and calculate the true spectral line widths after taking into account the positional drift. Figure 7-35 shows plots of this data for the 256 Å line from grating G4. The left hand plots show the thermal drift for a series of time bin numbers (from 1 to 10) over a two hour test, the central plots show the equivalent line widths while the right hand plot shows corrected line width versus number of time bins used. All vertical units are detector pixels, which are equivalent to 39.065 μm. Figure 7-36 shows a similar plot, but of image data of a detector

hotspot. This showed conclusively that the drift wasn't internal to the detector, the hotspot drift, at ~8 μm being 13% of the 60 μm spectral line drift in two hours.

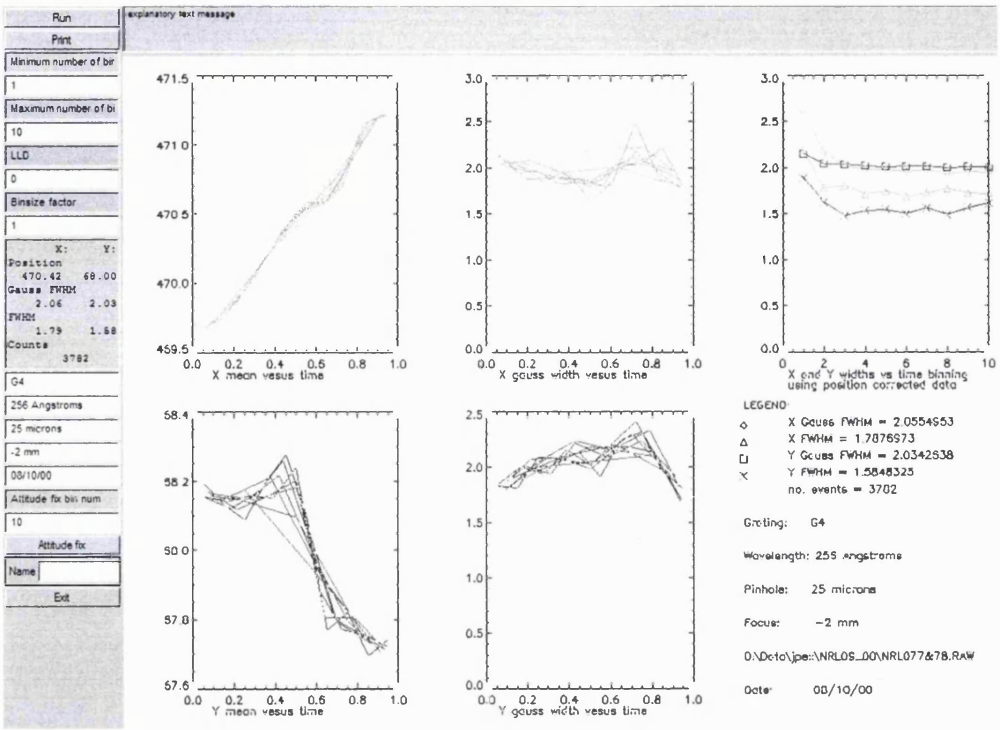

Figure 7-35. Analysis of the spectral line data showing drift with time and line width. The data analysis software was modified to allow time binning to correct for the position drift.

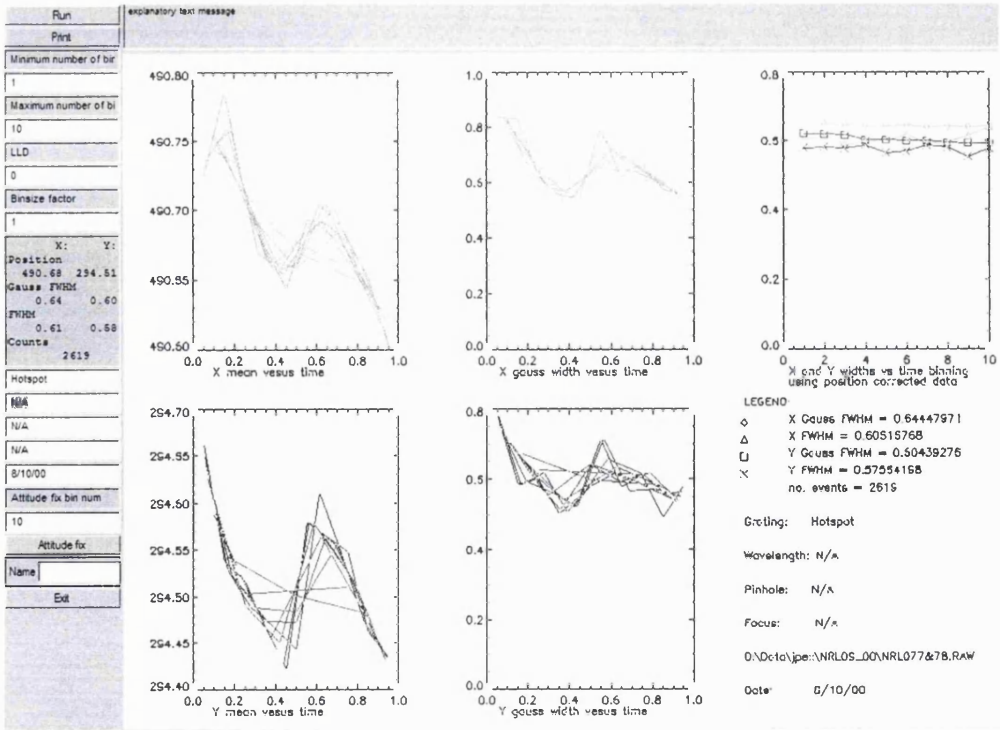

Figure 7-36. Analysis of a detector hotspot positional drift with time. The drift was ~8μm over 2 hours, much less than was seen in the spectral lines.

The modified acquisition software was used to identify, quantify and correct the thermal drift, and to evaluate methods aimed at reducing it. The thermal input from the detector electronics and high voltage unit which sat on the back of the detector was eventually identified as the main cause of the problem and its contribution was reduced by use of a cooling strap.

7.5.2.2 Flight Campaigns

The first J-PEX flight (NASA 36.162) took place from White Sands Missile Range (WSMR) on 25th February, 2000. This first launch was unsuccessful due to mission termination three seconds before the end of the rocket motor burn. This action was taken because the rocket trajectory was taking it off-range and was a result of incomplete monitoring of high altitude winds. Despite the mission termination, the instrument survived but tumbled during the flight. Though the detector operated perfectly no useful data was collected because of the lack of attitude control. A re-flight took place on 21st February 2001 during which the instrument performed faultlessly.

The flight data consisted of four spectra of the white dwarf, G181-B2B in the spectral range 225-245 Å together with electronic stim signals used for in-flight test and calibration of the detector electronics. The raw image data from the flight, without the electronic stim data, is shown in Figure 7-37. The two close bright peaks in the upper left hand corner of the image connected by faint lines of events represent the moving target star image produced by the secondary EUV mirror, and the green cross represents the bull's-eye i.e. the position calculated for the target star before flight and to be used for targeting should the automatic pointing system need to be manually overridden. The four near vertical dark stripes are the spectra from the gratings and the three other static peaks are caused by MCP hotspots.

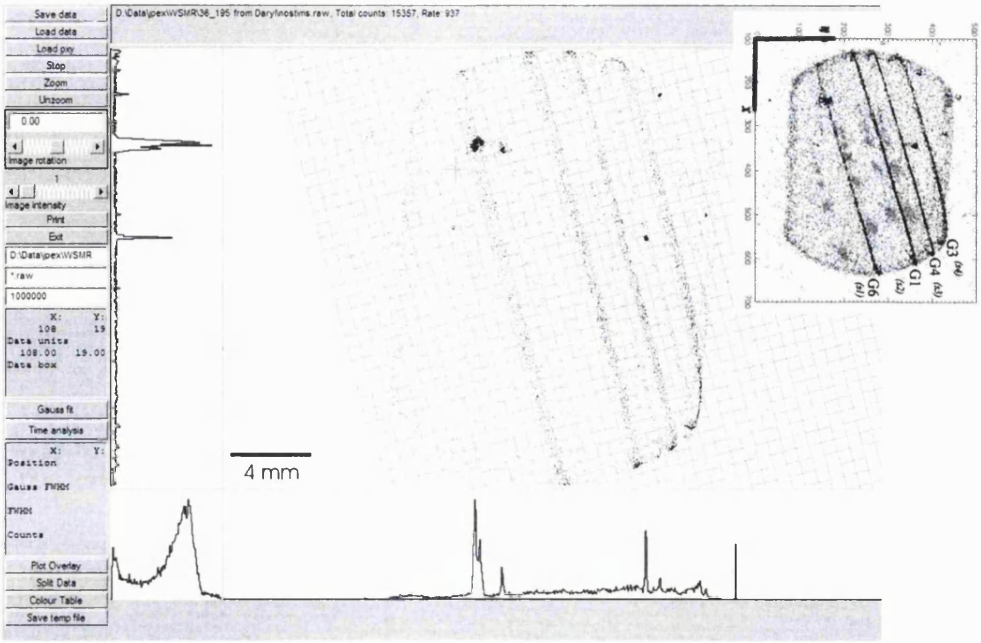

Figure 7-37. The raw flight data from the J-PEX detector. The four lines are the spectra. The cross was the bull's-eye for the target star, which is the dark spot adjacent to the cross. The inset figure shows the flight data overlaid with calibration data representing the four discrete Helium line spectra from a Penning UV source. The gratings are identified and the data illustrates an unexpected position shift of the spectra between calibration and flight.

7.5.2.3 Attitude Correction

One of the secondary instruments on J-PEX was an optical telescope equipped with a CCD camera whose purpose was to image the star field around the UV target and provide the high accuracy attitude correction data required by the spectrometer. In practice, the MCP detector data acquisition software, which had already been modified to track positional shifts during the calibration procedure, was used provide the initial attitude correction data. This was accomplished by tracking the centroid of the UV image of the target star imaged on the MCP detector by the secondary imaging UV mirror. The left hand plot on Figure 7-38 is the attitude correction data this generated, showing the x,y drift of the target star on the MCP detector. The right hand figure shows the equivalent data obtained using the optical CCD detector, n.b. the scales, offsets and rotations are not meant to match. Analysis of the width of the target star image showed that the MCP detector provided superior image reconstruction for the flight data set. The flight image, with the MCP generated attitude correction incorporated, is shown in Figure 7-39. The x and y histograms below and left of the 2d image clearly show the marked reduction in the width of the target star image compared with the raw image data. The detector hotspot is now broader however, due to convolution with the attitude correction function.

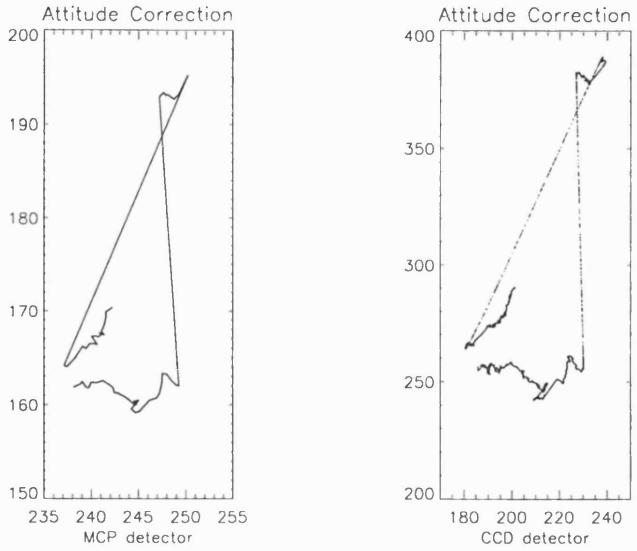

Figure 7-38 Attitude correction data from the MCP detector and CCD detector respectively.

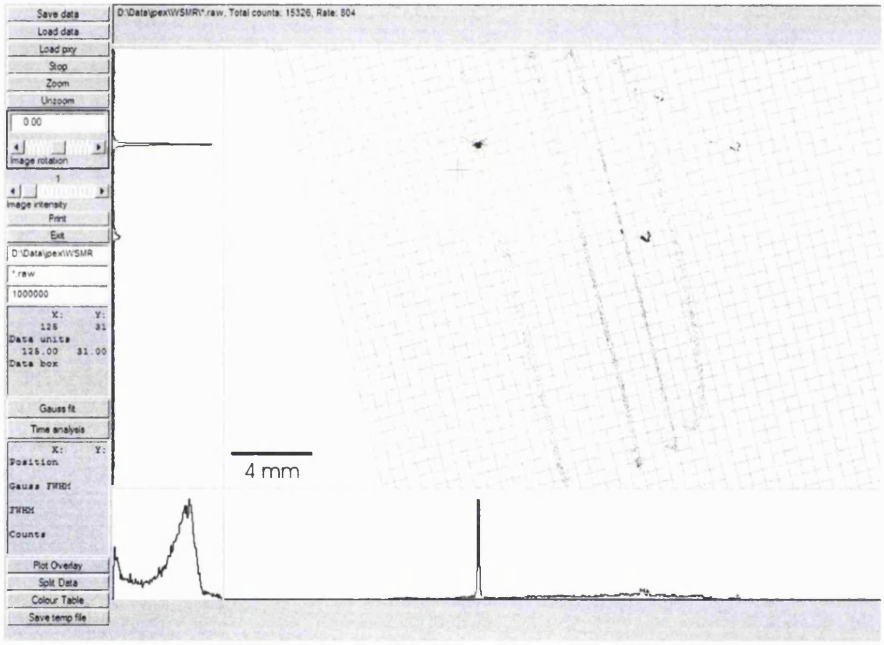

Figure 7-39. The flight data with the attitude correction applied. The best result, as judged by the target star width, was obtained using the MCP detector data.

7.5.2.4 Data Analysis

The results from the first J-PEX flight will be mentioned for completeness, though outside the scope of this thesis. A full account of the data analysis method is given by Bannister [162]. The data from the attitude corrected image were calibrated using the wavelength calibration data taken prior to launch. Events in each spectrum were then binned into 0.024 Å bins before being superposed into a single spectrum. The bin size was chosen to over-sample the nominal resolving power (4000) by a factor 2.4 to minimize information loss due to superposition. The bin width of

the final spectrum was increased by a factor 2 to maximize the signal to noise ratio, whose average was 5 per bin.

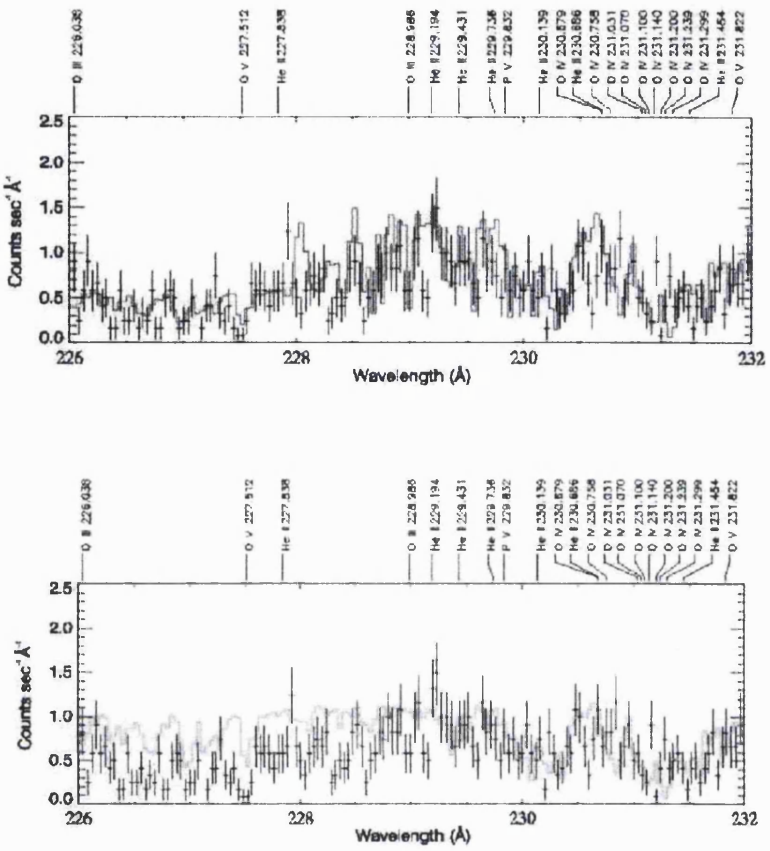

Figure 7-40. Analysis of the spectrum of G191-B2B from J-PEX flight data. An expanded view of the spectrum of in the wavelength range 226–232 Å fitted with two different models [20].

The observed spectrum was then compared to that predicted for:-

a) The best-fit of a model of white dwarf homogeneous stellar atmosphere and ISM absorption to the data.

b) The same model with the column density of He_{II} set to zero, removing the effect of absorption by interstellar and circumstellar He.

Figure 7-40 shows an expanded view of the J-PEX spectrum of G191-B2B in the wavelength range 226–232 Å spanning the He ii Lyman series limit .The solid histogram in the upper plot is the best-fitting model of the stellar atmosphere and absorption in the ISM. The lower plot shows the best fit, of a model in which absorption by interstellar and circumstellar He has been removed. It is clear that the upper model fits the data with much more success.

The results showed conclusively that ionized helium is present along the line of sight and predicted a column density of 5.97×10^{17} cm^{-2}. The best fit white dwarf atmosphere model

included a photospheric helium abundance of 1.6×10^{-5} and the data predicted a 99 % confidence level that the actual helium abundance was non-zero.

7.5.2.5 The Future for J-PEX

The Naval Research Laboratory submitted a proposal for a re-flight of the J-PEX instrument which was successful and the next launch is scheduled for mid-2004. The basic instrument design will remain unchanged though a new rocket motor and design modifications will increase the product of effective area × observing time by a factor 5. Instrument design improvements will include the development of multilayer-coated, ion-etched, blazed gratings offering higher diffraction efficiencies to replace the original laminar components, an improved grating support structure to eliminate grating distortion and improve focusing and resolving power, enhancement of MCP quantum efficiency by re-establishing the previously achieved MCP performance figures, and improvements in the test facilities to allow more accurate spectral and spatial instrument calibration.

The next step is to move this technology from the sub-orbital proof of concept stage, to a longer term orbital satellite mission. The Naval Research Laboratory are currently developing a proposal to fly a J-PEX type instrument consisting of 8 independent spectrometers on a NASA Small Explorer Mission (SMEX), which will be submitted shortly.

Chapter 8

In search of higher resolution and count rate

Though high spatial resolution performance figures are often claimed for a variety of MCP detectors using data obtained using fine pinhole masks (or similar) and a collimated source, the irrefutable acid test for any readout is to be able to image the pore structure of the MCP with flat field illumination. Several image readout technologies have demonstrated this capability [163][164][165][166] in a detector format with suitably low power and volume requirements for flight applications. Table 8-1 shows the specifications of four readout types which have convincingly demonstrated MCP pore-limited resolution with flat field illumination. Of course, while pore imaging provides a convincing test of the performance of the readout capabilities, it is important to note that it is a detector artefact. The development of smaller pore MCPs is enabling the true detector resolution, where response is uniform and linear, to be lowered. However, in practice, imaged pores may provide a useful fiducial reference.

The development of new, higher performance readout technologies is being aided by progress in the miniaturization of suitable electronics, which make possible the manufacture of single ICs comprising many parallel channels of charge pre-amplification and shaping etc. Whereas in the past, readout development for space applications focused on simple low channel count designs to achieve acceptable power and volume demands, these new ICs have relaxed readout design limitations. Designs requiring larger channel counts are now feasible, making possible the event rate enhancement potential offered by parallel event readout.

	Vernier Anode	Intensified CCD	Intensified CID	Cross-Strip
Image Format	30×20 mm^2	25 mm Ø	25 mm Ø	8×8 mm^2
Pixel Format (resolution elements)	3000×2000	2048×2048	4000×4000 (goal)	~1150×1150
Number of channels	9	256×256 (CCD pixels)	256×256 (CID pixels)	32
Readout Resolution (FWHM)	10 μm	<10 μm	6 μm (goal)	<7 μm
Dynamic range				
Global	1×10^5	2×10^5	3×10^5 (goal)	$>10^6$ (goal)
Local	MCP limited	CCD frame rate limited	MCP limited	MCP limited
Digital charge resolution	12 bit	-	8 bit	12 bit
MCP gain	1.5×10^7	5×10^5	5×10^5	5×10^6
Heritage	JPEX sounding rocket	XMM-OM	No	No
Comments	Higher MCP gain 4 μm electronic noise limited. 40 × 40 mm^2 format available	Can suffer from cyclic nonlinearity due to centroiding errors	Can suffer from cyclic nonlinearity due to centroiding errors	High channel count for realistic formats

Table 8-1. A comparison of readout systems capable of MCP pore limited resolution.

The availability of smaller pore MCPs with pore sizes down to 5 μm and below has justified the development of readout devices with higher spatial resolution. In order to achieve the required combination of finer resolution and larger format, design complexity has in general increased. To date, the trend has been an increase in channel number with a requirement to maintain signal-to-noise ratio (SNR). For example, the Vernier anode used in the JPEX spectrometer experiment, with its heritage in the WSA, requires three times as many electrodes for typically a six-fold increase in pixel number (to 6×10^6 pixels) with a similar SNR requirement. The Cross-strip prototype, which has recently demonstrated pore limited resolution, requires 2 channels per millimetre per axis. For comparison, a Cross-strip readout [89] in the JPEX format (30×20 mm^2) would thus require 100 electronic channels providing ~24×10^6 pixels assuming 5 μm resolution. The added complexity here though, does bring with it a slightly reduced SNR requirement, and the possibility of parallel readout capability. The delay line readout doesn't resort to high channel count or added complexity. However its promise to provide similar detector-wide, pore-limited resolution was never fully realized.

As well as resolution and pixel count, any new readout device also needs to address the other major goal, higher global event rate, which necessitates operation of the MCP at lower gain to maintain lifetime. The intensified CCD, as exemplified in the MIC detector [71], meets this low gain goal. However, the nature of the CCD frame readout speed coupled with the need to centroid for high spatial resolution limits the global event rate to ~200 kHz. Point source event rate is drastically limited by these features unless the active window size is reduced, allowing faster frame rates. The intensified CID escapes these drawbacks somewhat but has higher noise characteristics.

In developing a successor to the Vernier anode the goal was to develop a readout technology building on the strengths of past schemes; for example, the simplicity and speed of conductive charge division anodes, without the drawback of existing designs, such as high gain, high SNR requirement, and lack of parallel readout capability. In the past, channel count had to be kept low because of the practical considerations of size, mass and power. The readout technique described here will be able to exploit the high channel count of currently available charge measuring Application Specific Integrated Circuits (ASIC) to offer parallel event readout coupled with low SNR requirement for high speed, high rate operation. The rest of this chapter describes the first two conceptual designs, both using a charge comparison technique, developed on the road to fulfilling this goal.

8.1 FIRE - A Fast Image Readout and Electronics

The FIRE [167] position readout has much commonality with existing conductive charge division readouts such as the wedge and strip, and Vernier anodes. It comprises a planar set of electrodes arranged in pitches, the event charge being collected by all elements. In one major respect

next. Each electrode pair can change between the two states of modulation many times over the length of the readout, as long as the address defined by the states of all electrode pairs (i.e. the position) is unique at all times. The electrodes in each pitch are connected to their counterparts in neighbouring pitches.

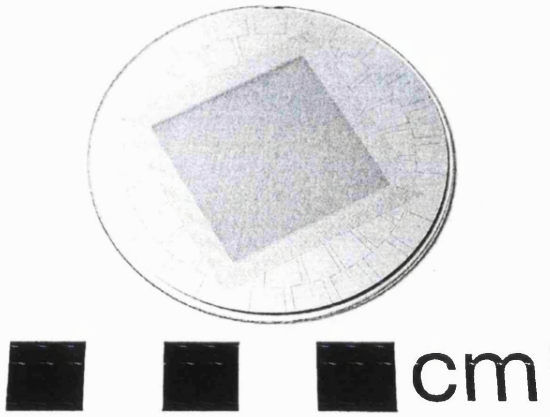

Figure 8-1. A photograph of a 32 × 32 pixel FIRE anode. The device is 24 mm square with a pattern pitch of 1.2 mm. Each pitch contains 20 electrodes.

In this simplest version of FIRE, a Gray code is used to encode the binary value for each pixel in order that each pixel is defined by a single 'bit' transition at either boundary. This avoids the ambiguities which would be present if multiple transitions occurred at a pixel boundary. In the latter case, the noise always present in the electronic amplification could cause the possible mis-coding of events lying close to the pixel boundary (since noise in the electronics encoding each `bit' is uncorrelated). Determination of the pixel address is carried out electronically by comparison of the signals from each pair of electrodes. The pixel boundary occurs at the comparator crossover point, i.e. the point at which the charge cloud is equally divided amongst the relevant pair of electrodes.

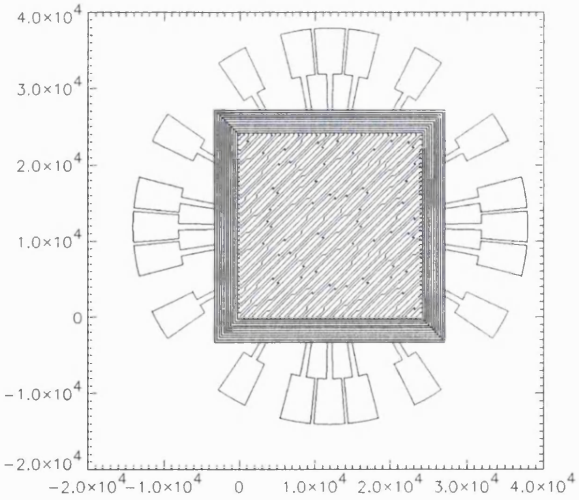

Figure 8-2. A schematic showing the FIRE pattern design using a coarse pitch for clarity.

however, it differs greatly from these devices, which are fundamentally analogue in their operation. Position encoding in FIRE is accomplished by using comparison of electrode signals alone and is effectively digital in nature. It was conceived to have much higher noise immunity than comparable analogue devices, enabling it to operate at high count rates, in excess of 10 MHz.

8.1.1 Introduction

When specifying the design for an electronic readout in a photon counting detector, the choice ends up being a compromise between pairs of factors in competition. The performance specification is usually a trade-off between position resolution and maximum count rate. The design specification is a trade-off between, on the one hand, simplicity of design coupled with complexity of operation - as typified by devices such as charge division anodes, and on the other hand, complexity of design coupled with simplicity of operation, e.g. highly parallel readouts such as discrete pixel devices. Increased position resolution is invariably accompanied by increased complexity, be it operational e.g. the added complexity of the Vernier [163] anode algorithm compared to the wedge and strip [101], or in design - discrete pixel devices simply require more channels. For true photon counting detectors, where each event is detected individually i.e. not an analogue integration mode, there is also the count rate limitation imposed by the MCP itself.

The FIRE readout was developed to provide a very high speed readout requiring a minimum number of electronic channels whilst retaining a simple decoding scheme. The readout was initially conceived to compete with a discrete pad readout, hence was initially optimized for moderate resolution at very high count rates to match the discrete pad capabilities.

The FIRE readout provides a means of encoding the position of the centroid of a charge cloud, (typically a cloud of electrons ~ 1mm in diameter). In its simplest form FIRE requires 2n isolated electrodes per axis of position encoding, where the number of unique, discrete positions capable of encryption is 2^n. The charge cloud may be collected directly by the pattern electrodes, or induced by a localized charge, through a dielectric material. The first two-dimensional readout to be manufactured, having a resolution of 32 × 32 pixels, requires twenty electrodes. However there is an efficiency of scale since doubling the resolution in both axes requires only four more electrodes. A photograph of this pattern is shown in Figure 8-1. The charge cloud is collected by one or other of the pair of electrodes, which encode each 'bit' of resolution for each axis. Each pair occupies a fixed fraction of the readout pattern

The readout pattern consists of repeated pitches, each pitch containing all pairs of electrodes arranged in parallel strips. Figure 8-2 shows a schematic of the pattern, surrounded by its twenty contact pads. The readout geometry is designed so that the charge is detected mainly on one or other electrode of each pair. This is accomplished by modulating the electrode areas. The position at which the electrode pair modulation changes defines the transition between one pixel and the

8.1.2 Lineage

The FIRE readout is a member of the group of charge division position readout such as the wedge and strip, and Vernier anode. These all rely on the division of charge amongst all the electrodes which constitute the device. The position encoding of each resolution element is defined by the unique ratio of the electrode areas and thus the collected charges.

Normally these devices require an algorithm to compute the position coordinate from the measured charges from each electrode. Almost invariably, the output coordinate is required in a digital format and thus the pixel boundaries end up being defined by the transition from one ADC (analogue to digital converter) result to an adjacent one.

In addition, many of these readouts require normalization within the decoding algorithm to accommodate the variation in the event pulse height. The imposes significant practical limitations, particularly for high speed devices, since it necessitates a division operation which is significantly slower than an addition or subtraction.

The FIRE readout can be seen as a special case of the above family of position readouts, sharing the fundamental attribute of charge division among all the electrodes, but only requiring analogue charge measurement at the one-bit level, hence, the device is essentially digital. A comparator whose output is defined by the ratio of charge collected on a pair of electrodes is used to encode each bit of the pattern. A sum signal from the electrodes or from the back of the MCP is used to strobe each event.

Unlike the other readouts discussed, the electrode areas of the proposed pattern do not vary continuously across the encoded axis as is the case for the wedge and strip etc. since the encryption technique is essentially digital. Since no analogue charge measurement is required and the position encoding is defined by simple signal comparison, there is potential to use very high speed electronics as signal to noise ratio is not as important an issue compared with the other devices described above.

The use of a comparison technique for readout anodes such as FIRE has several major advantages:-

1. Charge comparison provides much greater noise immunity, allowing the use of lower MCP gain, high speed electronics, both improving the detector count rate performance.
2. Although a larger number of electrodes are required compared to other charge division readouts, the charge comparison technique with its simplicity of operation, does not require processing other than histogramming of the event address defined by the comparator output
3. The comparison does not suffer from miscounting near the pixel boundaries. c.f. devices using discrete electrodes for each pixel or coincidence techniques where threshold levels

in combination with a wide pulse height distribution can produce multiple counting of single events.

4. At low signal levels, the amplifier noise simply broadens the pixel edge, softening the resolution but not causing miscoding or counting errors.
5. Counting losses encountered with coincidence techniques resulting from low level discrimination on each electrode are also avoided by the use of only a single discriminator.

8.1.3 Anode Design

The Fire pattern described, using two electrodes per bit of resolution, comprises 20 electrodes grouped as 10 pairs. This design provides a two dimensional spatial resolution of 32 × 32 pixels. The pattern is manufactured by laser micromachining a copper conductor deposited on to a quartz substrate. The pattern pitch is 1.2 mm divided into 10 equal width sub-pitches. Each sub-pitch is divided into the two electrodes whose signals are compared to determine one bit of the position resolution. The electrodes in each pair are modulated in width between 65%/35% and 35% /65% to encode a "1" or a "0" respectively. Each pitch is separated into two equal width halves, each half encoding one of the dimensions of the pattern. Figure 8-3 is an oscilloscope trace showing the output of a pair of electrodes from the pattern using traditional charge sensitive preamplifiers and shaping to measure the relative pulse heights. The two events demonstrate the complementary signal levels which define digital "0" and "1" outputs from the comparator.

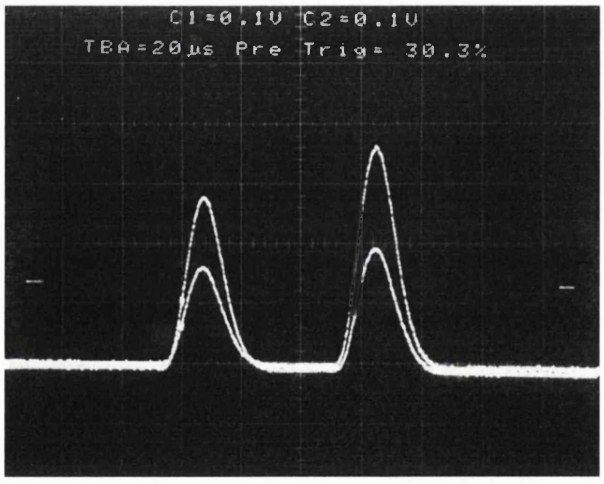

Figure 8-3. An oscilloscope trace showing the outputs from an electrode pair over-laid. The two events demonstrate the complementary signal levels which define digital "0" and "1" outputs from the comparator.

The pitch orientation is at 45° to the pattern axes. The *x* axis pattern is generated by projecting the nominal electrode form which varies along the *x* direction, on to the line given by $x=y$, and displacing this pattern vertically to fill in each pitch half encoding this axis. The *y* axis pattern is then simply given by the *x* axis pattern reflected about the line $x=y$. The patterns for both axes,

their mode of operation, and the simple position decoding map are thus identical for both axes, simplifying all aspects of operation. Interconnections to the 20 signal buses, which surround the pattern, are made using a wire-bonding technology proven on similar charge division patterns used in satellite and sounding rocket applications. The manufacturing techniques used to make the FIRE pattern share much in common with other charge division patterns whose production we have previously described. The novel elements of FIRE are its use of signal comparison technique and the use of very high speed electronics which we are developing to prove its ultimate speed capability.

In order for correct pattern operation, the electrode transitions are gray coded. This is necessary to avoid ambiguity at pixel boundaries, since without a gray code, uncorrelated noise between transitioning electrode pairs can lead to the production of spurious position codes. To improve the pattern performance further, the gray code needs to be optimized to minimize the spatial frequency of every electrode. This results in a pattern whose electrode transition density is as evenly matched as possible between all electrodes. The practical upshot is the benefit offered to the pattern design. Since FIRE is a serial device, the charge must be shared over all electrodes, but the footprint must not be so large that it that encompasses more than one electrode transition in any pair. This effect will tend to diminish the charge difference across the transition and distort its position when transition spacings are asymmetric. The charge footprint can be reduced and the pattern could in principle be manufactured with as small a pitch as required to produce a desired resolution. However in practice the electrode capacitance will rise, increasing the electronic noise, softening the pixel boundaries and eventually resulting in position ambiguities.

8.1.4 Front-end Electronics

The electronic scheme described here was entirely conceived and developed by Kerrin Rees at MSSL. Since it was a crucial component in the readout system a description is included for completeness.

The signals from the anode are not high enough to drive comparators directly and, in consequence, an amplifier is required for each electrode. This equates to a pair of amplifiers per bit of resolution, i.e. 22 amplifiers are required for a 128 x 16 pixel readout. Amongst the solutions investigated for high speed amplification were silicon MMIC amplifiers (Monolithic Microwave Integrated Circuit), which have the necessary wide bandwidth, low noise and high gain.

Figure 8-4 is an oscilloscope trace showing the output of one of the MMIC [168] amplifier channels, amplifying real events from a MCP detector. The timebase is 2 ns per division. It would be conceivable to design the pattern as a transmission line with impedance matching to the amplifier in order to minimize signal reflection. However, this data was obtained without such modifications, and despite this, signal oscillations do not dominate.

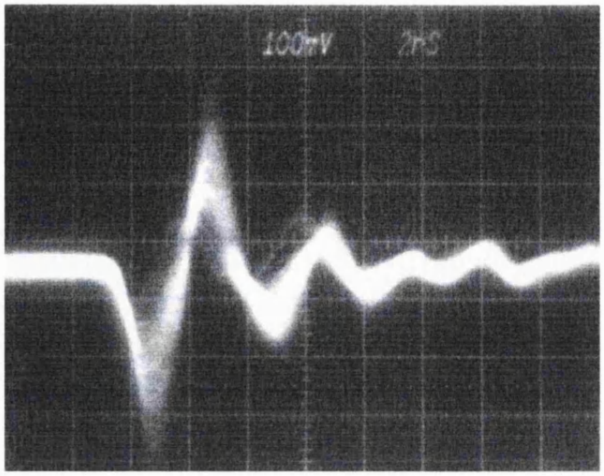

Figure 8-4. An oscilloscope trace of the output of the MMIC amplifiers. The amplifiers were attached to a FIRE anode in an MCP detector and used 2 gain stages producing a gain of 60 dB. This had to be attenuated by 20dB to match the MCP gain.

The signals from the amplifiers can be as short as 1ns. If the comparators sample the incoming pulses directly, propagation delay skew of as little as 100ps between the signals could give an erroneous position. Thus peak and hold circuits are required. The ECL logic gate [169] output circuit was investigated as a novel solution to this problem. The gates used in this circuit are operating in their linear region, a mode in which they are not characterized. The peak and hold is reset by a high speed transistor once the data from the comparators have been latched. The signals from the peak and hold circuits are sampled by latching comparators, type Motorola 10E1652, which have ECL logic level outputs, a propagation delay of <1ns and programmable hysteresis.

Figure 8-5 shows the output of the peak and hold circuits for real events. The variation in pulse height is due to the MCP pulse height distribution and the electrode modulation. The trace shows the output droop over time, but in normal operation the output would be reset after an event has been detected and processed, in as quickly as 5 ns.

The acquisition controller latches the comparators' states, stores the result in a register, clears the peak and hold circuits and then writes the registers' output to a bank of FIFOs. The data from the FIFOs is histogrammed to build up an image. The controller interleaves occasional reads from the histogram RAM and sends data to the host computer which uses a lookup table to give real X, Y coordinates. A block diagram showing the functional blocks of the FIRE readout electronics is shown in Figure 8-6.

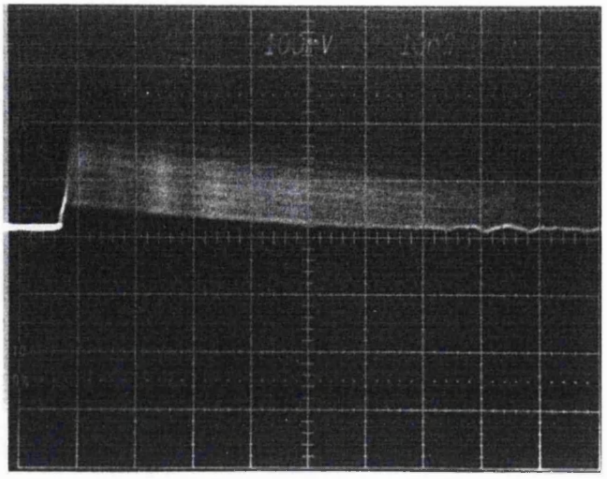

Figure 8-5. An oscilloscope trace of the output of the peak and hold circuit. This was constructed using ECL logic components. In normal operation the level would be reset after the comparators had been strobed.

A prototype anode with a 32x32 pixel pattern was manufactured on a fused silica substrate and mounted within a MCP detector using direct charge collection mode. Tests using charge sensitive amplifiers indicated that the pattern was operating as expected. However experiments using 20 channels of the high speed MMIC amplifier design indicated that crosstalk between electrodes was limiting the signal dynamic range, and a redesign of the front end amplifiers was considered.

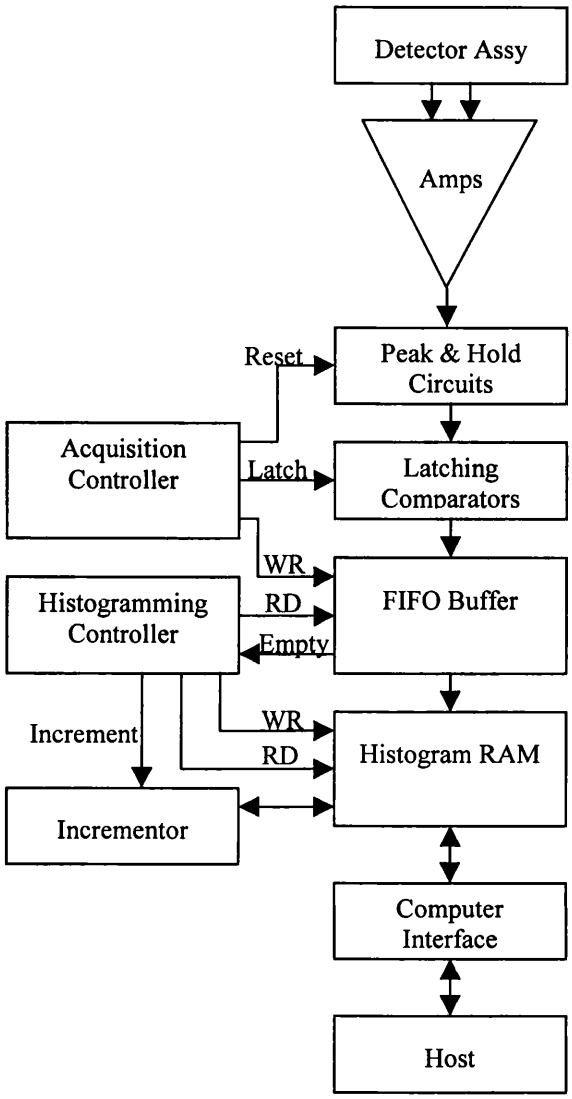

Figure 8-6. A block diagram of FIRE electronics design.

8.1.5 Results

Limited time was available to assemble the FIRE pattern into a MCP detector and to investigate the operation of the high speed MMIC amplifiers when attached to the load provided by the readout pattern. Initial results showed that the signal modulation between electrode pairs is reduced. This was to be expected since the low impedance provided by the interelectrode capacitance, causes signal crosstalk. The MMIC amplifiers are not true trans-impedance amplifiers, having relatively high 50Ω input impedance. One solution is to modify the pattern to reduce the interelectrode capacitance. Despite these problems, some dynamic range remains.

Figure 8-7 shows the simultaneous output of a pair of peak and hold circuits having detected an event from a MCP detector. The high speed electronics are problematic to analyse without even faster test equipment. This figure shows the signal distortion caused by a mismatch between the peak and hold output and a relatively slow digital storage oscilloscope. However the difference in the signal amplitude between to the two outputs is visible and indicates the level of signal modulation present using the MMIC high speed amplifiers.

The build status of the electronics precluded the collecting any imaging data. This would in any case be premature until either the pattern has been modified to improve the signal dynamic range, or an alternative amplification method less prone to signal crosstalk is pursued.

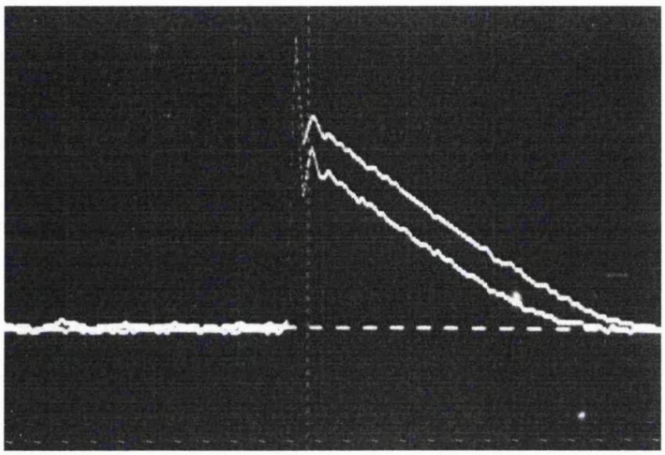

Figure 8-7. The outputs of the peak and hold circuits for an electrode pair from a single real event. The relative amplitudes indicate the level of modulation using the high speed amplifiers.

8.1.6 Further Development

The FIRE pattern described here is the simplest charge comparison pattern to visualize. A series of patterns are under development, similar to FIRE, but using three or more electrodes, comparisons taking place between all pairs of electrodes. These patterns offer significantly higher resolution than the FIRE design whilst still benefiting from the speed potential of charge comparison. The number of permutations of the electrodes gives the maximum possible resolution for these readouts. Like FIRE, each pixel is uniquely addressed by the comparator outputs. These devices offer the possibility of significantly higher resolution at little or no cost in terms of hardware. A detailed description of these patterns is given in the following section.

8.2 Charge comparison with greater than two electrodes

8.2.1 Introduction

Charge division readouts such as the Vernier anode require measurement of the charge collected on each and every electrode per event to a certain level of accuracy for a given position resolution. Take, for example, a single electrode triplet of the Vernier anode (which comprises three triplets in total). Measurement of the charge ratio collected allows a phase (or position) coordinate to be determined using a pattern design illustrated in the upper section of Figure 8-8. In this figure phase varies along the x axis. As we reduce the measurement precision, the accuracy of the phase coordinate is correspondingly degraded. In the limit, at very crude precision, an

alternative to measurement of the three amplitudes would be comparison of them. The upper section of Figure 8-8 shows the boundaries of pixels (dotted lines) defined by the digital address generated by the three electrode comparisons. In this mode of operation, the pattern no longer needs to exhibit the same continuous form. It could be digitized as shown in the lower section of Figure 8-8, or could even be constructed as a series of equal width strips orthogonal to the original phase axis. This example, in particular, is not too useful practically because it is non-unique beyond one wavelength, only six uniquely identifiable pixels being available. However if the number of electrodes is increased, the possibilities improve dramatically.

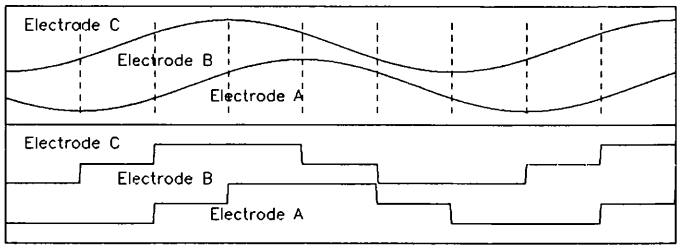

Figure 8-8. An explanation of charge comparison using the Vernier anode. The upper section shows the form of one electrode triplet of the Vernier anode. The dotted lines represent the position of pixel boundaries generated by comparing the collected charge levels. The lower section shows an alternative realization for this mode of operation. There are 6 uniquely defined positions within one wavelength after which the sequence repeats.

8.2.2 Charge Comparison - Potential

In theory, the number of uniquely available pixels is given by the number of different ways in which the electrode amplitudes can be ordered, i.e. the number of permutations of k from n :-

$$(8\text{-}1)\quad {}_nP_k = \frac{n!}{(n-k)!}$$

where n is the total number of electrodes, and k is the number of electrode amplitudes compared.

In principle, if we have ten electrodes and compare them all to find their order, we can define 3,628,800 unique pixels. In reality there are practical issues which constrain the number that can be used in a pattern. For example, in order to utilize as many of the available permutations as possible, all the electrode amplitudes will have to cycle many times. We can estimate a mean wavelength in terms of the number of pixels per cycle using the following reasoning. Assuming only one comparator changes state at any one position (not a requirement but the most efficient use of available pixels), and each electrode has the same mean wavelength, then the number of electrode state transitions per electrode per wavelength is given by :-

$$(8\text{-}2)\quad T_{elec} = 2(n-1)$$

and therefore the total number of transitions per wavelength for all electrodes is :-

(8-3) $T_{total} = 2n(n-1)$

Since the number of electrode transitions per pixel is two (the pixel edge is defined by two electrode amplitudes swapping order) the average number of pixels per wavelength is given by :-

(8-4) $Pixel/_{\lambda} = n(n-1)$

and thus the number of cycles required is the total number of pixels divided by the number of pixels per wavelength by :-

(8-5) $cycles_{total} = \frac{n!}{n(n-1)} = (n-2)!$

These numbers represent an estimate of the mean wavelength of electrodes and the number of pixels per cycle in a pattern constructed to be similar to the Vernier depicted in Figure 8-8 with the electrodes smoothly varying in width. In practice, the problem of arriving at a pattern design of smoothly varying electrodes which define a sequence of pixels using all (or even most) possible permutations has no obvious intuitive solution except for the three electrode pattern design shown in the example. The problem of determining a unique pixel sequence through each electrode wavelength cycle has an element in common with the travelling salesman problem (TSP), but instead of being concerned with minimizing the total distance travelled between cities, we are interested in the number of different cyclic tours passing through all cities/electrode amplitude states (ignoring the starting point and direction of travel). This corresponds to the number of different ways we can order our electrodes to generate one cycle, and is given by :-

(8-6) $cycles_{possible} = \frac{n!}{2n}$

Thus :-

(8-7) $\frac{cycles_{possible}}{cycles_{total}} = \frac{n-1}{2}$

which has unity value for $n = 3$, the straightforward case, but for $n > 3$ is always greater than 1. For n greater than 3 this means that any possible cycle must have an element or more in common with at least one other cycle making a unique sequence more difficult to generate, and reducing the total number of pixels available.

To illustrate this problem, we will consider the simplest possible schemes, having three and four electrodes. For three electrodes the cyclic progression through the six electrode amplitude permutations (corresponding to the pixels) can be illustrated graphically by assigning them amplitudes of 1, 2 and 3 respectively. .Thus each pixel can be assigned a unique 3D coordinate corresponding to the three amplitudes. The 6 pixel coordinates are:-

(8-8) ${}_3P_3 = \{1,2,3\},\{1,3,2\},\{2,3,1\},\{3,2,1\},\{3,1,2\},\{2,1,3\}$

written in the same cyclic order as Figure 8-8.

The points corresponding to each unique pixel coordinate are shown plotted in Figure 8-9. It is easy to see how all possible permutations are traversed using smoothly changing electrode amplitudes, in fact sinusoids. For four electrodes the equivalent solution is shown in Figure 8-10. Since the total electrode amplitude is a constant by necessity, the fourth coordinate is present defining the planes normal to the [1,1,1] diagonal. This polyhedron is a three dimensional shadow of the actual four dimensional object. It can be seen that there is no obvious way of traversing through all apexes (i.e. pixels) whilst not retracing one's steps and also maintaining smoothly varying electrode amplitudes with similar cyclic frequencies. If we calculate the number of cycles possible using the TSP theorem (equation (8-6)), then the four electrode solution has three cyclic order paths. These approximate three orthogonal great circle paths, one of which is visualized in Figure 8-10 by black circles.

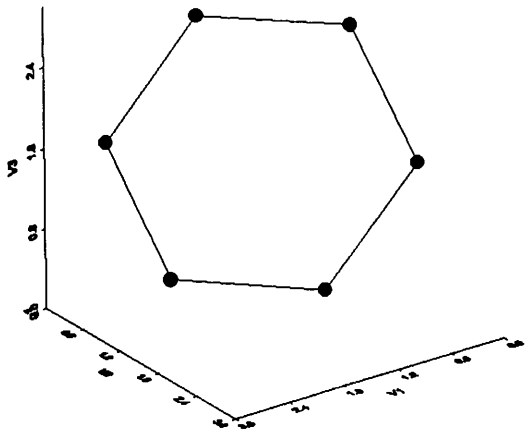

Figure 8-9. The six unique pixels defined by a 3 electrode pattern shown in Figure 8-8.

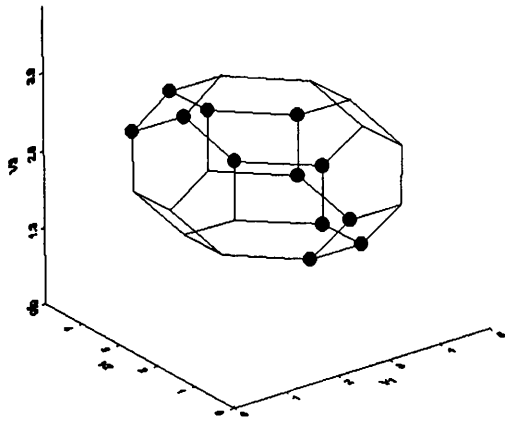

Figure 8-10. The equivalent plot to Figure 8-9 for four electrodes. The black circles indicate one of three possible cyclic paths which maintain uniformly varying electrode modulation.

For four electrodes, it can be seen from Figure 8-10 that the number of pixels traversed in one cycle with the constraints described is only twelve. For larger numbers of electrodes, where visualization is not as easy, equation (8-4) can be used. Even at relatively high electrode count,

the mean electrode cyclic frequency in terms of pixels is still rather low (only 90 pixels per wavelength with 10 electrodes). We could envisage constructing such a device in similar format to the Vernier anode, in which the pattern is subdivided into pitches, with all electrodes present in every pitch and varying continuously in width. We can also use the Vernier anode to provide a practical wavelength dimension: typically ~ 5 mm. Based on this dimension, the pixel size of a 10 electrode charge comparison scheme would be ~55 μm with a theoretically almost unlimited format (having potentially ~3.6M pixels), a significant achievement for an anode using 10 channels per axis with no requirement for charge measurement or high signal-to-noise ratio, and thus capable of higher event rate operation.

While at first sight, this scheme appears to offer much potential, it has a number of limitations. Firstly, even with a larger number of electrodes, the number of pixels per cycle is relatively low, and the pattern constraints limit how small the cycle length can be, putting a limit on the resolution of typically ~55 μm. The other major limitation, is that as described, it is a serial device, with charge being collected by all electrodes at any position. Before committing to such a readout design utilizing all electrodes in the permutation and in which all electrodes require to be present at all locations, it is useful to consider alternative pattern layouts which can offer other advantages.

8.2.3 Charge Comparison – A Practical Pattern Design

8.2.3.1 Modes of Charge Division

In order to practically implement a pattern utilizing charge comparison and exploit the potential of this technique, the type of electrode pattern used for the charge division is important. Charge division readouts operate in two quite distinct modes.

1. The simplest schemes utilize the distribution of the collected charge itself to perform the division. The quadrant anode is a good example of this. Apart from the events whose centroids lie on either x and/or y coordinates defining the electrode boundaries (and thus where the charge division is 50/50), the ratio of collected charges on the electrodes (and thus the calculated position) is dependent on the spatial distribution of the charge. This is obviously a serious limitation if not constant, which is commonly the case. Linearity and resolution are compromised in this mode of operation because the required decoding algorithm effectively changes from event to event. A similar problem potentially applies to other techniques using charge centroiding in this mode, and also to devices using similar division techniques on light spots such as intensified CCDs. However this mode does have significant benefits. Since the very nature of this pattern design involves localized (as opposed to distributed) conductors it is suitable for schemes where :-

    a. The inter-electrode capacitance needs to be kept low, e.g. higher speed applications.

b. The spatial extent where the electrode physically detects charge needs to be small.

c. Charge is to be collected on a subset of the pattern electrodes only.

2. The alternative mode of operation used, for example, by the Wedge and strip, and Vernier anodes, is where the electrode areas themselves are modulated at a spatial frequency much lower than that of the charge distribution, so that collected charge ratios are independent of this distribution. This allows the pattern design alone to accurately define the position decoding algorithm. In order to practically modulate the electrode areas in such a way, the pattern is commonly drawn as a series of pitches with much higher spatial frequency than the charge distribution, so that their contributions to the modulation of electrode areas are integrated out. This requirement that the pattern fine structure is smaller than the charge footprint, and that the charge footprint itself is much smaller than the scale of the electrode modulation limits the use of this technique. The limitation imposed by the scale of the pattern fine structure, which rapidly increases pattern capacitance and electronic noise if too small, effectively sets a minimum scale size for the electrode modulation. This limits the application of this pattern technique to devices having a large number of pixels per electrode wavelength, not a feature of the charge comparison technique as described. Practicalities of design also render this pattern technique incapable of allowing electrodes to go to zero in a controllable fashion without introducing undesirable sensitivity to the charge footprint distribution. Thus all electrodes must be present and of finite magnitude throughout the active pattern area. These pattern designs always have a large percentage of conductor in proportion to the overall pattern area in order to maximize electrode dynamic range. This also tends towards higher inter-electrode capacitance and resulting increase in electronic noise.

8.2.3.2 Charge Comparison Requirements

We have outlined the potential of charge comparison schemes to define a large number of unique pixel positions encoded by the order of a set of electrode amplitudes. While there are many possible ways this technique could be realized, any practical implementation needs to maximize the benefits offered by this encoding scheme, which are:-

1. A large number of uniquely defined pixel addresses available, making possible :-

    a. large format devices

    b. high resolution capability

2. Coded by charge comparison between electrode pairs, giving the following attributes :-

    a. Pixel boundaries defined by signal equality

    b. Avoids non-linearities through incorrect ratiometric division

c. Insensitive to variations in charge footprint distribution

d. Self-normalizing

e. No requirement for charge measurement

f. No analogue to digital conversion required

g. Undemanding signal-to-noise requirement

h. Simple electronic requirement, capable of high event rates

3. Simple 1:1 mapping between comparison generated pixel address and position

   a. No computational algorithm required

   b. High speed look-up table provides position decoding

The nature of the charge comparison scheme, with its low pixel count per electrode cycle, its potential for high rate operation and its insensitivity to charge footprint distribution, make it highly suited to the "division by charge distribution" mode of operation and the readout design proposed in the following section utilizes this mode. Using this mode we will be able to use a simple pattern design using equi-spaced parallel conductive electrodes. This will enable a low pattern capacitance, keeping noise down, lowering the required MCP gain, and enabling higher speed operation.

Any practical implementation must also take into account the availability of suitable electronic components. In recent years developments in ASIC technology have produced a number of high channel count charge preamplifier/shaper ICs, some with relatively fast shaping times, some with discriminator outputs. Such ICs have been manufactured for high energy physics applications where radiation hardness is a requirement, and extremely high channel count and component count necessitate low power consumption. These attributes make them suitable for space based applications. One such device [167] has already been flown in space.

8.2.3.3 A Practical Design

The first charge comparison readout will be demonstrated using a ${}_{16}P_3$ device; the pixel addresses being defined by the amplitude order of three electrode charges out of a total of sixteen. The simple pattern design will consist of parallel conductive strips separated with a centre to centre spacing of ~100 μm, enabling the pattern to define 50 μm wide pixels. An identical pattern orthogonal to the first will be used to encode the second position axis and the readout pattern will be manufactured using a multi-layer PCB type construction.

This widely used geometry of image readout electrodes was originally developed as cathode wire planes in multi wire proportional counters (MWPC) [172], and later in micro-strip [28] counters and MCP detectors such as CHANDRA HRC [173]. It has been applied with different electrical configurations: resistively coupled electrodes, delay coupled electrodes, fully populated with an

electronic readout channel per electrode, both with and without centroiding. A centroiding variant of this scheme, with a much reduced channel requirement [174], designed by the author originally for fluorescence gated multi wire proportional counters, is shown in Figure 8-11. This simple parallel electrode arrangement has recently been adopted for use in the cross-strip readout design.

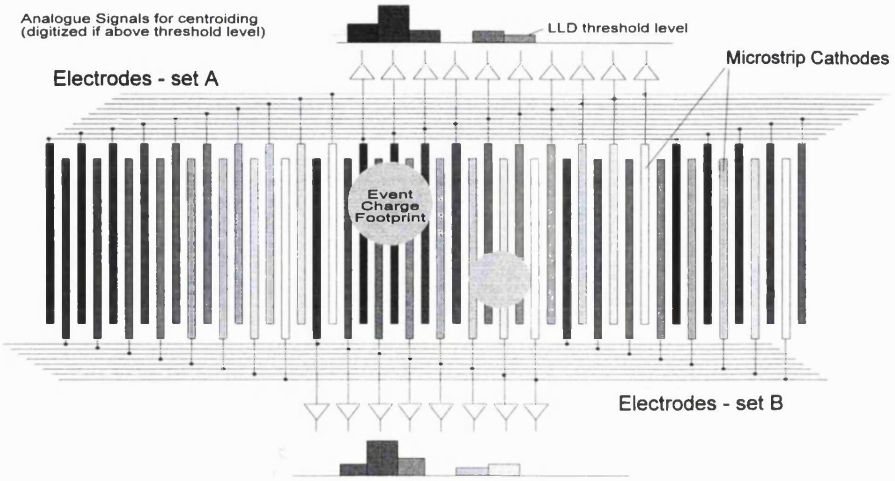

Figure 8-11. A centroiding readout for fluorescence gating. This figure shows a centroiding variant of the commonly used parallel electrode scheme, designed by the author originally for fluorescence gated MWPCs. It has a much reduced channel count compared with a fully populated scheme. Two such orthogonal patterns provide two-dimensional imaging.

The design we propose for a prototype charge comparison readout will operate in a conventional MCP detector at a gain of ~10^6 electrons, with the event charge proximity focused on to the resistive charge locator of an Image Charge [175] readout arrangement. The Image Charge technique will be used to accurately define the spatial charge distribution induced on to two sets of orthogonal conductive strips. The ${}_{16}P_3$ readout has 3360 possible permutations each capable of representing a unique position but only 800 of these will be needed for each axis of the 40 × 40 mm^2 readout area.

Though our prototype will initially use 16 electronic channels, a modification to the readout design to utilize 64 channels would increase the permutation count, ${}_{64}P_3$ to 249,984. Currently multi-channel ASICs [176] are available with channel counts up to 128 so this is not unrealistic. By suitably arranging the distribution of the physically used pixel addresses, the immense address redundancy available can be effectively used to provide a parallel readout capability. This offers the possibility to increase the global event rate by a large factor.

8.2.4 Charge comparison – an electronic solution

Our first readout device will utilize 16 electronic channels, each connected to several strips in an arrangement such that no consecutive triplet is repeated, satisfying the requirement that every occurrence of a permutation of 3 from 16 is unique. Although this particular readout is designed such that a subset of only three electrodes collect charge for any one event, all electrode

amplitudes must be compared, irrespective of the number in the subset, in order to determine the subset members. If comparators were used for this task, the number required is given by :-

$$(8\text{-}9)\quad N_{comparator} = \sum_{0}^{n-1} i$$

where n is the number of electrodes.

Our 16 channel device would require a total of 105 comparators, with the shaping amplifier of each channel having to drive 15 parallel comparator inputs. This design is clearly unrealistic but can be avoided by using a signal timing based solution. Instead of many comparators we propose a commonly used and widely available electronic channel design comprising a preamplifier, shaping amplifier and discriminator. This format is generally used for parallel event counting using many identical channels.

For our application, the threshold level of the discriminator on each channel would be set from a global reference. As soon as the shaped pulse exceeds the threshold level, the discriminator output changes from logic "0" to "1", and likewise, conversely as the pulse decays. The logic outputs of the discriminators contain timing information since larger signals trigger the discriminators earlier than those at lower amplitude. The 16 discriminator logic outputs are fed in parallel to a digital processing unit which could, for example, be implemented using a field programmable gate array (FPGA). The inputs are used to drive a state machine which identifies each channel address sequentially, as its logic output goes high, and generates an address identifying the three channels and their order. This address directly corresponds to the unique pixel address of the event location, which is determined using a look-up table.

8.2.4.1 Maintaining event rate and improving resolution

The event rate capability of the proposed electronic design is limited by the ability of the digital processing logic to correctly determine the temporal order of the discriminator outputs. We have manufactured a breadboard electronic channel consisting of a preamplifier (with representative capacitive load) and a 100 ns shaping amplifier to investigate the timing jitter of a discriminator signal.

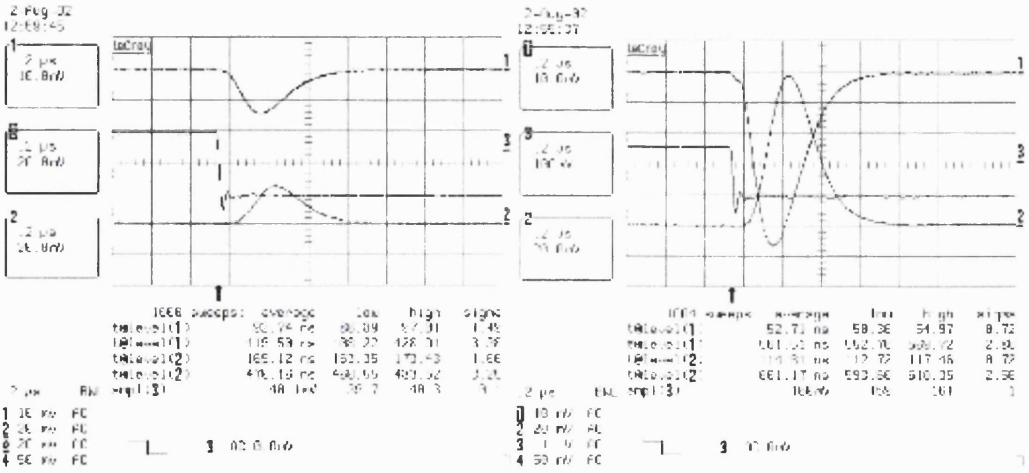

Figure 8-12. Timing measurements using breadboard electronics with fast shaping.

Figure 8-12 shows oscilloscope traces of the breadboard charge amplifier channel with 100 ns shaping time. Trace 1 and trace 2 are the outputs after the first and second shaping stage respectively. Trace 3 shows the tail-pulser input into the preamplifier 1 pF test capacitance. The measurement parameters on lines 1 to 4 represent the threshold crossing times for trace 1 –ve and +ve going, and trace 2 +ve and -ve going, respectively. Thresholds were 0.5 divisions from the signal baseline for both traces. Line 5 shows the tail-pulse amplitude; equivalent to 10^6 and 2.5 × 10^5 electrons on Figure 8-12a and Figure 8-12b respectively. The timebase is 200 ns/div.

These measurements demonstrate the timing jitter on the discriminator rise and fall times. The measured jitter on the first threshold crossing time is 0.72 and 1.49 ns at gains of 10^6 and 2.5 × 10^5 electrons respectively. A software simulation was used to determine the timing characteristics of a realistic readout system. This showed that the measured noise was more than adequate to provide the order of the electrode triplet collecting the event charge.

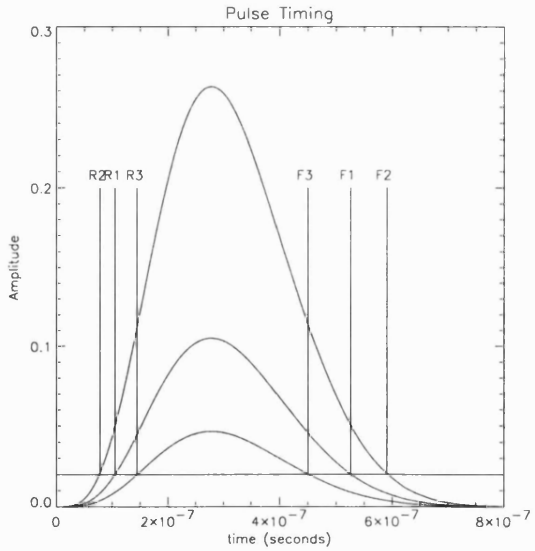

Figure 8-13. A simulation of the threshold crossing points for the shaped electrode signals. The crossing points define the times of rise and fall of the three discriminator outputs.

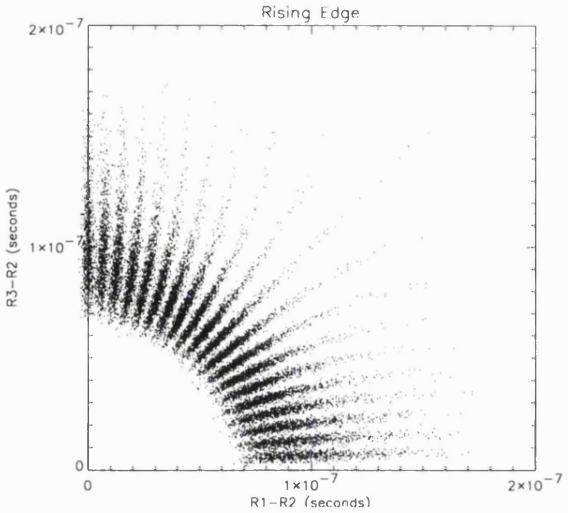

Figure 8-14. A plot of time differences between rising edge threshold crossing points. The differences between first and second, and first and third threshold crossings plotted as *xy*. Each line of points represents events from one of 20 positions spaced at 5 μm, indicating the potential readout resolution.

We used a pattern of three electrodes, 40 μm wide and 10 mm long with a centre to centre spacing of 100 μm. The charge induced using Image Charge was calculated and applied to this pattern to determine the substrate thickness required to give optimal charge division characteristics. The magnitudes of charge induced on the three electrodes from 20 uniformly spaced event positions, spaced at 5 μm was modulated by a realistic pulse height distribution, and the threshold crossing times determined using a pulse shape generated from the S-plane transforms for several shaping amplifier filter circuits at various threshold levels and including a noise component measured using the breadboard circuit. Figure 8-13 shows the threshold crossing points for the three electrode signals which are used to generate the data in Figure 8-14. In Figure 8-14 the two axes represent the difference between the first and second, and the first and third threshold crossing points for the rising signal. The quasi radial lines represent 1000 events at each position location, the locations being 5 μm apart. They are easily distinguishable giving an indication of the sharpness of the comparison pixel boundaries (which occur at 0, 45 and 90 degrees).

The projected maximum event rate of this simulated system using pile-up rejection is ~3×10^5 event s^{-1} operating in a totally serial mode, one event at a time. Our breadboard circuit measurements, simulations and estimate of electrode capacitance suggest the 100 ns shaping time may well be conservative, so this figure is likely to be pessimistic. We also aim to utilize a higher channel count after proof of concept to provide significant parallel readout capability. We envisage that a maximum event rate of ~1×10^7 event s^{-1} may be possible.

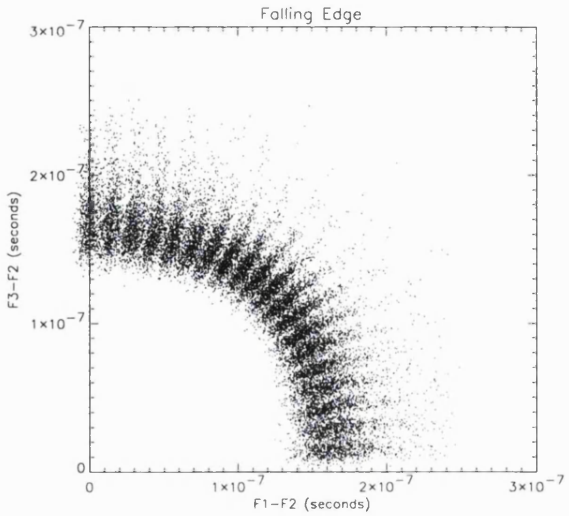

Figure 8-15. Data as in Figure 8-14 using the falling edge of the pulse. A timing resolution of 6 ns would easily resolve the 5 μm spacing of the points.

The results of the timing simulation also indicate another exciting possibility: using this information for sub-pixel centroiding. The rising or falling edge of the pulse can be used for this purpose, and the latter has the advantage of requiring lower time resolution. Figure 8-15 shows results from the same readout and electronic configuration as Figure 8-14 except that the two axes plot the difference in fall times of the discriminator logic outputs. Each line of data points representing a single position coordinate is clearly distinguishable.

This timing information, though non-linear with pulse height, provides sufficient information for centroiding to be used to produce sub-pixel image resolution, and is available for free from our proposed electronic design. Because of the small scale of the fixed pixels (~50 μm) the centroiding resolution can be relatively coarse. This coarse centroiding could be easily and efficiently carried out using a small look-up table, since the look-up address, comprised of the two timing values, would typically be less that 1 + 1 byte wide. The centroiding nature of this sub-pixel imaging revives the possibility of non-linearity due to variations in the spatial charge distribution. However, unlike other centroiding schemes such as the cross-strip, the scale of the potential cyclic non-linearity is much smaller (100 μm as opposed to 500 μm) and the image charge technique used to induce charge on to the readout electrodes through the substrate, produces a more stable distribution than that from directly collected charge. The latter is subject to variability in the MCP output and charge spreading region owing to gain related space charge effects, and secondary electron mediated redistribution on the readout structure itself.

Recent advances have pushed the capabilities of FPGAs such that it is also reasonable to use the data acquisition state machine to initiate counter/timer modules which can provide a signal timing resolution of ~ 6 ns. Given this figure, the results from our simulation suggest that a spatial resolution of 5 μm or less is readily achievable with this relatively modest anode design.

8.2.5 Conclusions

The charge comparison technique offers speed and simplicity advantages over other imaging techniques that require charge measurement. We have described a number of possible modes of implementation and have arrived at a prototype design with relatively modest hardware and electronic requirements. Our proposed electronics design uses only two major components, an analogue ASIC providing multiple preamplifier/shaping/discriminator channels coupled to a digital processing unit implemented using an FPGA. This readout scheme has a simple analogue to digital interface and does not require an array of analogue to digital converters. Identification of the pixel address is provided by the timing information inherent in the discriminator outputs. We have shown that this information can also be used to provide sub-pixel centroiding, which even at a relatively coarse resolution, will provide detector resolution of ~5μm. The simple prototype is projected to operate at event rates ~3×10^5 event s^{-1} and faster shaping speeds coupled with expansion of the electronics to a larger number of channels will allow parallel event processing, raising the predicted maximum event rate towards 10M event s^{-1}

Chapter 9

Conclusions

The focus of this research effort rapidly developed into a quest to improve and redesign electronic image readout devices use in photon-counting and particle detectors. Initially, new manufacturing techniques and designs were applied to gaseous counter applications, and as time progressed, the centre of effort moved towards MCP based detectors, with ever more demanding position resolution requirements.

Groundwork covered in the early stages of the research, when existing designs such as the WSA, and backgammon readout were used in a variety of detector types, provided a thorough understanding of the benefits and limitations of the available conductive charge division readouts.

The existing WSA design geometry was optimized to maximize its dynamic range and electronic noise reduced by fabrication on thin substrates. Large, thin substrate readout patterns were constructed and demonstrated, not merely for the accommodating laboratory environment, but as robust items for sounding rocket experiments, though scientific data collection remained illusive.

The application of the WSA to high spatial resolution microchannel detectors raised the priority of a number of performance issues, such as image modulation and stability, image non-linearity, and the inability of the WSA to achieve spatial resolution to match the performance potential set by the MCPs. These issues spawned a number of parallel lines of research. Several new linear readout designs were invented to increase the resolution attainable through linear division (though this was limited to up to 2 times improvement over the conventional WSA). Investigations were made into the charge footprint distributions collected by the readout and impacting image modulation and linearity, the split-strip being specifically invented for this purpose. An extensive range of experiments was undertaken to assess and quantify the role of secondary electrons and substrate charge-up in performance degradation due to charge redistribution. A solution, using an intermediate control grid, was proposed and its performance improvements experimentally verified.

In parallel, the spatial resolution limitations of linear charge division patterns were proving insurmountable, and a family of new designs, coined progressive geometry readouts [86], evolved from ideas spawned from the split-strip anode. This family of readouts, including the Vernier

anode [177] and SPAN designs, utilized cyclically varying electrode forms to improve the resolution by utilizing the electrode dynamic range several times over the length of the pattern axis, allowing the position resolution to greatly exceed the charge measurement accuracy. This performance claim was justified by the MCP pore-limited image resolution demonstrated by the Vernier anode using its J-PEX flight electronics with raw datasets from an open-faced detector without a mask, and representing state-of-the-art performance from a readout of this type.

The development of the progressive geometry readout was only made practicable because of the parallel development of the laser micromachining technique developed in-house. The laser machining capability facilitated an iterative pattern development programme which would not have been either practically or financially viable by any other means.

The identification of the image charge technique [175], as a method to finally overcome all the deleterious effects due charge redistribution, provided a means to demonstrate the true potential of charge division anodes. In this mode of operation they perform as theoretically intended, the induced charge developed on the readout electrodes truly reflecting the pattern geometry. The potential offered by image charge was verified for both the WSA, and the Vernier anode, which was shown to be capable of MCP pore-limited imaging [163], even while compromised due to substrate geometry. In this same un-optimized configuration the image charge Vernier has demonstrated the best position linearity achieved so far of ~13 μm rms. Further analysis of the Vernier linearity data, presented in chapter 7, has shown that residual non-linearity is accurately predicted if the position of every electrode within the pattern repeat pitch is considered, indicating that a simple modification to the decoding algorithm will be sufficient to effectively eradicate this.

The recent development and availability of small pore MCPs with pore diameters as low as 2 μm [178], will allow the performance improvements gained as a result of readout developments to be further exploited. The J-PEX detector performed as a test-bed for imaging with small pore MCPs, using 6 μm pore Photonis MCPs. J-PEX [20] was the first instrument to fly these, though its final flight configuration used an alternative top MCP owing to DQE problems. The emerging silicon MCP technology [179] may overcome the DQE limitation associated with glass MCPs, especially in the UV, which has been problematic over the last decade. Though the silicon MCP technology is not yet sufficiently mature to replace traditional MCPs, it offers exciting potential. These devices are manufactured lithographically and have a high degree of uniformity compared with their glass counterparts. Unlike standard glass MCPs they have low background rates (<0.05 count cm^{-2} s^{-1}) and are bakeable to much higher temperatures ~800° C. This makes them compatible with CVD coating processes which could be used for robust UV photocathodes, such as diamond, and to provide enhanced secondary electron emission characteristics, all of which should produce an MCP with higher DQE.

The J-PEX experiment has a re-flight scheduled for 2004. An obvious goal for the re-flight would be a detector reconfiguration using an image charge Vernier readout. One of the drawbacks of the first J-PEX collaboration was the impracticality of tuning an existing detector geometry to provide a satisfactory charge cloud distribution for the Vernier anode, which was operated in collected charge mode. An image charge Vernier would benefit from its lack of dependency on MCP charge footprint geometry, which can be proximity focused to the image charge layer, the substrate thickness itself being used to define the charge footprint.

This feature highlights a major advantage of the image charge mode. It effectively modularizes the detector, both in an operational and practical sense. Not only is the readout operation independent of the MCP charge footprint, it can be physically decoupled from it as well. Chapter 4 ended with a demonstration of a demountable WSA which was coupled to a detector inside a vacuum tank, the image charge substrate acting as part of the vacuum enclosure. A WSA outside the vacuum enclosure, brought into physical contact with the image charge substrate, performed identically to an integrated device. Such a technique has significant advantages for sealed intensifier design, where a generic design could be used for a variety of readouts, to accommodate different resolution/count rate trade-offs (discrete pads, charge division, charge comparison, etc.), or alternative geometries (Cartesian, polar, etc.).

Whilst the Vernier anode is capable of MCP pore-limited resolution, it is a serial device and its operation is fundamentally governed by the dead-time of the pulse-processing electronics which limit it to count rates of ~200 k count s^{-1} and the onset of MCP paralysis because of its high gain requirement. There is some potential with a device such as the Vernier to increase count rate at the expense of resolution, since its potential resolution has untapped reserves. For instance, the measured electronic noise of the J-PEX Vernier anode was ~4 μm FWHM. Position resolution could be sacrificed by up to an order of magnitude, and a WSA comparable performance (40 μm FWHM) still achieved, in favour of enhanced count rate, simply by speeding up the electronics. This assumes that the count rate bottleneck results from the time constant of the shaping amplifiers, which is generally the case at lower count rates, but at higher rates, the digital processing electronics themselves could become the limiting factor, especially when the multistage Vernier decoding algorithm is considered. Another crucial rate related issue is the need, particularly with MCP based detectors, to operate at lower gain. We have already discussed MCP gain depression in its several manifestations. An MCP detector designed to run at high rate will inevitably need to operate at substantially lower gain, if permanent gain reduction, long range gain depression and severe local count rate limitations are not to result, compromising detector performance enormously. One of the crucial elements of a readout designed for higher rates is that it can function at a lower gain, so not only will the shaping time of the electronics need to be reduced, but so will the signal to noise ratio. This sounds the death knell for devices which require the measurement of charge amplitudes, as do the vast majority of charge division readouts.

However the simplicity and practicality of the generic charge division readout need not be completely lost, despite the rejection of high resolution charge measurement. In its crudest form, we could conceive of using charge measurement at the 1-bit accuracy level for a position readout, requiring a low signal to noise ratio and correspondingly low detector gain. If, as with the MCP detectors, the pulse height varies between events, the only useful way of applying this practically is by comparing charges collected on pairs of electrodes, which is equivalent to a 1-bit amplitude measurement with in-built normalization. To achieve resolution comparable to existing charge division devices, such schemes will inevitably require a larger number of channels. In the past, with electronics utilizing discrete components, this was inconceivable for space applications with low power and mass requirements, even using surface mount technology. However advances in ASIC technology [180] have made available multi-channel charge sensitive devices (up to 128 channels), originally developed for extremely parallel, high density instrumented detectors used in high energy and particle physics experiments. Using these devices, one could conceive of a multi-electrode readout which, by using a small number of electrodes per event, can combine charge comparison to achieve resolution far beyond the total number of channels, with event parallelism made possible by the huge number of possible electrode combinations, the vast majority of which are unused. Early investigations into such devices are reported in chapter 8, though the idea is still in infancy.

A preliminary readout design has already been manufactured to verify the charge comparison technique. The FIRE detector [167] used a simple scheme which was serial in operation, using comparison between independent pairs of electrodes to produce a resolution of 32 × 32 pixels. The next stage in the readout development will be the development of a device using up to 128 individual electrodes to demonstrate the parallel capability of the charge comparison when events are collected on a small subset of electrodes. The timing technique [181] also described, is one of several potential ways that an interpolated position can be generated to improve on the resolution provided by the pixels defined by charge comparison. The performance goal of such a device will be a resolution of at least 1000 × 1000 pixels operating at a rate of ~10 M event s^{-1}. The ultimate goal of this readout development is the integration of the readout pattern on to the silicon used for the VLSI implementation of the processing electronics.

The logical next stage in this research, on which work has already begun, is the development of a compact, space-qualified MCP detector with the following attributes :-

1. A miniaturized detector, with low mass and power requirements, incorporating small pore MCPs manufactured to give optimal DQE, whose resolution will be limited by the MCP pore spacing.
2. An image charge signal interface providing improved resolution and linearity, with the practical benefits of mechanical modularity and electrical isolation. This will allow

readouts to be interchanged simply so that alternative resolution/rate/complexity trade-offs can be employed to suit specific applications.

3. A miniaturized imaging device comprising the readout pattern with its low power processing electronics integrated on to a single substrate. This could be manufactured initially using multi-chip module (MCM) hybridization, which would provide proof-of-concept for VLSI fabrication in silicon.

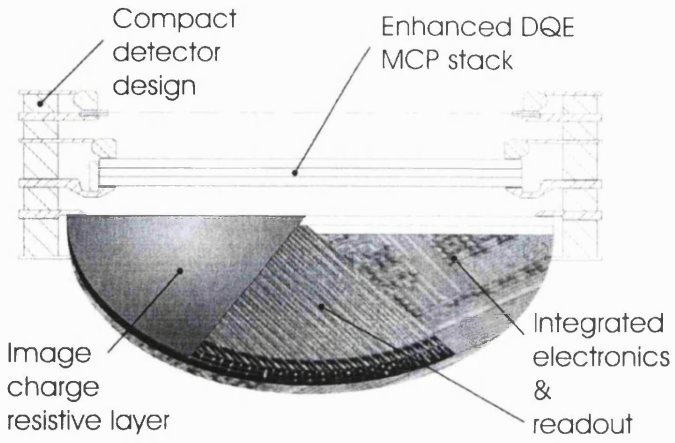

Figure 9-1. The future: a miniaturized, low power, low mass, modular detector.

Such a device, shown conceptually in Figure 9-1, will have significantly lower mass, volume and power requirements than traditional MCP detectors whilst offering enhanced image performance. The mechanical design shown, based on sealed tube techniques, could be developed as a sealed tube intensifier for optical applications, and its inherently modular design will provide the flexibility to easily reconfigure the readout to suite a variety of applications.

References

[1] Galileo Galilei, *Siderius Nuncius*, 1610

[2] T.R. Burnight, Phys. Rev., **76**, 1949, pp. 165

[3] Korff, Serge A. *Electron and Nuclear Counters*, Divan Nostrand Company, Inc., Toronto, 1955.

[4] Giacconi R., Gursky H., Paolini F., & Rossi B., 1962, Phys.Rev.Lett, **9**, pp. 439

[5] Mertz, L. & Young, N., "Fresnel Transformations of Images," Proc. Int'l Conf. on Optical Instruments and Techniques, Ed. K. J. Habell, p. 305, Chapman & Hall, London, 1961.

[6] Wolter H., Ann. Phys. NY, **10**, 1952, pp. 94

[7] J.A. Van Allen, G.H. Ludwig, E.C. Ray and C.E. McIlwain, "Observation of high intensity radiation by satellites 1958 Alpha and Gamma", Jet Propulsion, **28**, 1958, pp. 588.

[8] F. Sauli and A. Sharma, "Micro-Pattern Gaseous Detectors", CERN-EP/99-69 Ann. Rev. Nucl. Part. Sci **49**, 1999, pp. 341.

[9] J.L. Wiza, "Microchannel plate detectors", Nucl. Instr. Meth, **162**, 1979, pp. 587-601.

[10] S. Nikzad, T. J. Jones, S. T. Elliott, T. J. Cunningham, P. W. Deelman, A. B. Walker, and H. M. Oluseyi, "Ultrastable and uniform EUV and UV detectors", Proc. SPIE, **4139**, 2000, pp. 250

[11] P.A.J. de Korte, H.F. Hoevers, J.W. den Herder, J.A. Bleeker, W.B. Tiest, M.P. Bruijn, M.L. Ridder, R.J. Wiegerink, J.S. Kaastra, J. van der Kuur, W. A. Mels, "TES x-ray calorimeter-array for imaging spectroscopy", Proc. SPIE, **4851**, 2003, pp. 779.

[12] P. Verhoeve, N. Rando, A.J. Peacock, D.D. Martin, R.H. den Hartog, "Superconducting tunnel junctions as photon-counting imaging spectrometers from the optical to the x-ray band", Optical Engineering **41(06)**, 2002, pp. 1170.

[13] H.E.Schwarz and I.M.Mason, "A new imaging proportional counter using Penning gas improves energy resolution", Nature **309,** 1984, pp. 532.

[14] W. Tucker & K. Tucker, *Revealing the Universe: The Making of the Chandra X-ray Observatory*, Harvard U. Press, 2001.

[15] H.O. Anger, Instr.Soc.Am.Trans., **5,** 1966, pp. 311.

[16] Lapington, J.S., Trow, M.W., Bentley, R.D., and Culhane, J.L., "A Position Sensitive Proportional Counter for the Bent Crystal Spectrometer on Solar-A", Proc. SPIE, **1159,** 1989, pp. 252.

[17] N.Brosch, A.Shemi, J.Topaz and O.Braun,"The TAUVEX Experiment," ESA Symposium on Photon Detectors for Space Instrumentation, Vol. **ESA SP-356,** 1992, pp. 243.

[18] A.M. James, A.D. Johnstone, D.M. Walton,O. Vaisberg, & A. Federov, "A Fast Omni-directional Ion Detector for the study of space plasmas", AGU monograph, Eds. R. Pfaff, J. Borovsky & D. Young, **102,** 1998, pp. 281.

[19] Breeveld, A.A., Edgar, M.L., Smith, A., Lapington, J.S., and Thomas, P.D., "A SPAN MCP detector for the SOHO Coronal Diagnostic Spectrometer", Rev. Sci. Instrum., **63(1),** 1992, pp. 673.

[20] R. G. Cruddace, M . P. Kowalski, D.J. Yentis, C. M. Brown, H. Gursky, M. A. Barstow, N. P. Bannister, G. W. Fraser, J. E. Spragg, J. S. Lapington, J. A. Tandy, B. Sanderson, J. L. Culhane, T. W. Barbee, J. F. Kordas, W. Goldstein, and G. G. Fritz, "High-Resolution Spectroscopy of G191-B2B in the Extreme-Ultraviolet", The Astrophysical Journal, **565,** 2002, pp. L47.

[21] N. P. Bannister, B. M. A., G. W. Fraser, J. E. Spragg, R. G. Cruddace, M. Kowalski, G. Fritz, D. Yentis, J. Lapington, J. Tandy, B. Sanderson, T. Barbee, W. H. Goldstein and J. F. Kordasr, "The Joint Astrophysicsl Plasmadynamic Experiment (J-PEX)", 12th European White Dwarf Workshop, Delaware: ASP Conf Series, 2000.

[22] Charpak, G., Bouclier, R., Bressani, T., Favier, J. and Zupancic, C.: The use of Multiwire Proportional Counters to select and localize Charged Particles. Nucl. Instr. Meth., **62,** 1968, pp. 235.

[23] F Sauli, *Principles of Operation of Multiwire Proportional and Drift Chambers*, CERN 77-09, 1977.

[24] J.W. Stümpel, P.W. Sandford, H.F. Goddard, "A position sensitive proportional counter with high spatial resolution", J. Phys. E, **6,** 1973, pp. 397.

[25] G. Charpak, and F. Sauli, "The Multistep Avalanche Chamber: A New High-Rate, High-Accuracy Gaseous Detector". Phys. Letters **78B,** 1978, pp. 523.

[26] R.D.Andresen, E.A.Leimann and A.Peacock, Nucl.Instr.Meth.,**140,** 1977, pp. 371.

[27] Ochi A., Aoki S., Fujisawa T., Nishi Y., Suzuki M., Tanimori T., Toyokawa H., Ueki T., "Development of MicroStrip Gaseous Chamber for Realtime X-Ray Imaging Detector", SPring-8 Annual Report, 1996, pp. 205.

[28] A. Oed, "Position-sensitive detector with microstrip anode for electron multiplication with gases", Nucl. Instr. and Meth. **A263**, 1988, pp. 351,.

[29] F.Angelini, R.Bellazzini, A.Brez, M.M.Massai, R.Raffo, G.Spandre, M.A.Spezziga, "The Micro-Gap chamber", Nucl. Instr. and Meth., **A335**, 1993, pp. 69.

[30] A. Boksenberg , & A. Burgess, *Astronomical observations with television sensors*, eds Glaspey, J.W. & Walker, G.A.H., 1973, pp. 21,

[31] The AAO Observers' Guide, http://www.ast.cam.ac.uk/AAO/local/www/cgt/obsguide/obsguide.html

[32] Bosch, L.A., "Dynamic uses of image intensifiers," Proc. SPIE, **2551**, 1995, pp.159.

[33] Waynant, R., Ediger, M., *Electro-Optics Handbook*, McGraw-Hill, New York, 1994.

[34] Read P.D., Van Breda I.G., Norton, T.J., "Performance of a 40mm unfilmed microchannel plate intensifier", Proc. SPIE **1235**, 1990, pp. 305.

[35] S. Vasile, P. Gothoskar, D. Sdrulla and R. Farrell, "Photon Detection with High Gain Avalanche Photodiode Arrays", IEEE Trans. Nucl. Sci. **45**, 1998, pp. 720.

[36] B. Matthews, "An ultra high resolution, electro-optical framing camera for reconnaissance and other applications using a 9216 by 9216 pixel, wafer scale, focal plane array", Proc. SPIE **3431**, 1998, pp. 144.

[37] J. Carbone, Z. Alam, C. Borman, S. Czebiniak, H. Ziegler, "Large format CID x-ray image sensors", Proc. SPIE **3301**, 1998, pp. 90.

[38] P. Holl, P. Fischer, R. Hartmann, G. Hasinger, J. Kollmer, N. Krause, P. Lechner, G. Lutz, N. Meidinger, I. Peric, R.H. Richter, H. Soltau, L. Strueder, J. Treis, J.E. Truemper, N. Wermes, "Active pixel sensors for imaging X-ray spectrometers", Proc. SPIE **4851**, 2003, pp. 770.

[39] X.Llopart, M.Campbell, R.Dinapoli, D.SanSegundo, E.Pernigotti, "Medipix2, a 64k pixel readout chip with 55 μm square elements working in single photon counting mode", IEEE Trans. Nucl. Sci., **49(5)**, 2002, pp. 2279.

[40] G.M. Williams A.L. Reinheimer, C.B. Johnson, K.D. Wheeler, N.D. Wodecki, V.W. Aebi & K.A. Costello, "Back-illuminated and electron-bombarded CCD low light level imaging system performance," Proc. SPIE, **2551**, 1995, pp.208.

[41] C. Papaliolios, P. Nisenson, S. Ebstein, "Speckle imaging with the PAPA detector", Applied Optics, **24(2)**, 1985, pp. 287.

[42] M. Alemi, M. Campbell, T. Gys, B. Mikulec, D. Piedigrossi, D. Puertolas, E. Rosso, R. Schomaker, W. Snoeys & K. Wyllie, "First operation of a hybrid photon detector

prototype with electrostatic cross-focussing and integrated silicon pixel readout", Nucl. Instr. Meth., **A449**, 2000, pp. 48.

[43] D. McCammon, W. Cui, M. Juda, J. Morgentahler, J. Zhong, R.L. Kelley, S.S. Holt, G.M. Madejski, S.H. Moseley, and A.E. Szymkowiak, "Thermal calorimeters for high resolution X-ray spectroscopy", Nucl. Instr. Meth., **A326**, 1993, pp. 157.

[44] R. Bellazzini, G. Spandre & N. Lumb, "Progress with micro-pattern gas detectors", Nucl. Instr. Meth., **A478**, 2002, pp. 13.

[45] F. Sauli, "GEM: A new concept for electron amplification in gas detectors", Nucl. Instr. Meth., **A386**, 1997, pp. 531.

[46] J.K. Black, A.N. Brunton, N.P. Bannister, P. Deines-Jones & K. Jahoda, "The imaging X-ray detector for Lobster-ISS", to be published in Nucl. Instr. and Meth. A.

[47] P. Gorenstein, F.R. Harnden Jr. & D.G. Fabricant, IEEE Trans. Nucl. Sci., **NS-28**, 1981, pp. 869.

[48] B. Aschenbach, H. Bräuninger, U. Briel, H. Fink, G. Hasinger, H. Hippmann, E. Pfeffermann, P. Predehl, J. Schmitt, K.H. Stephan, J. Trümper, W. Voges, and H.U. Zimmermann, ROSAT PSPC - Scientific Data Processing Requirement Document, MPE Internal Report **44**, 1985.

[49] Korff, Serge A. *Electron and Nuclear Counters*, 2nd ed.; Divan Nostrand Company, Inc., Toronto, 1955.

[50] F.M.Penning, Physica Vol.**1**, 1934, pp. 1028.

[51] I.M.Mason, G.Branduardi-Raymont, J.L.Culhane, R.H.D.Corbet, J.C.Ives and P.W.Sanford, IEEE Trans. Nucl. Sci., **NS-31**, 1984, pp 795.

[52] Y. Giomataris, Ph. Rebourgeard, J.P. Robert, G. Charpak. MICROMEGAS:A high-granularity position-sensitive gaseous detector for high particle-fluxenvironments, Nucl. Instr. and Meth., **A376**, 1996, pp. 29.

[53] R. Bellazzini, M. Bozzo, A. Brez, G. Gariano, L. Latronico, N. Lumb, A. Papanestis, G. Spandre, M.M. Massai, R. Ra§o, M.A. Spezziga, "The micro-groove detector", Nucl. Instr. and Meth., **A424**, 1999, pp. 444.

[54] S.F. Biagi and T.J. Jones, "The microdot gas avalanche chamber: an investigation of new geometries", Nucl. Instr. Meth., **A361**, 1995, pp. 72.

[55] Simons, D.G., de Korte, P.A.J., Peacock, A., Smith, A., Bleeker, J.A.M., 1985, IEEE, Trans. Nucl. Sci., **NS-32**, 1985, pp. 345.

[56] J.P. Boutot, P. Lavoute & G. Eschard, "Multianode photomultiplier for detection and localization of low light level events", IEEE Trans. Nucl. Sci., **NS-34**, 1987, pp. 449.

[57] P.T. Farnsworth, Electron multiplier, U.S. Patent No. 1,969,399, 1930.

[58] P. K. Oschepkov, B. N. Skvortsov, B. A. Osanov and I.V. Siprikov, Pribory. Tekh. Eksper., **4**, 1960, pp. 89.

[59] W. C. Wiley and C. F. Hendee, IRE Trans. Nucl. Sci. **NS-9**, 1962, pp. 103.

[60] G.W. Fraser, *X-ray detectors in astronomy*, Cambridge University Press, 1989.

[61] G.W. Fraser, J.F. Pearson, G.C. Smith, M. Lewis & M.A. Barstow, "The gain characteristics of microchannel-plate for X-ray photon counting" IEEE Trans. Nucl. Sci. **NS-30**, 1983, pp. 455.

[62] J.G. Timothy, "Curved-channel microchannel array plates", Rev. Sci. Instrum., **52(8)**, 1981, pp. 1131.

[63] Edgar, M.L., Lapington, J.S. and Smith, A., "The spatial extent of gain depression for MCP-based photon detectors", Rev. Sci. Instrum., **63(1)**, 1992, pp. 816.

[64] A.S.Tremsin, J.F.Pearson, G.W.Fraser, B.W.Feller and P.White, "Microchannel plate operation at high count rates: new results", Nucl. Instr. Meth., **A379**, 1996, pp.139.

[65] Edgar, M.L., Smith, A. and Lapington, J.S., "Long range effects of gain depression in microchannel plates", Proc. SPIE, **1743**, 1992, pp. 283.

[66] M. R. Garcia, J. H. Chappell, S. S. Murray, W. B. Feller, and G. W. Fraser, Low Noise Microchannel Plate Detectors for X-ray Astronomy, Proc. SPIE, **1140**, 1989, pp. 101.

[67] G.W. Fraser & J.F. Pearson, "The direct detection of thermal neutrons by imaging microchannel-plate detectors", Nucl. Instr. Meth., **A293**, 1990, pp. 569.

[68] R.C. Taylor, M.C. Hettrick and R. Malina, "Maximizing the quantum efficiency of microchannel plate detectors: The collection of photoelectrons from the interchannel web using an electric field", Rev. Sci. Instrum., **54(2)**, 1983, pp. 171.

[69] A.S. Tremsin, O.H.W. Siegmund, "The dependence of quantum efficiency of alkali halide photocathodes on the radiation incidence angle", Proc. SPIE, 3765, 1999, p. 441

[70] O.H.W. Siegmund, M. Gummin, G. Gaines, G. Naletto, J. Stock, R. Raffanti, J. Hull, R. Abiad, T. Rodriguez-Bell, T. Magoncelli, P. Jelinsky, W. Donakowski, K. Kromer, ``Performance of the double delay line microchannel plate detectors for the Far Ultraviolet Spectroscopic Explorer", Proc. SPIE, **3114**, 1997, pp. 283.

[71] Fordham, J. L. A., Bone, D. A., Oldfield, M. K., Bellis, J. G., Norton, T. J. The MIC photon counting detector, Proceedings of an ESA Symposium on Photon Detectors for Space Instrumentation, 1994, pp 103.

[72] C. Johnson, "Review of electron-bombarded CCD cameras", Proc. SPIE **3434**, 1998, p. 45.

[73] Joseph, C.L., "UV Image Sensors and Associated Technologies", Experimental Astronomy, **6**, 1995, pp. 97.

[74] P. Nisenson, 'Diffraction Limited Imaging with Very Large Telescopes', ed. D.M. Alloin & J. -M. Mariotti, Proc. NATO-ASI, 1988, pp. 157

[75] S. K. Saha, "Emerging trends of optical interferometry in astronomy", Bull. Astron. Soc. India, **27**, 1999, pp. 441.

[76] C. Firmani, L. Gutierrez, E. Ruiz, G.F. Bisiacchi, L. Salas, F. Paresce, C.W. Carlson and M. Lampton, "High Dispersion Spectrophotometry with the Mepsicron Photon Counter," Astronomy and Astrophysics, **134**, 1984, pp. 251.

[77] M. Lampton, F. Paresce, "The Ranicon: a resistive anode image converter", Rev. Sci. Instrum, **45(9)**, 1974, pp. 1098.

[78] G.W. Fraser & E. Mathieson, Nucl. Instr. Meth,, **179**, 1981, pp. 591.

[79] Zombeck, M.V., J. H. Chappell, A. Kenter, R., W. Moore, S. S. Murray, G.W. Fraser ,S. Serio "The High Resolution Camera (HRC) on the Advanced X-Ray Astrophysics Facility (AXAF)", Proc. SPIE, **2518**, 1995, pp. 96.

[80] Lapington, J.S., and Schwarz, H.E., "The design and manufacture of Wedge and Strip Anodes", IEEE Trans. Nucl. Sci., **NS-33**, 1986, pp. 288.

[81] O.H.W. Siegmund, S. Chakrabarti, J. Vallerga, S. Bower, R.F. Malina, "Application of wedge and strip image readout systems to detectors for astronomy", Proc. SPIE, **627**, 1986, pp. 660.

[82] R.W. Wijnaendts van Resandt, H.C. den Harink & J. Los, "A position dependent particle counter using microchannel plates", J. Phys. E., Scientific Instruments **9**, 1976, pp. 503.

[83] M. Lampton, R.F. Malina, "Quadrant anode image sensor", Rev. Sci. Instrum, **47(11)**, 1976, pp. 1360.

[84] R. Allemand, G. Thomas, "Nouveau Détecteur De Localisation", Nucl. Instr. Meth., **137**, 1976, pp. 141.

[85] Lapington, J.S., Smith, A.D., Walton, D.M., and Schwarz, H.E., "Microchannel plate pore size limited imaging with ultra-thin Wedge and Strip Anodes", IEEE Trans. Nucl. Sci., **NS-34**, 1987, pp. 431.

[86] Lapington, J.S., Breeveld, A.A., Edgar, M.L., and Trow, M.W. "A novel imaging readout with improved speed and resolution", Nucl. Instr. Meth., **A310**, 1991, pp. 299.

[87] E. Mathieson, G.C. Smith, and P.J. Gilvin, "The Graded-Density Cathode: A New Method for Position-Sensitive Radiation Detection", J. Phys. E: **13**, 1980, pp. 792.

[88] R. Lewis, "Detectors for synchrotron radiation", presented at PSD 6, to be published in Nucl. Instr. and Meth. A.

[89] Siegmund O. H. W., Tremsin A. S., Vallerga J. V. and Hull J., "Cross strip imaging anodes for microchannel plate detectors". IEEE Trans. Nucl. Sci. **48**, 2001, pp. 430.

[90] R. Gott, W. Parkes & K. Pounds, "X-ray image dissection using a channel multiplier array", Nucl. Instr. Meth., **81**, 1970, pp. 152.

[91] R.M. Tromp, M. Copel, M.C. Reuter, M. Horn-von Hoegen and J. Speidell, "A new two-dimensional particle detector for a toroidal electrostatic analyzer", Rev. Sci. Instrum. **62**, 1991, pp. 2679.

[92] K. Oba, M. Sugiyama, Y, Suzuki & Y. Yoshimura, "A 400 anode chevron microchannel plate PMT for high energy application", IEEE Trans. Nucl. Sci., **NS-26(1)**, 1979, pp. 346.

[93] Timothy J.G., "Optical detectors for spectroscopy," Publications of the Astronomical Society of the Pacific, **95**, 1983, pp. 810.

[94] C.L. Joseph, V.S. Argabright, J. Abraham, D. Dieball, S. Franka, M. Styonavich, C. Van Houten, A. Danks, B.E. Woodgate, "Performance results of the STIS flight MAMA detectors", Proc. SPIE, **2551**, 1995, pp. 248.

[95] W.E. McClintock, C.A. Barth, R.E. Steele, G.M. Lawrence, J.G. Timothy, "Rocket-borne instrument with a high-resolution microchannel plate detector for planetary UV spectroscopy", Applied Optics, **21(17)**, 1982, pp. 3071.

[96] J. Pearson, "The Development of a Fast Imaging Electron Detector Based on the CODACON Concept", presented at PSD 6, to be published in Nucl. Instr. and Meth. A.

[97] M.B. Williams, S.E. Sobottka, "High resolution two-dimensional readout of microchannel plates with large area delay lines", IEEE Trans. Nucl. Sci., **36(1)**, 1989, pp. 227

[98] J.V. Vallerga, O.H.W. Siegmund, "2K]2K resolution element photon counting MCP sensor with >200 kHz event rate capability", Nucl. Instr. Meth., **A442**, 2000, pp. 159.

[99] G.C. Smith, J.F. Pearson, E. Mathieson, "Microchannel plate read-out using graded-density electrodes", Nucl. Instr. Meth, **192**, 1982, pp. 383.

[100] Schwarz, H.E., and Lapington, J.S., "Optimisation of wedge and Strip Anodes", IEEE Trans. Nucl. Sci., **NS-32**, 1985, pp. 433.

[101] C.Martin, M.Lampton, R.F.Malina and H.O.Anger, "Wedge and Strip Anodes for Centroid-Finding Position-Sensitive Photon and Particle Detectors," Rev. Sci. Instrum., **52**, 1981, pp. 1067.

[102] C. Martin, & A. Rasmussen, "Mosaic wedge-and-strip arrays for large format microchannel plate detectors", IEEE Trans. Nucl. Sci., **36(1)**, 1989, pp. 836.

[103] J. Allison, R.J. Barlow, R. Canas, I.P. Duerdoth, F.K. Loebinger, A.A. Macbeth, P.G. Murphy & K. Stephens, "Diamond shaped cathode pads for the longitudinal coordinate from a drift chamber", Nucl. Instr. Meth., **A236**, 1985, pp 284.

[104] D.F. Anderson, H.K. Arvela, A. Breskin, G. Charpak: A simple "vernier" method for improving the accuracy of coordinate read-out in large wire chambers, Nucl. Instr. Meth., **224**, 1984, pp. 315.

[105] J. Thornton, "The application of the partition noise theory", Nucl. Instr. Meth, **A264**, 1987, pp. 523-525.

[106] C.F.G. Delaney, *Electronics for the Physicist*, Penguin, 1969.

[107] P.W. Nicholson, *Nuclear Electronics*, Wiley and Sons, 1974.

[108] Smith, A.D., Kessel, R., Lapington, J.S., and Walton, D.M., "Modulation Effects in Wedge and Strip Anodes", Rev. Sci. Instrum., **60(11)**, 1989, pp. 3509.

[109] Lapington, J.S., "The effects of secondary electron emission on the operation of position sensitive anodes", Nucl. Instr. Meth., **A392**, 1997, pp. 336.

[110] A.A. Breeveld, P.D. Thomas, "The grazing incidence detectors for the SOHO coronal diagnostic spectrometer", Proc. ESA Symposium on Photon Detectors for Space Instrumentation (**SEE N94-15025 03-19**), 1992, pp. 237.

[111] Kaye & Labey, *Tables of Physical and Chemical Constants*, 16th Edition, published by Longman Group Ltd., ISBN 0-582-22629-5.

[112] D.R. Lide (Ed.), *CRC Handbook of Physics andChemistry*, 74th Edition, CRC Press, Boca Raton,1993.

[113] J.E. Lapington, Private communication,

[114] J. Bresenham, "Algorithm for Computer Control of a Digital Plotter," IBM Systems Journal, **4(1)**, 1965, pp. 25.

[115] N.N.Hoan, Nucl. Instr. and Meth., **154**, 1978, pp. 597.

[116] J.Davelaar, A.Peacock and B.G.Taylor, IEEE Trans. Nucl. Sci., **NS-29**, 1982, pp. 142.

[117] R.Bouclier,G.Charpak,Z. Dimcovski,G.Fischer and F.Sauli, Nucl. Instr. and Meth., **68**, 1970, pp. 149.

[118] G.Charpak, Nature **270**, 1977, pp. 479.

[119] H.Sipila, Nucl. Instr. and Meth., **133**, 1976, pp. 251.

[120] G.D.Alkhazov, A.P.Komar and A.A.Vorob'ev, Nucl. Instr. and Meth., **48**, 1967, pp. 1

[121] J.Marzec and Z.Pawlowski, Nucl. Instr. and Meth., **200**, 1982, pp. 355.

[122] J.S.Lapington, A.D.Smith, D.M.Walton and H.E.Schwarz, IEEE Trans. Nucl. Sci., **NS-34**. 1987, pp. 431.

[123] Schwarz, H.E., Lapington, J.S., Hilliard, N.S., Rose, J.G., Sheather, P.H., and Culhane, J.L., "Applications of the Penning Gas Imager", SPIE, X-ray intrumentation in astronomy, **597**, 1986, pp. 178.

[124] Catura, R.C., Stern, R.A, Cash, W., Windt, D.L., Culhane, J.L., Lapington, J.S., and Barnsdale, K., "X-ray Objective Grating Spectrograph", SPIE, Grazing Incidence Optics for Astronomical and Laboratory Applications, **830**, 1987, pp. 204.

[125] J. Va'vra, "Review of Wire Chamber Ageing," Nucl. Instr. and Meth., **A252**, 1986, pp. 547.

[126] T.J. Norton, Private communication.

[127] H. Kawakami, Private communication.

[128] L.W. Acton, J.L. Culhane, A.H. Gabriel, R.D. Bentley, J.A. Bowles, J.G. Firth, M.L. Finch, C.W. Gilbreth, P. Guttridge, R.W. Hayes, E.G. Joki, B.B. Jones, B.J. Kent, J.W. Leibacher, R.A. Nobles, T.J. Patrick, K.J.H. Phillips, C.G. Rapley, P.H. Sheather, J.C. Sherman, J.P. Stark, L.A. Springer, R.F. Turner and C.J. Wolfson, "The Soft X-Ray Polychromator for the Solar Maximum Mission," Sol. Phys., **65**, 1980, pp. 53.

[129] R.Z. Fuzesy, J. Jaros, L. Kaufman, J. Marriner, S. Parker, V. Perez-Mendez and S. Redner, "A Gas Mixture for Multi-Wire Chambers with High Proportional Gain," Nucl. Instr. and Meth., **100**, 1972, pp. 267-268.

[130] J. Thornton, "The Application of the Partition Noise Theory," Nucl. Instr. and Meth., **A264**, 1988, pp. 523.

[131] G.C. Smith, J. Fischer and V. Radeka, "Photoelectron Range Limitations to the Spatial Resolution for X-rays in Gas Proportional Chambers," IEEE Trans. Nucl. Sci., **NS-31**, 1984, pp. 111.

[132] A.J.F. Den Boggende and C.J. Schrijver, "Electron Cloud Sizes in Gas-Filled Detectors," Nucl. Instr. and Meth., **220**, 1984, pp. 561.

[133] M.W. Trow, A.C. Bento and A. Smith, Rate dependent image distortions in proportional Counters , Nucl. Instr. and Meth., **A324**, 1994, pp. 232.

[134] N. Koshida and M. Hosobuchi, "Energy distribution of output electrons from a microchannel plate", Rev. Sci. Instrum., **56(7)**, 1985, pp. 1329.

[135] G.T. Weststeijn, "The wedge and strip anode", MSc thesis, SRON, 1987.

[136] J.R. Allington-Smith and H.E. Schwarz, "Imaging Photon Detectors for Optical Astronomy," Q. Jl R. astr. Soc., **25**, 1984, pp. 267.

[137] Lapington, J.S., Kessel, R., and Walton, D.M., "Spatial resolution limitations of microchannel plate/conductive charge division readout devices", Nucl. Instr. and Meth., **A273**, 1987, pp. 663.

[138] Edgar, M.L., Kessel, R., Lapington, J.S., and Walton, D.M., "The Spatial Charge Cloud Distribution of Microchannel Plates", Rev. Sci. Instrum., **60(12)**, 1989, pp.3673.

[139] H.Bruining, *Physics and Applications of Secondary Electron Emission* , Pergamon Press, 1954.

[140] H. Seiler, "Secondary electron emission in the scanning electron microscope", J. Appl. Phys., **54**(11), R1 (1983)

[141] J.S.Lapington, "Investigation of image non-linearities in a photon counting image tube", Proc. SPIE, **2209**, 1994, pp. 549.

[142] Vallerga, J.V., G.C. Kaplan, O.H.W. Siegmund, M. Lampton and R.F. Malina, "Imaging Characteristics of the Extreme Ultraviolet Explorer Microchannel Plate Detectors", IEEE Trans. Nucl. Sci., **NS-36**, 1989, pp. 881.

[143] W.B. Cheston, *Elementary Theory of Electric and Magnetic Fields*, 1964.

[144] G. Battistoni, P. Campana, V. Chiarella, U. Denni, E. Iarocci, and G. Nicoletti, Nucl. Instr. and Meth., **202**, 1982, pp. 459.

[145] O. Jagutzki, J. Barnstedt, U. Spillmann, L. Spielberger, V. Mergel, K. Ullmann-Pfleger, M. Grewing, and H. Schmidt-Böcking, "Fast-position and time-sensitive read-out of image intensifier for single photon detection", Proc. SPIE, **3764**, 1999, pp. 61.

[146] J.S. Lapington, J. Milnes, M. Page, M. Ingle, and K. Rees, "Novel Electronic Readout Systems For Photon Counting Imagers", Proc. SPIE, **4128**, 2000, pp. 120.

[147] Breeveld, A.A., Edgar, M.L., Smith, A., Lapington, J.S., and Thomas, P.D., "A SPAN MCP detector for the SOHO Coronal Diagnostic Spectrometer", Rev. Sci. Instrum., **63(1)**, 1992, pp. 673.

[148] Kawakami, H., Bone, D., Fordham, J., Michel, R. "The effect of event shape on centroiding in photon counting detectors", Nucl. Instr. and Meth., **348,** 1994, pp. 707.

[149] G. Knapp, "Crossed grid anode and its image partitioning", Rev. Sci. Instrum., **49(7),** 1978, pp. 982.

[150] A.A. Breeveld, M.L. Edgar,A. Smith, J.S. Lapington, and P.D. Thomas, "A SPAN MCP detector for the SOHO Coronal Diagnostic Spectrometer", Rev. Sci. Instrum., **63(1),** 1992, pp. 673.

[151] M.L. Edgar, PhD thesis, University of London, 1994.

[152] Edgar, M.L., Smith, A. and Lapington, J.S., "Long range effects of gain depression in microchannel plates", Proc. SPIE, **1743**, 1992, pp. 283.

[153] A.S. Tremsin, J.V. Vallerga, O.H.W. Siegmund, "Image translational shifts in microchannel plate detectors due to the MCP channel bias", Nucl. Instr. Meth., **A477**, 2002, pp.262.

[154] B.Sanderson, "Development of high resolution microchannel plate detectors for spatially linear high resolution imaging with the Vernier anode", PhD thesis, University of London, June 2001.

[155] Lapington, J.S., Sanderson, B. and Worth, L.B.C., "The Vernier electronic readout - high resolution and image stability from a charge division readout for microchannel plates", Proc. SPIE, **3445**, 1998, pp. 535.

[156] S.R. Jelinsky, O.H.W. Siegmund, and J.A. Mir, "Progress in soft x-ray and UV photocathodes", Proc. SPIE, **2808,** 1996, pp. 617.

[157] A. S. Tremsin, O. H. W. Siegmund, M. A. Gummin, P. N. Jelinsky, and J. M. Stock, "Electronic and optical moire'interference with microchannel plates: artifacts and benefits,"Appl. Opt., **38**, 1999, pp. 2240.

[158] B. Sanderson – personal communication

[159] Carter, M. K.; Cutler, R.; Patchett, B. E.; Read, P. D.; Waltham, "Transputer based image photon counting detector", Instrumentation in astronomy VII; Tucson, Proc. SPIE, **A91-29601**, 1990, pp. 644.

[160] Jelinsky, S.R., Siegmund, O.H., Mir, J.A., Proc. SPIE, **2808**, 1996, pp. 617

[161] J.A. Tandy, personal communication.

[162] N.P. Bannister, "The Spectroscopy of DA white dwarfs at high resolution", PhD Thesis, University of Leicester, 2001. Chapter 6, pp 139-157

[163] J.S.Lapington, B.Sanderson, L.B.C.Worth and J.A.Tandy, "Imaging achievements with the Vernier readout", Nucl. Instr. Meth., **A477**, 2002, pp. 250.

[164] A.S. Tremsin, O.H.W. Siegmund, "New Developments in the Position Sensitive Detectors Based on Microchannel Plates", Proceedings of 7th International Conference on Advanced Technology and Particle Physics, Como, 2001

[165] T.J.Norton, R.W.Airey, B.L.Morgan, J.L.A.Fordham and D.A.Bone, "An MCP Intensifier with High DQE for Astronomical photon Counting", Proc. Conf. on photoelectronic Image Devices, 1991, pp. 97.

[166] R.A. Kimble,P.C. Chen, J.P. Haas, T.J. Norton, L.J. Payne, J. Carbone, M. Corba, Proc. SPIE, **2518**, 1995, pp. 397.

[167] J.S.Lapington, K.Rees, "FIRE - a novel high speed imaging system for MCPs", Nucl. Instr. Meth., **A477**, 2002, pp. 273.

[168] Hewlett Packard, *Communications Components Designers Catalogue, GaAs and Silicon products*, 1993 pp. 8-58 to 8-61.

[169] Motorola, *High Performance ECL Data*, DL140/D, revision 4, 1996.

[170] J.S.Lapington, B.Sanderson, L.B.C.Worth and J.A.Tandy, "Imaging achievements with the Vernier readout", Nucl. Instr. Meth., **A477**, 2002, pp. 250.

[171] Monfardini, P. Trampus, R. Stalio, M. Vidali, N. Mahne, R. Battiston, M. Menichelli, P. Mazzinghi, "Orbiting photon-counting observatory for the Earth night-sky background: AURORA on MEGSAT-1" Proc. SPIE, **4498**, 2001, pp. 258.

[172] G. Charpak, W. Dominik, J.C. Santiard, F. Sauli, N. Solomey ,"Gaseous detectors with parallel electrodes and anode mesh planes", Nucl. Instr. and Meth., **A274**, 1989, pp. 275.

[173] T. Kenter, J. H. Chappell, K. Kobayashi, R. P. Kraft, G. R. Meehan, S. S. Murray, M. V. Zombeck, G. W. Fraser, J. F. Pearson, J. E. Lees, A. N. Brunton, M. Barbera, A. Collura, and S. Serio, "Performance and calibration of the AXAF High-Resolution Camera I: Imaging read-out", Proc. SPIE, **3114**, 1997, pp. 26.

[174] M.W. Trow and J.S. Lapington, "A high resolution position readout for proportional counters with fluorescence gating capability", Proc. SPIE, **2518**, 1995, pp. 457.

[175] O. Jagutzki, J.S. Lapington, L.B.C.Worth, V. Mergel, H. Schmidt-Böcking, "Position sensitive anodes for MCP read-out via image charge detection", Nucl. Instr. Meth., **A477**, 2002, pp. 256

[176] O.Toker et al., "VIKING, a CMOS low noise monolithic 128 channel frontend for Si-strip detector readout", Nucl. Instr. and Meth., **A340**, 1994, pp. 572.

[177] J.S. Lapington, B. Sanderson, "Microchannel Plate Limited Resolution With The Vernier Anode", Proc. SPIE, **4139**, 2000, pp. 242.

[178] B. Laprade & R. Starcher, *The 2 micron pore microchannel plate*, Bulr Electro-Optics, Inc., Sales literature, 2001

[179] A. S. Tremsin, J. V. Vallerga, O. H. W. Siegmund, C. P. Beetz, R. W. Boerstler, "The latest developments of high gain Si microchannel plates", Proc. SPIE, **4854**, 2002, pp. 215.

[180] IDE AS, Integrated Detector and Electronics, Høvik, Norway, Technical literature, 2003.

[181] J.S.Lapington, "Microchannel plate image readouts: In search of high resolution and count rate", Nucl. Instr. Meth., submitted.